

PARTICLE PHYSICS BOOKLET TABLE OF CONTENTS

1. Physical constants	4
2. Astrophysical constants	6
<i>Summary Tables of Particle Physics</i>	
Gauge and Higgs bosons	8
Leptons	14
Quarks	23
Mesons	25
Baryons*	159
Searches	188
Tests of conservation laws*	193
<i>Reviews, Tables, and Plots</i>	
9. Quantum chromodynamics *	196
10. Electroweak model and constraints on new physics *	200
11. Status of Higgs boson physics *	209
12. The CKM quark-mixing matrix *	211
13. <i>CP</i> violation *	218
14. Neutrino mass, mixing and oscillations *	221
15. Quark model *	228
16. Grand unified theories *	231
19. Structure functions *	237
22. Big-bang cosmology *	242
23. Inflation *	248
25. The cosmological parameters *	249
26. Dark matter *	253
27. Dark energy *	256
28. Cosmic microwave background *	257
29. Cosmic rays *	260
30. Accelerator physics of colliders *	261
31. High-energy collider parameters *	262
33. Passage of particles through matter *	263
34. Particle detectors at accelerators *	278
35. Particle detectors for non-accelerator physics *	290
36. Radioactivity and radiation protection *	297
37. Commonly used radioactive sources	299
38. Probability *	301
39. Statistics *	305
44. Clebsch-Gordan coefficients, spherical harmonics, and d functions	319
47. Kinematics *	321
49. Cross-section formulae for specific processes *	330
50. Neutrino cross-section measurements *	335
51. Plots of cross sections and related quantities *	337
6. Atomic and nuclear properties of materials *	338
4. Periodic table of the elements	inside back cover

*Abridged from the full *Review of Particle Physics*.

The following are found only in the full *Review* and on the Web:

<http://pdg.lbl.gov>

3. International System of Units (SI)
5. Electronic structure of the elements
7. Electromagnetic relations
8. Naming scheme for hadrons
17. Heavy-quark & soft-collinear effective theory
18. Lattice quantum chromodynamics
20. Fragmentation functions in e^+e^- , ep and pp collisions
21. Experimental tests of gravitational theory
24. Big-bang nucleosynthesis
32. Neutrino beam lines at proton synchrotrons
40. Monte Carlo techniques
41. Monte Carlo event generators
42. Monte Carlo neutrino event generators
43. Monte Carlo particle numbering scheme
45. SU(3) isoscalar factors and representation matrices
46. SU(n) multiplets and Young diagrams
48. Resonances

Table 1.1. Reviewed 2015 by P.J. Mohr and D.B. Newell (NIST). The set of constants excluding the last group (which come from the Particle Data Group) is recommended by CODATA for international use. The $1\text{-}\sigma$ uncertainties in the last digits are given in parentheses after the values. See the full edition of this *Review* for references and further explanation.

Quantity	Symbol, equation	Value	Uncertainty (ppb)
speed of light in vacuum	c	299 792 458 m s ⁻¹	exact*
Planck constant	h	6.626 070 040(81)×10 ⁻³⁴ J s	12
Planck constant, reduced	$\hbar \equiv h/2\pi$	1.054 571 800(13)×10 ⁻³⁴ J s = 6.582 119 514(40)×10 ⁻²² MeV s	12 6.1
electron charge magnitude	e	1.602 176 6208(98)×10 ⁻¹⁹ C = 4.803 204 673(30)×10 ⁻¹⁰ esu	6.1, 6.1
conversion constant	$\hbar c$	197.326 9788(12) MeV fm	6.1
conversion constant	$(\hbar c)^2$	0.389 379 3656(48) GeV ² mbarn	12
electron mass	m_e	0.510 998 9461(31) MeV/c ² = 9.109 383 56(11)×10 ⁻³¹ kg	6.2, 12
proton mass	m_p	938.272 0813(58) MeV/c ² = 1.672 621 898(21)×10 ⁻²⁷ kg = 1.007 276 466 879(91) u = 1836.152 673 89(17) m_e	6.2, 12 0.090, 0.095
deuteron mass	m_d	1875.612 928(12) MeV/c ²	6.2
unified atomic mass unit (u)	(mass ¹² C atom)/12 = (1 g)/(N _A mol)	931.494 0954(57) MeV/c ² = 1.660 539 040(20)×10 ⁻²⁷ kg	6.2, 12
permittivity of free space	$\epsilon_0 = 1/\mu_0 c^2$	8.854 187 817 ... ×10 ⁻¹² F m ⁻¹	exact
permeability of free space	μ_0	4π × 10 ⁻⁷ N A ⁻² = 12.566 370 614 ... ×10 ⁻⁷ N A ⁻²	exact
fine-structure constant	$\alpha = e^2/4\pi\epsilon_0\hbar c$	7.297 352 5664(17)×10 ⁻³ = 1/137.035 999 139(31) [†]	0.23, 0.23
classical electron radius	$r_e = e^2/4\pi\epsilon_0 m_e c^2$	2.817 940 3227(19)×10 ⁻¹⁵ m	0.68
(e ⁻ Compton wavelength)/2π	$\lambda_e = \hbar/m_e c = r_e \alpha^{-1}$	3.861 592 6764(18)×10 ⁻¹³ m	0.45
Bohr radius ($m_{\text{nucleus}} = \infty$)	$a_\infty = 4\pi\epsilon_0\hbar^2/m_e e^2 = r_e \alpha^{-2}$	0.529 177 210 67(12)×10 ⁻¹⁰ m	0.23
wavelength of 1 eV/c particle	$hc/(1 \text{ eV})$	1.239 841 9739(76)×10 ⁻⁶ m	6.1
Rydberg energy	$hcR_\infty = m_e e^4/2(4\pi\epsilon_0)^2\hbar^2 = m_e c^2 \alpha^2/2$	13.605 693 009(84) eV	6.1
Thomson cross section	$\sigma_T = 8\pi r_e^2/3$	0.665 245 871 58(91) barn	1.4

Bohr magneton	$\mu_B = e\hbar/2m_e$	$5.788\ 381\ 8012(26)\times 10^{-11}$ MeV T ⁻¹	0.45
nuclear magneton	$\mu_N = e\hbar/2m_p$	$3.152\ 451\ 2550(15)\times 10^{-14}$ MeV T ⁻¹	0.46
electron cyclotron freq./field	$\omega_{\text{cycl}}^e/B = e/m_e$	$1.758\ 820\ 024(11)\times 10^{11}$ rad s ⁻¹ T ⁻¹	6.2
proton cyclotron freq./field	$\omega_{\text{cycl}}^p/B = e/m_p$	$9.578\ 833\ 226(59)\times 10^7$ rad s ⁻¹ T ⁻¹	6.2
gravitational constant [‡]	G_N	$6.674\ 08(31)\times 10^{-11}$ m ³ kg ⁻¹ s ⁻² = $6.708\ 61(31)\times 10^{-39}$ $\hbar c$ (GeV/c ²) ⁻²	4.7×10^4 4.7×10^4
standard gravitational accel.	g_N	$9.806\ 65$ m s ⁻²	exact
Avogadro constant	N_A	$6.022\ 140\ 857(74)\times 10^{23}$ mol ⁻¹	12
Boltzmann constant	k	$1.380\ 648\ 52(79)\times 10^{-23}$ J K ⁻¹ = $8.617\ 3303(50)\times 10^{-5}$ eV K ⁻¹	570 570
molar volume, ideal gas at STP	$N_A k(273.15\text{ K})/(101\ 325\text{ Pa})$	$22.413\ 962(13)\times 10^{-3}$ m ³ mol ⁻¹	570
Wien displacement law constant	$b = \lambda_{\text{max}} T$	$2.897\ 7729(17)\times 10^{-3}$ m K	570
Stefan-Boltzmann constant	$\sigma = \pi^2 k^4/60\hbar^3 c^2$	$5.670\ 367(13)\times 10^{-8}$ W m ⁻² K ⁻⁴	2300
Fermi coupling constant**	$G_F/(\hbar c)^3$	$1.166\ 378\ 7(6)\times 10^{-5}$ GeV ⁻²	500
weak-mixing angle	$\sin^2 \hat{\theta}(M_Z)$ ($\overline{\text{MS}}$)	$0.231\ 29(5)^{\dagger\dagger}$	2.2×10^5
W^\pm boson mass	m_W	$80.385(15)$ GeV/c ²	1.9×10^5
Z^0 boson mass	m_Z	$91.1876(21)$ GeV/c ²	2.3×10^4
strong coupling constant	$\alpha_s(m_Z)$	$0.1182(12)$	1.0×10^7
$\pi = 3.141\ 592\ 653\ 589\ 793\ 238$ $e = 2.718\ 281\ 828\ 459\ 045\ 235$ $\gamma = 0.577\ 215\ 664\ 901\ 532\ 861$			
1 in $\equiv 0.0254$ m 1 G $\equiv 10^{-4}$ T		1 eV = $1.602\ 176\ 6208(98) \times 10^{-19}$ J	kT at 300 K = $[38.681\ 740(22)]^{-1}$ eV
1 Å $\equiv 0.1$ nm 1 dyne $\equiv 10^{-5}$ N		1 eV/c ² = $1.782\ 661\ 907(11) \times 10^{-36}$ kg	0 °C $\equiv 273.15$ K
1 barn $\equiv 10^{-28}$ m ² 1 erg $\equiv 10^{-7}$ J $2.997\ 924\ 58 \times 10^9$ esu = 1 C		1 atmosphere $\equiv 760$ Torr $\equiv 101\ 325$ Pa	

* The meter is the length of the path traveled by light in vacuum during a time interval of 1/299 792 458 of a second.

† At $Q^2 = 0$. At $Q^2 \approx m_W^2$ the value is $\sim 1/128$. • ‡ Absolute lab measurements of G_N have been made only on scales of about 1 cm to 1 m.

** See the discussion in Sec. 10, “Electroweak model and constraints on new physics.”

†† The corresponding $\sin^2 \theta$ for the effective angle is 0.23155(5).

2. ASTROPHYSICAL CONSTANTS AND PARAMETERS

Table 2.1. Revised March 2016 by D.E. Groom (LBNL). Figures in parentheses give 1- σ uncertainties in last place(s). This table represents neither a critical review nor an adjustment of the constants, and is not intended as a primary reference. See the full *Review* for references and details.

Quantity	Symbol, equation	Value	Reference, footnote
speed of light	c	$299\,792\,458\text{ m s}^{-1}$	exact[4]
Newtonian constant of gravitation	G_N	$6.674\,08(31) \times 10^{-11}\text{ m}^3\text{ kg}^{-1}\text{ s}^{-2}$	[1]
Planck mass	$\sqrt{\hbar c/G_N}$	$1.220\,910(29) \times 10^{19}\text{ GeV}/c^2$ $= 2.176\,47(5) \times 10^{-8}\text{ kg}$	[1]
Planck length	$\sqrt{\hbar G_N/c^3}$	$1.616\,229(38) \times 10^{-35}\text{ m}$	[1]
standard acceleration of gravity	g_N	$9.806\,65\text{ m s}^{-2}$	exact[1]
jansky (flux density)	Jy	$10^{-26}\text{ W m}^{-2}\text{ Hz}^{-1}$	definition
tropical year (equinox to equinox) (2011)	yr	$31\,556\,925.2\text{ s} \approx \pi \times 10^7\text{ s}$	[5]
sidereal year (fixed star to fixed star) (2011)		$31\,558\,149.8\text{ s} \approx \pi \times 10^7\text{ s}$	[5]
mean sidereal day (2011) (time between vernal equinox transits)		$23^{\text{h}}\,56^{\text{m}}\,04^{\text{s}}.090\,53$	[5]
astronomical unit	au	$149\,597\,870\,700\text{ m}$	exact [6]
parsec (1 au/1 arc sec)	pc	$3.085\,677\,581\,49 \times 10^{16}\text{ m} = 3.262 \dots\text{ ly}$	exact [7]
light year (deprecated unit)	ly	$0.306\,6 \dots\text{ pc} = 0.946\,053 \dots \times 10^{16}\text{ m}$	
Schwarzschild radius of the Sun	$2G_N M_\odot/c^2$	$2.953\,250\,24\text{ km}$	[8]
Solar mass	M_\odot	$1.988\,48(9) \times 10^{30}\text{ kg}$	[9]
nominal Solar equatorial radius	R_\odot	$6.957 \times 10^8\text{ m}$	exact [10]
nominal Solar luminosity	L_\odot	$3.828 \times 10^{26}\text{ W}$	exact [10,12]
Schwarzschild radius of the Earth	$2G_N M_\oplus/c^2$	$8.870\,056\,580(18)\text{ mm}$	[13]
Earth mass	M_\oplus	$5.972\,4(3) \times 10^{24}\text{ kg}$	[14]
nominal Earth equatorial radius	R_\oplus	$6.378\,1 \times 10^6\text{ m}$	exact [10]
luminosity conversion	L	$3.0128 \times 10^{28} \times 10^{-0.4 M_{\text{bol}}}\text{ W}$	[15]
flux conversion	\mathcal{F}	$(M_{\text{bol}} = \text{absolute bolometric magnitude} = \text{bolometric magnitude at 10 pc})$ $2.5180 \times 10^{-8} \times 10^{-0.4 m_{\text{bol}}}\text{ W m}^{-2}$ $(m_{\text{bol}} = \text{apparent bolometric magnitude})$	[15]
ABsolute monochromatic magnitude	AB	$-2.5 \log_{10} f_\nu - 56.10$ (for f_ν in $\text{W m}^{-2}\text{ Hz}^{-1}$) $= -2.5 \log_{10} f_\nu + 8.90$ (for f_ν in Jy)	[16]
Solar angular velocity around the Galactic center	Θ_0/R_0	$30.3 \pm 0.9\text{ km s}^{-1}\text{ kpc}^{-1}$	[17]
Solar distance from Galactic center	R_0	$8.00 \pm 0.25\text{ kpc}$	[17,18]
circular velocity at R_0	v_0 or Θ_0	$254(16)\text{ km s}^{-1}$	[17]
escape velocity from Galaxy	v_{esc}	$498\text{ km/s} < v_{\text{esc}} < 608\text{ km/s}$	[19]
local disk density	ρ_{disk}	$3\text{--}12 \times 10^{-24}\text{ g cm}^{-3} \approx 2\text{--}7\text{ GeV}/c^2\text{ cm}^{-3}$	[20]
local dark matter density	ρ_χ	canonical value $0.3\text{ GeV}/c^2\text{ cm}^{-3}$ within factor 2-3	[21]

present day CMB temperature	T_0	2.7255(6) K	[22,24]
present day CMB dipole amplitude		3.3645(20) mK	[22,23]
Solar velocity with respect to CMB		369(1) km s ⁻¹ towards $(\ell, b) = (263.99(14)^\circ, 48.26(3)^\circ)$	[22,25]
Local Group velocity with respect to CMB	v_{LG}	627(22) km s ⁻¹ towards $(\ell, b) = (276(3)^\circ, 30(3)^\circ)$	[22,25]
number density of CMB photons	n_γ	410.7($T/2.7255$) ³ cm ⁻³	[26]
entropy density/Boltzmann constant	s/k	2 891.2 ($T/2.7255$) ³ cm ⁻³	[26]
present day Hubble expansion rate	H_0	100 h km s ⁻¹ Mpc ⁻¹ = $h \times (9.777\,752 \text{ Gyr})^{-1}$	[27]
scale factor for Hubble expansion rate	h	0.678(9)	[2,3]
Hubble length	c/H_0	0.925 0629 $\times 10^{26} h^{-1}$ m = 1.374(18) $\times 10^{26}$ m	
scale factor for cosmological constant	$c^2/3H_0^2$	2.85247 $\times 10^{51} h^{-2}$ m ² = 6.20(17) $\times 10^{51}$ m ²	
critical density of the Universe	$\rho_{\text{crit}} = 3H_0^2/8\pi G_N$	1.878 40(9) $\times 10^{-29} h^2$ g cm ⁻³ = 1.053 71(5) $\times 10^{-5} h^2$ (GeV/ c^2) cm ⁻³ = 2.775 37(13) $\times 10^{11} h^2 M_\odot \text{Mpc}^{-3}$	
baryon-to-photon ratio (from BBN)	$\eta = n_{\text{b}}/n_\gamma$	(5.8 $\times 10^{-10} \leq \eta \leq 6.6 \times 10^{-10}$) (95% CL)	[28]
number density of baryons	n_{b}	2.503(26) $\times 10^{-7} \text{ cm}^{-3}$ (2.4 $\times 10^{-7} < n_{\text{b}} < 2.7 \times 10^{-7}$) cm ⁻³ (95% CL)	[2,3,29,30]
CMB radiation density of the Universe	$\Omega_\gamma = \rho_\gamma/\rho_{\text{crit}}$	2.473 $\times 10^{-5} (T/2.7255)^4 h^{-2} = 5.38(15) \times 10^{-5}$	$\eta \times n_\gamma$ [26]
baryon density of the Universe	$\Omega_{\text{b}} = \rho_{\text{b}}/\rho_{\text{crit}}$	$\ddagger 0.02226(23) h^{-2} = \dagger 0.0484(10)$	[2,3,23]
cold dark matter density of the universe	$\Omega_{\text{cdm}} = \rho_{\text{cdm}}/\rho_{\text{crit}}$	$\ddagger 0.1186(20) h^{-2} = \dagger 0.258(11)$	[2,3,23]
100 \times approx to r_*/D_{A}	$100 \times \theta_{\text{MC}}$	$\ddagger 1.0410(5)$	[2,3]
reionization optical depth	τ	$\ddagger 0.066(16)$	[2,3]
scalar spectral index	n_{s}	$\ddagger 0.968(6)$	[2,3]
ln pwr primordial curvature pert. ($k_0=0.05 \text{ Mpc}^{-1}$)	$\ln(10^{10} \Delta_{\mathcal{R}}^2)$	$\ddagger 3.062(29)$	[2,3]
dark energy density of the Λ CDM Universe	Ω_Λ	$\dagger 0.692 \pm 0.012$	[2,3]
pressureless matter density of the Universe	$\Omega_{\text{m}} = \Omega_{\text{cdm}} + \Omega_{\text{b}}$	$\dagger 0.308 \pm 0.012$	[2,3]
fluctuation amplitude at 8 h ⁻¹ Mpc scale	σ_8	$\dagger 0.815 \pm 0.009$	[2,3]
redshift of matter-radiation equality	z_{eq}	$\dagger 3365 \pm 44$	[2]
redshift at half reionization	z_{reion}	$\dagger 8.8_{-1.4}^{+1.7}$	[2]
age of the Universe	t_0	$\dagger 13.80 \pm 0.04 \text{ Gyr}$	[2]
effective number of neutrinos	N_{eff}	$\# 3.1 \pm 0.6$	[2,33]
sum of neutrino masses	$\sum m_\nu$	$\# < 0.68 \text{ eV}$ (Planck CMB); $\geq 0.05 \text{ eV}$ (mixing)	[2,34,35]
neutrino density of the Universe	$\Omega_\nu = h^{-2} \sum m_{\nu_i}/93.04 \text{ eV}$	$\# < 0.016$ (Planck CMB); ≥ 0.0012 (mixing)	[2,34,35]
curvature	Ω_{K}	$\# -0.005_{-0.017}^{+0.016}$ (95%CL)	[2]
running spectral index slope, $k_0 = 0.002 \text{ Mpc}^{-1}$	$dn_{\text{s}}/d \ln k$	$\# -0.003(15)$	[2]
tensor-to-scalar field perturbations ratio, $k_0=0.002 \text{ Mpc}^{-1}$	$r = T/S$	$\# < 0.114$ at 95% CL; no running	[2,3]
dark energy equation of state parameter	w	-0.97 ± 0.05	[31,36]

TESTS OF CONSERVATION LAWS

Updated June 2016 by L. Wolfenstein (Carnegie-Mellon University) and C.-J. Lin (LBNL).

In the following text, we list the best limits from the Test of Conservation Laws table from the full *Review of Particle Physics*. Complete details are in that full *Review*. Limits in this text are for CL=90% unless otherwise specified. The Table is in two parts: “Discrete Space-Time Symmetries,” *i.e.*, C , P , T , CP , and CPT ; and “Number Conservation Laws,” *i.e.*, lepton, baryon, hadronic flavor, and charge conservation. The references for these data can be found in the the Particle Listings in the *Review*. A discussion of these tests follows.

CPT INVARIANCE

General principles of relativistic field theory require invariance under the combined transformation CPT . The simplest tests of CPT invariance are the equality of the masses and lifetimes of a particle and its antiparticle. The best test comes from the limit on the mass difference between K^0 and \bar{K}^0 . Any such difference contributes to the CP -violating parameter ϵ .

CP AND T INVARIANCE

Given CPT invariance, CP violation and T violation are equivalent. The original evidence for CP violation came from the measurement of $|\eta_{+-}| = |A(K_L^0 \rightarrow \pi^+\pi^-)/A(K_S^0 \rightarrow \pi^+\pi^-)| = (2.232 \pm 0.011) \times 10^{-3}$. This could be explained in terms of K^0 - \bar{K}^0 mixing, which also leads to the asymmetry $[\Gamma(K_L^0 \rightarrow \pi^-e^+\nu) - \Gamma(K_L^0 \rightarrow \pi^+e^-\bar{\nu})]/[\text{sum}] = (0.334 \pm 0.007)\%$. Evidence for CP violation in the kaon decay amplitude comes from the measurement of $(1 - |\eta_{00}/\eta_{+-}|)/3 = \text{Re}(\epsilon'/\epsilon) = (1.66 \pm 0.23) \times 10^{-3}$. In the Standard Model much larger CP -violating effects are expected. The first of these, which is associated with B - \bar{B} mixing, is the parameter $\sin(2\beta)$ now measured quite accurately to be 0.679 ± 0.020 . A number of other CP -violating observables are being measured in B decays; direct evidence for CP violation in the B decay amplitude comes from the asymmetry $[\Gamma(\bar{B}^0 \rightarrow K^-\pi^+) - \Gamma(B^0 \rightarrow K^+\pi^-)]/[\text{sum}] = -0.082 \pm 0.006$. Direct tests of T violation are much more difficult; a measurement by CPLEAR of the difference between the oscillation probabilities of K^0 to \bar{K}^0 and \bar{K}^0 to K^0 is related to T violation [3]. A nonzero value of the electric dipole

moment of the neutron and electron requires both P and T violation. The current experimental results are $< 3.0 \times 10^{-26}$ e cm (neutron), and $< 8.7 \times 10^{-29}$ e cm (electron) at the 90% C.L. The BABAR experiment reported the first direct observation of T violation in the B system. The measured T -violating parameters in the time evolution of the neutral B mesons are $\Delta S_T^+ = -1.37 \pm 0.15$ and $\Delta S_T^- = 1.17 \pm 0.21$, with a significance of 14σ [4]. This observation of T violation, with exchange of initial and final states of the neutral B , was made possible in a B -factory using the Einstein-Podolsky-Rosen Entanglement of the two B 's produced in the decay of the $\Upsilon(4S)$ and the two time-ordered decays of the B 's as filtering measurements of the meson state [5].

CONSERVATION OF LEPTON NUMBERS

Present experimental evidence and the standard electroweak theory are consistent with the absolute conservation of three separate lepton numbers: electron number L_e , muon number L_μ , and tau number L_τ , except for the effect of neutrino mixing associated with neutrino masses. Searches for violations are of the following types:

a) $\Delta L = 2$ for one type of charged lepton. The best limit comes from the search for neutrinoless double beta decay $(Z, A) \rightarrow (Z + 2, A) + e^- + e^-$. The best laboratory limit is $t_{1/2} > 1.07 \times 10^{26}$ yr (CL=90%) for ^{136}Xe from the KamLAND-Zen experiment [6].

b) Conversion of one charged-lepton type to another. For purely leptonic processes, the best limits are on $\mu \rightarrow e\gamma$ and $\mu \rightarrow 3e$, measured as $\Gamma(\mu \rightarrow e\gamma)/\Gamma(\mu \rightarrow \text{all}) < 5.7 \times 10^{-13}$ and $\Gamma(\mu \rightarrow 3e)/\Gamma(\mu \rightarrow \text{all}) < 1.0 \times 10^{-12}$.

c) Conversion of one type of charged lepton into another type of charged antilepton. The case most studied is $\mu^- + (Z, A) \rightarrow e^+ + (Z - 2, A)$, the strongest limit being $\Gamma(\mu^- \text{Ti} \rightarrow e^+ \text{Ca})/\Gamma(\mu^- \text{Ti} \rightarrow \text{all}) < 3.6 \times 10^{-11}$.

d) Neutrino oscillations. It is expected even in the standard electroweak theory that the lepton numbers are not separately conserved, as a consequence of lepton mixing analogous to Cabibbo-Kobayashi-Maskawa quark mixing. However, if the only source of lepton-number violation is the mixing of low-mass neutrinos then processes such as $\mu \rightarrow e\gamma$ are expected to have extremely small

unobservable probabilities. For small neutrino masses, the lepton-number violation would be observed first in neutrino oscillations, which have been the subject of extensive experimental studies.

CONSERVATION OF HADRONIC FLAVORS

In strong and electromagnetic interactions, hadronic flavor is conserved, *i.e.* the conversion of a quark of one flavor (d, u, s, c, b, t) into a quark of another flavor is forbidden. In the Standard Model, the weak interactions violate these conservation laws in a manner described by the Cabibbo-Kobayashi-Maskawa mixing (see the section “Cabibbo-Kobayashi-Maskawa Mixing Matrix”). The way in which these conservation laws are violated is tested as follows:

(a) $\Delta S = \Delta Q$ rule. In the strangeness-changing semileptonic decay of strange particles, the strangeness change equals the change in charge of the hadrons. Tests come from limits on decay rates such as $\Gamma(\Sigma^+ \rightarrow ne^+\nu)/\Gamma(\Sigma^+ \rightarrow \text{all}) < 5 \times 10^{-6}$, and from a detailed analysis of $K_L \rightarrow \pi e \nu$, which yields the parameter x , measured to be $(\text{Re } x, \text{Im } x) = (-0.002 \pm 0.006, 0.0012 \pm 0.0021)$. Corresponding rules are $\Delta C = \Delta Q$ and $\Delta B = \Delta Q$.

(b) Change of flavor by two units. In the Standard Model this occurs only in second-order weak interactions. The classic example is $\Delta S = 2$ via $K^0 - \bar{K}^0$ mixing. The $\Delta B = 2$ transitions in the B^0 and B_s^0 systems via mixing are also well established. There is now strong evidence of $\Delta C = 2$ transition in the charm sector. with the mass difference All results are consistent with the second-order calculations in the Standard Model.

(c) Flavor-changing neutral currents. In the Standard Model the neutral-current interactions do not change flavor. The low rate $\Gamma(K_L \rightarrow \mu^+ \mu^-)/\Gamma(K_L \rightarrow \text{all}) = (6.84 \pm 0.11) \times 10^{-9}$ puts limits on such interactions; the nonzero value for this rate is attributed to a combination of the weak and electromagnetic interactions. The best test should come from $K^+ \rightarrow \pi^+ \nu \bar{\nu}$. The LHCb and CMS experiments have recently observed the FCNC decay of $B_s^0 \rightarrow \mu^+ \mu^-$. The current world average value is $\Gamma(B_s^0 \rightarrow \mu^+ \mu^-)/\Gamma(B_s^0 \rightarrow \text{all}) = (2.9_{-0.6}^{+0.7}) \times 10^{-9}$, which is consistent with the Standard Model expectation.

9. QUANTUM CHROMODYNAMICS

Revised September 2015 (April 2016 for section on α_s) by S. Bethke (Max-Planck-Institute of Physics, Munich), G. Dissertori (ETH Zurich), and G.P. Salam (CERN).

9.1. Basics

Quantum Chromodynamics (QCD), the gauge field theory that describes the strong interactions of colored quarks and gluons, is the SU(3) component of the SU(3)×SU(2)×U(1) Standard Model of Particle Physics.

The Lagrangian of QCD is given by

$$\mathcal{L} = \sum_q \bar{\psi}_{q,a} (i\gamma^\mu \partial_\mu \delta_{ab} - g_s \gamma^\mu t_{ab}^C \mathcal{A}_\mu^C - m_q \delta_{ab}) \psi_{q,b} - \frac{1}{4} F_{\mu\nu}^A F^{A\mu\nu}, \quad (9.1)$$

where repeated indices are summed over. The γ^μ are the Dirac γ -matrices. The $\psi_{q,a}$ are quark-field spinors for a quark of flavor q and mass m_q , with a color-index a that runs from $a = 1$ to $N_c = 3$, *i.e.* quarks come in three “colors.” Quarks are said to be in the fundamental representation of the SU(3) color group.

The \mathcal{A}_μ^C correspond to the gluon fields, with C running from 1 to $N_c^2 - 1 = 8$, *i.e.* there are eight kinds of gluon. Gluons transform under the adjoint representation of the SU(3) color group. The t_{ab}^C correspond to eight 3×3 matrices and are the generators of the SU(3) group (cf. the section on “SU(3) isoscalar factors and representation matrices” in this *Review* with $t_{ab}^C \equiv \lambda_{ab}^C/2$). They encode the fact that a gluon’s interaction with a quark rotates the quark’s color in SU(3) space. The quantity g_s is the QCD coupling constant. Finally, the field tensor $F_{\mu\nu}^A$ is given by

$$F_{\mu\nu}^A = \partial_\mu \mathcal{A}_\nu^A - \partial_\nu \mathcal{A}_\mu^A - g_s f_{ABC} \mathcal{A}_\mu^B \mathcal{A}_\nu^C \quad [t^A, t^B] = i f_{ABC} t^C, \quad (9.2)$$

where the f_{ABC} are the structure constants of the SU(3) group.

Neither quarks nor gluons are observed as free particles. Hadrons are color-singlet (*i.e.* color-neutral) combinations of quarks, anti-quarks, and gluons.

Ab-initio predictive methods for QCD include lattice gauge theory and perturbative expansions in the coupling. The Feynman rules of QCD involve a quark-antiquark-gluon ($q\bar{q}g$) vertex, a 3-gluon vertex (both proportional to g_s), and a 4-gluon vertex (proportional to g_s^2). A full set of Feynman rules is to be found for example in Ref. 1.

Useful color-algebra relations include: $t_{ab}^A t_{bc}^A = C_F \delta_{ac}$, where $C_F \equiv (N_c^2 - 1)/(2N_c) = 4/3$ is the color-factor (“Casimir”) associated with gluon emission from a quark; $f_{ACD} f_{BCD} = C_A \delta_{AB}$ where $C_A \equiv N_c = 3$ is the color-factor associated with gluon emission from a gluon; $t_{ab}^A t_{ab}^B = T_R \delta_{AB}$, where $T_R = 1/2$ is the color-factor for a gluon to split to a $q\bar{q}$ pair.

The fundamental parameters of QCD are the coupling g_s (or $\alpha_s = \frac{g_s^2}{4\pi}$) and the quark masses m_q .

9.1.1. Running coupling: In the framework of perturbative QCD (pQCD), predictions for observables are expressed in terms of the renormalized coupling $\alpha_s(\mu_R^2)$, a function of an (unphysical) renormalization scale μ_R . When one takes μ_R close to the scale of the momentum transfer Q in a given process, then $\alpha_s(\mu_R^2 \simeq Q^2)$ is indicative of the effective strength of the strong interaction in that process.

The coupling satisfies the following renormalization group equation (RGE):

$$\mu_R^2 \frac{d\alpha_s}{d\mu_R^2} = \beta(\alpha_s) = -(b_0\alpha_s^2 + b_1\alpha_s^3 + b_2\alpha_s^4 + \dots) \quad (9.3)$$

where $b_0 = (11C_A - 4n_f T_R)/(12\pi) = (33 - 2n_f)/(12\pi)$ is referred to as the 1-loop beta-function coefficient, the 2-loop coefficient is $b_1 = (17C_A^2 - n_f T_R(10C_A + 6C_F))/(24\pi^2) = (153 - 19n_f)/(24\pi^2)$, and the 3-loop coefficient is, in $\overline{\text{MS}}$ scheme, $b_2 = (2857 - \frac{5033}{9}n_f + \frac{325}{27}n_f^2)/(128\pi^3)$ for the SU(3) values of C_A and C_F . The 4-loop coefficient, b_3 , is to be found in Refs. 11, 12. The minus sign in Eq. (9.3) is the origin of Asymptotic Freedom, *i.e.* the fact that the strong coupling becomes weak for processes involving large momentum transfers (“hard processes”), $\alpha_s \sim 0.1$ for momentum transfers in the 100 GeV – TeV range.

The β -function coefficients, the b_i , are given for the coupling of an *effective theory* in which n_f of the quark flavors are considered light ($m_q \ll \mu_R$), and in which the remaining heavier quark flavors decouple from the theory. One may relate the coupling for the theory with $n_f + 1$ light flavors to that with n_f flavors through an equation of the form

$$\alpha_s^{(n_f+1)}(\mu_R^2) = \alpha_s^{(n_f)}(\mu_R^2) \left(1 + \sum_{n=1}^{\infty} \sum_{\ell=0}^n c_{n\ell} [\alpha_s^{(n_f)}(\mu_R^2)]^n \ln^\ell \frac{\mu_R^2}{m_h^2} \right), \quad (9.4)$$

where m_h is the mass of the $(n_f + 1)^{\text{th}}$ flavor, and the first few $c_{n\ell}$ coefficients are $c_{11} = \frac{1}{6\pi}$, $c_{10} = 0$, $c_{22} = c_{11}^2$, $c_{21} = \frac{19}{24\pi^2}$, and $c_{20} = -\frac{11}{72\pi^2}$ when m_h is the $\overline{\text{MS}}$ mass at scale m_h ($c_{20} = \frac{7}{24\pi^2}$ when m_h is the pole mass — mass definitions are discussed below and in the review on “Quark Masses”). Terms up to $c_{4\ell}$ are to be found in Refs. 16, 17. Numerically, when one chooses $\mu_R = m_h$, the matching is a modest effect, owing to the zero value for the c_{10} coefficient.

Working in an energy range where the number of flavors is taken constant, a simple exact analytic solution exists for Eq. (9.3) only if one neglects all but the b_0 term, giving $\alpha_s(\mu_R^2) = (b_0 \ln(\mu_R^2/\Lambda^2))^{-1}$. Here Λ is a constant of integration, which corresponds to the scale where the perturbatively-defined coupling would diverge, *i.e.* it is the non-perturbative scale of QCD. A convenient approximate analytic solution to the RGE that includes also the b_1 , b_2 , and b_3 terms is given by (see for example Ref. 19),

$$\alpha_s(\mu_R^2) \simeq \frac{1}{b_0 t} \left(1 - \frac{b_1 \ln t}{b_0^2 t} + \frac{b_1^2 (\ln^2 t - \ln t - 1) + b_0 b_2}{b_0^4 t^2} - \frac{b_1^3 (\ln^3 t - \frac{5}{2} \ln^2 t - 2 \ln t + \frac{1}{2}) + 3b_0 b_1 b_2 \ln t - \frac{1}{2} b_0^2 b_3}{b_0^6 t^3} \right), \quad t \equiv \ln \frac{\mu_R^2}{\Lambda^2}, \quad (9.5)$$

again parametrized in terms of a constant Λ . Note that Eq. (9.5) is one of several possible approximate 4-loop solutions for $\alpha_s(\mu_R^2)$, and that a value for Λ only defines $\alpha_s(\mu_R^2)$ once one knows which particular approximation is being used. An alternative to the use of formulas such as Eq. (9.5) is to solve the RGE exactly, numerically (including the discontinuities, Eq. (9.4), at flavor thresholds). In such cases the quantity Λ is not defined

at all. For these reasons, in determinations of the coupling, it has become standard practice to quote the value of α_s at a given scale (typically the mass of the Z boson, M_Z) rather than to quote a value for Λ .

The value of the coupling, as well as the exact forms of the b_2 , c_{10} (and higher-order) coefficients, depend on the renormalization scheme in which the coupling is defined, *i.e.* the convention used to subtract infinities in the context of renormalization. The coefficients given above hold for a coupling defined in the $\overline{\text{MS}}$ scheme.

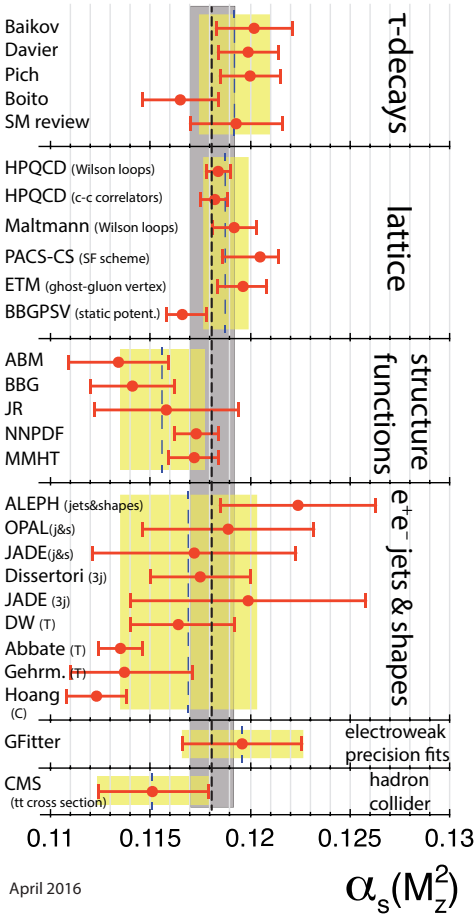


Figure 9.2: Summary of determinations of $\alpha_s(M_Z^2)$ from the six sub-fields discussed in the text. The yellow (light shaded) bands and dashed lines indicate the pre-average values of each sub-field. The dotted line and grey (dark shaded) band represent the final world average value of $\alpha_s(M_Z^2)$.

9.4. Determinations of the strong coupling constant

Beside the quark masses, the only free parameter in the QCD Lagrangian is the strong coupling constant α_s . The coupling constant in itself is not a physical observable, but rather a quantity defined in the context of perturbation theory, which enters predictions for experimentally measurable observables, such as R in Eq. (9.7).

In this review, we update the measurements of α_s summarized in the 2013 edition, and we extract a new world average value of $\alpha_s(M_Z^2)$ from the most significant and complete results available today.

We have chosen to determine pre-averages for classes of measurements which are considered to exhibit a maximum of independence between each other, considering experimental as well as theoretical issues. The six classes are summarized in Fig. 9.2. The respective pre-averages are then combined to the final world average value of $\alpha_s(M_Z^2)$:

$$\alpha_s(M_Z^2) = 0.1181 \pm 0.0011, \quad (9.23)$$

with an uncertainty of 0.9 %.^{***} This world average value is in reasonable agreement with that from the 2013 version of this *Review*, which was $\alpha_s(M_Z^2) = 0.1185 \pm 0.0006$, however at a somewhat decreased central value and with an overall uncertainty that has almost doubled.

Notwithstanding the many open issues still present within each of the sub-fields summarized in this *Review*, the wealth of available results provides a rather precise and reasonably stable world average value of $\alpha_s(M_Z^2)$ as well as a clear signature and proof of the energy dependence of α_s , in full agreement with the QCD prediction of Asymptotic Freedom. This is demonstrated in Fig. 9.3, where results of $\alpha_s(Q^2)$ obtained at discrete energy scales Q , now also including those based just on NLO QCD, are summarized.

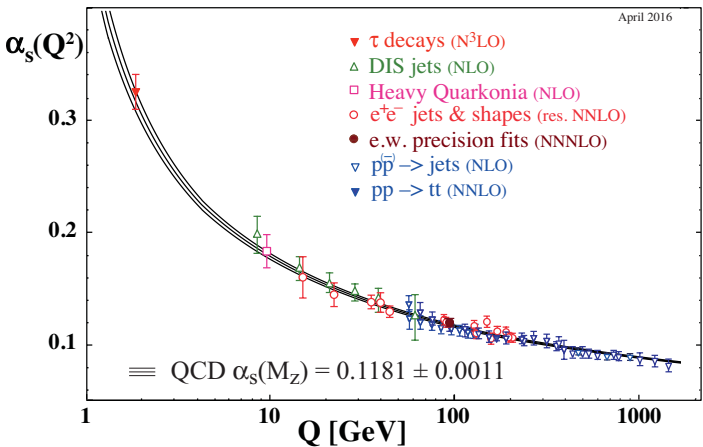


Figure 9.3: Summary of measurements of α_s as a function of the energy scale Q .

Further discussion and all references may be found in the full *Review*.

10. ELECTROWEAK MODEL AND CONSTRAINTS ON NEW PHYSICS

Revised November 2015 by J. Erler (U. Mexico) and A. Freitas (Pittsburgh U.).

10.1. Introduction

The standard model of the electroweak interactions (SM) [1] is based on the gauge group $SU(2) \times U(1)$, with gauge bosons W_μ^i , $i = 1, 2, 3$, and B_μ for the $SU(2)$ and $U(1)$ factors, respectively, and the corresponding gauge coupling constants g and g' . The left-handed fermion fields of the i^{th} fermion family transform as doublets $\Psi_i = \begin{pmatrix} \nu_i \\ \ell_i^- \end{pmatrix}$ and $\begin{pmatrix} u_i \\ d_i' \end{pmatrix}$ under $SU(2)$, where $d_i' \equiv \sum_j V_{ij} d_j$, and V is the Cabibbo-Kobayashi-Maskawa mixing matrix. [Constraints on V are discussed and in the Section on “The CKM Quark-Mixing Matrix”. The extension of the mixing formalism to leptons is discussed in the Section on “Neutrino Mass, Mixing, and Oscillations”.] The right-handed fields are $SU(2)$ singlets. There are three sequential fermion families.

A complex scalar Higgs doublet, $\phi \equiv \begin{pmatrix} \phi^+ \\ \phi^0 \end{pmatrix}$, is added to the model for mass generation through spontaneous symmetry breaking with potential given by,

$$V(\phi) = \mu^2 \phi^\dagger \phi + \frac{\lambda^2}{2} (\phi^\dagger \phi)^2. \quad (10.1)$$

For μ^2 negative, ϕ develops a vacuum expectation value, $v/\sqrt{2} = \mu/\lambda$, where $v \approx 246$ GeV, breaking part of the electroweak (EW) gauge symmetry, after which only one neutral Higgs scalar, H , remains in the physical particle spectrum. In non-minimal models there are additional charged and neutral scalar Higgs particles [3].

After symmetry breaking the Lagrangian for the fermions, ψ_i , is

$$\begin{aligned} \mathcal{L}_F = & \sum_i \bar{\psi}_i \left(i \not{\partial} - m_i - \frac{m_i H}{v} \right) \psi_i \\ & - \frac{g}{2\sqrt{2}} \sum_i \bar{\Psi}_i \gamma^\mu (1 - \gamma^5) (T^+ W_\mu^+ + T^- W_\mu^-) \Psi_i \\ & - e \sum_i Q_i \bar{\psi}_i \gamma^\mu \psi_i A_\mu - \frac{g}{2 \cos \theta_W} \sum_i \bar{\psi}_i \gamma^\mu (g_V^i - g_A^i \gamma^5) \psi_i Z_\mu. \end{aligned} \quad (10.2)$$

Here $\theta_W \equiv \tan^{-1}(g'/g)$ is the weak angle; $e = g \sin \theta_W$ is the positron electric charge; and $A \equiv B \cos \theta_W + W^3 \sin \theta_W$ is the photon field (γ). $W^\pm \equiv (W^1 \mp iW^2)/\sqrt{2}$ and $Z \equiv -B \sin \theta_W + W^3 \cos \theta_W$ are the charged and neutral weak boson fields, respectively. The Yukawa coupling of H to ψ_i in the first term in \mathcal{L}_F , which is flavor diagonal in the minimal model, is $gm_i/2M_W$. The boson masses in the EW sector are given (at tree level, *i.e.*, to lowest order in perturbation theory) by,

$$M_H = \lambda v, \quad (10.3a)$$

$$M_W = \frac{1}{2} g v = \frac{e v}{2 \sin \theta_W}, \quad (10.3b)$$

$$M_Z = \frac{1}{2} \sqrt{g^2 + g'^2} v = \frac{e v}{2 \sin \theta_W \cos \theta_W} = \frac{M_W}{\cos \theta_W}, \quad (10.3c)$$

$$M_\gamma = 0. \quad (10.3d)$$

The second term in \mathcal{L}_F represents the charged-current weak interaction [4–7], where T^+ and T^- are the weak isospin raising and lowering operators. For example, the coupling of a W to an electron and a neutrino is

$$-\frac{e}{2\sqrt{2}\sin\theta_W} \left[W_\mu^- \bar{e} \gamma^\mu (1 - \gamma^5) \nu + W_\mu^+ \bar{\nu} \gamma^\mu (1 - \gamma^5) e \right]. \quad (10.4)$$

For momenta small compared to M_W , this term gives rise to the effective four-fermion interaction with the Fermi constant given by $G_F/\sqrt{2} = 1/2v^2 = g^2/8M_W^2$. The third term in \mathcal{L}_F describes electromagnetic interactions (QED) [8,9], and the last is the weak neutral-current interaction [5–7]. Here

$$g_V^i \equiv t_{3L}(i) - 2Q_i \sin^2 \theta_W, \quad g_A^i \equiv t_{3L}(i), \quad (10.5)$$

where $t_{3L}(i)$ and Q_i are the weak isospin and charge ψ_i , respectively.

The first term in Eq. (10.2) also gives rise to fermion masses, and in the presence of right-handed neutrinos to Dirac neutrino masses. The possibility of Majorana masses is discussed in the Section on “Neutrino Mass, Mixing, and Oscillations”.

10.2. Renormalization and radiative corrections

In addition to the Higgs boson mass, M_H , the fermion masses and mixings, and the strong coupling constant, α_s , the SM has three parameters. The set with the smallest experimental errors contains the Z mass, $M_Z = 91.1876 \pm 0.0021$ GeV, which has been determined from the Z lineshape scan at LEP 1 [10], the Fermi constant, $G_F = 1.1663787(6) \times 10^{-5}$ GeV⁻², which is derived from the muon lifetime, and the fine structure constant, $\alpha = 1/137.035999074(44)$, which is best determined from the e^\pm anomalous magnetic moment [16]. It is convenient to define a running $\alpha(Q) = \frac{\alpha}{1 - \Delta\alpha(Q)}$ dependent on the energy scale Q of the process. The hadronic contribution to $\Delta\alpha$, $\Delta\alpha_{\text{had}}^{(5)}$, is non-perturbative for low Q and can be derived from e^+e^- annihilation and τ decay data. Various evaluations of $\Delta\alpha_{\text{had}}^{(5)}$ are summarized in Table 10.1 in the full *Review*. For the top quark pole mass, we use $m_t = 173.34 \pm 0.37_{\text{stat.}} \pm 0.52_{\text{sys.}}$ GeV [48], which is an average of 12 individual CDF and D0 measurements.

$\sin^2 \theta_W$ and M_W can be calculated from these inputs, or conversely, M_H can be constrained by $\sin^2 \theta_W$ and M_W . The value of $\sin^2 \theta_W$ is extracted from neutral-current processes (see Sec. 10.3 in the full *Review*) and Z pole observables (see Sec. 10.4 in the full *Review*) and depends on the renormalization prescription. There are a number of popular schemes [56–62] leading to values which differ by small factors depending on m_t and M_H , including the $\overline{\text{MS}}$ definition \widehat{s}_Z^2 and the on-shell definition $s_W^2 \equiv 1 - M_W^2/M_Z^2$.

Experiments are at such level of precision that complete one-loop, dominant two-loop, and partial three and four-loop radiative corrections must be applied. These are discussed in the full edition of this *Review*. A

variety of related cross-section and asymmetry formulae are also discussed there.

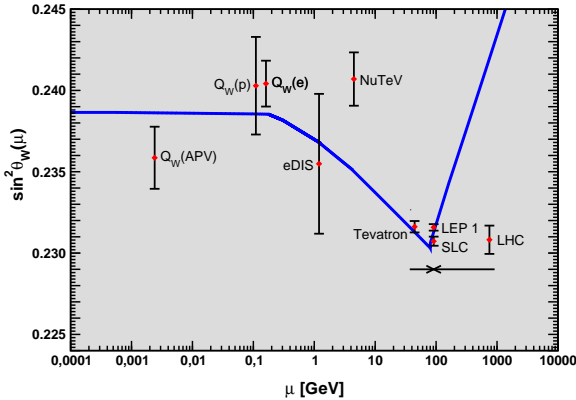


Figure 10.2: Scale dependence of the weak mixing angle in the $\overline{\text{MS}}$ scheme [122]. The width of the curve reflects the theory uncertainty from strong interaction effects which at low energies is at the level of $\pm 7 \times 10^{-5}$ [122]. For NuTeV we display the updated value from Ref. 125. The Tevatron and LHC measurements are strongly dominated by invariant masses of the final state dilepton pair of $\mathcal{O}(M_Z)$ and can thus be considered as additional Z pole data points. For clarity we displayed the Tevatron and LHC points horizontally to the left and to the right, respectively.

10.4.5. H decays :

The ATLAS and CMS collaborations at LHC observed a Higgs boson [183] with properties appearing well consistent with the SM Higgs (see the Section on “Status of Higgs Boson Physics”). A recent combination [184] of ATLAS and CMS results for the Higgs boson mass from kinematical reconstruction yields

$$M_H = 125.09 \pm 0.24 \text{ GeV}. \tag{10.49}$$

We can include some of the Higgs decay properties into the global analysis of Sec. 10.6. However, the total Higgs decay width, which in the SM amounts to $\Gamma_H = 4.15 \pm 0.06 \text{ MeV}$, is too small to be resolved at the LHC. However, one can employ results of Higgs branching ratios into different final states. The most useful channels are Higgs decays into WW^* and ZZ^* (with at least one gauge boson off-shell), as well as $\gamma\gamma$ and $\tau\tau$. We define

$$\rho_{XY} \equiv \ln \frac{\text{BR}_{H \rightarrow XX}}{\text{BR}_{H \rightarrow YY}}. \tag{10.51}$$

These quantities are constructed to have a SM expectation of zero, and their physical range is over all real numbers, which allows one to straightforwardly use Gaussian error propagation (in view of the fairly large errors). Moreover, possible effects of new physics on Higgs production rates would also cancel and one may focus on the decay side of

the processes. From a combination of ATLAS and CMS results [184], we find

$$\rho_{\gamma W} = -0.03 \pm 0.20, \quad \rho_{\tau Z} = -0.27 \pm 0.31,$$

which we take to be uncorrelated as they involve distinct final states. We evaluate the decay rates with the package HDECAY [185].

10.6. Global fit results

Table 10.4: Principal non- Z pole observables, compared with the SM best fit predictions. The first M_W and Γ_W values are from the Tevatron [219,220] and the second ones from LEP 2 [173]. The value of m_t differs from the one in the Particle Listings since it includes recent preliminary results. The world averages for $g_{V,A}^{\nu e}$ are dominated by the CHARM II [86] results, $g_V^{\nu e} = -0.035 \pm 0.017$ and $g_A^{\nu e} = -0.503 \pm 0.017$. The errors are the total (experimental plus theoretical) uncertainties. The τ_τ value is the τ lifetime world average computed by combining the direct measurements with values derived from the leptonic branching ratios [45]; in this case, the theory uncertainty is included in the SM prediction. In all other SM predictions, the uncertainty is from M_Z , M_H , m_t , m_b , m_c , $\hat{\alpha}(M_Z)$, and α_s , and their correlations have been accounted for. The column denoted Pull gives the standard deviations.

Quantity	Value	Standard Model	Pull
m_t [GeV]	173.34 ± 0.81	173.76 ± 0.76	-0.5
M_W [GeV]	80.387 ± 0.016 80.376 ± 0.033	80.361 ± 0.006	1.6 0.4
Γ_W [GeV]	2.046 ± 0.049 2.195 ± 0.083	2.089 ± 0.001	-0.9 1.3
M_H [GeV]	125.09 ± 0.24	125.11 ± 0.24	0.0
$\rho_{\gamma W}$	-0.03 ± 0.20	-0.02 ± 0.02	0.0
$\rho_{\tau Z}$	-0.27 ± 0.31	0.00 ± 0.03	-0.9
$g_V^{\nu e}$	-0.040 ± 0.015	-0.0397 ± 0.0002	0.0
$g_A^{\nu e}$	-0.507 ± 0.014	-0.5064	0.0
$Q_W(e)$	-0.0403 ± 0.0053	-0.0473 ± 0.0003	1.3
$Q_W(p)$	0.064 ± 0.012	0.0708 ± 0.0003	-0.6
$Q_W(\text{Cs})$	-72.62 ± 0.43	-73.25 ± 0.02	1.5
$Q_W(\text{Tl})$	-116.4 ± 3.6	-116.91 ± 0.02	0.1
$\hat{s}_Z^2(\text{eDIS})$	0.2299 ± 0.0043	0.23129 ± 0.00005	-0.3
τ_τ [fs]	290.88 ± 0.35	289.85 ± 2.12	0.4
$\frac{1}{2}(g_\mu - 2 - \frac{\alpha}{\pi})$	$(4511.18 \pm 0.78) \times 10^{-9}$	$(4507.89 \pm 0.08) \times 10^{-9}$	4.2

The values for m_t [48], M_W [173,219], Γ_W [173,220], M_H and the ratios of Higgs branching fractions [184] discussed in Sec. 10.4.5, ν -lepton scattering [83–88], the weak charges of the electron [121], the

Table 10.5: Principal Z pole observables and their SM predictions (*cf.* Table 10.4). The first \bar{s}_ℓ^2 is the effective weak mixing angle extracted from the hadronic charge asymmetry, the second is the combined value from the Tevatron [164–166], and the third from the LHC [170–172]. The values of A_e are (i) from A_{LR} for hadronic final states [159]; (ii) from A_{LR} for leptonic final states and from polarized Bhabba scattering [161]; and (iii) from the angular distribution of the τ polarization at LEP 1. The A_τ values are from SLD and the total τ polarization, respectively.

Quantity	Value	Standard Model	Pull
M_Z [GeV]	91.1876 ± 0.0021	91.1880 ± 0.0020	-0.2
Γ_Z [GeV]	2.4952 ± 0.0023	2.4943 ± 0.0008	0.4
$\Gamma(\text{had})$ [GeV]	1.7444 ± 0.0020	1.7420 ± 0.0008	—
$\Gamma(\text{inv})$ [MeV]	499.0 ± 1.5	501.66 ± 0.05	—
$\Gamma(\ell^+\ell^-)$ [MeV]	83.984 ± 0.086	83.995 ± 0.010	—
σ_{had} [nb]	41.541 ± 0.037	41.484 ± 0.008	1.5
R_e	20.804 ± 0.050	20.734 ± 0.010	1.4
R_μ	20.785 ± 0.033	20.734 ± 0.010	1.6
R_τ	20.764 ± 0.045	20.779 ± 0.010	-0.3
R_b	0.21629 ± 0.00066	0.21579 ± 0.00003	0.8
R_c	0.1721 ± 0.0030	0.17221 ± 0.00003	0.0
$A_{FB}^{(0,e)}$	0.0145 ± 0.0025	0.01622 ± 0.00009	-0.7
$A_{FB}^{(0,\mu)}$	0.0169 ± 0.0013		0.5
$A_{FB}^{(0,\tau)}$	0.0188 ± 0.0017		1.5
$A_{FB}^{(0,b)}$	0.0992 ± 0.0016	0.1031 ± 0.0003	-2.4
$A_{FB}^{(0,c)}$	0.0707 ± 0.0035	0.0736 ± 0.0002	-0.8
$A_{FB}^{(0,s)}$	0.0976 ± 0.0114	0.1032 ± 0.0003	-0.5
\bar{s}_ℓ^2	0.2324 ± 0.0012	0.23152 ± 0.00005	0.7
	0.23185 ± 0.00035		0.9
	0.23105 ± 0.00087		-0.5
A_e	0.15138 ± 0.00216	0.1470 ± 0.0004	2.0
	0.1544 ± 0.0060		1.2
	0.1498 ± 0.0049		0.6
A_μ	0.142 ± 0.015		-0.3
A_τ	0.136 ± 0.015		-0.7
	0.1439 ± 0.0043		-0.7
A_b	0.923 ± 0.020	0.9347	-0.6
A_c	0.670 ± 0.027	0.6678 ± 0.0002	0.1
A_s	0.895 ± 0.091	0.9356	-0.4

proton [126], cesium [129,130] and thallium [131], the weak mixing angle extracted from eDIS [113], the muon anomalous magnetic moment [196], and the τ lifetime are listed in Table 10.4. Likewise, the principal Z pole observables can be found in Table 10.5, where the LEP 1 averages of the ALEPH, DELPHI, L3 and OPAL results include common systematic errors and correlations [10]. The heavy flavor results of LEP 1 and SLD are based on common inputs and correlated, as well [10]. Note

that the values of $\Gamma(\ell^+\ell^-)$, $\Gamma(\text{had})$, and $\Gamma(\text{inv})$ are not independent of Γ_Z , the R_ℓ , and σ_{had} and that the SM errors in those latter are largely dominated by the uncertainty in α_s . Also shown in both tables are the SM predictions for the values of M_Z , M_H , and m_t . The predictions result from a global least-square (χ^2) fit to all data using the minimization package MINUIT [221] and the EW library GAPP [21]. In most cases, we treat all input errors (the uncertainties of the values) as Gaussian. The reason is not that we assume that theoretical and systematic errors are intrinsically bell-shaped (which they are not) but because in most cases the input errors are either dominated by the statistical components or they are combinations of many different (including statistical) error sources, which should yield approximately Gaussian *combined* errors by the large number theorem. Sizes and shapes of the output errors (the uncertainties of the predictions and the SM fit parameters) are fully determined by the fit, and 1 σ errors are defined to correspond to $\Delta\chi^2 = \chi^2 - \chi_{\text{min}}^2 = 1$, and do not necessarily correspond to the 68.3% probability range or the 39.3% probability contour (for 2 parameters).

The agreement is generally very good. Despite the few discrepancies discussed in the following, the fit describes the data well, with a $\chi^2/\text{d.o.f.} = 53.6/42$. The probability of a larger χ^2 is 11%. Only the final result for $g_\mu - 2$ from BNL is currently showing a large (4.2 σ) conflict. In addition, $A_{FB}^{(0,b)}$ from LEP 1 and A_{LR}^0 (SLD) from hadronic final states deviate at the 2 σ level. g_L^2 from NuTeV is nominally in conflict with the SM, as well, but the precise status is still unresolved (see Sec. 10.3 in the full *Review*).

A_b can be extracted from $A_{FB}^{(0,b)}$ when $A_e = 0.1501 \pm 0.0016$ is taken from a fit to leptonic asymmetries (using lepton universality). The result, $A_b = 0.881 \pm 0.017$, is 3.1 σ below the SM prediction and also 1.6 σ below $A_b = 0.923 \pm 0.020$ obtained from $A_{LR}^{FB}(b)$ at SLD. Thus, it appears that at least some of the problem in A_b is due to a statistical fluctuation or other experimental effect in one of the asymmetries. Note, however, that the uncertainty in $A_{FB}^{(0,b)}$ is strongly statistics dominated. The combined value, $A_b = 0.899 \pm 0.013$ deviates by 2.8 σ .

The left-right asymmetry, $A_{LR}^0 = 0.15138 \pm 0.00216$ [159], based on all hadronic data from 1992–1998 differs 2.0 σ from the SM expectation of 0.1470 ± 0.0004 . However, it is consistent with the value $A_\ell = 0.1481 \pm 0.0027$ from LEP 1, obtained from a fit to $A_{FB}^{(0,\ell)}$, $A_e(\mathcal{P}_\tau)$, and $A_\tau(\mathcal{P}_\tau)$, assuming lepton universality.

The observables in Table 10.4 and Table 10.5, as well as some other less precise observables, are used in the global fits described below. In all fits, the errors include full statistical, systematic, and theoretical uncertainties. The correlations on the LEP 1 lineshape and τ polarization, the LEP/SLD heavy flavor observables, the SLD lepton asymmetries, and the ν - e scattering observables, are included. The theoretical correlations between $\Delta\alpha_{\text{had}}^{(5)}$ and $g_\mu - 2$, and between the charm and bottom quark masses, are also accounted for.

As a cross-check, one can also perform a fit without the direct mass constraint, $M_H = 125.09 \pm 0.24$ GeV, in Eq. (10.49). In this case we obtain a 2% indirect mass determination,

$$M_H = 126.1 \pm 1.9 \text{ GeV} , \quad (10.56)$$

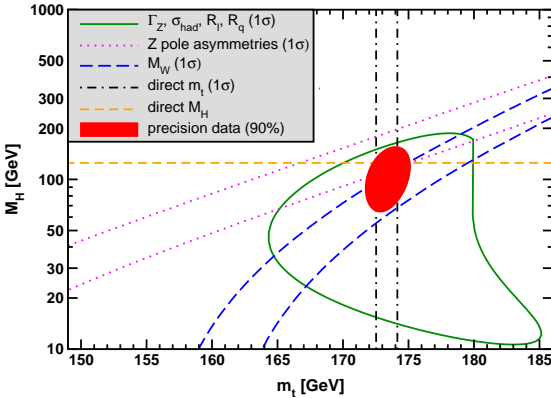


Figure 10.4: Fit result and one-standard-deviation (39.35% for the closed contours and 68% for the others) uncertainties in M_H as a function of m_t for various inputs, and the 90% CL region ($\Delta\chi^2 = 4.605$) allowed by all data. $\alpha_s(M_Z) = 0.1182$ is assumed except for the fits including the Z lineshape. The width of the horizontal dashed band is not visible on the scale of the plot.

arising predominantly from the quantities in Eq. (10.51), since the branching ratio for $H \rightarrow ZZ^*$ varies very rapidly as a function of M_H for Higgs masses near 125 GeV. Removing also the branching ratio constraints gives the loop-level determination from the precision data alone,

$$M_H = 96^{+22}_{-19} \text{ GeV} , \tag{10.57}$$

which is 1.2σ below the kinematical constraint, but the latter is inside the 90% central confidence range,

$$66 \text{ GeV} < M_H < 134 \text{ GeV} . \tag{10.58}$$

This is mostly a reflection of the Tevatron determination of M_W , which is 1.6σ higher than the SM best fit value in Table 10.4., see Fig. 10.4.

The extracted Z pole value of $\alpha_s(M_Z)$ is based on a formula with negligible theoretical uncertainty if one assumes the exact validity of the SM. One should keep in mind, however, that this value, $\alpha_s(M_Z) = 0.1203 \pm 0.0028$, is very sensitive to certain types of new physics such as non-universal vertex corrections. In contrast, the value derived from τ decays, $\alpha_s(M_Z) = 0.1174^{+0.0019}_{-0.0017}$, is theory dominated but less sensitive to new physics. The two values are in reasonable agreement with each other. They are also in good agreement with the averages from jet-event shapes in e^+e^- annihilation (0.1169 ± 0.0034) and lattice simulations (0.1187 ± 0.0012), whereas the DIS average (0.1156 ± 0.0023) is somewhat lower than the Z pole value. For more details, see Section 9 on “Quantum Chromodynamics” in this *Review*.

10.7. Constraints on new physics

The masses and decay properties of the electroweak bosons and low energy data can be used to search for and set limits on deviations from the SM. We will mainly discuss the effects of exotic particles (with heavy masses $M_{\text{new}} \gg M_Z$ in an expansion in M_Z/M_{new}) on the gauge boson self-energies. Most of the effects on precision measurements can be described by three gauge self-energy parameters S , T , and U . We will define these, as well as the related parameter ρ_0 , to arise from new physics only. In other words, they are equal to zero ($\rho_0 = 1$) exactly in the SM, and do not include any (loop induced) contributions that depend on m_t or M_H , which are treated separately.

The dominant effect of many extensions of the SM can be described by the ρ_0 parameter,

$$\rho_0 \equiv \frac{M_W^2}{M_Z^2 \widehat{c}_Z^2 \widehat{\rho}}, \quad (10.59)$$

which describes new sources of SU(2) breaking that cannot be accounted for by the SM Higgs doublet or m_t effects. From the global fit,

$$\rho_0 = 1.00037 \pm 0.00023. \quad (10.60)$$

The result in Eq. (10.60) is 1.6 σ above the SM expectation, $\rho_0 = 1$. It can be used to constrain higher-dimensional Higgs representations to have vacuum expectation values of less than a few percent of those of the doublets. Furthermore, it implies the following limit on the mass splitting, Δm_i^2 , of all new scalar or fermion SU(2) doublets at the 95% CL,

$$\sum_i \frac{C_i}{3} \Delta m_i^2 \leq (49 \text{ GeV})^2. \quad (10.65)$$

where the sum runs over all new-physics doublets, and $C = 1$ (3) for color singlets (triplets).

A number of authors [230–235] have considered the general effects on neutral-current and Z and W boson observables of various types of heavy (*i.e.*, $M_{\text{new}} \gg M_Z$) physics which contribute to the W and Z self-energies but which do not have any direct coupling to the ordinary fermions.

Such effects can be described by just three parameters, S , T , and U . Denoting the contributions of new physics to the various self-energies by Π_{ij}^{new} , we have

$$\widehat{\alpha}(M_Z)T \equiv \frac{\Pi_{WW}^{\text{new}}(0)}{M_W^2} - \frac{\Pi_{ZZ}^{\text{new}}(0)}{M_Z^2}, \quad (10.66a)$$

$$\begin{aligned} \frac{\widehat{\alpha}(M_Z)}{4\widehat{s}_Z^2\widehat{c}_Z^2}S &\equiv \frac{\Pi_{ZZ}^{\text{new}}(M_Z^2) - \Pi_{ZZ}^{\text{new}}(0)}{M_Z^2} - \\ &\frac{\widehat{c}_Z^2 - \widehat{s}_Z^2}{\widehat{c}_Z\widehat{s}_Z} \frac{\Pi_{Z\gamma}^{\text{new}}(M_Z^2)}{M_Z^2} - \frac{\Pi_{\gamma\gamma}^{\text{new}}(M_Z^2)}{M_Z^2}, \end{aligned} \quad (10.66b)$$

$$\begin{aligned} \frac{\widehat{\alpha}(M_Z)}{4\widehat{s}_Z^2}(S+U) &\equiv \frac{\Pi_{WW}^{\text{new}}(M_W^2) - \Pi_{WW}^{\text{new}}(0)}{M_W^2} - \\ &\frac{\widehat{c}_Z}{\widehat{s}_Z} \frac{\Pi_{Z\gamma}^{\text{new}}(M_Z^2)}{M_Z^2} - \frac{\Pi_{\gamma\gamma}^{\text{new}}(M_Z^2)}{M_Z^2}. \end{aligned} \quad (10.66c)$$

S , T , and U are defined with a factor proportional to $\widehat{\alpha}$ removed, so that they are expected to be of order unity in the presence of new physics.

A heavy non-degenerate multiplet of fermions or scalars contributes positively to T , which is related to the ρ_0 parameter via $\rho_0 - 1 \simeq \hat{\alpha}(M_Z)T$. A heavy degenerate ordinary or mirror family would contribute $2/3\pi$ to S . Large positive values $S > 0$ can also be generated in Technicolor models with QCD-like dynamics, and in models with warped extra dimensions.

The data allow a simultaneous determination of \hat{s}_Z^2 (from the Z pole asymmetries), S (from M_Z), U (from M_W), T (mainly from Γ_Z), α_s (from R_ℓ , σ_{had} , and τ_τ), M_H and m_t (from the hadron colliders), with little correlation among the SM parameters:

$$S = 0.05 \pm 0.10, \quad T = 0.08 \pm 0.12, \quad U = 0.02 \pm 0.10, \quad (10.72)$$

$\hat{s}_Z^2 = 0.23131 \pm 0.00015$, and $\alpha_s(M_Z) = 0.1182 \pm 0.0017$, where the uncertainties are from the inputs. The parameters in Eqs. (10.72), which by definition are due to new physics only, are in excellent agreement with the SM values of zero. There is a strong correlation (91%) between the S and T parameters. The U parameter is -61% (-82%) anti-correlated with S (T).

As discussed in Sec. 10.6, there is a 4.0% deviation in the asymmetry parameter A_b . Assuming that this is due to new physics affecting preferentially the third generation, we can perform a fit allowing additional $Z \rightarrow b\bar{b}$ vertex corrections ρ_b and κ_b as in Eq. (10.33) (here defined to be due to new physics only with the SM contributions removed), as well as S , T , U , and the SM parameters, with the result,

$$\rho_b = 0.056 \pm 0.020, \quad \kappa_b = 0.182 \pm 0.068, \quad (10.73)$$

with an almost perfect correlation of 99% (because R_b is much better determined than A_b). The central values of the oblique parameters are close to their SM values of zero, and there is little change in the SM parameters, except that the value of $\alpha_s(M_Z)$ is lower by 0.0006 compared to the SM fit. Given that almost a $\sim 20\%$ correction to κ_b would be necessary, it would be difficult to account for the deviation in A_b by new physics that enters only at the level of radiative corrections. Thus, if it is due to new physics, it is most likely of tree-level type affecting preferentially the third generation.

More examples for constraints on new physics can be found in the full *Review*.

Further discussion and all references may be found in the full *Review of Particle Physics*; the equation and reference numbering corresponds to that version.

11. STATUS OF HIGGS BOSON PHYSICS

Revised September 2016 by M. Carena (Fermi National Accelerator Laboratory and the University of Chicago), C. Grojean (DESY, Hamburg, on leave from ICREA, Barcelona), M. Kado (Laboratoire de l'Accélérateur Linéaire, Orsay), and V. Sharma (University of California, San Diego).

The Standard Model (SM) fermions are chiral and should therefore be massless if the electroweak symmetry were exact. Understanding the mechanism that breaks the electroweak symmetry and generates the masses of the known elementary particles has been one of the fundamental endeavors in particle physics. The discovery in 2012 by the ATLAS and the CMS collaborations of the Higgs boson was a major milestone as well as an extraordinary success of the LHC machine and the ATLAS and CMS experiments.

This is an update of the 2014 review which followed the discovery of the Higgs boson. Since then the ATLAS and CMS experiments have made substantial progress, yielding an increasingly precise profile of the properties of the Higgs boson, all being consistent with the Standard Model. Nevertheless, many theoretical questions remain unanswered and new conundrums about what lies behind the Higgs boson have come to fore. Four years since its discovery, the Higgs boson has turned into a new tool to explore the manifestations of the SM and to probe the physics landscape beyond it.

An experimental profile of the Higgs boson

The ATLAS and CMS experiments have made a combined measurement of the mass of the Higgs boson in the diphoton and the four-lepton channels at per mille precision, $m_H = 125.09 \pm 0.24 \text{ GeV}$. The quantum numbers of the Higgs boson have been probed in greater detail and show an excellent consistency with the $J^{PC} = 0^{++}$ hypothesis. Anomalous CP-even and CP-odd couplings have also been probed, mostly using angular distributions in diboson events. Higgs boson production and decay mechanisms have been further characterized through the measurement of various differential and fiducial cross sections.

Combining ATLAS and CMS data, the production by vector boson fusion has been directly established and the decay into a pair of tau's observed. This combination also provides the most precise probes of the coupling structure of the Higgs boson, with a 10%-20% accuracy. This precision could not have been reached without the rapid and profound theoretical developments on many fronts: higher order calculations, Monte Carlo simulations, and new ideas on how to extract further informations on the nature of the Higgs boson. All measurements are consistent with the SM predictions and provide stringent constraints on a large number of scenarios of new physics predicting sizeable deviations in the couplings of the Higgs boson.

Without assumptions on or a measurement of the Higgs boson width, the measurements at the LHC do not provide constraints on the absolute couplings of the Higgs boson. The direct experimental measurements using the Higgs boson mass lineshape yield an upper bound on the total Higgs width still three orders of magnitude above its SM value (4.2 MeV). However, new ideas have emerged through the study of the Higgs couplings away from its mass shell or through mass shifts due to interference between

signal and background.

Further useful information on the components of the width of the Higgs boson can also be obtained from searches for rare and exotic decay modes, including invisible decays. Insights on the couplings of the Higgs boson are also obtained from the searches for rare production modes. No significant deviation from the SM Higgs boson expectations has been found in the channels analyzed so far.

Finally, all extensions of the SM at higher energies call for an enlargement of the EWSB sector. Therefore invaluable insights can also be acquired from searches for new additional scalar states. Since the 2014 review, an ample number of new searches for CP-even and CP-Odd neutral Higgs bosons, and charged Higgs bosons have been carried out. No significant deviations from the minimal SM Higgs sector has been found in the ranges of mass and couplings of the additional states that have been explored so far.

Fundamental questions and outlook

Perturbative unitarity in vector boson scattering (VBS) is preserved to a large amount with the sole exchange of the Higgs boson and without the need for any additional states within the reach of the LHC. VBS is, however, still an important channel to investigate further in order to directly access the Higgs couplings above the weak scale and to identify the possible completion of the SM. In association with the double Higgs boson production channel by vector boson fusion, VBS could, for instance, confirm that the Higgs boson is part of a weak doublet and also establish whether it is an elementary object or a composite state of a new strong interaction.

The Higgs boson couplings are not dictated by any local gauge symmetry. Thus, in addition to a new particle, the LHC has also discovered a new force, different in nature from the other fundamental interactions since it is non-universal and distinguishes between the three families of quarks and leptons.

The existence of the Higgs boson embodies the problem of an unnatural cancellation among the quantum corrections to its mass, if new physics is present at scale significantly higher than the EW scale. The non-observation of additional states which could stabilize the Higgs mass is a challenge for natural scenarios like supersymmetry or models with a new strong interaction in which the Higgs boson is not a fundamental particle. This increasingly pressing paradox starts questioning the principle of naturalness.

The review discusses in detail the latest developments in theories extending the SM to solve the fundamental questions raised by the existence of the Higgs boson.

Further discussion and references may be found in the full *Review of Particle Physics*.

12. THE CKM QUARK-MIXING MATRIX

Revised January 2016 by A. Ceccucci (CERN), Z. Ligeti (LBNL), and Y. Sakai (KEK).

12.1. Introduction

The masses and mixings of quarks have a common origin in the Standard Model (SM). They arise from the Yukawa interactions of the quarks with the Higgs condensate. When the Higgs field acquires a vacuum expectation value, quark mass terms are generated. The physical states are obtained by diagonalizing the up and down quark mass matrices by four unitary matrices, $V_{L,R}^{u,d}$. As a result, the charged current W^\pm interactions couple to the physical up and down-type quarks with couplings given by

$$V_{\text{CKM}} \equiv V_L^u V_L^{d\dagger} = \begin{pmatrix} V_{ud} & V_{us} & V_{ub} \\ V_{cd} & V_{cs} & V_{cb} \\ V_{td} & V_{ts} & V_{tb} \end{pmatrix}. \quad (12.2)$$

This Cabibbo-Kobayashi-Maskawa (CKM) matrix [1,2] is a 3×3 unitary matrix. It can be parameterized by three mixing angles and a CP -violating phase,

$$V = \begin{pmatrix} c_{12}c_{13} & s_{12}c_{13} & s_{13}e^{-i\delta} \\ -s_{12}c_{23} - c_{12}s_{23}s_{13}e^{i\delta} & c_{12}c_{23} - s_{12}s_{23}s_{13}e^{i\delta} & s_{23}c_{13} \\ s_{12}s_{23} - c_{12}c_{23}s_{13}e^{i\delta} & -c_{12}s_{23} - s_{12}c_{23}s_{13}e^{i\delta} & c_{23}c_{13} \end{pmatrix}, \quad (12.3)$$

where $s_{ij} = \sin \theta_{ij}$, $c_{ij} = \cos \theta_{ij}$, and δ is the phase responsible for all CP -violating phenomena in flavor changing processes in the SM. The angles θ_{ij} can be chosen to lie in the first quadrant.

It is known experimentally that $s_{13} \ll s_{23} \ll s_{12} \ll 1$, and it is convenient to exhibit this hierarchy using the Wolfenstein parameterization. We define [4–6]

$$s_{12} = \lambda = \frac{|V_{us}|}{\sqrt{|V_{ud}|^2 + |V_{us}|^2}}, \quad s_{23} = A\lambda^2 = \lambda \left| \frac{V_{cb}}{V_{us}} \right|, \\ s_{13}e^{i\delta} = V_{ub}^* = A\lambda^3(\rho + i\eta) = \frac{A\lambda^3(\bar{\rho} + i\bar{\eta})\sqrt{1 - A^2\lambda^4}}{\sqrt{1 - \lambda^2}[1 - A^2\lambda^4(\bar{\rho} + i\bar{\eta})]}. \quad (12.4)$$

These ensure that $\bar{\rho} + i\bar{\eta} = -(V_{ud}V_{ub}^*)/(V_{cd}V_{cb}^*)$ is phase-convention independent and the CKM matrix written in terms of λ , A , $\bar{\rho}$ and $\bar{\eta}$ is unitary to all orders in λ . To $\mathcal{O}(\lambda^4)$,

$$V = \begin{pmatrix} 1 - \lambda^2/2 & \lambda & A\lambda^3(\rho - i\eta) \\ -\lambda & 1 - \lambda^2/2 & A\lambda^2 \\ A\lambda^3(1 - \rho - i\eta) & -A\lambda^2 & 1 \end{pmatrix} + \mathcal{O}(\lambda^4). \quad (12.5)$$

Unitarity implies $\sum_i V_{ij}V_{ik}^* = \delta_{jk}$ and $\sum_j V_{ij}V_{kj}^* = \delta_{ik}$. The six vanishing combinations can be represented as triangles in a complex plane. The most commonly used unitarity triangle arises from

$$V_{ud}V_{ub}^* + V_{cd}V_{cb}^* + V_{td}V_{tb}^* = 0, \quad (12.6)$$

by dividing each side by $V_{cd}V_{cb}^*$ (see Fig. 1). The vertices are exactly $(0, 0)$, $(1, 0)$ and, due to the definition in Eq. (12.4), $(\bar{\rho}, \bar{\eta})$. An important goal of flavor physics is to overconstrain the CKM elements, many of which can be displayed and compared in the $\bar{\rho}, \bar{\eta}$ plane.

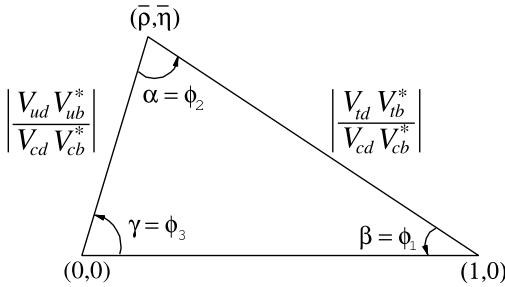


Figure 12.1: Sketch of the unitarity triangle.

12.2. Magnitudes of CKM elements

12.2.1. $|V_{ud}|$:

The most precise determination of $|V_{ud}|$ comes from the study of super-allowed $0^+ \rightarrow 0^+$ nuclear beta decays, which are pure vector transitions. Taking the average of the twenty most precise determinations [9] yields

$$|V_{ud}| = 0.97417 \pm 0.00021. \quad (12.7)$$

12.2.2. $|V_{us}|$:

The magnitude of V_{us} is extracted from semileptonic kaon decays or leptonic kaon decays. Combining the data on $K_L^0 \rightarrow \pi e \nu$, $K_L^0 \rightarrow \pi \mu \nu$, $K^\pm \rightarrow \pi^0 e^\pm \nu$, $K^\pm \rightarrow \pi^0 \mu^\pm \nu$ and $K_S^0 \rightarrow \pi e \nu$ gives $|V_{us}| = 0.2237 \pm 0.0009$ with the unquenched lattice QCD calculation value, $f_+(0) = 0.9677 \pm 0.0037$ [13]. The KLOE measurement of the $K^+ \rightarrow \mu^+ \nu(\gamma)$ branching ratio [19] with the lattice QCD value, $f_K/f_\pi = 1.1928 \pm 0.0026$ [13] leads to $|V_{us}| = 0.2254 \pm 0.0008$. The average of these two determinations is quoted by Ref. [10] as

$$|V_{us}| = 0.2248 \pm 0.0006. \quad (12.8)$$

12.2.3. $|V_{cd}|$:

There are three comparable determinations of $|V_{cd}|$, from semileptonic $D \rightarrow \pi \ell \nu$ decay, leptonic $D^+ \rightarrow \mu^+ \nu$ decay, and from neutrino and antineutrino interactions. The former two use lattice QCD for the normalization of the of the form factor or decay constant [14]. The latter utilizes that the difference of the ratio of double-muon to single-muon production by neutrino and antineutrino beams [31–34] is proportional to the charm cross section off valence d -quarks. Averaging the results,

$$|V_{cd}| = 0.220 \pm 0.005. \quad (12.9)$$

12.2.4. $|V_{cs}|$:

The determination of $|V_{cs}|$ is possible from semileptonic D or leptonic D_s decays. Using the recent $D_s^+ \rightarrow \mu^+ \nu$ [40–42] and $D_s^+ \rightarrow \tau^+ \nu$ [40–45] data gives $|V_{cs}| = 1.008 \pm 0.021$ with $f_{D_s} = (248.6 \pm 2.7) \text{ MeV}$ [14]. The recent $D \rightarrow K \ell \nu$ measurements [27,28,46] combined with the lattice QCD calculation of the form factor [14] gives $|V_{cs}| = 0.975 \pm 0.007 \pm 0.025$. Averaging these two determinations, we obtain

$$|V_{cs}| = 0.995 \pm 0.016. \quad (12.10)$$

12.2.5. $|V_{cb}|$:

The determination of $|V_{cb}|$ from inclusive semileptonic B decays use the semileptonic rate measurement together with the leptonic energy and the hadronic invariant-mass spectra. Determinations from exclusive $B \rightarrow D^{(*)}\ell\bar{\nu}$ decays are based on the fact that in the $m_{b,c} \gg \Lambda_{\text{QCD}}$ limit all form factors are given by a single Isgur-Wise function [53], which is normalized at zero recoil. The V_{cb} and V_{ub} minireview [15] quotes the combination with a scaled error as

$$|V_{cb}| = (40.5 \pm 1.5) \times 10^{-3}. \quad (12.11)$$

12.2.6. $|V_{ub}|$:

The determination of $|V_{ub}|$ from inclusive $B \rightarrow X_u\ell\bar{\nu}$ decay suffers from large $B \rightarrow X_c\ell\bar{\nu}$ backgrounds. In most regions of phase space where the charm background is kinematically forbidden the rate is determined by nonperturbative shape functions. At leading order in Λ_{QCD}/m_b there is only one such function, which is related to the photon energy spectrum in $B \rightarrow X_s\gamma$ [55,56]. The large and pure $B\bar{B}$ samples at the B factories permit the selection of $B \rightarrow X_u\ell\bar{\nu}$ decays in events where the other B is fully reconstructed [61]. With this full-reconstruction tag method, one can measure the four-momenta of both the leptonic and hadronic systems, and access wider kinematic regions because of improved signal purity.

To extract $|V_{ub}|$ from exclusive channels, the form factors have to be known. Unquenched lattice QCD calculations of the $B \rightarrow \pi\ell\bar{\nu}$ form factor for $q^2 > 16 \text{ GeV}^2$ are available [62,63]. The theoretical uncertainties in the inclusive and exclusive determinations are different. The V_{cb} and V_{ub} minireview [15] quotes the combination

$$|V_{ub}| = (4.09 \pm 0.39) \times 10^{-3}. \quad (12.12)$$

12.2.7. $|V_{td}|$ and $|V_{ts}|$:

These CKM elements are not likely to be precisely measurable in tree-level processes involving top quarks, so one has to use $B-\bar{B}$ oscillations or loop-mediated rare K and B decays. The mass difference of the two neutral B meson mass eigenstates is well measured, $\Delta m_d = (0.5064 \pm 0.0019) \text{ ps}^{-1}$ [68]. In the B_s^0 system, the average of the CDF [69] and recent more precise LHCb [70] measurements yields $\Delta m_s = (17.757 \pm 0.021) \text{ ps}^{-1}$. Using unquenched lattice QCD calculations [14] and assuming $|V_{tb}| = 1$, we find

$$|V_{td}| = (8.2 \pm 0.6) \times 10^{-3}, \quad |V_{ts}| = (40.0 \pm 2.7) \times 10^{-3}. \quad (12.13)$$

Several uncertainties are reduced in the lattice QCD calculation of the ratio $\Delta m_d/\Delta m_s$, which gives a significantly improved constraint,

$$|V_{td}/V_{ts}| = 0.215 \pm 0.001 \pm 0.011. \quad (12.14)$$

12.2.8. $|V_{tb}|$:

The determination of $|V_{tb}|$ from top decays uses the ratio of branching fractions $\mathcal{B}(t \rightarrow Wb)/\mathcal{B}(t \rightarrow Wq) = |V_{tb}|^2/(\sum_q |V_{tq}|^2) = |V_{tb}|^2$, where $q = b, s, d$ [77-79]. The direct determination of $|V_{tb}|$ without assuming unitarity has become possible from the single top quark production cross section. The $(3.30^{+0.52}_{-0.40}) \text{ pb}$ average Tevatron cross section [80] implies $|V_{tb}| = 1.02^{+0.06}_{-0.05}$. The LHC experiments, ATLAS and CMS, have

measured single-top production cross sections (and extracted $|V_{tb}|$) in t -channel, Wt -channel, and s -channel at 7 TeV, 8 TeV, and 13 TeV [81], resulting the average $|V_{tb}|$ value to be $|V_{tb}| = 1.005 \pm 0.036$. The average of Tevatron and LHC values gives

$$|V_{tb}| = 1.009 \pm 0.031. \quad (12.15)$$

12.3. Phases of CKM elements

The angles of the unitarity triangle are

$$\begin{aligned} \beta = \phi_1 &= \arg\left(-\frac{V_{cd}V_{cb}^*}{V_{td}V_{tb}^*}\right), & \alpha = \phi_2 &= \arg\left(-\frac{V_{td}V_{tb}^*}{V_{ud}V_{ub}^*}\right), \\ \gamma = \phi_3 &= \arg\left(-\frac{V_{ud}V_{ub}^*}{V_{cd}V_{cb}^*}\right). \end{aligned} \quad (12.16)$$

Since CP violation involves phases of CKM elements, many measurements of CP -violating observables can be used to constrain these angles and the $\bar{\rho}, \bar{\eta}$ parameters.

12.3.1. ϵ and ϵ' :

The measurement of CP violation in $K^0-\bar{K}^0$ mixing, $|\epsilon| = (2.233 \pm 0.015) \times 10^{-3}$ [83], provides constraints in the $\bar{\rho}, \bar{\eta}$ plane bounded by hyperbolas approximately. Lattice QCD has determined the bag parameter well enough that the main uncertainties come from perturbation theory and the parametric uncertainty proportional to $\sigma(A^4)$ [*i.e.*, $\sigma(|V_{cb}|^4)$].

The measurement of ϵ' provides a qualitative test of the CKM mechanism because its nonzero experimental average, $\text{Re}(\epsilon'/\epsilon) = (1.67 \pm 0.23) \times 10^{-3}$ [83], demonstrated the existence of direct CP violation, a prediction of the KM ansatz. While $\text{Re}(\epsilon'/\epsilon) \propto \text{Im}(V_{td}V_{ts}^*)$, this quantity cannot easily be used to extract CKM parameters, because of hadronic uncertainties.

12.3.2. β / ϕ_1 :

The time-dependent CP asymmetry of neutral B decays to a final state f common to B^0 and \bar{B}^0 is given by [93,94]

$$A_f = \frac{\Gamma(\bar{B}^0(t) \rightarrow f) - \Gamma(B^0(t) \rightarrow f)}{\Gamma(\bar{B}^0(t) \rightarrow f) + \Gamma(B^0(t) \rightarrow f)} = S_f \sin(\Delta m t) - C_f \cos(\Delta m t), \quad (12.18)$$

where $S_f = 2\text{Im}\lambda_f/(1 + |\lambda_f|^2)$, $C_f = (1 - |\lambda_f|^2)/(1 + |\lambda_f|^2)$, and $\lambda_f = (q/p)(\bar{A}_f/A_f)$. Here q/p describes $B^0-\bar{B}^0$ mixing and, to a good approximation in the SM, $q/p = V_{tb}^*V_{td}/V_{tb}V_{td}^* = e^{-2i\beta + \mathcal{O}(\lambda^4)}$ in the usual phase convention. A_f (\bar{A}_f) is the amplitude of $B^0 \rightarrow f$ ($\bar{B}^0 \rightarrow f$) decay. If f is a CP eigenstate and amplitudes with one CKM phase dominate, then $|A_f| = |\bar{A}_f|$, $C_f = 0$ and $S_f = \sin(\arg \lambda_f) = \eta_f \sin 2\phi$, where η_f is the CP eigenvalue of f and 2ϕ is the phase difference between the $B^0 \rightarrow f$ and $B^0 \rightarrow \bar{B}^0 \rightarrow f$ decay paths.

The $b \rightarrow c\bar{c}s$ decays to CP eigenstates ($B^0 \rightarrow \text{charmonium } K_{S,L}^0$) are the theoretically cleanest examples, measuring $S_f = -\eta_f \sin 2\beta$. The world average is [98]

$$\sin 2\beta = 0.691 \pm 0.017. \quad (12.20)$$

This measurement of β has a four-fold ambiguity. Of these, $\beta \rightarrow \pi/2 - \beta$ (but not $\beta \rightarrow \pi + \beta$) has been resolved by a time-dependent angular

analysis of $B^0 \rightarrow J/\psi K^{*0}$ [99,100] and a time-dependent Dalitz plot analysis of $B^0 \rightarrow \bar{D}^0 h^0$ ($h^0 = \pi^0, \eta, \omega$) [101,102].

The $b \rightarrow s\bar{q}q$ penguin dominated decays have the same CKM phase as the $b \rightarrow c\bar{c}s$ tree dominated decays, up to corrections suppressed by λ^2 . Therefore, decays such as $B^0 \rightarrow \phi K^0$ and $\eta' K^0$ provide $\sin 2\beta$ measurements in the SM. If new physics contributes to the $b \rightarrow s$ loop diagrams and has a different weak phase, it would give rise to $S_f \neq -\eta_f \sin 2\beta$ and possibly $C_f \neq 0$. The results and their uncertainties are summarized in Fig. 12.3 and Table 12.1 of Ref. [94].

12.3.3. α / ϕ_2 :

Since α is the phase between $V_{tb}^* V_{td}$ and $V_{ub}^* V_{ud}$, only time-dependent CP asymmetries in $b \rightarrow u\bar{u}d$ dominated modes can directly measure it. In such decays the penguin contribution can be sizable. Then $S_{\pi^+\pi^-}$ no longer measures $\sin 2\alpha$, but α can still be extracted using the isospin relations among the $B^0 \rightarrow \pi^+\pi^-$, $B^0 \rightarrow \pi^0\pi^0$, and $B^+ \rightarrow \pi^+\pi^0$ amplitudes and their CP conjugates [104]. Because the isospin analysis gives 16 mirror solutions, only a loose constraint is obtained at present.

The $B^0 \rightarrow \rho^+\rho^-$ decay can in general have a mixture of CP -even and CP -odd components. However, the longitudinal polarization fractions in $B^+ \rightarrow \rho^+\rho^0$ and $B^0 \rightarrow \rho^+\rho^-$ are measured to be close to unity [106], which implies that the final states are almost purely CP -even. Furthermore, $\mathcal{B}(B^0 \rightarrow \rho^0\rho^0) = (0.97 \pm 0.24) \times 10^{-6}$ implies that the effect of the penguin diagrams is small. The isospin analysis gives $\alpha = (89.8 \pm 5.5)^\circ$ [105] with a mirror solution at $3\pi/2 - \alpha$.

The final state in $B^0 \rightarrow \rho^+\pi^-$ decay is not a CP eigenstate, but mixing induced CP violations can still occur in the four decay amplitudes, $B^0, \bar{B}^0 \rightarrow \rho^\pm\pi^\mp$. Because of the more complicated isospin relations, the time-dependent Dalitz plot analysis of $B^0 \rightarrow \pi^+\pi^-\pi^0$ gives the best model independent extraction of α [109]. The combination of Belle [110] and BABAR [111] measurements yield $\alpha = (54.1^{+7.7}_{-10.3})^\circ$ and $(141.8^{+4.7}_{-5.4})^\circ$ [105].

Combining these three decay modes [105], α is constrained as

$$\alpha = (87.6^{+3.5}_{-3.3})^\circ. \quad (12.23)$$

12.3.4. γ / ϕ_3 :

The angle γ does not depend on CKM elements involving the top quark, so it can be measured in tree-level B decays. This is an important distinction from α and β , implying that the measurements of γ are unlikely to be affected by physics beyond the SM.

The interference of $B^- \rightarrow D^0 K^-$ ($b \rightarrow c\bar{u}s$) and $B^- \rightarrow \bar{D}^0 K^-$ ($b \rightarrow u\bar{c}s$) transitions can be studied in final states accessible in both D^0 and \bar{D}^0 decays [93]. It is possible to extract from the data the B and D decay amplitudes, their relative strong phases, and γ . Analyses in two-body D decays using the GLW [113,114] and ADS methods [115] have been made [98] by the B factories, CDF, and LHCb. The Dalitz plot analysis of $D^0, \bar{D}^0 \rightarrow K_S \pi^+\pi^-$ [116,117] by the B factories gives the best present determination of γ [118,119].

Combining these analyses [105],

$$\gamma = (73.2^{+6.3}_{-7.0})^\circ. \quad (12.25)$$

12.4. Global fit in the Standard Model

Using the independently measured CKM elements mentioned in the previous sections, the unitarity of the CKM matrix can be checked. We obtain $|V_{ud}|^2 + |V_{us}|^2 + |V_{ub}|^2 = 0.9996 \pm 0.0005$ (1st row), $|V_{cd}|^2 + |V_{cs}|^2 + |V_{cb}|^2 = 1.040 \pm 0.032$ (2nd row), $|V_{ud}|^2 + |V_{cd}|^2 + |V_{td}|^2 = 0.9975 \pm 0.0022$ (1st column), and $|V_{us}|^2 + |V_{cs}|^2 + |V_{ts}|^2 = 1.042 \pm 0.032$ (2nd column), respectively. For the second row, a slightly better check is obtained subtracting the sum of the first row from the measurement of $\sum_{u,c,d,s,b} |V_{ij}|^2$ from the W leptonic branching ratio [47], yielding $|V_{cd}|^2 + |V_{cs}|^2 + |V_{cb}|^2 = 1.002 \pm 0.027$. The sum of the three angles, $\alpha + \beta + \gamma = (183_{-8}^{+7})^\circ$, is also consistent with the SM expectation.

The CKM matrix elements can be most precisely determined by a global fit that uses all available measurements and imposes the SM constraints. There are several approaches to combining the experimental data [6,105,112,129], which provide similar results. The results for the Wolfenstein parameters are

$$\begin{aligned} \lambda &= 0.22506 \pm 0.00050, & A &= 0.811 \pm 0.026, \\ \bar{\rho} &= 0.124_{-0.018}^{+0.019}, & \bar{\eta} &= 0.356 \pm 0.011. \end{aligned} \quad (12.26)$$

The allowed ranges of the magnitudes of all nine CKM elements are

$$V_{\text{CKM}} = \begin{pmatrix} 0.97434_{-0.00012}^{+0.00011} & 0.22506 \pm 0.00050 & 0.00357 \pm 0.00015 \\ 0.22492 \pm 0.00050 & 0.97351 \pm 0.00013 & 0.0411 \pm 0.0013 \\ 0.00875_{-0.00033}^{+0.00032} & 0.0403 \pm 0.0013 & 0.99915 \pm 0.00005 \end{pmatrix}, \quad (12.27)$$

and the Jarlskog invariant is $J = (3.04_{-0.20}^{+0.21}) \times 10^{-5}$. Fig. 12.2 illustrates the constraints on the $\bar{\rho}, \bar{\eta}$ plane from various measurements and the global fit result. The shaded 95% CL regions all overlap consistently around the global fit region.

12.5. Implications beyond the SM

The effects in B , K , and D decays and mixings due to high-scale physics (W , Z , t , h in the SM, or new physics particles) can be parameterized by operators composed of SM fields, obeying the $SU(3) \times SU(2) \times U(1)$ gauge symmetry. The observable effects of non-SM interactions are encoded in the coefficients of these operators, and are suppressed by powers of the new physics scale. In the SM, these coefficients are determined by just the four CKM parameters, and the W , Z , and quark masses. For example, Δm_d , $\Gamma(B \rightarrow \rho\gamma)$, and $\Gamma(B \rightarrow X_d \ell^+ \ell^-)$ are all proportional to $|V_{td} V_{tb}^*|^2$ in the SM, however, they may receive unrelated new physics contributions. Similar to measurements of $\sin 2\beta$ in tree- and loop-dominated decays, overconstraining the magnitudes and phases of flavor-changing neutral-current amplitudes give good sensitivity to new physics.

To illustrate the level of suppression required for non-SM contributions, consider a class of models in which the dominant effect of new physics is to modify the neutral meson mixing amplitudes [132] by $(z_{ij}/\Lambda^2)(\bar{q}_i \gamma^\mu P_L q_j)^2$. New physics with a generic weak phase may still contribute to meson mixings at a significant fraction of the SM [137,129]. The data imply that $\Lambda/|z_{ij}|^{1/2}$ has to exceed about 10^4 TeV for $K^0 - \bar{K}^0$ mixing, 10^3 TeV for $D^0 - \bar{D}^0$ mixing, 500 TeV for $B^0 - \bar{B}^0$ mixing, and 100 TeV for $B_s^0 - \bar{B}_s^0$ mixing [129,134]. Thus, if there is new physics at the TeV scale, $|z_{ij}| \ll 1$

13. *CP VIOLATION IN THE QUARK SECTOR*

Revised August 2015 by T. Gershon (University of Warwick) and Y. Nir (Weizmann Institute).

The *CP* transformation combines charge conjugation *C* with parity *P*. Under *C*, particles and antiparticles are interchanged, by conjugating all internal quantum numbers, *e.g.*, $Q \rightarrow -Q$ for electromagnetic charge. Under *P*, the handedness of space is reversed, $\vec{x} \rightarrow -\vec{x}$. Thus, for example, a left-handed electron e_L^- is transformed under *CP* into a right-handed positron, e_R^+ .

If *CP* were an exact symmetry, the laws of Nature would be the same for matter and for antimatter. We observe that most phenomena are *C*- and *P*-symmetric, and therefore, also *CP*-symmetric. In particular, these symmetries are respected by the gravitational, electromagnetic, and strong interactions. The weak interactions, on the other hand, violate *C* and *P* in the strongest possible way. For example, the charged *W* bosons couple to left-handed electrons, e_L^- , and to their *CP*-conjugate right-handed positrons, e_R^+ , but to neither their *C*-conjugate left-handed positrons, e_L^+ , nor their *P*-conjugate right-handed electrons, e_R^- . While weak interactions violate *C* and *P* separately, *CP* is still preserved in most weak interaction processes. The *CP* symmetry is, however, violated in certain rare processes, as discovered in neutral *K* decays in 1964 [1], and observed in recent years in *B* decays. A K_L meson decays more often to $\pi^- e^+ \nu_e$ than to $\pi^+ e^- \bar{\nu}_e$, thus allowing electrons and positrons to be unambiguously distinguished, but the decay-rate asymmetry is only at the 0.003 level. The *CP*-violating effects observed in the *B* system are larger: the parameter describing the *CP* asymmetry in the decay time distribution of B^0/\bar{B}^0 meson transitions to *CP* eigenstates like $J/\psi K_S$ is about 0.7 [2,3]. These effects are related to $K^0-\bar{K}^0$ and $B^0-\bar{B}^0$ mixing, but *CP* violation arising solely from decay amplitudes has also been observed, first in $K \rightarrow \pi\pi$ decays [4–6], and more recently in B^0 [7,8], B^+ [9–11], and B_s^0 [12] decays. Similar effects could also occur, but have not yet been observed, in decays of *b* baryons. *CP* violation is not yet experimentally established in the *D* system, where the Standard Model effects are expected to be $\mathcal{O}(10^{-3})$. Moreover, *CP* violation has not yet been observed in processes involving the top quark, nor in flavor-conserving processes such as electric dipole moments, nor in the lepton sector; for all of these any significant observation would be a clear indication of physics beyond the Standard Model.

In addition to parity and to continuous Lorentz transformations, there is one other spacetime operation that could be a symmetry of the interactions: time reversal *T*, $t \rightarrow -t$. Violations of *T* symmetry have been observed in neutral *K* decays [13]. More recently, exploiting the fact that for neutral *B* mesons both flavor tagging and *CP* tagging can be used [14], *T* violation has been observed between states that are not *CP*-conjugate [15]. Moreover, *T* violation is expected as a corollary of *CP* violation if the combined *CPT* transformation is a fundamental symmetry of Nature [16]. All observations indicate that *CPT* is indeed a symmetry of Nature. Furthermore, one cannot build a locally Lorentz-invariant quantum field theory with a Hermitian Hamiltonian that violates *CPT*. (At several points in our discussion, we avoid assumptions about *CPT*, in order to identify cases where evidence for *CP* violation relies on assumptions about *CPT*.)

Within the Standard Model, CP symmetry is broken by complex phases in the Yukawa couplings (that is, the couplings of the Higgs scalar to quarks). When all manipulations to remove unphysical phases in this model are exhausted, one finds that there is a single CP -violating parameter [17]. In the basis of mass eigenstates, this single phase appears in the 3×3 unitary matrix that gives the W -boson couplings to an up-type antiquark and a down-type quark. (If the Standard Model is supplemented with Majorana mass terms for the neutrinos, the analogous mixing matrix for leptons has three CP -violating phases.) The beautifully consistent and economical Standard-Model description of CP violation in terms of Yukawa couplings, known as the Kobayashi-Maskawa (KM) mechanism [17], agrees with all measurements to date.

The current level of experimental accuracy and the theoretical uncertainties involved in the interpretation of the various observations leave room, however, for additional subdominant sources of CP violation from new physics. Indeed, almost all extensions of the Standard Model imply that there are such additional sources. Moreover, CP violation is a necessary condition for baryogenesis, the process of dynamically generating the matter-antimatter asymmetry of the Universe [20]. Despite the phenomenological success of the KM mechanism, it fails (by several orders of magnitude) to accommodate the observed asymmetry [21]. This discrepancy strongly suggests that Nature provides additional sources of CP violation beyond the KM mechanism. The evidence for neutrino masses implies that CP can be violated also in the lepton sector. This situation makes leptogenesis [22,23], a scenario where CP -violating phases in the Yukawa couplings of the neutrinos play a crucial role in the generation of the baryon asymmetry, a very attractive possibility. The expectation of new sources motivates the large ongoing experimental effort to find deviations from the predictions of the KM mechanism.

CP violation can be experimentally searched for in a variety of processes, such as hadron decays, electric dipole moments of neutrons, electrons and nuclei, and neutrino oscillations. Hadron decays via the weak interaction probe flavor-changing CP violation. The search for electric dipole moments may find (or constrain) sources of CP violation that, unlike the KM phase, are not related to flavor-changing couplings. Following the discovery of the Higgs boson [24,25], searches for CP violation in the Higgs sector are becoming feasible. Future searches for CP violation in neutrino oscillations might provide further input on leptogenesis.

The present measurements of CP asymmetries provide some of the strongest constraints on the weak couplings of quarks. Future measurements of CP violation in K , D , B , and B_s^0 meson decays will provide additional constraints on the flavor parameters of the Standard Model, and can probe new physics. In this review, we give the formalism and basic physics that are relevant to present and near future measurements of CP violation in the quark sector.

Before going into details, we list here the observables where CP violation has been observed at a level above 5σ [26–28]:

- Indirect CP violation in $K \rightarrow \pi\pi$ and $K \rightarrow \pi\ell\nu$ decays, and in the $K_L \rightarrow \pi^+\pi^-e^+e^-$ decay, is given by

$$|\epsilon| = (2.228 \pm 0.011) \times 10^{-3}. \quad (13.1)$$

- Direct *CP* violation in $K \rightarrow \pi\pi$ decays is given by

$$\mathcal{R}e(\epsilon'/\epsilon) = (1.65 \pm 0.26) \times 10^{-3}. \quad (13.2)$$

- *CP* violation in the interference of mixing and decay in the tree-dominated $b \rightarrow c\bar{c}s$ transitions, such as $B^0 \rightarrow \psi K^0$, is given by (we use K^0 throughout to denote results that combine K_S and K_L modes, but use the sign appropriate to K_S):

$$S_{\psi K^0} = +0.691 \pm 0.017. \quad (13.3)$$

- *CP* violation in the interference of mixing and decay in modes governed by the tree-dominated $b \rightarrow c\bar{u}d$ transitions is given by

$$S_{D_{CP}^{(*)}h^0} = +0.63 \pm 0.11, \quad (13.4)$$

- *CP* violation in the interference of mixing and decay in various modes related to $b \rightarrow c\bar{c}d$ transitions is given by

$$S_{\psi\pi^0} = -0.93 \pm 0.15, \quad (13.5)$$

$$S_{D^+D^-} = -0.98 \pm 0.17. \quad (13.6)$$

$$S_{D^{*+}D^{*-}} = -0.71 \pm 0.09. \quad (13.7)$$

- *CP* violation in the interference of mixing and decay in various modes related to $b \rightarrow q\bar{q}s$ (penguin) transitions is given by

$$S_{\phi K^0} = +0.74^{+0.11}_{-0.13}, \quad (13.8)$$

$$S_{\eta' K^0} = +0.63 \pm 0.06, \quad (13.9)$$

$$S_{f_0 K^0} = +0.69^{+0.10}_{-0.12}, \quad (13.10)$$

$$S_{K^+K^-K_S} = +0.68^{+0.09}_{-0.10}, \quad (13.11)$$

- *CP* violation in the interference of mixing and decay in the $B^0 \rightarrow \pi^+\pi^-$ mode is given by

$$S_{\pi^+\pi^-} = -0.66 \pm 0.06. \quad (13.12)$$

- Direct *CP* violation in the $B^0 \rightarrow \pi^+\pi^-$ mode is given by

$$C_{\pi^+\pi^-} = -0.31 \pm 0.05. \quad (13.13)$$

- Direct *CP* violation in the $\bar{B}^0 \rightarrow K^-\pi^+$ mode is given by

$$\mathcal{A}_{\bar{B}^0 \rightarrow K^-\pi^+} = -0.082 \pm 0.006. \quad (13.14)$$

- Direct *CP* violation in $B^+ \rightarrow D_+K^+$ decays (D_+ is the *CP*-even neutral D state) is given by

$$\mathcal{A}_{B^+ \rightarrow D_+K^+} = +0.195 \pm 0.027. \quad (13.15)$$

- Direct *CP* violation in the $\bar{B}_s^0 \rightarrow K^+\pi^-$ mode is given by

$$\mathcal{A}_{\bar{B}_s^0 \rightarrow K^+\pi^-} = +0.26 \pm 0.04. \quad (13.16)$$

- Direct *CP* violation in $B^+ \rightarrow K^+K^-\pi^+$ decays is given by

$$\mathcal{A}_{B^+ \rightarrow K^+K^-\pi^+} = -0.118 \pm 0.022. \quad (13.17)$$

In addition, large *CP* violation effects have recently been observed in certain regions of the phase space of $B^+ \rightarrow K^+K^-K^+$, $\pi^+\pi^-K^+$, $\pi^+\pi^-\pi^+$ and $K^+K^-\pi^+$ decays.

Further discussion and all references may be found in the full *Review of Particle Physics*. The numbering of references and equations used here corresponds to that version.

14. NEUTRINO MASS, MIXING, AND OSCILLATIONS

Updated June 2016 by K. Nakamura (Kavli IPMU (WPI), U. Tokyo, KEK), and S.T. Petcov (SISSA/INFN Trieste, Kavli IPMU (WPI), U. Tokyo, Bulgarian Academy of Sciences).

14.1. Massive neutrinos and neutrino mixing

It is a well-established experimental fact that the neutrinos and antineutrinos which take part in the standard charged current (CC) and neutral current (NC) weak interaction are of three varieties (types) or flavours: electron, ν_e and $\bar{\nu}_e$, muon, ν_μ and $\bar{\nu}_\mu$, and tauon, ν_τ and $\bar{\nu}_\tau$. The notion of neutrino type or flavour is dynamical: ν_e is the neutrino which is produced with e^+ , or produces an e^- , in CC weak interaction processes; ν_μ is the neutrino which is produced with μ^+ , or produces μ^- , etc. The flavour of a given neutrino is Lorentz invariant.

The experiments with solar, atmospheric, reactor and accelerator neutrinos have provided compelling evidences for the existence of neutrino oscillations [4,5], transitions in flight between the different flavour neutrinos ν_e , ν_μ , ν_τ (antineutrinos $\bar{\nu}_e$, $\bar{\nu}_\mu$, $\bar{\nu}_\tau$), caused by nonzero neutrino masses and neutrino mixing. The existence of flavour neutrino oscillations implies that if a neutrino of a given flavour, say ν_μ , with energy E is produced in some weak interaction process, at a sufficiently large distance L from the ν_μ source the probability to find a neutrino of a different flavour, say ν_τ , $P(\nu_\mu \rightarrow \nu_\tau; E, L)$, is different from zero. $P(\nu_\mu \rightarrow \nu_\tau; E, L)$ is called the $\nu_\mu \rightarrow \nu_\tau$ oscillation or transition probability. If $P(\nu_\mu \rightarrow \nu_\tau; E, L) \neq 0$, the probability that ν_μ will not change into a neutrino of a different flavour, *i.e.*, the “ ν_μ survival probability” $P(\nu_\mu \rightarrow \nu_\mu; E, L)$, will be smaller than one. If only muon neutrinos ν_μ are detected in a given experiment and they take part in oscillations, one would observe a “disappearance” of muon neutrinos on the way from the ν_μ source to the detector.

Oscillations of neutrinos are a consequence of the presence of flavour neutrino mixing, or lepton mixing, in vacuum. In the local quantum field theory, used to construct the Standard Model, this means that the LH flavour neutrino fields $\nu_{lL}(x)$, which enter into the expression for the lepton current in the CC weak interaction Lagrangian, are linear combinations of the fields of three (or more) neutrinos ν_j , having masses $m_j \neq 0$:

$$\nu_{lL}(x) = \sum_j U_{lj} \nu_{jL}(x), \quad l = e, \mu, \tau, \quad (14.1)$$

where $\nu_{jL}(x)$ is the LH component of the field of ν_j possessing a mass m_j and U is a unitary matrix - the neutrino mixing matrix [1,4,5]. The matrix U is often called the Pontecorvo-Maki-Nakagawa-Sakata (PMNS) or Maki-Nakagawa-Sakata (MNS) mixing matrix. Obviously, Eq. (14.1) implies that the individual lepton charges L_l , $l = e, \mu, \tau$, are not conserved.

All compelling neutrino oscillation data can be described assuming 3-flavour neutrino mixing in vacuum. The data on the invisible decay width of the Z -boson is compatible with only 3 light flavour neutrinos coupled to Z [43]. The number of massive neutrinos ν_j , n , can, in general, be bigger than 3, $n > 3$, if, for instance, there exist sterile neutrinos and they mix with the flavour neutrinos. It is firmly established on the basis of the current data that at least 3 of the neutrinos ν_j , say ν_1, ν_2, ν_3 , must be light, $m_{1,2,3} \lesssim 1$ eV, and must have different masses. At present there are several experimental hints for existence of one or

two light sterile neutrinos at the eV scale, which mix with the flavour neutrinos, implying the presence in the neutrino mixing of additional one or two neutrinos, ν_4 or $\nu_{4,5}$, with masses m_4 ($m_{4,5}$) ~ 1 eV (see the full Review for details).

Being electrically neutral, the neutrinos with definite mass ν_j can be Dirac fermions or Majorana particles [44,45]. The first possibility is realized when there exists a lepton charge carried by the neutrinos ν_j , which is conserved by the particle interactions. This could be, *e.g.*, the total lepton charge $L = L_e + L_\mu + L_\tau$: $L(\nu_j) = 1, j = 1, 2, 3$. In this case the neutrino ν_j has a distinctive antiparticle $\bar{\nu}_j$: $\bar{\nu}_j$ differs from ν_j by the value of the lepton charge L it carries, $L(\bar{\nu}_j) = -1$. The massive neutrinos ν_j can be Majorana particles if no lepton charge is conserved (see, *e.g.*, Refs. [46,47]) . A massive Majorana particle χ_j is identical with its antiparticle $\bar{\chi}_j$: $\chi_j \equiv \bar{\chi}_j$. On the basis of the existing neutrino data it is impossible to determine whether the massive neutrinos are Dirac or Majorana fermions.

In the case of n neutrino flavours and n massive neutrinos, the $n \times n$ unitary neutrino mixing matrix U can be parametrized by $n(n - 1)/2$ Euler angles and $n(n + 1)/2$ phases. If the massive neutrinos ν_j are Dirac particles, only $(n - 1)(n - 2)/2$ phases are physical and can be responsible for CP violation in the lepton sector. In this respect the neutrino (lepton) mixing with Dirac massive neutrinos is similar to the quark mixing. For $n = 3$ there is just one CP violating phase in U , which is usually called “the Dirac CP violating phase.” CP invariance holds if (in a certain standard convention) U is real, $U^* = U$.

If, however, the massive neutrinos are Majorana fermions, $\nu_j \equiv \chi_j$, the neutrino mixing matrix U contains $n(n - 1)/2$ CP violation phases [48,49], *i.e.*, by $(n - 1)$ phases more than in the Dirac neutrino case: in contrast to Dirac fields, the massive Majorana neutrino fields cannot “absorb” phases. In this case U can be cast in the form [48]

$$U = V P \tag{14.2}$$

where the matrix V contains the $(n - 1)(n - 2)/2$ Dirac CP violation phases, while P is a diagonal matrix with the additional $(n - 1)$ Majorana CP violation phases $\alpha_{21}, \alpha_{31}, \dots, \alpha_{n1}$,

$$P = \text{diag} \left(1, e^{i\frac{\alpha_{21}}{2}}, e^{i\frac{\alpha_{31}}{2}}, \dots, e^{i\frac{\alpha_{n1}}{2}} \right). \tag{14.3}$$

The Majorana phases will conserve CP if [50] $\alpha_{j1} = \pi q_j, q_j = 0, 1, 2, j = 2, 3, \dots, n$. In this case $\exp[i(\alpha_{j1} - \alpha_{k1})] = \pm 1$ has a simple physical interpretation: this is the relative CP-parity of Majorana neutrinos χ_j and χ_k . The condition of CP invariance of the leptonic CC weak interaction in the case of mixing and massive Majorana neutrinos reads [46]:

$$U_{lj}^* = U_{lj} \rho_j, \quad \rho_j = \frac{1}{i} \eta_{CP}(\chi_j) = \pm 1, \tag{14.4}$$

where $\eta_{CP}(\chi_j) = i\rho_j = \pm i$ is the CP parity of the Majorana neutrino χ_j [50]. Thus, if CP invariance holds, the elements of U are either real or purely imaginary.

In the case of $n = 3$ there are altogether 3 CP violation phases - one Dirac and two Majorana. Even in the mixing involving only 2 massive Majorana neutrinos there is one physical CP violation Majorana phase.

14.2. The three neutrino mixing

All existing compelling data on neutrino oscillations can be described assuming 3-flavour neutrino mixing in vacuum. This is the minimal

neutrino mixing scheme which can account for the currently available data on the oscillations of the solar (ν_e), atmospheric (ν_μ and $\bar{\nu}_\mu$), reactor ($\bar{\nu}_e$) and accelerator (ν_e and $\bar{\nu}_\mu$) neutrinos. The (left-handed) fields of the flavour neutrinos ν_e , ν_μ and ν_τ in the expression for the weak charged lepton current in the CC weak interaction Lagrangian, are linear combinations of the LH components of the fields of three massive neutrinos ν_j :

$$\mathcal{L}_{CC} = -\frac{g}{\sqrt{2}} \sum_{l=e,\mu,\tau} \bar{l}_L(x) \gamma_\alpha \nu_{lL}(x) W^{\alpha\dagger}(x) + h.c.,$$

$$\nu_{lL}(x) = \sum_{j=1}^3 U_{lj} \nu_{jL}(x), \quad (14.5)$$

where U is the 3×3 unitary neutrino mixing matrix [4,5]. As we have discussed in the preceding Section, the mixing matrix U can be parameterized by 3 angles, and, depending on whether the massive neutrinos ν_j are Dirac or Majorana particles, by 1 or 3 CP violation phases [48,49]:

$$U = \begin{bmatrix} c_{12}c_{13} & s_{12}c_{13} & s_{13}e^{-i\delta} \\ -s_{12}c_{23} - c_{12}s_{23}s_{13}e^{i\delta} & c_{12}c_{23} - s_{12}s_{23}s_{13}e^{i\delta} & s_{23}c_{13} \\ s_{12}s_{23} - c_{12}c_{23}s_{13}e^{i\delta} & -c_{12}s_{23} - s_{12}c_{23}s_{13}e^{i\delta} & c_{23}c_{13} \end{bmatrix} \\ \times \text{diag}(1, e^{i\frac{\alpha_{21}}{2}}, e^{i\frac{\alpha_{31}}{2}}). \quad (14.6)$$

where $c_{ij} = \cos \theta_{ij}$, $s_{ij} = \sin \theta_{ij}$, the angles $\theta_{ij} = [0, \pi/2]$, $\delta = [0, 2\pi]$ is the Dirac CP violation phase and α_{21} , α_{31} are two Majorana CP violation (CPV) phases. Thus, in the case of massive Dirac neutrinos, the neutrino mixing matrix U is similar, in what concerns the number of mixing angles and CPV phases, to the CKM quark mixing matrix. The presence of two additional physical CPV phases in U if ν_j are Majorana particles is a consequence of the special properties of the latter (*e.g.*, Refs. [46,48]).

The fundamental parameters characterizing the 3-neutrino mixing are: i) the 3 angles θ_{12} , θ_{23} , θ_{13} , ii) depending on the nature of massive neutrinos ν_j - 1 Dirac (δ), or 1 Dirac + 2 Majorana ($\delta, \alpha_{21}, \alpha_{31}$), CPV phases, and iii) the 3 neutrino masses, m_1 , m_2 , m_3 . Thus, depending on whether the massive neutrinos are Dirac or Majorana particles, this makes 7 or 9 additional parameters in the minimally extended Standard Model of particle interactions with massive neutrinos.

The angles θ_{12} , θ_{23} and θ_{13} can be defined via the elements of the neutrino mixing matrix:

$$c_{12}^2 \equiv \cos^2 \theta_{12} = \frac{|U_{e1}|^2}{1 - |U_{e3}|^2}, \quad s_{12}^2 \equiv \sin^2 \theta_{12} = \frac{|U_{e2}|^2}{1 - |U_{e3}|^2}, \quad (14.7)$$

$$s_{13}^2 \equiv \sin^2 \theta_{13} = |U_{e3}|^2, \quad s_{23}^2 \equiv \sin^2 \theta_{23} = \frac{|U_{\mu 3}|^2}{1 - |U_{e3}|^2},$$

$$c_{23}^2 \equiv \cos^2 \theta_{23} = \frac{|U_{\tau 3}|^2}{1 - |U_{e3}|^2}. \quad (14.8)$$

The neutrino oscillation probabilities depend, in general, on the neutrino energy, E , the source-detector distance L , on the elements of U and, for relativistic neutrinos used in all neutrino experiments performed so far, on $\Delta m_{ij}^2 \equiv (m_i^2 - m_j^2)$, $i \neq j$. In the case of 3-neutrino mixing there are only two independent neutrino mass squared differences, say $\Delta m_{21}^2 \neq 0$ and $\Delta m_{31}^2 \neq 0$. The numbering of massive neutrinos ν_j is arbitrary. It proves

convenient from the point of view of relating the mixing angles θ_{12} , θ_{23} and θ_{13} to observables, to identify $|\Delta m_{21}^2|$ with the smaller of the two neutrino mass squared differences, which, as it follows from the data, is responsible for the solar ν_e and, the observed by KamLAND, reactor $\bar{\nu}_e$ oscillations. We will number (just for convenience) the massive neutrinos in such a way that $m_1 < m_2$, so that $\Delta m_{21}^2 > 0$. With these choices made, there are two possibilities: either $m_1 < m_2 < m_3$, or $m_3 < m_1 < m_2$. Then the larger neutrino mass square difference $|\Delta m_{31}^2|$ or $|\Delta m_{32}^2|$, can be associated with the experimentally observed oscillations of the atmospheric and accelerator ν_μ and $\bar{\nu}_\mu$, as well as of the reactor $\bar{\nu}_e$ at $L \sim 1$ km. The effects of Δm_{31}^2 or Δm_{32}^2 in the oscillations of solar ν_e , and of Δm_{21}^2 in the oscillations of atmospheric and accelerator ν_μ and $\bar{\nu}_\mu$ or of the reactor $\bar{\nu}_e$ at $L \sim 1$ km, are relatively small and subdominant as a consequence of the facts that i) L , E and L/E in the experiments with solar ν_e and with atmospheric and accelerator ν_μ and $\bar{\nu}_\mu$, or with reactor $\bar{\nu}_e$ and baseline $L \sim 1$ km, are very different, ii) the conditions of production and propagation (on the way to the detector) of the solar ν_e and of the atmospheric or accelerator ν_μ and $\bar{\nu}_\mu$ and of the reactor $\bar{\nu}_e$, are very different, and iii) $|\Delta m_{21}^2|$ and $|\Delta m_{31}^2|$ ($|\Delta m_{32}^2|$) in the case of $m_1 < m_2 < m_3$ ($m_3 < m_1 < m_2$), as it follows from the data, differ by approximately a factor of 30, $|\Delta m_{21}^2| \ll |\Delta m_{31(32)}^2|$, $|\Delta m_{21}^2|/|\Delta m_{31(32)}^2| \cong 0.03$. This implies that in both cases of $m_1 < m_2 < m_3$ and $m_3 < m_1 < m_2$ we have $\Delta m_{32}^2 \cong \Delta m_{31}^2$ with $|\Delta m_{31}^2 - \Delta m_{32}^2| = |\Delta m_{21}^2| \ll |\Delta m_{31,32}^2|$. Obviously, in the case of $m_1 < m_2 < m_3$ ($m_3 < m_1 < m_2$) we have $\Delta m_{31(32)}^2 > 0$ ($\Delta m_{31(32)}^2 < 0$).

It followed from the results of the Chooz experiment [51] with reactor $\bar{\nu}_e$ and from the more recent data of the Daya Bay, RENO, Double Chooz and T2K experiments that, in the convention we use, in which $0 < \Delta m_{21}^2 < |\Delta m_{31(32)}^2|$, the element $|U_{e3}| = \sin \theta_{13}$ of the neutrino mixing matrix U is relatively small. This makes it possible to identify the angles θ_{12} and θ_{23} as the neutrino mixing angles associated with the solar ν_e and the dominant atmospheric ν_μ (and $\bar{\nu}_\mu$) oscillations, respectively. The angles θ_{12} and θ_{23} are sometimes called “solar” and “atmospheric” neutrino mixing angles, and are sometimes denoted as $\theta_{12} = \theta_\odot$ and $\theta_{23} = \theta_A$ (or θ_{atm}), while Δm_{21}^2 and Δm_{31}^2 are often referred to as the “solar” and “atmospheric” neutrino mass squared differences and are often denoted as $\Delta m_{21}^2 \equiv \Delta m_\odot^2$, $\Delta m_{31}^2 \equiv \Delta m_A^2$ (or Δm_{atm}^2).

The solar neutrino data tell us that $\Delta m_{21}^2 \cos 2\theta_{12} > 0$. In the convention employed by us we have $\Delta m_{21}^2 > 0$. Correspondingly, in this convention one must have $\cos 2\theta_{12} > 0$.

In August 2015 the first results of the NO ν A neutrino oscillation experiment were announced [55,56]. These results together with the latest neutrino and the first antineutrino data from the T2K experiment [57,58] (see also Ref. 59) were included, in particular, in the latest analysis of the global neutrino oscillation data performed in Ref. 60. Thus, in Ref. 60 the authors updated the results obtained earlier in [52,53,54]. We present in Table 14.1 the best fit values and the 99.73% CL allowed ranges of the neutrino oscillation parameters found in Ref. 60 using, in particular, the more “conservative” LID NO ν A data from Ref. 56. The best fit value of $\sin^2 \theta_{23}$ found for $\Delta m_{31(32)}^2 > 0$ ($\Delta m_{31(32)}^2 < 0$) in Ref. 60 reads: $\sin^2 \theta_{23} = 0.437$ (0.569). The authors of Ref. 60 also find that the hint for $\delta \cong 3\pi/2$ is strengthened by the NO ν A $\nu_\mu \rightarrow \nu_e$ and T2K $\bar{\nu}_\mu \rightarrow \bar{\nu}_e$

oscillation data. The values of $\delta = \pi/2$ and $\delta = 0$ (2π) are disfavored at 3σ CL and 2σ CL, respectively, while $\delta = \pi$ is allowed at approximately 1.6σ CL (1.2σ CL) for $\Delta m_{31(32)}^2 > 0$ ($\Delta m_{31(32)}^2 < 0$).

Table 14.1: The best-fit values and 3σ allowed ranges of the 3-neutrino oscillation parameters, derived from a global fit of the current neutrino oscillation data (from [60]). For the Dirac phase δ we give the best fit value and the 2σ allowed ranges; at 3σ no physical values of δ are disfavored. The values (values in brackets) correspond to $m_1 < m_2 < m_3$ ($m_3 < m_1 < m_2$). The definition of Δm^2 used is: $\Delta m^2 = m_3^2 - (m_2^2 + m_1^2)/2$. Thus, $\Delta m^2 = \Delta m_{31}^2 - \Delta m_{21}^2/2 > 0$, if $m_1 < m_2 < m_3$, and $\Delta m^2 = \Delta m_{32}^2 + \Delta m_{21}^2/2 < 0$ for $m_3 < m_1 < m_2$.

Parameter	best-fit	3σ
Δm_{21}^2 [10^{-5} eV ²]	7.37	6.93 – 7.97
$ \Delta m^2 $ [10^{-3} eV ²]	2.50 (2.46)	2.37 – 2.63 (2.33 – 2.60)
$\sin^2 \theta_{12}$	0.297	0.250 – 0.354
$\sin^2 \theta_{23}$, $\Delta m^2 > 0$	0.437	0.379 – 0.616
$\sin^2 \theta_{23}$, $\Delta m^2 < 0$	0.569	0.383 – 0.637
$\sin^2 \theta_{13}$, $\Delta m^2 > 0$	0.0214	0.0185 – 0.0246
$\sin^2 \theta_{13}$, $\Delta m^2 < 0$	0.0218	0.0186 – 0.0248
δ/π	1.35 (1.32)	(0.92 – 1.99) ((0.83 – 1.99))

It follows from the results given in Table 14.1 that θ_{23} is close to, but can be different from, $\pi/4$, $\theta_{12} \cong \pi/5.4$ and that $\theta_{13} \cong \pi/20$. Correspondingly, the pattern of neutrino mixing is drastically different from the pattern of quark mixing.

Note also that Δm_{21}^2 , $\sin^2 \theta_{12}$, $|\Delta m_{31(32)}^2|$, $\sin^2 \theta_{23}$ and $\sin^2 \theta_{13}$ are determined from the data with a 1σ uncertainty (= 1/6 of the 3σ range) of approximately 2.3%, 5.8%, 1.7%, 9.0% and 4.8%, respectively.

The existing SK atmospheric neutrino, K2K, MINOS, T2K and NO ν A data do not allow to determine the sign of $\Delta m_{31(32)}^2$. Maximal solar neutrino mixing, *i.e.*, $\theta_{12} = \pi/4$, is ruled out at more than 6σ by the data. Correspondingly, one has $\cos 2\theta_{12} \geq 0.29$ (at 99.73% CL).

Apart from the hint that the Dirac phase $\delta \cong 3\pi/2$, no other experimental information on the Dirac and Majorana CPV phases in the neutrino mixing matrix is available at present. Thus, the status of CP symmetry in the lepton sector is essentially unknown. With $\theta_{13} \cong 0.15 \neq 0$, the Dirac phase δ can generate CP violating effects in neutrino oscillations [48,61,62], *i.e.*, a difference between the probabilities of the $\nu_l \rightarrow \nu_{l'}$ and $\bar{\nu}_l \rightarrow \bar{\nu}_{l'}$ oscillations, $l \neq l' = e, \mu, \tau$. The magnitude of CP violation in $\nu_l \rightarrow \nu_{l'}$ and $\bar{\nu}_l \rightarrow \bar{\nu}_{l'}$ oscillations, $l \neq l' = e, \mu, \tau$, is determined by [63] the rephasing invariant J_{CP} , associated with the Dirac CPV phase in U :

$$J_{CP} = \text{Im} \left(U_{\mu 3} U_{e 3}^* U_{e 2} U_{\mu 2}^* \right). \quad (14.9)$$

It is analogous to the rephasing invariant associated with the Dirac CPV phase in the CKM quark mixing matrix [64]. In the “standard” parametrization of the neutrino mixing matrix (Eq. (14.6)), J_{CP} has the form:

$$J_{CP} \equiv \text{Im}(U_{\mu 3} U_{e 3}^* U_{e 2} U_{\mu 2}^*) = \frac{1}{8} \cos \theta_{13} \sin 2\theta_{12} \sin 2\theta_{23} \sin 2\theta_{13} \sin \delta. \tag{14.10}$$

Thus, given the fact that $\sin 2\theta_{12}$, $\sin 2\theta_{23}$ and $\sin 2\theta_{13}$ have been determined experimentally with a relatively good precision, the size of CP violation effects in neutrino oscillations depends essentially only on the magnitude of the currently not well determined value of the Dirac phase δ . The current data implies $J_{CP} \lesssim 0.035 \sin \delta$, where we have used the 3σ ranges of $\sin^2 \theta_{12}$, $\sin^2 \theta_{23}$ and $\sin^2 \theta_{13}$ given in Table 14.1. For the best fit values of $\sin^2 \theta_{12}$, $\sin^2 \theta_{23}$, $\sin^2 \theta_{13}$ and δ we find in the case of $\Delta m_{31(2)}^2 > 0$ ($\Delta m_{31(2)}^2 < 0$): $J_{CP} \cong 0.0327 \sin \delta \cong -0.0291$ ($J_{CP} \cong 0.0327 \sin \delta \cong -0.0276$). Thus, if the indication that $\delta \cong 3\pi/2$ is confirmed by future more precise data, the CP violation effects in neutrino oscillations would be relatively large.

If the neutrinos with definite masses ν_i , $i = 1, 2, 3$, are Majorana particles, the 3-neutrino mixing matrix contains two additional Majorana CPV phases [48]. However, the flavour neutrino oscillation probabilities $P(\nu_l \rightarrow \nu_{l'})$ and $P(\bar{\nu}_l \rightarrow \bar{\nu}_{l'})$, $l, l' = e, \mu, \tau$, do not depend on the Majorana phases [48,65]. The Majorana phases can play important role, e.g., in $|\Delta L| = 2$ processes like neutrinoless double beta $((\beta\beta)_{0\nu^-})$ decay $(A, Z) \rightarrow (A, Z + 2) + e^- + e^-$, L being the total lepton charge, in which the Majorana nature of massive neutrinos ν_i manifests itself (see, e.g., Refs. [46,66]). Our interest in the CPV phases present in the neutrino mixing matrix is stimulated also by the intriguing possibility that the Dirac phase and/or the Majorana phases in U_{PMNS} can provide the CP violation necessary for the generation of the observed baryon asymmetry of the Universe [67,68].

The existing data do not allow one to determine the sign of $\Delta m_A^2 = \Delta m_{31(2)}^2$. In the case of 3-neutrino mixing, the two possible signs of $\Delta m_{31(2)}^2$ correspond to two types of neutrino mass spectrum. In the widely used conventions of numbering the neutrinos with definite mass, the two spectra read: *i) Normal Ordering*: $m_1 < m_2 < m_3$, $\Delta m_{31}^2 = \Delta m_A^2 > 0$, $\Delta m_{21}^2 \equiv \Delta m_\odot^2 > 0$, $m_{2(3)} = (m_1^2 + \Delta m_{21(31)}^2)^{\frac{1}{2}}$; *ii) Inverted Ordering*: $m_3 < m_1 < m_2$, $\Delta m_{32}^2 = \Delta m_A^2 < 0$, $\Delta m_{21}^2 \equiv \Delta m_\odot^2 > 0$, $m_2 = (m_3^2 + \Delta m_{23}^2)^{\frac{1}{2}}$, $m_1 = (m_3^2 + \Delta m_{23}^2 - \Delta m_{21}^2)^{\frac{1}{2}}$.

14.8. Matter effects in neutrino oscillations

The presence of matter can change drastically the pattern of neutrino oscillations: neutrinos can interact with the particles forming the matter. Accordingly, the Hamiltonian of the neutrino system in matter H_m , differs from the Hamiltonian in vacuum H_0 , $H_m = H_0 + H_{int}$, where H_{int} describes the interaction of neutrinos with the particles of matter. When, for instance, ν_e and ν_μ propagate in matter, they can scatter (due to H_{int}) on the electrons (e^-), protons (p) and neutrons (n) present in matter. The incoherent elastic and the quasi-elastic scattering, in which the states of the initial particles change in the process (destroying the coherence between the neutrino states), are not of interest - they have a negligible effect on the solar neutrino propagation in the Sun and on the

solar, atmospheric and reactor neutrino propagation in the Earth [144]: even in the center of the Sun, where the matter density is relatively high ($\sim 150 \text{ g/cm}^3$), a ν_e with energy of 1 MeV has a mean free path with respect to the indicated scattering processes $\sim 10^{10}$ km. We recall that the solar radius is much smaller: $R_\odot = 6.96 \times 10^5$ km. The oscillating ν_e and ν_μ can scatter also elastically in the forward direction on the e^- , p and n , with the momenta and the spin states of the particles remaining unchanged. In such a process the coherence of the neutrino states is preserved.

The ν_e and ν_μ coherent elastic scattering on the particles of matter generates nontrivial indices of refraction of the ν_e and ν_μ in matter [26]: $\kappa(\nu_e) \neq 1$, $\kappa(\nu_\mu) \neq 1$. Most importantly, we have $\kappa(\nu_e) \neq \kappa(\nu_\mu)$. The difference $\kappa(\nu_e) - \kappa(\nu_\mu)$ is determined essentially by the difference of the real parts of the forward $\nu_e - e^-$ and $\nu_\mu - e^-$ elastic scattering amplitudes [26] $\text{Re} [F_{\nu_e e^-}(0)] - \text{Re} [F_{\nu_\mu e^-}(0)]$: due to the flavour symmetry of the neutrino - quark (neutrino - nucleon) neutral current interaction, the forward $\nu_e - p, n$ and $\nu_\mu - p, n$ elastic scattering amplitudes are equal and therefore do not contribute to the difference of interest [145]. The imaginary parts of the forward scattering amplitudes (responsible, in particular, for decoherence effects) are proportional to the corresponding total scattering cross-sections and in the case of interest are negligible in comparison with the real parts. The real parts of the amplitudes $F_{\nu_e e^-}(0)$ and $F_{\nu_\mu e^-}(0)$ can be calculated in the Standard Model. To leading order in the Fermi constant G_F , only the term in $F_{\nu_e e^-}(0)$ due to the diagram with exchange of a virtual W^\pm -boson contributes to $F_{\nu_e e^-}(0) - F_{\nu_\mu e^-}(0)$. One finds the following result for $\kappa(\nu_e) - \kappa(\nu_\mu)$ in the rest frame of the scatters [26,146,147]:

$$\begin{aligned} \kappa(\nu_e) - \kappa(\nu_\mu) &= \frac{2\pi}{p^2} \left(\text{Re} [F_{\nu_e e^-}(0)] - \text{Re} [F_{\nu_\mu e^-}(0)] \right) \\ &= -\frac{1}{p} \sqrt{2} G_F N_e, \end{aligned} \quad (14.53)$$

where N_e is the electron number density in matter. Given $\kappa(\nu_e) - \kappa(\nu_\mu)$, the system of evolution equations describing the $\nu_e \leftrightarrow \nu_\mu$ oscillations in matter reads [26]:

$$i \frac{d}{dt} \begin{pmatrix} A_e(t, t_0) \\ A_\mu(t, t_0) \end{pmatrix} = \begin{pmatrix} -\epsilon(t) & \epsilon'(t) \\ \epsilon'(t) & \epsilon(t) \end{pmatrix} \begin{pmatrix} A_e(t, t_0) \\ A_\mu(t, t_0) \end{pmatrix} \quad (14.54)$$

where $A_e(t, t_0)$ ($A_\mu(t, t_0)$) is the amplitude of the probability to find ν_e (ν_μ) at time t of the evolution of the system if at time $t_0 \leq t$ the neutrino ν_e or ν_μ has been produced and

$$\epsilon(t) = \frac{1}{2} \left[\frac{\Delta m^2}{2E} \cos 2\theta - \sqrt{2} G_F N_e(t) \right], \quad \epsilon'(t) = \frac{\Delta m^2}{4E} \sin 2\theta. \quad (14.55)$$

The term $\sqrt{2} G_F N_e(t)$ in $\epsilon(t)$ accounts for the effects of matter on neutrino oscillations. The system of evolution equations describing the oscillations of antineutrinos $\bar{\nu}_e \leftrightarrow \bar{\nu}_\mu$ in matter has exactly the same form except for the matter term in $\epsilon(t)$ which changes sign. The effect of matter in neutrino oscillations is usually called the Mikheyev, Smirnov, Wolfenstein (or MSW) effect.

Further discussion and all references may be found in the full *Review of Particle Physics*. The numbering of references and equations used here corresponds to that version.

15. QUARK MODEL

Revised August 2015 by C. Amsler (University of Bern), T. DeGrand (University of Colorado, Boulder), and B. Krusche (University of Basel).

15.1. Quantum numbers of the quarks

Quarks are strongly interacting fermions with spin $1/2$ and, by convention, positive parity. Antiquarks have negative parity. Quarks have the additive baryon number $1/3$, antiquarks $-1/3$. Table 15.1 gives the other additive quantum numbers (flavors) for the three generations of quarks. They are related to the charge Q (in units of the elementary charge e) through the generalized Gell-Mann-Nishijima formula

$$Q = I_z + \frac{B + S + C + B + T}{2}, \quad (15.1)$$

where B is the baryon number. The convention is that the *flavor* of a quark (I_z , S , C , B , or T) has the same sign as its *charge* Q . With this convention, any flavor carried by a charged meson has the same sign as its charge, *e.g.*, the strangeness of the K^+ is $+1$, the bottomness of the B^+ is $+1$, and the charm and strangeness of the D_s^- are each -1 . Antiquarks have the opposite flavor signs. The hypercharge is defined as

$$Y = B + S - \frac{C - B + T}{3}.$$

Thus Y is equal to $\frac{1}{3}$ for the u and d quarks, $-\frac{2}{3}$ for the s quark, and 0 for all other quarks.

15.2. Mesons

Mesons have baryon number $B = 0$. In the quark model, they are $q\bar{q}'$ bound states of quarks q and antiquarks \bar{q}' (the flavors of q and q' may be different). If the orbital angular momentum of the $q\bar{q}'$ state is ℓ , then the parity P is $(-1)^{\ell+1}$. The meson spin J is given by the usual relation $|\ell - s| \leq J \leq |\ell + s|$, where s is 0 (antiparallel quark spins) or 1 (parallel quark spins). The charge conjugation, or C -parity $C = (-1)^{\ell+s}$, is defined only for the $q\bar{q}$ states made of quarks and their own antiquarks. The C -parity can be generalized to the G -parity $G = (-1)^{I+\ell+s}$ for mesons made of quarks and their own antiquarks (isospin $I_z = 0$), and for the charged $u\bar{d}$ and $d\bar{u}$ states (isospin $I = 1$).

The mesons are classified in J^{PC} multiplets. The $\ell = 0$ states are the pseudoscalars (0^{-+}) and the vectors (1^{--}). The orbital excitations $\ell = 1$ are the scalars (0^{++}), the axial vectors (1^{++}) and (1^{+-}), and the tensors (2^{++}). Assignments for many of the known mesons are given in Tables 15.2 and 15.3. Radial excitations are denoted by the principal quantum number n . The very short lifetime of the t quark makes it likely that bound-state hadrons containing t quarks and/or antiquarks do not exist.

States in the natural spin-parity series $P = (-1)^J$ must, according to the above, have $s = 1$ and hence, $CP = +1$. Thus, mesons with natural spin-parity and $CP = -1$ (0^{+-} , 1^{-+} , 2^{+-} , 3^{-+} , *etc.*) are forbidden in the $q\bar{q}'$ model. The $J^{PC} = 0^{--}$ state is forbidden as well. Mesons with such *exotic* quantum numbers may exist, but would lie outside the $q\bar{q}'$ model (see section below on exotic mesons).

Following $SU(3)$, the nine possible $q\bar{q}'$ combinations containing the light u , d , and s quarks are grouped into an octet and a singlet of light quark mesons:

$$\mathbf{3} \otimes \bar{\mathbf{3}} = \mathbf{8} \oplus \mathbf{1} . \quad (15.2)$$

A fourth quark such as charm c can be included by extending SU(3) to SU(4). However, SU(4) is badly broken owing to the much heavier c quark. Nevertheless, in an SU(4) classification, the sixteen mesons are grouped into a 15-plet and a singlet:

$$\mathbf{4} \otimes \bar{\mathbf{4}} = \mathbf{15} \oplus \mathbf{1} . \quad (15.3)$$

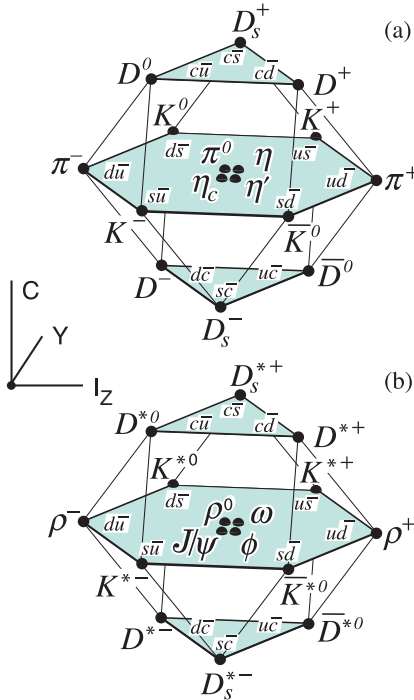


Figure 15.1: SU(4) weight diagram showing the 16-plets for the pseudoscalar (a) and vector mesons (b) made of the u , d , s , and c quarks as a function of isospin I_z , charm C , and hypercharge $Y = B + S - \frac{C}{3}$. The nonets of light mesons occupy the central planes to which the $c\bar{c}$ states have been added.

The *weight diagrams* for the ground-state pseudoscalar (0^{-+}) and vector (1^{-}) mesons are depicted in Fig. 15.1. The light quark mesons are members of nonets building the middle plane in Fig. 15.1(a) and (b).

Isoscalar states with the same J^{PC} will mix, but mixing between the two light quark isoscalar mesons, and the much heavier charmonium or bottomonium states, are generally assumed to be negligible.

15.3. Exotic mesons

The existence of a light nonet composed of four quarks with masses below 1 GeV was suggested a long time ago [9]. Coupling two triplets of light quarks u , d , and s , one obtains nine states, of which the six symmetric (uu , dd , ss , $ud+du$, $us+su$, $ds+sd$) form the six dimensional representation $\mathbf{6}$, while the three antisymmetric ($ud-du$, $us-su$, $ds-sd$) form the three dimensional representation $\bar{\mathbf{3}}$ of SU(3):

$$\mathbf{3} \otimes \mathbf{3} = \mathbf{6} \oplus \bar{\mathbf{3}} . \quad (15.20)$$

Combining with spin and color and requiring antisymmetry, one finds that the most deeply bound diquark (and hence the lightest) is the one in the $\bar{\mathbf{3}}$ and spin singlet state. The combination of the diquark with an antiquark in the $\mathbf{3}$ representation then gives a light nonet of four-quark scalar states.

15.4. Baryons: qqq states

Baryons are fermions with baryon number $\mathcal{B} = 1$, *i.e.*, in the most general case, they are composed of three quarks plus any number of quark - antiquark pairs. So far all established baryons are 3-quark (qqq) configurations (the LHCb collaboration has very recently announced observation of two charmed ‘pentaquark’ states of minimal quark content $c\bar{c}uud$ at invariant masses close to 4.4 GeV [23]). The color part of their state functions is an SU(3) singlet, a completely antisymmetric state of the three colors. Since the quarks are fermions, the state function must be antisymmetric under interchange of any two equal-mass quarks (up and down quarks in the limit of isospin symmetry). Thus it can be written as

$$|qqq\rangle_A = |\text{color}\rangle_A \times |\text{space, spin, flavor}\rangle_S , \quad (15.21)$$

where the subscripts S and A indicate symmetry or antisymmetry under interchange of any two equal-mass quarks. Note the contrast with the state function for the three nucleons in ${}^3\text{H}$ or ${}^3\text{He}$:

$$|NNN\rangle_A = |\text{space, spin, isospin}\rangle_A . \quad (15.22)$$

This difference has major implications for internal structure, magnetic moments, *etc.*

The “ordinary” baryons are made up of u , d , and s quarks. The three flavors imply an approximate flavor SU(3), which requires that baryons made of these quarks belong to the multiplets on the right side of

$$\mathbf{3} \otimes \mathbf{3} \otimes \mathbf{3} = \mathbf{10}_S \oplus \mathbf{8}_M \oplus \mathbf{8}_M \oplus \mathbf{1}_A . \quad (15.23)$$

Further discussion and all references may be found in the full *Review of Particle Physics*. The numbering of references and equations used here corresponds to that version.

16. GRAND UNIFIED THEORIES

Revised September 2016 by A. Hebecker (U. Heidelberg) and J. Hisano (Nagoya U.)

The Standard Model (SM) has gauge group $G_{SM} = SU(3)_C \times SU(2)_L \times U(1)_Y$, three generations of fermions in the representation

$$(\mathbf{3}, \mathbf{2})_{1/3} + (\bar{\mathbf{3}}, \mathbf{1})_{-4/3} + (\bar{\mathbf{3}}, \mathbf{1})_{2/3} + (\mathbf{1}, \mathbf{2})_{-1} + (\mathbf{1}, \mathbf{1})_2, \quad (16.1)$$

and a scalar Higgs doublet H transforming as $(\mathbf{1}, \mathbf{2})_1$. In our convention the electric charge is $Q = T_3 + Y/2$ and all our spinor fields are left-handed. We use boldface numbers to specify the dimension of representations of non-Abelian groups (in this case fundamental and antifundamental) and lower indices for $U(1)$ charges. The fields of Eq. (16.1) should also be familiar as $[Q, u^c, d^c, L, e^c]$, with $Q = (u, d)$ and $L = (\nu, e)$ being the quark and lepton $SU(2)$ -doublets and u^c, d^c, e^c charge conjugate $SU(2)$ -singlets. Though neutrinos are massless in the original SM, finite neutrino masses are incorporated by allowing for the dimension-five operator $(HL)^2$, which is in turn generated by the see-saw mechanism.

Within the SM, the rather complex group-theoretic data of Eq. (16.1) remains unexplained. In addition, there are 19 seemingly arbitrary coupling constants, including the gauge couplings* g_3, g_2 and g_1 and fermion masses and mixings. The paradigm of Grand Unification Theories (GUTs) addresses mainly the group theoretic data and the values of the three gauge couplings. It may also impact other issues of the SM.

More specifically, after precision measurements of the Weinberg angle θ_W in the LEP experiments, supersymmetric GUTs (SUSY GUTs) have become the leading paradigm for ‘Physics beyond the SM’. This is due to their correct prediction of θ_W . The measured Higgs mass (~ 125 GeV) is in principle consistent with this picture, but it suggests heavy superpartners. Independently, the LHC has disfavored light colored superpartners. These are new hints for future work on SUSY GUTs or on GUTs without TeV-scale supersymmetry.

The minimal choice for unification in a simple group is $SU(5)$. Embedding G_{SM} in $SU(5)$ is straightforward, with $SU(3)_C$ and $SU(2)_L$ corresponding e.g. to the upper-left 3×3 and lower-right 2×2 blocks, respectively, in traceless 5×5 matrices for $SU(5)$ generators of the fundamental representation. The $U(1)_Y$ corresponds to matrices generated by $\text{diag}(-2/3, -2/3, -2/3, 1, 1)$, which hence commute with $SU(3)_C \times SU(2)_L \subset SU(5)$. Quantization of $U(1)_Y$ hypercharge is automatic. It is then easy to derive how one SM generation precisely comes from the $\mathbf{10} + \bar{\mathbf{5}}$ of $SU(5)$ (where $\mathbf{10}$ is the antisymmetric rank-2 tensor):

$$\mathbf{10} : \begin{pmatrix} 0 & u_b^c & -u_g^c & u_r & d_r \\ -u_b^c & 0 & u_1^c & u_g & d_g \\ u_g^c & -u_r^c & 0 & u_b & d_b \\ -u_r & -u_g & -u_b & 0 & e^c \\ -d_r & -d_g & -d_b & -e^c & 0 \end{pmatrix} \quad \text{and} \quad \bar{\mathbf{5}} : \begin{pmatrix} d_r^c \\ d_g^c \\ d_b^c \\ e \\ -\nu_e \end{pmatrix} \quad (16.2)$$

* Equivalently, the $SU(2)_L$ and $U(1)_Y$ couplings are denoted as $g = g_2$ and $g' = \sqrt{3/5} g_1$. One also uses $\alpha_s = \alpha_3 = (g_3^2/4\pi)$, $\alpha_{EM} = (e^2/4\pi)$ with $e = g \sin \theta_W$ and $\sin^2 \theta_W = (g')^2/(g^2 + (g')^2)$.

$SU(5)$ GUTs have 12 new gauge bosons known as X bosons (or X/Y bosons) in addition to the SM. X bosons form an $SU(3)_C$ -triplet and $SU(2)_L$ -doublet. Their interactions connect quarks and leptons, violating baryon (B) and lepton numbers (L). Hence nucleon decay is predicted.

The unification group $SO(10)$ has the remarkable feature that its 16-dimensional spinor representation accommodates a full SM generation together with an extra singlet, potentially a r.h. neutrino. This makes $SO(10)$ GUTs particularly interesting. It is noteworthy that G_{SM} is a maximal subgroup of $SU(5)$, which together with an extra factor $U(1)_X$ is a maximal subgroup of $SO(10)$. This logic continues very elegantly up to the largest exceptional group E_8 .

The SM Higgs can sit in either a $\mathbf{5}_H$ or $\bar{\mathbf{5}}_H$ of $SU(5)$, with the additional states known as color-triplet Higgs scalars. They also induce nucleon decay, leading to a lower mass bound of $\sim 10^{11}$ GeV. In SUSY GUTs, both Higgs multiplets $\mathbf{5}_H$, and $\bar{\mathbf{5}}_H$ are required and the mass bound from nucleon decay is much more severe – the mass is required to be above the GUT scale M_G .

The unified gauge group can be broken spontaneously by an appropriate GUT Higgs sector. In the simplest case of $SU(5)$, the $\mathbf{24}$ (adjoint) GUT Higgs develops a vacuum expectation value (VEV) along the G_{SM} -singlet direction as $\langle \Phi \rangle \propto \text{diag}(-2/3, -2/3, -2/3, 1, 1)$. The masses of doublet and triplet in the $\mathbf{5}_H$ (and $\bar{\mathbf{5}}_H$) generically split due to their coupling to the GUT Higgs. In addition, both the doublet and the triplet mass get an equal contribution from an $SU(5)$ -invariant GUT-scale mass term. Without any further structure, an extreme fine-tuning between two large effects is then necessary to keep the doublet mass at the electroweak scale. Supersymmetry can forbid large radiative corrections to the doublet mass, but the tree-level fine tune remains. This is the doublet-triplet splitting problem. Many mechanisms for its natural solution have been suggested over the years.

In general, GUT-breaking sectors successfully resolving the doublet-triplet splitting problem, dynamically stabilizing all GUT-scale VEVs and allowing for realistic fermion masses require many ingredients. Thus models beyond 4d field theory appear attractive. In such models, in particular in string constructions, GUT breaking may occur due to boundary conditions in the compactified dimensions. Moreover, such boundary conditions can give mass only to the triplet, leaving the doublet massless.

The proximity of the GUT scale to the Planck scale provides an independent motivation to go beyond 4d field theory. The leading model at such energies is Superstring or M-theory. From it, five 10d and one 11d effective supergravity theories arise. Grand unification is realized most naturally in the context of the two ‘heterotic’ theories with gauge groups $E_8 \times E_8$ and $SO(32)$. To describe particle physics, solutions of the 10d theory with geometry $R^{1,3} \times M_6$ are considered, where M_6 is a Calabi-Yau 3-fold (with 6 real dimensions). These solutions involve VEVs of higher-dimensional components of the $E_8 \times E_8$ gauge fields, leading to symmetry breaking. Heterotic orbifold models represent an important limiting case: Here the internal space is a six-torus, modded out by a discrete symmetry group (e.g. T^6/Z_n). An even simpler approach is provided by Orbifold GUTs. These are 5d or 6d field theories with unified gauge group (e.g.

$SU(5)$ or $SO(10)$), broken in the process of compactifying to 4d.

With the advent of the string-theory ‘flux landscape’, which is best understood in 10d type-IIB supergravity, the focus in string model building has shifted to this framework. In type IIB, gauge fields do not live in 10d but on brane-stacks. For example, models with 8d gauge theories on D7 branes have been considered. Certain problems of such constructions can be overcome on the non-perturbative branch of type IIB, also known as F-theory. This framework combines the advantages of the heterotic approach with the more recent progress in the ‘flux landscape’. It is the presently most active branch of theory-driven GUT model building. A final important issue in string GUTs is the so-called string-scale/GUT-scale problem - a failure of heterotic models to realize the phenomenological goal of $M_G \sim 2 \times 10^{16}$ GeV. In F-theory GUTs, this situation is improved.

The quantitative unification of the three SM gauge couplings at the energy scale M_G is one of the cornerstones of the GUT paradigm. In the simplest case, the relevant effective field theory (EFT) at energies $\mu \gg M_G$ has a unified gauge symmetry and a single running gauge coupling $\alpha_G(\mu)$. At energies $\mu \ll M_G$, states with mass $\sim M_G$ (such as X bosons, GUT Higgs, color-triplet Higgs) have to be integrated out. The EFT now has three independent couplings and SM (or MSSM) matter content. One-loop renormalization group equations readily allow for an extrapolation to the weak scale ($\alpha_i \equiv g_i^2/(4\pi)$):

$$\alpha_i^{-1}(m_Z) = \alpha_G^{-1}(M_G) + \frac{b_i}{2\pi} \log\left(\frac{M_G}{m_Z}\right) + \delta_i. \quad (16.3)$$

Here we defined δ_i to absorb all sub-leading effects, including in particular threshold corrections. It is apparent from Eq. (16.3) that the three low-scale couplings can be very different. Inverting the argument, one expects that extrapolating the measured couplings to the high scale, we find quantitative unification at $\mu \sim M_G$. While this fails in the SM, it works intriguingly well in the MSSM (cf. Fig. 1).

The three equations contained in Eq. (16.3) can be used to determine the three ‘unknowns’ $\alpha_G^{-1}(M_G) \simeq 24.3$, $M_G \simeq 2 \times 10^{16}$ GeV, and

$$\alpha_3^{-1}(m_Z) = (\alpha_3^{\text{LO}})^{-1}(m_Z) + \Delta_3 = (0.117)^{-1} + \Delta_3.$$

Remarkably, the leading order result for α_3 is in excellent agreement with experiments: $\alpha_3^{\text{EXP}}(m_Z) = 0.1185 \pm 0.0006$. However, this near perfection is to some extent accidental. Indeed,

$$\Delta_3 \simeq -0.82 + \frac{19}{28\pi} \log\left(\frac{m_{\text{SUSY}}}{m_Z}\right),$$

based on two-loop running and low-scale thresholds. For an effective SUSY scale m_{SUSY} near 1 TeV, a discrepancy results. This can be fixed by invoking high-scale threshold corrections and/or raising m_{SUSY} . For non-SUSY GUTs or GUTs with a very high SUSY breaking scale to fit the data, new light states in incomplete GUT multiplets or multiple GUT breaking scales are required.

Quarks and leptons are indistinguishable in any 4d GUT. This leads to B -violating nucleon decay. The lowest-dimension operators relevant for nucleon decay are $(B+L)$ violating dimension-six four-fermion-terms. In $SU(5)$ GUTs, they are induced by X boson exchange. These

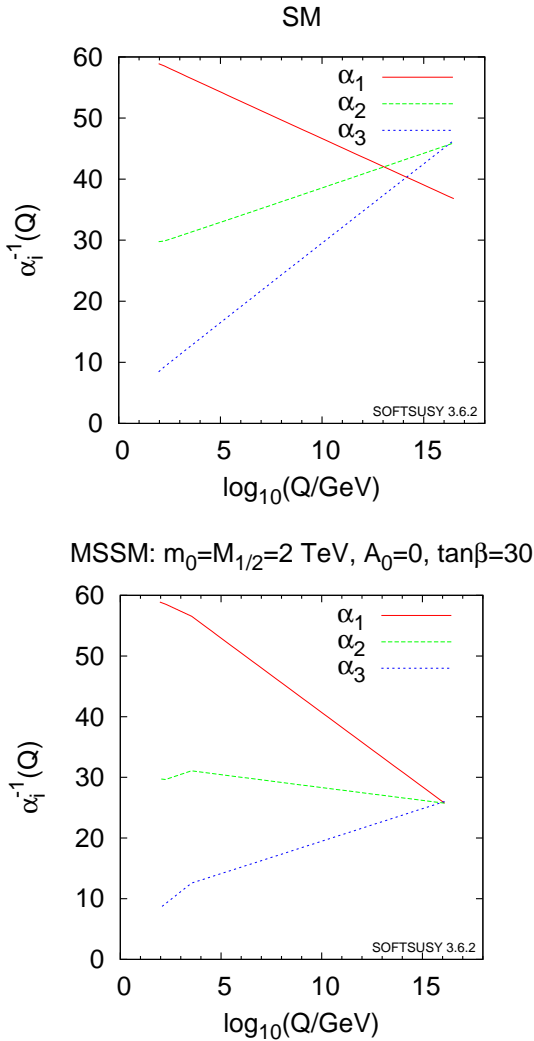


Figure 16.1: Running couplings in SM and MSSM using two-loop RG evolution. (We thank Ben Allanach for providing the plots created using SOFTSUSY.)

operators are suppressed by $(1/M_G^2)$, and the nucleon lifetime is given by $\tau_N \propto M_G^4/(\alpha_G^2 m_p^5)$ (m_p is the proton mass). The dominant decay mode of the proton, via X boson exchange, is $p \rightarrow e^+ \pi^0$. In any simple gauge symmetry with one universal GUT coupling α_G and scale M_G , the nucleon lifetime from gauge boson exchange is calculable. Hence, the GUT scale may be directly observed via the extremely rare decay of the nucleon. The

present experimental bounds on the modes come from Super-Kamiokande, e.g. $\tau_p/\text{Br}(p \rightarrow e^+\pi^0) > 1.67 \times 10^{34}$ years. While non-SUSY GUTs are constrained by the non-observation of nucleon decay, a precise and general statement is hard to make due to failure of the simple gauge coupling unification. In SUSY GUTs one generically has $M_G \sim 2 \times 10^{16}$ GeV, and dimension-six B -violating operators are predicted to induce a lifetime of about $\tau_p \sim 10^{36}$ years.

In SUSY GUTs there are additional sources for B and/or L violation – dimension-four and five operators. These arise since, in the SUSY SM, quarks and leptons have scalar partners (squarks and sleptons). Although our notation does not change, when discussing SUSY models our fields are chiral superfields and both fermionic and bosonic matter is implicitly represented by those. Within the context of $SU(5)$ the B - and/or L -violating dimension-four and five operators have the form $(\mathbf{10} \mathbf{\bar{5}} \mathbf{\bar{5}}) \supset (u^c d^c d^c) + (Q L d^c) + (e^c L L)$, and $(\mathbf{10} \mathbf{10} \mathbf{10} \mathbf{\bar{5}}) \supset (Q Q Q L) + (u^c u^c d^c e^c) + B$ - and L -conserving terms, respectively, which contain two fermionic components and the rest scalars or products of scalars.

The dimension-four operators are either B - or L -violating. The nucleon lifetime is extremely short if both types of dimension-four operators are present in the SUSY SM since squark or slepton exchange induces the dangerous dimension-six SM operators. Even in the case that they violate B or L only but not both, they are constrained by various phenomena. Both types of operators can be eliminated by requiring R parity, which distinguishes Higgs from ordinary matter multiplets. R parity acts as $F \rightarrow -F$, $H \rightarrow H$ with $F = \{\mathbf{10}, \mathbf{\bar{5}}\}$, $H = \{\mathbf{\bar{5}}_H, \mathbf{5}_H\}$ in $SU(5)$.

The dimension-five operators have a dimensionful coupling of order $(1/M_G)$. They are generated by integrating out the color-triplet Higgs with GUT-scale mass. The operators include squarks and/or sleptons. To allow for nucleon decay, these must be converted to light quarks or leptons by exchange of a gaugino or Higgsino in the SUSY SM. The nucleon lifetime is proportional to $M_G^2 m_{\text{SUSY}}^2/m_p^5$, where m_{SUSY} is the SUSY breaking scale. Thus, dimension-five operators may predict a shorter nucleon lifetime than dimension-six operators. Unless accidental cancellations are present, the dominant decay modes from dimension-five operators include a K meson, such as $p \rightarrow K^+ \bar{\nu}$, due to a simple symmetry argument.

Recent Super-Kamiokande bounds on the proton lifetime severely constrain the dimension-six and five operators. The lower bound on the X boson mass from null results in nucleon decay searches is approaching 10^{16} GeV in SUSY $SU(5)$ GUTs. In the minimal SUSY $SU(5)$, the proton lifetime is smaller than about 10^{31} years if the triplet Higgs mass is 10^{16} GeV and $m_{\text{SUSY}} = 1$ TeV. The triplet Higgs mass bound from nucleon decay is then in conflict with gauge coupling unification so that this model is considered to be ruled out.

Since nucleon decay induced by the triplet Higgs is a severe problem in SUSY GUTs, various proposals for its suppression have been made. The null results may also suggest heavy superpartners. Future experiments with larger neutrino detectors, such as JUNO, Hyper-Kamiokande and DUNE, are planned and will have higher sensitivities to nucleon decay.

Masses and mixings for quarks and leptons come from the Yukawa

couplings with the Higgs doublet in the SM, but the values of these couplings remain a mystery. GUTs provide at least a partial understanding since each generation is embedded in unified multiplet(s). Specifically, since quarks and leptons are two sides of the same coin, the GUT symmetry relates the Yukawa couplings (and hence the masses) of quarks and leptons. In $SU(5)$, we have relations between Yukawa coupling constants for charged lepton and down quark masses at the GUT scale, such as $\lambda_b = \lambda_\tau$ in which $\lambda_{b/\tau}$ are the bottom quark / τ lepton Yukawa coupling constants. In $SO(10)$, there is only one type of independent renormalizable Yukawa interaction, leading to relations among all Yukawa coupling constants and the fermion masses within one generation (such as $\lambda_t = \lambda_b = \lambda_\tau$, with λ_t the top quark Yukawa coupling constant). Comparing these relations with the observed values of fermion masses, we get constraints on the parameter space in the MSSM.

Now we know that neutrinos have finite, but tiny masses. The seesaw mechanism, *naturally* explaining such tiny neutrino masses, introduces three “sterile” neutrinos to have Yukawa couplings with lepton doublets, λ_ν . The sterile neutrinos have no SM gauge quantum numbers so that there is no symmetry other than global lepton number which forbids the Majorana mass terms, M . Note also that sterile neutrinos can be identified with the r.h. neutrinos necessarily contained in complete families of $SO(10)$ or Pati-Salam models. Since the Majorana mass term violates $U(1)_X$ in $SO(10)$, one might expect it is around M_G . The heavy sterile neutrinos can be integrated out, the Majorana mass terms of light active Majorana neutrinos are given as $m = m_\nu^T M^{-1} m_\nu$ where $m_\nu = \lambda_\nu \langle H \rangle$. When assuming hierarchical neutrino masses and also a neutrino Yukawa coupling equal to the top quark Yukawa coupling, $\lambda_{\nu\tau} = \lambda_t$ at the GUT scale, as in $SO(10)$ or $SU(4) \times SU(2)_L \times SU(2)_R$ models, the atmospheric neutrino oscillation implies $M \sim 10^{14}$ GeV. This is remarkably close to the GUT scale. On the other hand, neutrinos pose a special problem for GUTs. The question is why are the quark mixing angles in the CKM matrix small, while there are two large lepton mixing angles in the PMNS matrix.

To conclude, we recall that quantitative gauge coupling unification with supersymmetry still works well even if the SUSY scale is somewhat high. However, once it so high that the gauge-hierarchy motivation for SUSY must be abandoned, it becomes a free parameter and the ‘GUT prediction’ of α_3 crumbles. It is the more important to keep pushing bounds on nucleon decay which is arguably a more generic part of the GUT paradigm. Furthermore, due to limitations of the 4d approach, especially free parameters or ad hoc assumptions in models of flavor and GUT breaking, the string theoretic approach has become more important in GUT model building.

Further discussion and references may be found in the full *Review*.

19. STRUCTURE FUNCTIONS

Updated September 2015 by B. Foster (University of Hamburg/DESY), A.D. Martin (University of Durham), R.S. Thorne (University College London) and M.G. Vincter (Carleton University).

This section has been abridged from the full version of the *Review*.

19.1. Deep inelastic scattering

High-energy lepton-nucleon scattering (deep inelastic scattering) plays a key role in determining the partonic structure of the proton. The process $\ell N \rightarrow \ell' X$ is illustrated in Fig. 19.1. The filled circle in this figure represents the internal structure of the proton which can be expressed in terms of structure functions.

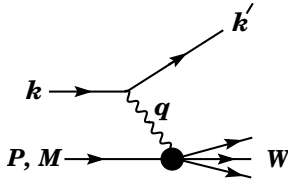


Figure 19.1: Kinematic quantities for the description of deep inelastic scattering. The quantities k and k' are the four-momenta of the incoming and outgoing leptons, P is the four-momentum of a nucleon with mass M , and W is the mass of the recoiling system X . The exchanged particle is a γ , W^\pm , or Z ; it transfers four-momentum $q = k - k'$ to the nucleon.

Invariant quantities:

$\nu = \frac{q \cdot P}{M} = E - E'$ is the lepton's energy loss in the nucleon rest frame (in earlier literature sometimes $\nu = q \cdot P$). Here, E and E' are the initial and final lepton energies in the nucleon rest frame.

$Q^2 = -q^2 = 2(E E' - \vec{k} \cdot \vec{k}') - m_\ell^2 - m_{\ell'}^2$ where $m_\ell (m_{\ell'})$ is the initial (final) lepton mass. If $E E' \sin^2(\theta/2) \gg m_\ell^2, m_{\ell'}^2$, then $\approx 4 E E' \sin^2(\theta/2)$, where θ is the lepton's scattering angle with respect to the lepton beam direction.

$x = \frac{Q^2}{2M\nu}$ where, in the parton model, x is the fraction of the nucleon's momentum carried by the struck quark.

$y = \frac{q \cdot P}{k \cdot P} = \frac{\nu}{E}$ is the fraction of the lepton's energy lost in the nucleon rest frame.

$W^2 = (P + q)^2 = M^2 + 2M\nu - Q^2$ is the mass squared of the system X recoiling against the scattered lepton.

$s = (k + P)^2 = \frac{Q^2}{xy} + M^2 + m_\ell^2$ is the center-of-mass energy squared of the lepton-nucleon system.

The process in Fig. 19.1 is called deep ($Q^2 \gg M^2$) inelastic ($W^2 \gg M^2$) scattering (DIS). In what follows, the masses of the initial and scattered leptons, m_ℓ and $m_{\ell'}$, are neglected.

19.1.1. DIS cross sections :

$$\frac{d^2\sigma}{dx dy} = x(s - M^2) \frac{d^2\sigma}{dx dQ^2} = \frac{2\pi M\nu}{E'} \frac{d^2\sigma}{d\Omega_{\text{Nrest}} dE'} . \quad (19.1)$$

In lowest-order perturbation theory, the cross section for the scattering of polarized leptons on polarized nucleons can be expressed in terms of the products of leptonic and hadronic tensors associated with the coupling of the exchanged bosons at the upper and lower vertices in Fig. 19.1 (see Refs. 1-4)

$$\frac{d^2\sigma}{dx dy} = \frac{2\pi y\alpha^2}{Q^4} \sum_j \eta_j L_j^{\mu\nu} W_{\mu\nu}^j . \quad (19.2)$$

For neutral-current processes, the summation is over $j = \gamma, Z$ and γZ representing photon and Z exchange and the interference between them, whereas for charged-current interactions there is only W exchange, $j = W$. (For transverse nucleon polarization, there is a dependence on the azimuthal angle of the scattered lepton.) The lepton tensor $L_{\mu\nu}$ is associated with the coupling of the exchange boson to the leptons. For incoming leptons of charge $e = \pm 1$ and helicity $\lambda = \pm 1$,

$$\begin{aligned} L_{\mu\nu}^\gamma &= 2 \left(k_\mu k'_\nu + k'_\mu k_\nu - (k \cdot k' - m_\ell^2) g_{\mu\nu} - i\lambda \varepsilon_{\mu\nu\alpha\beta} k^\alpha k'^\beta \right), \\ L_{\mu\nu}^{\gamma Z} &= (g_V^e + e\lambda g_A^e) L_{\mu\nu}^\gamma, \quad L_{\mu\nu}^Z = (g_V^e + e\lambda g_A^e)^2 L_{\mu\nu}^\gamma, \\ L_{\mu\nu}^W &= (1 + e\lambda)^2 L_{\mu\nu}^\gamma, \end{aligned} \quad (19.3)$$

where $g_V^e = -\frac{1}{2} + 2\sin^2\theta_W$, $g_A^e = -\frac{1}{2}$.

Although here the helicity formalism is adopted, an alternative approach is to express the tensors in Eq. (19.3) in terms of the polarization of the lepton.

The factors η_j in Eq. (19.2) denote the ratios of the corresponding propagators and couplings to the photon propagator and coupling squared

$$\begin{aligned} \eta_\gamma &= 1 \quad ; \quad \eta_{\gamma Z} = \left(\frac{G_F M_Z^2}{2\sqrt{2}\pi\alpha} \right) \left(\frac{Q^2}{Q^2 + M_Z^2} \right); \\ \eta_Z &= \eta_{\gamma Z}^2 \quad ; \quad \eta_W = \frac{1}{2} \left(\frac{G_F M_W^2}{4\pi\alpha} \frac{Q^2}{Q^2 + M_W^2} \right)^2. \end{aligned} \quad (19.4)$$

The hadronic tensor, which describes the interaction of the appropriate electroweak currents with the target nucleon, is given by

$$W_{\mu\nu} = \frac{1}{4\pi} \int d^4z e^{iq \cdot z} \langle P, S \left[\left[J_\mu^\dagger(z), J_\nu(0) \right] \right] P, S \rangle, \quad (19.5)$$

where S denotes the nucleon-spin 4-vector, with $S^2 = -M^2$ and $S \cdot P = 0$.

19.2. Structure functions of the proton

The structure functions are defined in terms of the hadronic tensor (see Refs. 1-3)

$$\begin{aligned} W_{\mu\nu} &= \left(-g_{\mu\nu} + \frac{q_\mu q_\nu}{q^2} \right) F_1(x, Q^2) + \frac{\hat{P}_\mu \hat{P}_\nu}{P \cdot q} F_2(x, Q^2) \\ &\quad - i\varepsilon_{\mu\nu\alpha\beta} \frac{q^\alpha P^\beta}{2P \cdot q} F_3(x, Q^2) \\ &\quad + i\varepsilon_{\mu\nu\alpha\beta} \frac{q^\alpha}{P \cdot q} \left[S^\beta g_1(x, Q^2) + \left(S^\beta - \frac{S \cdot q}{P \cdot q} P^\beta \right) g_2(x, Q^2) \right] \end{aligned}$$

$$\begin{aligned}
& + \frac{1}{P \cdot q} \left[\frac{1}{2} \left(\hat{P}_\mu \hat{S}_\nu + \hat{S}_\mu \hat{P}_\nu \right) - \frac{S \cdot q}{P \cdot q} \hat{P}_\mu \hat{P}_\nu \right] g_3(x, Q^2) \\
& + \frac{S \cdot q}{P \cdot q} \left[\frac{\hat{P}_\mu \hat{P}_\nu}{P \cdot q} g_4(x, Q^2) + \left(-g_{\mu\nu} + \frac{q_\mu q_\nu}{q^2} \right) g_5(x, Q^2) \right] \quad (19.6)
\end{aligned}$$

where

$$\hat{P}_\mu = P_\mu - \frac{P \cdot q}{q^2} q_\mu, \quad \hat{S}_\mu = S_\mu - \frac{S \cdot q}{q^2} q_\mu. \quad (19.7)$$

The cross sections for neutral- and charged-current deep inelastic scattering on unpolarized nucleons can be written in terms of the structure functions in the generic form

$$\begin{aligned}
\frac{d^2 \sigma^i}{dx dy} &= \frac{4\pi \alpha^2}{xy Q^2} \eta^i \left\{ \left(1 - y - \frac{x^2 y^2 M^2}{Q^2} \right) F_2^i \right. \\
& \left. + y^2 x F_1^i \mp \left(y - \frac{y^2}{2} \right) x F_3^i \right\}, \quad (19.8)
\end{aligned}$$

where $i = \text{NC}, \text{CC}$ corresponds to neutral-current ($eN \rightarrow eX$) or charged-current ($eN \rightarrow \nu X$ or $\nu N \rightarrow eX$) processes, respectively. For incoming neutrinos, $L_{\mu\nu}^W$ of Eq. (19.3) is still true, but with e, λ corresponding to the outgoing charged lepton. In the last term of Eq. (19.8), the $-$ sign is taken for an incoming e^+ or $\bar{\nu}$ and the $+$ sign for an incoming e^- or ν . The factor $\eta^{\text{NC}} = 1$ for unpolarized e^\pm beams, whereas

$$\eta^{\text{CC}} = (1 \pm \lambda)^2 \eta_W \quad (19.9)$$

with \pm for ℓ^\pm ; and where λ is the helicity of the incoming lepton and η_W is defined in Eq. (19.4); for incoming neutrinos $\eta^{\text{CC}} = 4\eta_W$. The CC structure functions, which derive exclusively from W exchange, are

$$F_1^{\text{CC}} = F_1^W, \quad F_2^{\text{CC}} = F_2^W, \quad xF_3^{\text{CC}} = xF_3^W. \quad (19.10)$$

The NC structure functions $F_2^\gamma, F_2^{\gamma Z}, F_2^Z$ are, for $e^\pm N \rightarrow e^\pm X$, given by Ref. 5,

$$F_2^{\text{NC}} = F_2^\gamma - (g_V^e \pm \lambda g_A^e) \eta_{\gamma Z} F_2^{\gamma Z} + (g_V^e{}^2 + g_A^e{}^2 \pm 2\lambda g_V^e g_A^e) \eta_Z F_2^Z \quad (19.11)$$

and similarly for F_1^{NC} , whereas

$$xF_3^{\text{NC}} = -(g_A^e \pm \lambda g_V^e) \eta_{\gamma Z} x F_3^{\gamma Z} + [2g_V^e g_A^e \pm \lambda (g_V^e{}^2 + g_A^e{}^2)] \eta_Z x F_3^Z. \quad (19.12)$$

The polarized cross-section difference

$$\Delta \sigma = \sigma(\lambda_n = -1, \lambda_\ell) - \sigma(\lambda_n = 1, \lambda_\ell), \quad (19.13)$$

where λ_ℓ, λ_n are the helicities (± 1) of the incoming lepton and nucleon, respectively, may be expressed in terms of the five structure functions $g_{1, \dots, 5}(x, Q^2)$ of Eq. (19.6). Thus,

$$\begin{aligned}
\frac{d^2 \Delta \sigma^i}{dx dy} &= \frac{8\pi \alpha^2}{xy Q^2} \eta^i \left\{ -\lambda_\ell y \left(2 - y - 2x^2 y^2 \frac{M^2}{Q^2} \right) x g_1^i + \lambda_\ell 4x^3 y^2 \frac{M^2}{Q^2} g_2^i \right. \\
& + 2x^2 y \frac{M^2}{Q^2} \left(1 - y - x^2 y^2 \frac{M^2}{Q^2} \right) g_3^i \\
& \left. - \left(1 + 2x^2 y \frac{M^2}{Q^2} \right) \left[\left(1 - y - x^2 y^2 \frac{M^2}{Q^2} \right) g_4^i + xy^2 g_5^i \right] \right\} \quad (19.14)
\end{aligned}$$

with $i = \text{NC}$ or CC as before. In the $M^2/Q^2 \rightarrow 0$ limit, Eq. (19.8) and Eq. (19.14) may be written in the form

$$\begin{aligned} \frac{d^2\sigma^i}{dx dy} &= \frac{2\pi\alpha^2}{xyQ^2} \eta^i \left[Y_+ F_2^i \mp Y_- x F_3^i - y^2 F_L^i \right], \\ \frac{d^2\Delta\sigma^i}{dx dy} &= \frac{4\pi\alpha^2}{xyQ^2} \eta^i \left[-Y_+ g_4^i \mp Y_- 2xg_1^i + y^2 g_L^i \right], \end{aligned} \quad (19.16)$$

with $i = \text{NC}$ or CC , where $Y_{\pm} = 1 \pm (1-y)^2$ and

$$F_L^i = F_2^i - 2xF_1^i, \quad g_L^i = g_4^i - 2xg_5^i. \quad (19.17)$$

In the naive quark-parton model, the analogy with the Callan-Gross relations [6] $F_L^i = 0$, are the Dicus relations [7] $g_L^i = 0$. Therefore, there are only two independent polarized structure functions: g_1 (parity conserving) and g_5 (parity violating), in analogy with the unpolarized structure functions F_1 and F_3 .

19.2.1. Structure functions in the quark-parton model :

In the quark-parton model [8,9], contributions to the structure functions F^i and g^i can be expressed in terms of the quark distribution functions $q(x, Q^2)$ of the proton, where $q = u, \bar{u}, d, \bar{d}$ etc. The quantity $q(x, Q^2)dx$ is the number of quarks (or antiquarks) of designated flavor that carry a momentum fraction between x and $x + dx$ of the proton's momentum in a frame in which the proton momentum is large.

For the neutral-current processes $ep \rightarrow eX$,

$$\begin{aligned} [F_2^\gamma, F_2^{\gamma Z}, F_2^Z] &= x \sum_q [e_q^2, 2e_q g_V^q, g_V^{q2} + g_A^{q2}] (q + \bar{q}), \\ [F_3^\gamma, F_3^{\gamma Z}, F_3^Z] &= \sum_q [0, 2e_q g_A^q, 2g_V^q g_A^q] (q - \bar{q}), \\ [g_1^\gamma, g_1^{\gamma Z}, g_1^Z] &= \frac{1}{2} \sum_q [e_q^2, 2e_q g_V^q, g_V^{q2} + g_A^{q2}] (\Delta q + \Delta \bar{q}), \\ [g_5^\gamma, g_5^{\gamma Z}, g_5^Z] &= \sum_q [0, e_q g_A^q, g_V^q g_A^q] (\Delta q - \Delta \bar{q}), \end{aligned} \quad (19.18)$$

where $g_V^q = \pm \frac{1}{2} - 2e_q \sin^2 \theta_W$ and $g_A^q = \pm \frac{1}{2}$, with \pm according to whether q is a u - or d -type quark respectively. The quantity Δq is the difference $q \uparrow - q \downarrow$ of the distributions with the quark spin parallel and antiparallel to the proton spin.

For the charged-current processes $e^-p \rightarrow \nu X$ and $\bar{\nu}p \rightarrow e^+X$, the structure functions are:

$$\begin{aligned} F_2^{W^-} &= 2x(u + \bar{d} + \bar{s} + c \dots), \quad F_3^{W^-} = 2(u - \bar{d} - \bar{s} + c \dots), \\ g_1^{W^-} &= (\Delta u + \Delta \bar{d} + \Delta \bar{s} + \Delta c \dots), \quad g_5^{W^-} = (-\Delta u + \Delta \bar{d} + \Delta \bar{s} - \Delta c \dots), \end{aligned} \quad (19.19)$$

where only the active flavors are to be kept and where CKM mixing has been neglected. For $e^+p \rightarrow \bar{\nu}X$ and $\nu p \rightarrow e^-X$, the structure functions F^{W^+}, g^{W^+} are obtained by the flavor interchanges $d \leftrightarrow u, s \leftrightarrow c$ in the expressions for F^{W^-}, g^{W^-} . The structure functions for scattering on a neutron are obtained from those of the proton by the interchange $u \leftrightarrow d$. For both the neutral- and charged-current processes, the quark-parton model predicts $2xF_1^i = F_2^i$ and $g_4^i = 2xg_5^i$.

Further discussion may be found in the full *Review of Particle Physics*.

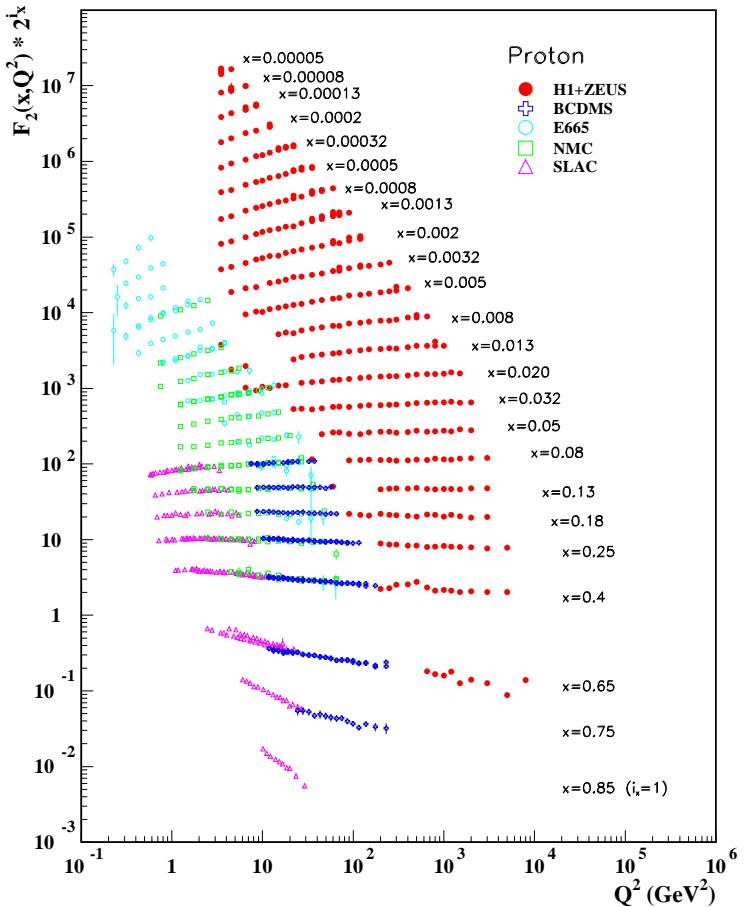


Figure 19.8: The proton structure function F_2^p measured in electromagnetic scattering of electrons and positrons on protons (collider experiments H1 and ZEUS for $Q^2 \geq 2$ GeV 2), in the kinematic domain of the HERA data (see Fig. 19.10 for data at smaller x and Q^2), and for electrons (SLAC) and muons (BCDMS, E665, NMC) on a fixed target. Statistical and systematic errors added in quadrature are shown. The data are plotted as a function of Q^2 in bins of fixed x . Some points have been slightly offset in Q^2 for clarity. The H1+ZEUS combined binning in x is used in this plot; all other data are rebinned to the x values of these data. For the purpose of plotting, F_2^p has been multiplied by 2^{i_x} , where i_x is the number of the x bin, ranging from $i_x = 1$ ($x = 0.85$) to $i_x = 24$ ($x = 0.00005$).

22. BIG-BANG COSMOLOGY

Revised September 2015 by K.A. Olive (University of Minnesota) and J.A. Peacock (University of Edinburgh).

22.1. Introduction to Standard Big-Bang Model

The observed expansion of the Universe [1–3] is a natural (almost inevitable) result of any homogeneous and isotropic cosmological model based on general relativity. In order to account for the possibility that the abundances of the elements had a cosmological origin, Alpher and Herman proposed that the early Universe which was once very hot and dense (enough so as to allow for the nucleosynthetic processing of hydrogen), and has expanded and cooled to its present state [4,5]. In 1948, Alpher and Herman predicted that a direct consequence of this model is the presence of a relic background radiation with a temperature of order a few K [6,7]. It was the observation of the 3 K background radiation that singled out the Big-Bang model as the prime candidate to describe our Universe. Subsequent work on Big-Bang nucleosynthesis further confirmed the necessity of our hot and dense past. These relativistic cosmological models face severe problems with their initial conditions, to which the best modern solution is inflationary cosmology.

22.1.1. *The Robertson-Walker Universe :*

The observed homogeneity and isotropy enable us to describe the overall geometry and evolution of the Universe in terms of two cosmological parameters accounting for the spatial curvature and the overall expansion (or contraction) of the Universe. These two quantities appear in the most general expression for a space-time metric which has a (3D) maximally symmetric subspace of a 4D space-time, known as the Robertson-Walker metric:

$$ds^2 = dt^2 - R^2(t) \left[\frac{dr^2}{1 - kr^2} + r^2 (d\theta^2 + \sin^2 \theta d\phi^2) \right]. \quad (22.1)$$

Note that we adopt $c = 1$ throughout. By rescaling the radial coordinate, we can choose the curvature constant k to take only the discrete values $+1$, -1 , or 0 corresponding to closed, open, or spatially flat geometries.

22.1.2. *The redshift :*

The cosmological redshift is a direct consequence of the Hubble expansion, determined by $R(t)$. A local observer detecting light from a distant emitter sees a redshift in frequency. We can define the redshift as

$$z \equiv \frac{\nu_1 - \nu_2}{\nu_2} \simeq v_{12}, \quad (22.2)$$

where ν_1 is the frequency of the emitted light, ν_2 is the observed frequency and v_{12} is the relative velocity between the emitter and the observer. While the definition, $z = (\nu_1 - \nu_2)/\nu_2$ is valid on all distance scales, relating the redshift to the relative velocity in this simple way is only true on small scales (*i.e.*, less than cosmological scales) such that the expansion velocity is non-relativistic. For light signals, we can use the metric given by Eq. (22.1) and $ds^2 = 0$ to write

$$1 + z = \frac{\nu_1}{\nu_2} = \frac{R_2}{R_1}. \quad (22.5)$$

This result does not depend on the non-relativistic approximation.

22.1.3. *The Friedmann equations of motion :*

The cosmological equations of motion are derived from Einstein's equations

$$\mathcal{R}_{\mu\nu} - \frac{1}{2}g_{\mu\nu}\mathcal{R} = 8\pi G_N T_{\mu\nu} + \Lambda g_{\mu\nu}. \quad (22.6)$$

Gliner [17] and Zeldovich [18] have pioneered the modern view, in which the Λ term is set on the rhs and interpreted as an effective energy-momentum tensor $T_{\mu\nu}$ for the vacuum of $\Lambda g_{\mu\nu}/8\pi G_N$. It is common to assume that the matter content of the Universe is a perfect fluid, for which

$$T_{\mu\nu} = -pg_{\mu\nu} + (p + \rho)u_\mu u_\nu, \quad (22.7)$$

where $g_{\mu\nu}$ is the space-time metric described by Eq. (22.1), p is the isotropic pressure, ρ is the energy density and $u = (1, 0, 0, 0)$ is the velocity vector for the isotropic fluid in co-moving coordinates. With the perfect fluid source, Einstein's equations lead to the Friedmann equations

$$H^2 \equiv \left(\frac{\dot{R}}{R}\right)^2 = \frac{8\pi G_N \rho}{3} - \frac{k}{R^2} + \frac{\Lambda}{3}, \quad (22.8)$$

and

$$\frac{\ddot{R}}{R} = \frac{\Lambda}{3} - \frac{4\pi G_N}{3}(\rho + 3p), \quad (22.9)$$

where $H(t)$ is the Hubble parameter and Λ is the cosmological constant. The first of these is sometimes called the Friedmann equation. Energy conservation via $T^{\mu\nu}_{;\mu} = 0$, leads to a third useful equation

$$\dot{\rho} = -3H(\rho + p). \quad (22.10)$$

Eq. (22.10) can also be simply derived as a consequence of the first law of thermodynamics. For $\Lambda = 0$, it is clear that the Universe must be expanding or contracting.

22.1.4. Definition of cosmological parameters :

The Friedmann equation can be used to define a critical density such that $k = 0$ when $\Lambda = 0$,

$$\begin{aligned} \rho_c &\equiv \frac{3H^2}{8\pi G_N} = 1.88 \times 10^{-26} h^2 \text{ kg m}^{-3} \\ &= 1.05 \times 10^{-5} h^2 \text{ GeV cm}^{-3}, \end{aligned} \quad (22.11)$$

where the scaled Hubble parameter, h , is defined by

$$\begin{aligned} H &\equiv 100 h \text{ km s}^{-1} \text{ Mpc}^{-1} \\ \Rightarrow H^{-1} &= 9.78 h^{-1} \text{ Gyr} \\ &= 2998 h^{-1} \text{ Mpc}. \end{aligned} \quad (22.12)$$

The cosmological density parameter Ω_{tot} is defined as the energy density relative to the critical density,

$$\Omega_{\text{tot}} = \rho/\rho_c. \quad (22.13)$$

Note that one can now rewrite the Friedmann equation as

$$k/R^2 = H^2(\Omega_{\text{tot}} - 1). \quad (22.14)$$

From Eq. (22.14), one can see that when $\Omega_{\text{tot}} > 1$, $k = +1$ and the Universe is closed, when $\Omega_{\text{tot}} < 1$, $k = -1$ and the Universe is open, and when $\Omega_{\text{tot}} = 1$, $k = 0$, and the Universe is spatially flat.

It is often necessary to distinguish different contributions to the density. It is therefore convenient to define present-day density parameters for pressureless matter (Ω_m) and relativistic particles (Ω_r), plus the quantity $\Omega_\Lambda = \Lambda/3H^2$. In more general models, we may wish to drop the assumption that the vacuum energy density is constant, and we therefore denote the present-day density parameter of the vacuum by Ω_v . The Friedmann equation then becomes

$$k/R_0^2 = H_0^2(\Omega_m + \Omega_r + \Omega_v - 1), \quad (22.15)$$

where the subscript 0 indicates present-day values. Thus, it is the sum of the densities in matter, relativistic particles, and vacuum that determines the overall sign of the curvature. Note that the quantity $-k/R_0^2 H_0^2$ is sometimes (unfortunately) referred to as Ω_k .

22.1.5. Standard Model solutions :

During inflation and again today the expansion rate for the Universe is accelerating, and domination by a cosmological constant or some other form of dark energy should be considered.

Let us first assume a general equation of state parameter for a single component, $w = p/\rho$ which is constant. In this case, Eq. (22.10) can be written as $\dot{\rho} = -3(1+w)\rho\dot{R}/R$ and is easily integrated to yield

$$\rho \propto R^{-3(1+w)} . \tag{22.16}$$

Note that at early times when R is small, k/R^2 in the Friedmann equation can be neglected so long as $w > -1/3$. Curvature domination occurs at rather late times (if a cosmological constant term does not dominate sooner). For $w \neq -1$,

$$R(t) \propto t^{2/[3(1+w)]} . \tag{22.17}$$

22.1.5.2. A Radiation-dominated Universe:

In the early hot and dense Universe, it is appropriate to assume an equation of state corresponding to a gas of radiation (or relativistic particles) for which $w = 1/3$. In this case, Eq. (22.16) becomes $\rho \propto R^{-4}$. Similarly, one can substitute $w = 1/3$ into Eq. (22.17) to obtain

$$R(t) \propto t^{1/2} ; \quad H = 1/2t . \tag{22.18}$$

22.1.5.3. A Matter-dominated Universe:

Non-relativistic matter eventually dominates the energy density over radiation. A pressureless gas ($w = 0$) leads to the expected dependence $\rho \propto R^{-3}$, and, if $k = 0$, we get

$$R(t) \propto t^{2/3} ; \quad H = 2/3t . \tag{22.19}$$

If there is a dominant source of vacuum energy, acting as a cosmological constant with equation of state $w = -1$. This leads to an exponential expansion of the Universe:

$$R(t) \propto e^{\sqrt{\Lambda/3}t} . \tag{22.20}$$

The equation of state of the vacuum need not be the $w = -1$ of Λ , and may not even be constant [19–21]. There is now much interest in the more general possibility of a dynamically evolving vacuum energy, for which the name ‘dark energy’ has become commonly used. A variety of techniques exist whereby the vacuum density as a function of time may be measured, usually expressed as the value of w as a function of epoch [22,23]. The best current measurement for the equation of state (assumed constant, but without assuming zero curvature) is $w = -0.97 \pm 0.05$ [24]. Unless stated otherwise, we will assume that the vacuum energy is a cosmological constant with $w = -1$ exactly.

The presence of vacuum energy can dramatically alter the fate of the Universe. For example, if $\Lambda < 0$, the Universe will eventually recollapse independent of the sign of k . For large values of $\Lambda > 0$ (larger than the Einstein static value needed to halt any cosmological expansion or contraction), even a closed Universe will expand forever. One way to quantify this is the deceleration parameter, q_0 , defined as

$$q_0 = - \left. \frac{R\ddot{R}}{\dot{R}^2} \right|_0 = \frac{1}{2}\Omega_m + \Omega_r + \frac{(1+3w)}{2}\Omega_v . \tag{22.21}$$

This equation shows us that $w < -1/3$ for the vacuum may lead to an accelerating expansion. data indicate that vacuum energy is indeed the largest contributor to the cosmological density budget, with $\Omega_v = 0.692 \pm 0.012$ and $\Omega_m = 0.308 \pm 0.012$ if $k = 0$ is assumed (Planck) [31].

The existence of this constituent is without doubt the greatest puzzle raised by the current cosmological model; the final section of this review discusses some of the ways in which the vacuum-energy problem is being addressed.

22.2. Introduction to Observational Cosmology

22.2.1. Fluxes, luminosities, and distances : The key quantities for observational cosmology can be deduced quite directly from the metric.

(1) The *proper* transverse size of an object seen by us to subtend an angle $d\psi$ is its comoving size $d\psi r$ times the scale factor at the time of emission:

$$d\ell = d\psi R_0 r / (1 + z) . \tag{22.22}$$

(2) The apparent flux density of an object is deduced by allowing its photons to flow through a sphere of current radius $R_0 r$; but photon energies and arrival rates are redshifted, and the bandwidth $d\nu$ is reduced. These relations lead to the following common definitions:

$$\text{angular-diameter distance: } D_A = (1 + z)^{-1} R_0 r \tag{22.24}$$

$$\text{luminosity distance: } D_L = (1 + z) R_0 r .$$

These distance-redshift relations are expressed in terms of observables by using the equation of a null radial geodesic plus the Friedmann equation:

$$\begin{aligned} \frac{R_0}{R(t)} dt = \frac{1}{H(z)} dz = \frac{1}{H_0} \left[(1 - \Omega_m - \Omega_v - \Omega_r)(1 + z)^2 \right. \\ \left. + \Omega_v(1 + z)^{3+3w} + \Omega_m(1 + z)^3 + \Omega_r(1 + z)^4 \right]^{-1/2} dz . \end{aligned} \tag{22.25}$$

The main scale for the distance here is the Hubble length, $1/H_0$.

In combination with Cepheid data from the HST and a direct geometrical distance to the maser galaxy NGC4258, SNe results extend the distance ladder to the point where deviations from uniform expansion are negligible, leading to the best existing direct value for H_0 : $72.0 \pm 3.0 \text{ km s}^{-1} \text{ Mpc}^{-1}$ [32]. Better still, the analysis of high- z SNe has allowed a simple and direct test of cosmological geometry to be carried out.

22.2.2. Age of the Universe :

The dynamical result for the age of the Universe may be written as

$$H_0 t_0 = \int_0^\infty \frac{dz}{(1 + z) [(1 + z)^2(1 + \Omega_m z) - z(2 + z)\Omega_v]^{1/2}} , \tag{22.28}$$

where we have neglected Ω_r and chosen $w = -1$. Over the range of interest ($0.1 \lesssim \Omega_m \lesssim 1$, $|\Omega_v| \lesssim 1$), this exact answer may be approximated to a few % accuracy by

$$H_0 t_0 \simeq \frac{2}{3} (0.7\Omega_m + 0.3 - 0.3\Omega_v)^{-0.3} . \tag{22.29}$$

For the special case that $\Omega_m + \Omega_v = 1$, the integral in Eq. (22.28) can be expressed analytically as

$$H_0 t_0 = \frac{2}{3\sqrt{\Omega_v}} \ln \frac{1 + \sqrt{\Omega_v}}{\sqrt{1 - \Omega_v}} \quad (\Omega_m < 1) . \tag{22.30}$$

The present consensus favors ages for the oldest clusters of about 12 Gyr [36,37].

These methods are all consistent with the age deduced from studies of structure formation, using the microwave background and large-scale structure: $t_0 = 13.80 \pm 0.04$ Gyr [31], where the extra accuracy comes at the price of assuming the Cold Dark Matter model to be true.

22.3. The Hot Thermal Universe

22.3.1. Thermodynamics of the early Universe :

Through much of the radiation-dominated period, thermal equilibrium is established by the rapid rate of particle interactions relative to the expansion rate of the Universe. In equilibrium, it is straightforward to compute the thermodynamic quantities, ρ, p , and the entropy density, s .

In the Standard Model, a chemical potential is often associated with baryon number, and since the net baryon density relative to the photon density is known to be very small (of order 10^{-10}), we can neglect any such chemical potential when computing total thermodynamic quantities.

For photons, we have (in units where $\hbar = k_B = 1$)

$$\rho_\gamma = \frac{\pi^2}{15} T^4 ; \quad p_\gamma = \frac{1}{3} \rho_\gamma ; \quad s_\gamma = \frac{4\rho_\gamma}{3T} ; \quad n_\gamma = \frac{2\zeta(3)}{\pi^2} T^3 . \quad (22.39)$$

Eq. (22.10) can be converted into an equation for entropy conservation,

$$d(sR^3)/dt = 0 . \quad (22.40)$$

For radiation, this corresponds to the relationship between expansion and cooling, $T \propto R^{-1}$ in an adiabatically expanding universe. Note also that both s and n_γ scale as T^3 .

22.3.2. Radiation content of the Early Universe :

At the very high temperatures associated with the early Universe, massive particles are pair produced, and are part of the thermal bath. If for a given particle species i we have $T \gg m_i$, then we can neglect the mass and the thermodynamic quantities are easily computed. In general, we can approximate the energy density (at high temperatures) by including only those particles with $m_i \ll T$. In this case, we have

$$\rho = \left(\sum_B g_B + \frac{7}{8} \sum_F g_F \right) \frac{\pi^2}{30} T^4 \equiv \frac{\pi^2}{30} N(T) T^4 , \quad (22.41)$$

where $g_{B(F)}$ is the number of degrees of freedom of each boson (fermion) and the sum runs over all boson and fermion states with $m \ll T$.

Eq. (22.41) defines the effective number of degrees of freedom, $N(T)$, by taking into account new particle degrees of freedom as the temperature is raised.

The value of $N(T)$ at any given temperature depends on the particle physics model. In the standard $SU(3) \times SU(2) \times U(1)$ model, we can specify $N(T)$ up to temperatures of $O(100)$ GeV. The change in N (ignoring mass effects) can be seen in the table below. At higher temperatures, $N(T)$ will be model-dependent.

In the radiation-dominated epoch, Eq. (22.10) can be integrated (neglecting the T -dependence of N) giving us a relationship between the age of the Universe and its temperature

$$t = \left(\frac{90}{32\pi^3 G_N N(T)} \right)^{1/2} T^{-2} . \quad (22.42)$$

Put into a more convenient form

$$t T_{\text{MeV}}^2 = 2.4 [N(T)]^{-1/2} , \quad (22.43)$$

where t is measured in seconds and T_{MeV} in units of MeV.

Temperature	New Particles	$4N(T)$
$T < m_e$	γ 's + ν 's	29
$m_e < T < m_\mu$	e^\pm	43
$m_\mu < T < m_\pi$	μ^\pm	57
$m_\pi < T < T_c^\dagger$	π 's	69
$T_c < T < m_{\text{strange}}$	π 's + u, \bar{u}, d, \bar{d} + gluons	205
$m_s < T < m_{\text{charm}}$	s, \bar{s}	247
$m_c < T < m_\tau$	c, \bar{c}	289
$m_\tau < T < m_{\text{bottom}}$	τ^\pm	303
$m_b < T < m_{W,Z}$	b, \bar{b}	345
$m_{W,Z} < T < m_{\text{Higgs}}$	W^\pm, Z	381
$m_H < T < m_{\text{top}}$	H^0	385
$m_t < T$	t, \bar{t}	427

$^\dagger T_c$ corresponds to the confinement-deconfinement transition between quarks and hadrons.

22.3.7. Nucleosynthesis :

An essential element of the standard cosmological model is Big-Bang nucleosynthesis (BBN), the theory which predicts the abundances of the light element isotopes D, ^3He , ^4He , and ^7Li . Nucleosynthesis takes place at a temperature scale of order 1 MeV. The nuclear processes lead primarily to ^4He , with a primordial mass fraction of about 25%. Lesser amounts of the other light elements are produced: about 10^{-5} of D and ^3He and about 10^{-10} of ^7Li by number relative to H. The abundances of the light elements depend almost solely on one key parameter, the baryon-to-photon ratio, η . The nucleosynthesis predictions can be compared with observational determinations of the abundances of the light elements. Consistency between theory and observations driven primarily by recent D/H measurements [60] leads to a range of

$$5.8 \times 10^{-10} < \eta < 6.6 \times 10^{-10} . \quad (22.54)$$

η is related to the fraction of Ω contained in baryons, Ω_b ,

$$\Omega_b = 3.66 \times 10^7 \eta h^{-2} , \quad (22.55)$$

or $10^{10} \eta = 274 \Omega_b h^2$.

22.4. The Universe at late times

We are beginning to inventory the composition of the Universe:

total: $\Omega = 1.000 \pm 0.005$ (from the CMB, BAO, and lensing)

matter: $\Omega_m = 0.308 \pm 0.012$

baryons: $\Omega_b = 0.048 \pm 0.001$

CDM: $\Omega_{\text{CDM}} = \Omega_m - \Omega_b$

neutrinos: $0.0012 \lesssim \Omega_\nu \lesssim 0.016$

dark energy: $\Omega_v = 0.692 \pm 0.012$

photons: $\Omega_\gamma = 5.38 \times 10^{-5}$

Further discussion and all references may be found in the full *Review of Particle Physics*. The numbering of references and equations used here corresponds to that version.

23. INFLATION

Written May 2016 by J. Ellis (King's College London; CERN) and D. Wands (U. of Portsmouth).

23.1. Motivation and Introduction

The hypothesis of inflation [1,2] postulates a period of accelerated expansion, $\ddot{R} > 0$, in the very early Universe, preceding the standard radiation-dominated era. Such a period of accelerated expansion (i) drives a curved Robertson-Walker spacetime (with spherical or hyperbolic spatial geometry) towards spatial flatness, and (ii) it also expands the causal horizon beyond the present Hubble length, so as to encompass all the scales relevant to describe the large-scale structure observed in our Universe today, via the following two mechanisms.

- (i) A spatially-flat universe with vanishing spatial curvature, $k = 0$, has the dimensionless density parameter $\Omega_{\text{tot}} = 1$. Observations require $|1 - \Omega_{\text{tot},0}| < 0.005$ today [8], where the subscript 0 denotes the present-day value. An extended period of accelerated expansion in the very early Universe, with $\dot{R} > 0$ and $\ddot{R} > 0$ can drive Ω_{tot} sufficiently close to unity, so that $|1 - \Omega_{\text{tot},0}|$ remains unobservably small today, even after the radiation- and matter-dominated eras, for a wide range of initial values of Ω_{tot} .
- (ii) In standard decelerated (radiation- or matter-dominated) cosmology there is a finite comoving distance traversed by light (a particle horizon) since the Big Bang. However, during a period of inflation, $1/\dot{R}$ increases towards the past, and hence the comoving distance diverges from the big bang, allowing an arbitrarily large causal horizon, dependent only upon the duration of the accelerated expansion.

Producing an accelerated expansion in general relativity requires an energy-momentum tensor with negative pressure, $p < -\rho/3$. The work done by the cosmological expansion must be negative so that the local vacuum energy density remains constant in an expanding universe, $\dot{\rho}_V = -3H(\rho_V + p_V) = 0$. A positive vacuum energy $V > 0$ does exert a negative pressure, $p_V = -\rho_V$ and a false vacuum state can drive an exponential expansion, corresponding to a de Sitter spacetime with a constant Hubble rate $H^2 = 8\pi\rho_V/3M_P^2$ on spatially-flat hypersurfaces. A first-order phase transition would produce a very inhomogeneous Universe [9]. However, a second-order phase transition [13,14], controlled by a slowly-rolling scalar field, can lead to a smooth classical exit from the vacuum-dominated phase.

As a spectacular bonus, quantum fluctuations in that scalar field could provide a source of almost scale-invariant density fluctuations [15,16], as detected in the CMB (see section CosmicMicrowaveBackground), which are thought to be the origin of the structures seen in the Universe today.

Accelerated expansion and primordial perturbations can also be produced in some modified gravity theories (e.g., [1,17]), which introduce additional non-minimally coupled degrees of freedom. Such inflation models can often be conveniently studied by transforming variables to an 'Einstein frame' in which Einstein's equations apply with minimally coupled scalar fields [18,19,20].

Further discussion and all references may be found in the full *Review*.

25. THE COSMOLOGICAL PARAMETERS

Updated November 2015, by O. Lahav (University College London) and A.R. Liddle (University of Edinburgh).

25.1. Parametrizing the Universe

The term ‘cosmological parameters’ is forever increasing in its scope, and nowadays often includes the parameterization of some functions, as well as simple numbers describing properties of the Universe. The original usage referred to the parameters describing the global dynamics of the Universe, such as its expansion rate and curvature. Also now of great interest is how the matter budget of the Universe is built up from its constituents: baryons, photons, neutrinos, dark matter, and dark energy. We need to describe the nature of perturbations in the Universe, through global statistical descriptors such as the matter and radiation power spectra. There may also be parameters describing the physical state of the Universe, such as the ionization fraction as a function of time during the era since recombination. Typical comparisons of cosmological models with observational data now feature between five and ten parameters.

25.1.1. *The global description of the Universe :*

The complete present-epoch state of the homogeneous Universe can be described by giving the current- values of all the density parameters and the Hubble constant h . A typical collection would be baryons Ω_b , photons Ω_γ , neutrinos Ω_ν , and cold dark matter Ω_c . These parameters also allow us to track the history of the Universe, at least back until an epoch where interactions allow interchanges between the densities of the different species; this is believed to have last happened at neutrino decoupling, shortly before Big Bang Nucleosynthesis (BBN). To probe further back into the Universe’s history requires assumptions about particle interactions, and perhaps about the nature of physical laws themselves.

25.1.3. *The standard cosmological model :*

Observations are consistent with spatial flatness, and the inflation models so far described automatically generate negligible spatial curvature, so we can set $k = 0$; the density parameters then must sum to unity, and so one of them can be eliminated. The neutrino energy density is often not taken as an independent parameter. Provided that the neutrino sector has the standard interactions, the neutrino energy density, while relativistic, can be related to the photon density using thermal physics arguments, and a minimal assumption takes the neutrino mass sum to be that of the lowest mass solution to the neutrino oscillation constraints, namely 0.06 eV. In addition, there is no observational evidence for the existence of tensor perturbations (though the upper limits are fairly weak), and so r could be set to zero. This leaves seven parameters, which is the smallest set that can usefully be compared to the present cosmological data set. This model is referred to by various names, including Λ CDM, the concordance cosmology, and the standard cosmological model.

Of these parameters, only Ω_γ is accurately measured directly. The radiation density is dominated by the energy in the CMB, and the COBE satellite FIRAS experiment determined its temperature to be $T = 2.7255 \pm 0.0006$ K [10], corresponding to $\Omega_\gamma = 2.47 \times 10^{-5} h^{-2}$. The minimum number of cosmological parameters varied in fits to data is six, though as described below there may additionally be many ‘nuisance’

parameters necessary to describe astrophysical processes influencing the data.

25.2. Extensions to the standard model

25.2.1. *More general perturbations* :

The standard cosmology assumes adiabatic, Gaussian perturbations. Adiabaticity means that all types of material in the Universe share a common perturbation, so that if the space-time is foliated by constant-density hypersurfaces, then all fluids and fields are homogeneous on those slices, with the perturbations completely described by the variation of the spatial curvature of the slices. Gaussianity means that the initial perturbations obey Gaussian statistics, with the amplitudes of waves of different wavenumbers being randomly drawn from a Gaussian distribution of width given by the power spectrum. Note that gravitational instability generates non-Gaussianity; in this context, Gaussianity refers to a property of the initial perturbations, before they evolve.

The simplest inflation models, based on one dynamical field, predict adiabatic perturbations and a level of non-Gaussianity that is too small to be detected by any experiment so far conceived. For present data, the primordial spectra are usually assumed to be power laws.

25.2.1.2. *Isocurvature perturbations*:

An isocurvature perturbation is one that leaves the total density unperturbed, while perturbing the relative amounts of different materials. If the Universe contains N fluids, there is one growing adiabatic mode and $N - 1$ growing isocurvature modes (for reviews see Ref. 7 and Ref. 13). These can be excited, for example, in inflationary models where there are two or more fields that acquire dynamically-important perturbations. If one field decays to form normal matter, while the second survives to become the dark matter, this will generate a cold dark matter isocurvature perturbation.

25.3. Probes

25.3.1. *Direct measures of the Hubble constant* :

One of the most reliable results on the Hubble constant comes from the Hubble Space Telescope Key Project [20]. This study used the empirical period–luminosity relation for Cepheid variable stars, and calibrated a number of secondary distance indicators—Type Ia Supernovae (SNe Ia), the Tully–Fisher relation, surface-brightness fluctuations, and Type II Supernovae.

The most recent derivation based on this approach utilizes the maser-based distance to NGC4258 to re-calibrate its Cepheid distance scale [21] to obtain $H_0 = 72.0 \pm 3.0 \text{ km s}^{-1} \text{ Mpc}^{-1}$ [22]. The major sources of uncertainty in this result are due to the heavy element abundance of the Cepheids and the distance to the fiducial nearby galaxy, the Large Magellanic Cloud, relative to which all Cepheid distances are measured.

The indirect determination of H_0 by the *Planck* Collaboration [2] found a lower value, $H_0 = 67.8 \pm 0.9 \text{ km s}^{-1} \text{ Mpc}^{-1}$. As discussed in that paper, there is strong degeneracy of H_0 with other parameters, *e.g.*, Ω_m and the neutrino mass. The tension between the H_0 from *Planck* and the traditional cosmic distance-ladder methods is under investigation.

25.3.4.3. Limits on neutrino mass from galaxy surveys and other probes:

Large-scale structure data place constraints on Ω_ν due to the neutrino free-streaming effect [47]. Presently there is no clear detection, and upper limits on neutrino mass are commonly estimated by comparing the observed galaxy power spectrum with a four-component model of baryons, cold dark matter, a cosmological constant, and massive neutrinos. Such analyses also assume that the primordial power spectrum is adiabatic, scale-invariant, and Gaussian. Potential systematic effects include biasing of the galaxy distribution and non-linearities of the power spectrum. An upper limit can also be derived from CMB anisotropies alone, while combination with additional cosmological data-sets can improve the results.

Results using a photometric redshift sample of LRGs combined with *WMAP*, BAO, Hubble constant and SNe Ia data gave a 95% confidence upper limit on the total neutrino mass of 0.28 eV [48]. Recent spectroscopic redshift surveys, with more accurate redshifts but fewer galaxies, yield similar upper limits for assumed flat Λ CDM model and additional data-sets: 0.34 eV from BOSS [49] and 0.29 eV from WiggleZ [50].

The *Planck* collaboration [2] derived from only TT+lensing data (see their Table 5), without external data sets, a neutrino mass upper limit of 0.675 eV (95% CL) and $N_{\text{eff}} = 3.13 \pm 0.31$ (68% CL), in good agreement with the standard value $N_{\text{eff}} = 3.046$. When adding external data the upper limit on the neutrino mass is reduced to 0.234 eV, consistent with the above-mentioned pre-Planck results. The Planck result for N_{eff} changes little when adding external data.

While the latest cosmological data do not yet constrain the sum of neutrino masses to below 0.2 eV, because the lower limit on neutrino mass from terrestrial experiments is 0.06 eV it appears promising that future cosmological surveys will detect effects from the neutrino mass.

25.4. Bringing observations together

The most powerful data source is the CMB, which on its own supports all these main tenets. Values for some parameters, as given in Ref. 2, are reproduced in Table 25.1. These particular results presume a flat Universe.

One derived parameter that is very robust is the age of the Universe, since there is a useful coincidence that for a flat Universe the position of the first peak is strongly correlated with the age. The CMB data give 13.80 ± 0.04 Gyr (assuming flatness). This is in good agreement with the ages of the oldest globular clusters and with radioactive dating.

The baryon density Ω_b is now measured with high accuracy from CMB data alone, and is consistent with and much more precise than the determination from BBN. The value quoted in the Big Bang Nucleosynthesis chapter in this volume is $0.021 \leq \Omega_b h^2 \leq 0.024$ (95% confidence).

While Ω_Λ is measured to be non-zero with very high confidence, there is no evidence of evolution of the dark energy density. As shown in the Dark Energy chapter in this volume, from a compilation of CMB, SN and BAO measurements, assuming a flat universe, $w = -0.97 \pm 0.05$, consistent with the cosmological constant case $w = -1$. Allowing more complicated forms of dark energy weakens the limits.

The data provide strong support for the main predictions of the simplest inflation models: spatial flatness and adiabatic, Gaussian, nearly

Table 25.1: Parameter constraints reproduced from Ref. 2 (Table 4), with some additional rounding. Both columns assume the Λ CDM cosmology with a power-law initial spectrum, no tensors, spatial flatness, a cosmological constant as dark energy, and the sum of neutrino masses fixed to 0.06eV. Above the line are the six parameter combinations actually fit to the data (θ_{MC} is a measure of the sound horizon at last scattering); those below the line are derived from these. The first column uses *Planck* primary CMB data, restricting polarization data to low multipoles as currently recommended by the Planck collaboration, plus the *Planck* measurement of CMB lensing. This column gives our present recommended values. The second column adds additional data and is included to show that the effect of its inclusion is modest; the extra data are the Hubble parameter, BAO measurements from the SDSS, BOSS, and 6dF surveys, and supernova constraints from the JLA analysis. Uncertainties are shown at 68% confidence.

	<i>Planck</i> TT+lowP+lensing	<i>Planck</i> TT+lowP+lensing+ext
$\Omega_b h^2$	0.02226 ± 0.00023	0.02227 ± 0.00020
$\Omega_c h^2$	0.1186 ± 0.0020	0.1184 ± 0.0012
$100 \theta_{\text{MC}}$	1.0410 ± 0.0005	1.0411 ± 0.0004
n_s	0.968 ± 0.006	0.968 ± 0.004
τ	0.066 ± 0.016	0.067 ± 0.013
$\ln(10^{10} \Delta_{\mathcal{R}}^2)$	3.062 ± 0.029	3.064 ± 0.024
h	0.678 ± 0.009	0.679 ± 0.006
σ_8	0.815 ± 0.009	0.815 ± 0.009
Ω_m	0.308 ± 0.012	0.306 ± 0.007
Ω_Λ	0.692 ± 0.012	0.694 ± 0.007

scale-invariant density perturbations. But it is disappointing that there is no sign of primordial gravitational waves, with an upper limit $r < 0.11$ at 95% confidence [58] (weakening if running is allowed). The spectral index is clearly required to be less than one by current data, though the strength of that conclusion can weaken if additional parameters are included in the model fits.

Further discussion and all references may be found in the full *Review of Particle Physics*. The numbering of references and equations used here corresponds to that version.

26. DARK MATTER

Revised September 2015 by M. Drees (Bonn University) and G. Gerbier (Queen's University, Canada).

26.1. Theory

26.1.1. Evidence for Dark Matter :

The existence of Dark (*i.e.*, non-luminous and non-absorbing) Matter (DM) is by now well established [1,2]. An important example is the measurement of galactic rotation curves. The rotational velocity v of an object on a stable Keplerian orbit with radius r around a galaxy scales like $v(r) \propto \sqrt{M(r)/r}$, where $M(r)$ is the mass inside the orbit. If r lies outside the visible part of the galaxy and mass tracks light, one would expect $v(r) \propto 1/\sqrt{r}$. Instead, in most galaxies one finds that v becomes approximately constant out to the largest values of r where the rotation curve can be measured. This implies the existence of a *dark halo*, with mass density $\rho(r) \propto 1/r^2$, *i.e.*, $M(r) \propto r$ and a lower bound on the DM mass density, $\Omega_{\text{DM}} \gtrsim 0.1$.

The observation of clusters of galaxies tends to give somewhat larger values, $\Omega_{\text{DM}} \simeq 0.2$. These observations include measurements of the peculiar velocities of galaxies in the cluster, which are a measure of their potential energy if the cluster is virialized; measurements of the *X-ray* temperature of hot gas in the cluster, which again correlates with the gravitational potential felt by the gas; and—most directly—studies of (weak) gravitational lensing of background galaxies on the cluster.

The currently most accurate, if somewhat indirect, determination of Ω_{DM} comes from global fits of cosmological parameters to a variety of observations; see the Section on Cosmological Parameters for details. For example, using measurements of the anisotropy of the cosmic microwave background (CMB) and of the spatial distribution of galaxies, Ref. 7 finds a density of cold, non-baryonic matter

$$\Omega_{\text{nbm}} h^2 = 0.1186 \pm 0.0020, \quad (26.1)$$

where h is the Hubble constant in units of 100 km/(s·Mpc). Some part of the baryonic matter density [7],

$$\Omega_{\text{b}} h^2 = 0.02226 \pm 0.00023, \quad (26.2)$$

may well contribute to (baryonic) DM, *e.g.*, MACHOs [8] or cold molecular gas clouds [9].

A recent estimate finds a quite similar result for the smooth component of the local Dark Matter density [10]: $(0.39 \pm 0.03) \cdot (1.2 \pm 0.2) \cdot (1 \pm \delta_{\text{triax}}) \text{GeVcm}^{-3}$.

26.1.2. Candidates for Dark Matter :

Candidates for non-baryonic DM in Eq. (26.1) must satisfy several conditions: they must be stable on cosmological time scales (otherwise they would have decayed by now), they must interact very weakly with electromagnetic radiation (otherwise they wouldn't qualify as *dark matter*), and they must have the right relic density. Candidates include primordial black holes, axions, sterile neutrinos, and weakly interacting massive particles (WIMPs).

The existence of axions [15] was first postulated to solve the strong *CP* problem of QCD; they also occur naturally in superstring theories. They are pseudo Nambu-Goldstone bosons associated with the (mostly) spontaneous breaking of a new global ‘‘Peccei-Quinn’’ (PQ) U(1) symmetry

at scale f_a ; see the Section on Axions in this *Review* for further details. Although very light, axions would constitute cold DM, since they were produced non-thermally. At temperatures well above the QCD phase transition, the axion is massless, and the axion field can take any value, parameterized by the “misalignment angle” θ_i . At $T \lesssim 1$ GeV, the axion develops a mass $m_a \sim f_\pi m_\pi / f_a$ due to instanton effects. Unless the axion field happens to find itself at the minimum of its potential ($\theta_i = 0$), it will begin to oscillate once m_a becomes comparable to the Hubble parameter H . These coherent oscillations transform the energy originally stored in the axion field into physical axion quanta. The contribution of this mechanism to the present axion relic density is [1]

$$\Omega_a h^2 = \kappa_a \left(f_a / 10^{12} \text{ GeV} \right)^{1.175} \theta_i^2, \quad (26.5)$$

where the numerical factor κ_a lies roughly between 0.5 and a few. If $\theta_i \sim \mathcal{O}(1)$, Eq. (26.5) will saturate Eq. (26.1) for $f_a \sim 10^{11}$ GeV, comfortably above laboratory and astrophysical constraints [15]; this would correspond to an axion mass around 0.1 meV. However, if the post-inflationary reheat temperature $T_R > f_a$, cosmic strings will form during the PQ phase transition at $T \simeq f_a$. Their decay will give an additional contribution to Ω_a , which is often bigger than that in Eq. (26.5) [1], leading to a smaller preferred value of f_a , *i.e.*, larger m_a . On the other hand, values of f_a near the Planck scale become possible if θ_i is for some reason very small.

Weakly interacting massive particles (WIMPs) χ are particles with mass roughly between 10 GeV and a few TeV, and with cross sections of approximately weak strength. Within standard cosmology, their present relic density can be calculated reliably if the WIMPs were in thermal and chemical equilibrium with the hot “soup” of Standard Model (SM) particles after inflation. Their present relic density is then approximately given by (ignoring logarithmic corrections) [3]

$$\Omega_\chi h^2 \simeq \text{const.} \cdot \frac{T_0^3}{M_{\text{Pl}}^3 \langle \sigma_A v \rangle} \simeq \frac{0.1 \text{ pb} \cdot c}{\langle \sigma_A v \rangle}. \quad (26.6)$$

Here T_0 is the current CMB temperature, M_{Pl} is the Planck mass, c is the speed of light, σ_A is the total annihilation cross section of a pair of WIMPs into SM particles, v is the relative velocity between the two WIMPs in their cms system, and $\langle \dots \rangle$ denotes thermal averaging. Freeze out happens at temperature $T_F \simeq m_\chi / 20$ almost independently of the properties of the WIMP. Notice that the 0.1 pb in Eq. (26.6) contains factors of T_0 and M_{Pl} ; it is, therefore, quite intriguing that it “happens” to come out near the typical size of weak interaction cross sections.

The currently best motivated WIMP candidate is, therefore, the lightest superparticle (LSP) in supersymmetric models [17] with exact R-parity (which guarantees the stability of the LSP). Detailed calculations [1] show that the lightest neutralino will have the desired thermal relic density Eq. (26.1) in at least four distinct regions of parameter space. χ could be (mostly) a bino or photino (the superpartner of the $U(1)_Y$ gauge boson and photon, respectively), if both χ and some sleptons have mass below ~ 150 GeV, or if m_χ is close to the mass of some sfermion (so that its relic density is reduced through co-annihilation with this sfermion), or if $2m_\chi$ is close to the mass of the CP -odd Higgs boson present in supersymmetric models. Finally, Eq. (26.1) can also be satisfied if χ has a large higgsino or wino component.

26.2. Experimental detection of Dark Matter

26.2.2. Axion searches :

Axions can be detected by looking for $a \rightarrow \gamma$ conversion in a strong magnetic field [1]. Such a conversion proceeds through the loop-induced $a\gamma\gamma$ coupling, whose strength $g_{a\gamma\gamma}$ is an important parameter of axion models. There is currently only one experiment searching for axionic DM: the ADMX experiment [30], originally situated at the LLNL in California but now running at the University of Washington, started taking data in the first half of 1996. It employs a high quality cavity, whose “Q factor” enhances the conversion rate on resonance, *i.e.*, for $m_a(c^2 + v_a^2/2) = \hbar\omega_{\text{res}}$. One then needs to scan the resonance frequency in order to cover a significant range in m_a or, equivalently, f_a .

26.2.3. Basics of direct WIMP search :

The WIMP mean velocity inside our galaxy relative to its center is expected to be similar to that of stars, *i.e.*, a few hundred kilometers per second at the location of our solar system. For these velocities, WIMPs interact with ordinary matter through elastic scattering on nuclei. With expected WIMP masses in the range 10 GeV to 10 TeV, typical nuclear recoil energies are of order of 1 to 100 keV.

Expected interaction rates depend on the product of the local WIMP flux and the interaction cross section. The first term is fixed by the local density of dark matter, taken as 0.39 GeV/cm^3 , the mean WIMP velocity, typically 220 km/s, the galactic escape velocity, typically 544 km/s [34] and the mass of the WIMP. The expected interaction rate then mainly depends on two unknowns, the mass and cross section of the WIMP (with some uncertainty [10] due to the halo model). This is why the experimental observable, which is basically the scattering rate as a function of energy, is usually expressed as a contour in the WIMP mass-cross section plane.

The cross section depends on the nature of the couplings. For non-relativistic WIMPs, one in general has to distinguish spin-independent and spin-dependent couplings. The former can involve scalar and vector WIMP and nucleon currents (vector currents are absent for Majorana WIMPs, *e.g.*, the neutralino), while the latter involve axial vector currents (and obviously only exist if χ carries spin). Due to coherence effects, the spin-independent cross section scales approximately as the square of the mass of the nucleus, so higher mass nuclei, from Ge to Xe, are preferred for this search. For spin-dependent coupling, the cross section depends on the nuclear spin factor; used target nuclei include ^{19}F , ^{23}Na , ^{73}Ge , ^{127}I , ^{129}Xe , ^{131}Xe , and ^{133}Cs .

Cross sections calculated in MSSM models [35] induce rates of at most $1 \text{ evt day}^{-1} \text{ kg}^{-1}$ of detector, much lower than the usual radioactive backgrounds. This indicates the need for underground laboratories to protect against cosmic ray induced backgrounds, and for the selection of extremely radio-pure materials.

The typical shape of exclusion contours can be anticipated from this discussion: at low WIMP mass, the sensitivity drops because of the detector energy threshold, whereas at high masses, the sensitivity also decreases because, for a fixed mass density, the WIMP flux decreases $\propto 1/m_\chi$. The sensitivity is best for WIMP masses near the mass of the recoiling nucleus.

27. DARK ENERGY

Revised November 2015 by D. H. Weinberg (OSU) and M. White (UCB, LBL); written November 2013 by M. J. Mortonson (UCB, LBL), D. H. Weinberg (OSU), and M. White (UCB, LBL).

27.1. Repulsive Gravity and Cosmic Acceleration

In the late 1990s, supernova surveys by two independent teams provided direct evidence for accelerating cosmic expansion [8,9], establishing the cosmological constant model (with $\Omega_m \approx 0.3$, $\Omega_\Lambda \approx 0.7$) as the preferred alternative to the $\Omega_m = 1$ scenario. Shortly thereafter, CMB evidence for a spatially flat universe [10,11], and thus for $\Omega_{\text{tot}} \approx 1$, cemented the case for cosmic acceleration by firmly eliminating the free-expansion alternative with $\Omega_m \ll 1$ and $\Omega_\Lambda = 0$. Today, the accelerating universe is well established by multiple lines of independent evidence from a tight web of precise cosmological measurements.

As discussed in the Big Bang Cosmology article of this *Review* (Sec. 22), the scale factor $R(t)$ of a homogeneous and isotropic universe governed by GR grows at an accelerating rate if the pressure $p < -\frac{1}{3}\rho$ (in $c = 1$ units). A cosmological constant has $\rho_\Lambda = \text{constant}$ and pressure $p_\Lambda = -\rho_\Lambda$ (see Eq. 22.10), so it will drive acceleration if it dominates the total energy density. However, acceleration could arise from a more general form of “dark energy” that has negative pressure, typically specified in terms of the equation-of-state-parameter $w = p/\rho$ ($= -1$ for a cosmological constant). Furthermore, the conclusion that acceleration requires a new energy component beyond matter and radiation relies on the assumption that GR is the correct description of gravity on cosmological scales.

27.2. Theories of Cosmic Acceleration

A cosmological constant is the mathematically simplest, and perhaps the physically simplest, theoretical explanation for the accelerating universe. The problem is explaining its unnaturally small magnitude, as discussed in Sec. 22.4.7 of this *Review*. An alternative (which still requires finding a way to make the cosmological constant zero or at least negligibly small) is that the accelerating cosmic expansion is driven by a new form of energy such as a scalar field [13] with potential $V(\phi)$. In the limit that $\frac{1}{2}\dot{\phi}^2 \ll |V(\phi)|$, the scalar field acts like a cosmological constant, with $p_\phi \approx -\rho_\phi$. In this scenario, today’s cosmic acceleration is closely akin to the epoch of inflation, but with radically different energy and timescale.

More generally, the value of $w = p_\phi/\rho_\phi$ in scalar field models evolves with time in a way that depends on $V(\phi)$ and on the initial conditions ($\phi_i, \dot{\phi}_i$); some forms of $V(\phi)$ have attractor solutions in which the late-time behavior is insensitive to initial values. Many forms of time evolution are possible, including ones where w is approximately constant and broad classes where w “freezes” towards or “thaws” away from $w = -1$, with the transition occurring when the field comes to dominate the total energy budget. If ρ_ϕ is even approximately constant, then it becomes dynamically insignificant at high redshift, because the matter density scales as $\rho_m \propto (1+z)^3$.

Further discussion and all references may be found in the full *Review*.

28. COSMIC MICROWAVE BACKGROUND

Revised September 2015 by D. Scott (University of British Columbia) and G.F. Smoot (UCB/LBNL).

28.2. CMB Spectrum

The spectrum of the microwave background is very precisely that of blackbody radiation, whose temperature evolves with redshift as $T(z) = T_0(1+z)$ in an expanding universe. As a direct test of its cosmological origin, this relationship is being tested by measuring the strengths of emission and absorption lines in high-redshift systems [16].

Measurements of the spectrum are consistent with a blackbody distribution over more than three decades in frequency. All viable cosmological models predict a very nearly Planckian spectrum to within the current observational limits.

28.3. Description of CMB Anisotropies

Observations show that the CMB contains temperature anisotropies at the 10^{-5} level and polarization anisotropies at the 10^{-6} (and lower) level, over a wide range of angular scales. These anisotropies are usually expressed by using a spherical harmonic expansion of the CMB sky:

$$T(\theta, \phi) = \sum_{\ell m} a_{\ell m} Y_{\ell m}(\theta, \phi)$$

(with the linear polarization pattern written in a similar way using the so-called spin-2 spherical harmonics). Because there are only very weak phase correlations seen in the CMB sky and since we notice no preferred direction, the vast majority of the cosmological information is contained in the temperature 2-point function, *i.e.*, the variance as a function only of angular separation. Equivalently, the power per unit $\ln \ell$ is $\ell \sum_m |a_{\ell m}|^2 / 4\pi$.

28.3.1. The Monopole :

The CMB has a mean temperature of $T_\gamma = 2.7255 \pm 0.0006 \text{ K}$ (1σ) [21], which can be considered as the monopole component of CMB maps, a_{00} . Since all mapping experiments involve difference measurements, they are insensitive to this average level; monopole measurements can only be made with absolute temperature devices, such as the FIRAS instrument on the *COBE* satellite [22]. The measured kT_γ is equivalent to 0.234 meV or $4.60 \times 10^{-10} m_e c^2$. A blackbody of the measured temperature has a number density $n_\gamma = (2\zeta(3)/\pi^2) T_\gamma^3 \simeq 411 \text{ cm}^{-3}$, energy density $\rho_\gamma = (\pi^2/15) T_\gamma^4 \simeq 4.64 \times 10^{-34} \text{ g cm}^{-3} \simeq 0.260 \text{ eV cm}^{-3}$, and a fraction of the critical density $\Omega_\gamma \simeq 5.38 \times 10^{-5}$.

28.3.2. The Dipole :

The largest anisotropy is in the $\ell = 1$ (dipole) first spherical harmonic, with amplitude $3.3645 \pm 0.0020 \text{ mK}$ [12]. The dipole is interpreted to be the result of the Doppler boosting of the monopole caused by the solar system motion relative to the nearly isotropic blackbody field, as broadly confirmed by measurements of the radial velocities of local galaxies (*e.g.*, Ref. [23]).

The dipole is a frame-dependent quantity, and one can thus determine the ‘absolute rest frame’ as that in which the CMB dipole would be zero.

28.3.3. Higher-Order Multipoles :

The variations in the CMB temperature maps at higher multipoles ($\ell \geq 2$) are interpreted as being mostly the result of perturbations in the

density of the early Universe, manifesting themselves at the epoch of the last scattering of the CMB photons. In the hot Big Bang picture, the expansion of the Universe cools the plasma so that by a redshift $z \simeq 1100$ (with little dependence on the details of the model), the hydrogen and helium nuclei can bind electrons into neutral atoms, a process usually referred to as recombination [27]. Before this epoch, the CMB photons were tightly coupled to the baryons, while afterwards they could freely stream towards us. By measuring the $a_{\ell m}$ s we are thus learning directly about physical conditions in the early Universe.

A statistically isotropic sky means that all m s are equivalent, *i.e.*, there is no preferred axis, so that the temperature correlation function between two positions on the sky depends only on angular separation and not orientation. Together with the assumption of Gaussian statistics (*i.e.*, no correlations between the modes), the variance of the temperature field (or equivalently the power spectrum in ℓ) then fully characterizes the anisotropies. The power summed over all m s at each ℓ is $(2\ell + 1)C_\ell/(4\pi)$, where $C_\ell \equiv \langle |a_{\ell m}|^2 \rangle$. Thus averages of $a_{\ell m}$ s over m can be used as estimators of the C_ℓ s to constrain their expectation values, which are the quantities predicted by a theoretical model. For an idealized full-sky observation, the variance of each measured C_ℓ (*i.e.*, the variance of the variance) is $[2/(2\ell + 1)]C_\ell^2$. This sampling uncertainty (known as ‘cosmic variance’) comes about because each C_ℓ is χ^2 distributed with $(2\ell + 1)$ degrees of freedom for our observable volume of the Universe.

It is important to understand that theories predict the expectation value of the power spectrum, whereas our sky is a single realization. Hence the cosmic variance is an unavoidable source of uncertainty when constraining models; it dominates the scatter at lower ℓ s, while the effects of instrumental noise and resolution dominate at higher ℓ s [28].

28.3.4. Angular Resolution and Binning :

There is no one-to-one conversion between multipole ℓ and the angle subtended by a particular spatial scale projected onto the sky. However, a single spherical harmonic $Y_{\ell m}$ corresponds to angular variations of $\theta \sim \pi/\ell$. CMB maps contain anisotropy information from the size of the map (or in practice some fraction of that size) down to the beam-size of the instrument, σ (the standard deviation of the beam, in radians). One can think of the effect of a Gaussian beam as rolling off the power spectrum with the function $e^{-\ell(\ell+1)\sigma^2}$.

28.6. Current Temperature Anisotropy Data

There has been a steady improvement in the quality of CMB data that has led to the development of the present-day cosmological model. The most robust constraints currently available come from *Planck* satellite [50,51] data combined with smaller scale results from the ACT [52] and SPT [53] experiments (together with constraints from non-CMB cosmological data-sets). We plot power spectrum estimates from these experiments in Fig. 28.1, along with *WMAP* data [8] to show the consistency.

28.7. CMB Polarization

Thomson scattering of an anisotropic radiation field also generates linear polarization, the CMB is predicted to be polarized at the level of roughly 5% of the temperature anisotropies [54]. The linear polarization pattern can be decomposed in a number of ways, with two quantities required for each pixel in a map, often given as the Q and U Stokes

parameters. However, the most intuitive and physical decomposition is a geometrical one, splitting the polarization pattern into a part that comes from a divergence (often referred to as the ‘ E -mode’) and a part with a curl (called the ‘ B -mode’) [56]. Globally one sees that the E -modes have $(-1)^\ell$ parity (like the spherical harmonics), while the B -modes have $(-1)^{\ell+1}$ parity.

Since inflationary scalar perturbations give only E -modes, while tensors generate roughly equal amounts of E - and B -modes, then the determination of a non-zero B -mode signal is a way to measure the gravitational wave contribution (and thus potentially derive the energy scale of inflation), even if it is rather weak.

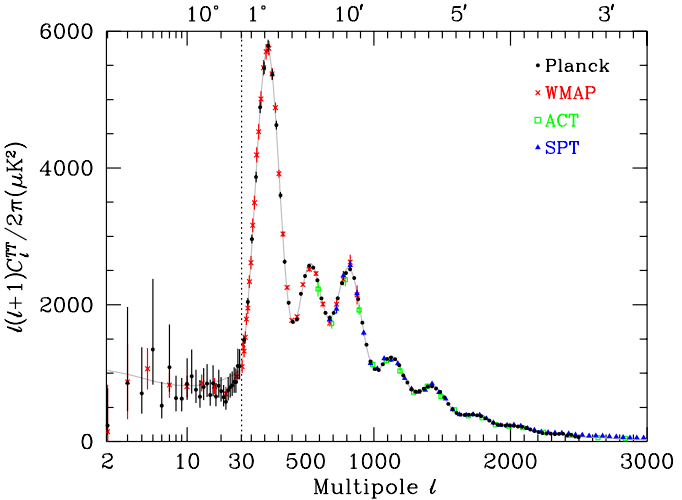


Figure 28.1: CMB temperature anisotropy band-power estimates from the *Planck*, *WMAP*, ACT, and SPT experiments.

28.9. Constraints on Cosmological Parameters

Within the context of a six parameter family of models (which fixes $\Omega_{\text{tot}} = 1$, $dn_s/d\ln k = 0$, $r = 0$, and $w = -1$) the *Planck* results for TT , together with low- ℓ polarization and CMB lensing, and the use of high- ℓ data from ACT and SPT to constrain foregrounds, yields [13]: $\ln(10^{10} A_s) = 3.062 \pm 0.029$; $n_s = 0.968 \pm 0.006$; $\Omega_b h^2 = 0.02226 \pm 0.00023$; $\Omega_c h^2 = 0.1186 \pm 0.0020$; $100\theta_* = 1.0410 \pm 0.0005$; and $\tau = 0.066 \pm 0.016$. Other parameters can be derived from this basic set, including $h = 0.678 \pm 0.009$, $\Omega_\Lambda = 0.692 \pm 0.012$ ($= 1 - \Omega_m$) and $\sigma_8 = 0.815 \pm 0.009$. The evidence for $n_s < 1$ remains above the 5σ level. The value of the reionization optical depth has decreased compared with earlier estimates; it is convincingly detected, but still not of very high significance.

The 95% confidence upper limit on r (measured at $k = 0.002 \text{ Mpc}^{-1}$) from the effect of tensors solely on C_ℓ^{TT} is 0.11. This limit depends on how the slope n is restricted and whether $dn_s/d\ln k \neq 0$ is allowed. The joint constraints on n_s and r allows specific inflationary models to be tested [33,34].

29. COSMIC RAY FLUXES*

In the lower half of the atmosphere (altitude $\lesssim 5$ km) most cosmic rays are muons. Some typical sea-level values for charged particles are given below, where

- I_v flux per unit solid angle per unit horizontal area about vertical direction
 $\equiv j(\theta = 0, \phi)[\theta = \text{zenith angle}, \phi = \text{azimuthal angle}] ;$
- J_1 total flux crossing unit horizontal area from above
 $\equiv \int_{\theta \leq \pi/2} j(\theta, \phi) \cos \theta \, d\Omega \ [d\Omega = \sin \theta \, d\theta \, d\phi] ;$
- J_2 total flux from above (crossing a sphere of unit cross-sectional area)
 $\equiv \int_{\theta \leq \pi/2} j(\theta, \phi) \, d\Omega .$

	Total Intensity	Hard ($\approx \mu^\pm$) Component	Soft ($\approx e^\pm$) Component
I_v	110	80	$30 \text{ m}^{-2} \text{ s}^{-1} \text{ sr}^{-1}$
J_1	180	130	$50 \text{ m}^{-2} \text{ s}^{-1}$
J_2	240	170	$70 \text{ m}^{-2} \text{ s}^{-1}$

At 4300 m (*e.g.*, Mt. Evans or Mauna Kea) the hard component is 2.3 times more intense than at sea level.

The p/μ^\pm vertical flux ratio at sea level is about 3.5% at 1 GeV/ c , decreasing to about 0.5% at 10 GeV/ c . The π^\pm/μ^\pm ratio is an order of magnitude smaller.

The mean energy of muons at the ground is ≈ 4 GeV. The energy spectrum is almost flat below 1 GeV, steepens gradually to reflect the primary spectrum ($\propto E^{-2.7}$) in the 10–100 GeV range, and asymptotically becomes one power steeper ($E_\mu \gg 1$ TeV). The measurements reported above are for $E_\mu \gtrsim 225$ MeV. The angular distribution is very nearly proportional to $\cos^2 \theta$, changing to $\sec \theta$ at energies above a TeV (where θ is the zenith angle at production). The μ^+/μ^- ratio is 1.25–1.30.

The mean energy of muons originating in the atmosphere is roughly 300 GeV at slant depths underground \gtrsim a few hundred meters. Beyond slant depths of ≈ 10 km water-equivalent, the muons are due primarily to in-the-earth neutrino interactions (roughly 1/8 interaction $\text{ton}^{-1} \text{ yr}^{-1}$ for $E_\nu > 300$ MeV, \approx constant throughout the earth). These muons arrived with a mean energy of 20 GeV, and have a flux of $2 \times 10^{-9} \text{ m}^{-2} \text{ s}^{-1} \text{ sr}^{-1}$ in the vertical direction and about twice that in the horizontal, down at least as far as the deepest mines.

* Reprint of “Cosmic-ray fluxes” from the 1986 *Review*, as updated by D.E. Groom (2000). The data (by Greisen) are reported in B. Rossi, *Rev. Mod. Phys.* **20**, 537 (1948). See the full *Review* on Cosmic Rays for a more extensive discussion and references.

30. ACCELERATOR PHYSICS OF COLLIDERS

Revised August 2015 by M.J. Syphers (NIU/FNAL) and F. Zimmermann (CERN).

30.1. Luminosity

The number of events, N_{exp} , is the product of the cross section of interest, σ_{exp} , and the time integral over the instantaneous *luminosity*, \mathcal{L} :

$$N_{exp} = \sigma_{exp} \times \int \mathcal{L}(t) dt. \quad (30.1)$$

If two bunches containing n_1 and n_2 particles collide head-on with frequency f_{coll} , a basic expression for the luminosity is

$$\mathcal{L} = f_{coll} \frac{n_1 n_2}{4\pi \sigma_x \sigma_y} \quad (30.2)$$

where σ_x and σ_y characterize the rms transverse beam sizes in the horizontal (bend) and vertical directions. In this form it is assumed that the bunches are identical in transverse profile, that the profiles are Gaussian and independent of position along the bunch, and the particle distributions are not altered during bunch crossing. Nonzero beam crossing angles and long bunches will reduce the luminosity from this value.

Whatever the distribution at the source, by the time the beam reaches high energy, the normal form is a useful approximation as suggested by the σ -notation.

The beam size can be expressed in terms of two quantities, one termed the *transverse emittance*, ϵ , and the other, the *amplitude function*, β . The transverse emittance is a beam quality concept reflecting the process of bunch preparation, extending all the way back to the source for hadrons and, in the case of electrons, mostly dependent on synchrotron radiation. The amplitude function is a beam optics quantity and is determined by the accelerator magnet configuration. When expressed in terms of σ and β the transverse emittance becomes

$$\epsilon = \sigma^2 / \beta .$$

Of particular significance is the value of the amplitude function at the interaction point, β^* . Clearly one wants β^* to be as small as possible; how small depends on the capability of the hardware to make a near-focus at the interaction point.

Eq. (30.2) can be recast in terms of emittances and amplitude functions as

$$\mathcal{L} = f \frac{n_1 n_2}{4\pi \sqrt{\epsilon_x \beta_x^* \epsilon_y \beta_y^*}} . \quad (30.10)$$

So to achieve high luminosity, all one has to do is make high population bunches of low emittance collide at high frequency at locations where the beam optics provides as low values of the amplitude functions as possible.

Further discussion and all references may be found in the full *Review of Particle Physics*.

31. HIGH-ENERGY COLLIDER PARAMETERS

Updated in January 2016 with numbers received from representatives of the colliders (contact S. Pagan Griso, LBNL). Except for SuperKEKB, where design values are quoted, the table shows the parameter values achieved. Quantities are, where appropriate, r.m.s.; energies refer to beam energy; H and V indicate horizontal and vertical directions. Only selected operating colliders are included. See full *Review* for complete tables.

	VEPP-2000 (Novosibirsk)	VEPP-4M (Novosibirsk)	BEPc-II (China)	DAΦNE (Frascati)	SuperKEKB (KEK)	LHC† (CERN)
Physics start date	2010	1994	2008	1999	2017	2009 (2015)
Particles collided	e^+e^-	e^+e^-	e^+e^-	e^+e^-	e^+e^-	pp
Maximum beam energy (GeV)	1.0	6	1.89 (2.3 max)	0.510	e^- : 7, e^+ : 4	4.0 (6.5)
Luminosity ($10^{30} \text{ cm}^{-2}\text{s}^{-1}$)	100	20	853	453	8×10^5	7.7×10^3 (5×10^3)
Time between collisions (ns)	40	600	8	2.7	4	49.9 (24.95)
Energy spread (units 10^{-3})	0.64	1	0.52	0.40	e^-/e^+ : 0.64/0.81	0.1445 (0.105)
Bunch length (cm)	4	5	≈ 1.5	1 - 2	e^-/e^+ : 0.5/0.6	9.4 (9)
Beam radius (10^{-6} m)	125 (round)	H : 1000 V : 30	H : 358 V : 4.8	H : 260 V : 4.8	e^- : 11 (H), 0.062 (V) e^+ : 10 (H), 0.048 (V)	18.8 (21)
Free space at interaction point (m)	± 1	± 2	± 0.63	± 0.295	e^- : +1.20/−1.28 e^+ : +0.78/−0.73	38
β^* , amplitude function at interaction point (m)	H : 0.06 – 0.11 V : 0.06 – 0.10	H : 0.75 V : 0.05	H : 1.0 V : 0.0135	H : 0.26 V : 0.009	e^- : 0.025 (H), 3×10^{-4} (V) e^+ : 0.032 (H), 2.7×10^{-4} (V)	0.6 (0.8)
Interaction regions	2	1	1	1	1	4

† Parameters for LHC Run 2 in 2015 given in parenthesis.

33. PASSAGE OF PARTICLES THROUGH MATTER

Revised August 2015 by H. Bichsel (University of Washington), D.E. Groom (LBNL), and S.R. Klein (LBNL).

33.1. Notation

Table 33.1: Summary of variables used in this section. The kinematic variables β and γ have their usual relativistic meanings.

Symbol	Definition	Value or (usual) units
$m_e c^2$	electron mass $\times c^2$	0.510 998 928(11) MeV
r_e	classical electron radius $e^2/4\pi\epsilon_0 m_e c^2$	2.817 940 3267(27) fm
α	fine structure constant $e^2/4\pi\epsilon_0 \hbar c$	1/137.035 999 074(44)
N_A	Avogadro's number	$6.022\,141\,29(27) \times 10^{23} \text{ mol}^{-1}$
ρ	density	g cm^{-3}
x	mass per unit area	g cm^{-2}
M	incident particle mass	MeV/c^2
E	incident part. energy $\gamma M c^2$	MeV
T	kinetic energy, $(\gamma - 1) M c^2$	MeV
W	energy transfer to an electron in a single collision	MeV
k	bremsstrahlung photon energy	MeV
z	charge number of incident particle	
Z	atomic number of absorber	
A	atomic mass of absorber	g mol^{-1}
K	$4\pi N_A r_e^2 m_e c^2$	$0.307\,075 \text{ MeV mol}^{-1} \text{ cm}^2$
I	mean excitation energy	eV (<i>Nota bene!</i>)
$\delta(\beta\gamma)$	density effect correction to ionization energy loss	
$\hbar\omega_p$	plasma energy $\sqrt{4\pi N_e r_e^3} m_e c^2 / \alpha$	$\sqrt{\rho \langle Z/A \rangle} \times 28.816 \text{ eV}$ $\hookrightarrow \rho$ in g cm^{-3}
N_e	electron density	(units of r_e) $^{-3}$
w_j	weight fraction of the j th element in a compound or mixture	
n_j	\propto number of j th kind of atoms in a compound or mixture	
X_0	radiation length	g cm^{-2}
E_c	critical energy for electrons	MeV
$E_{\mu c}$	critical energy for muons	GeV
E_s	scale energy $\sqrt{4\pi/\alpha} m_e c^2$	21.2052 MeV
R_M	Molière radius	g cm^{-2}

33.2. Electronic energy loss by heavy particles [1–32]

33.2.1. Moments and cross sections :

The electronic interactions of fast charged particles with speed $v = \beta c$ occur in *single collisions with energy losses* W [1], leading to ionization, atomic, or collective excitation. Most frequently the energy losses are small (for 90% of all collisions the energy losses are less than 100 eV). In thin absorbers few collisions will take place and the total energy loss will show a large variance [1]; also see Sec. 33.2.9 below. For particles with charge ze more massive than electrons (“heavy” particles), scattering from

free electrons is adequately described by the Rutherford differential cross section [2],

$$\frac{d\sigma_R(W; \beta)}{dW} = \frac{2\pi r_e^2 m_e c^2 z^2}{\beta^2} \frac{(1 - \beta^2 W/W_{\max})}{W^2}, \quad (33.1)$$

where W_{\max} is the maximum energy transfer possible in a single collision. But in matter electrons are not free. For electrons bound in atoms Bethe [3] used “Born Theorie” to obtain the differential cross section

$$\frac{d\sigma_B(W; \beta)}{dW} = \frac{d\sigma_R(W, \beta)}{dW} B(W). \quad (33.2)$$

At high energies σ_B is further modified by polarization of the medium, and this “density effect,” discussed in Sec 33.2.5, must also be included. Less important corrections are discussed below.

The mean number of collisions with energy loss between W and $W + dW$ occurring in a distance δx is $N_e \delta x (d\sigma/dW) dW$, where $d\sigma(W; \beta)/dW$ contains all contributions. It is convenient to define the moments

$$M_j(\beta) = N_e \delta x \int W^j \frac{d\sigma(W; \beta)}{dW} dW, \quad (33.3)$$

so that M_0 is the mean number of collisions in δx , M_1 is the mean energy loss in δx , $M_2 - M_1^2$ is the variance, *etc.* The number of collisions is Poisson-distributed with mean M_0 . N_e is either measured in electrons/g ($N_e = N_A Z/A$) or electrons/cm³ ($N_e = N_A \rho Z/A$).

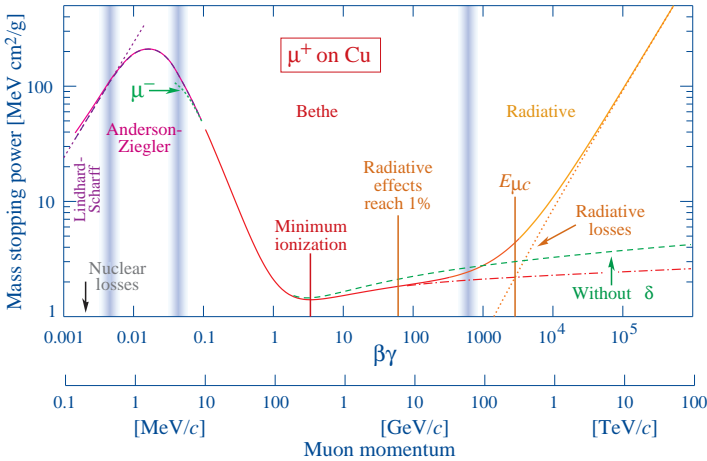


Fig. 33.1: Mass stopping power ($= \langle -dE/dx \rangle$) for positive muons in copper as a function of $\beta\gamma = p/Mc$ over nine orders of magnitude in momentum (12 orders of magnitude in kinetic energy). Solid curves indicate the total stopping power. Data below the break at $\beta\gamma \approx 0.1$ are taken from ICRU 49 [4], and data at higher energies are from Ref. 5. Vertical bands indicate boundaries between different approximations discussed in the text. The short dotted lines labeled “ μ^- ” illustrate the “Barkas effect,” the dependence of stopping power on projectile charge at very low energies [6].

33.2.2. Maximum energy transfer in a single collision : For a particle with mass M and momentum $M\beta\gamma c$, W_{\max} is given by

$$W_{\max} = \frac{2m_e c^2 \beta^2 \gamma^2}{1 + 2\gamma m_e/M + (m_e/M)^2}. \quad (33.4)$$

In older references [2,8] the “low-energy” approximation $W_{\max} = 2m_e c^2 \beta^2 \gamma^2$, valid for $2\gamma m_e \ll M$, is often implicit. For hadrons with $E \simeq 100$ GeV, it is limited by structure effects.

33.2.3. Stopping power at intermediate energies : The mean rate of energy loss by moderately relativistic charged heavy particles, $M_1/\delta x$, is well-described by the “Bethe” equation,

$$-\left\langle \frac{dE}{dx} \right\rangle = K z^2 \frac{Z}{A} \frac{1}{\beta^2} \left[\frac{1}{2} \ln \frac{2m_e c^2 \beta^2 \gamma^2 W_{\max}}{I^2} - \beta^2 - \frac{\delta(\beta\gamma)}{2} \right]. \quad (33.5)$$

It describes the mean rate of energy loss in the region $0.1 \lesssim \beta\gamma \lesssim 1000$ for intermediate- Z materials with an accuracy of a few %.

With definitions and values in Table 33.1, the units are MeV g^{-1}cm^2 .

At the lower limit the projectile velocity becomes comparable to atomic electron “velocities” (Sec. 33.2.4), and at the upper limit radiative effects begin to be important (Sec. 33.6). Both limits are Z dependent. A minor dependence on M at the highest energies is introduced through W_{\max} , but for all practical purposes $\langle dE/dx \rangle$ in a given material is a function of β alone.

Few concepts in high-energy physics are as misused as $\langle dE/dx \rangle$. The main problem is that the mean is weighted by very rare events with large single-collision energy deposits. Even with samples of hundreds of events a dependable value for the mean energy loss cannot be obtained. Far better and more easily measured is the most probable energy loss, discussed in Sec 33.2.9. It is considerably below the mean given by the Bethe equation.

In a TPC (Sec. 34.6.5), the mean of 50%–70% of the samples with the smallest signals is often used as an estimator.

Although it must be used with cautions and caveats, $\langle dE/dx \rangle$ as described in Eq. (33.5) still forms the basis of much of our understanding of energy loss by charged particles. Extensive tables are available[4,5, pdg.lbl.gov/AtomicNuclearProperties/].

The function as computed for muons on copper is shown as the “Bethe” region of Fig. 33.1. Mean energy loss behavior below this region is discussed in Sec. 33.2.6, and the radiative effects at high energy are discussed in Sec. 33.6. Only in the Bethe region is it a function of β alone; the mass dependence is more complicated elsewhere. The stopping power in several other materials is shown in Fig. 33.2. Except in hydrogen, particles with the same velocity have similar rates of energy loss in different materials, although there is a slow decrease in the rate of energy loss with increasing Z . The qualitative behavior difference at high energies between a gas (He in the figure) and the other materials shown in the figure is due to the density-effect correction, $\delta(\beta\gamma)$, discussed in Sec. 33.2.5. The stopping power functions are characterized by broad minima whose position drops from $\beta\gamma = 3.5$ to 3.0 as Z goes from 7 to 100. The values of minimum ionization go roughly as $0.235 - 0.28 \ln(Z)$, in MeV g^{-1}cm^2 , for $Z > 6$.

Eq. (33.5) may be integrated to find the total (or partial) “continuous slowing-down approximation” (CSDA) range R for a particle which loses energy only through ionization and atomic excitation. Since dE/dx in the “Bethe region” depends only on β , R/M is a function of E/M or pc/M . In practice, range is a useful concept only for low-energy hadrons ($R \lesssim \lambda_I$, where λ_I is the nuclear interaction length), and for muons below a few hundred GeV (above which radiative effects dominate). R/M as a function of $\beta\gamma = p/Mc$ is shown for a variety of materials in Fig. 33.4.

The mass scaling of dE/dx and range is valid for the electronic losses described by the Bethe equation, but not for radiative losses, relevant only

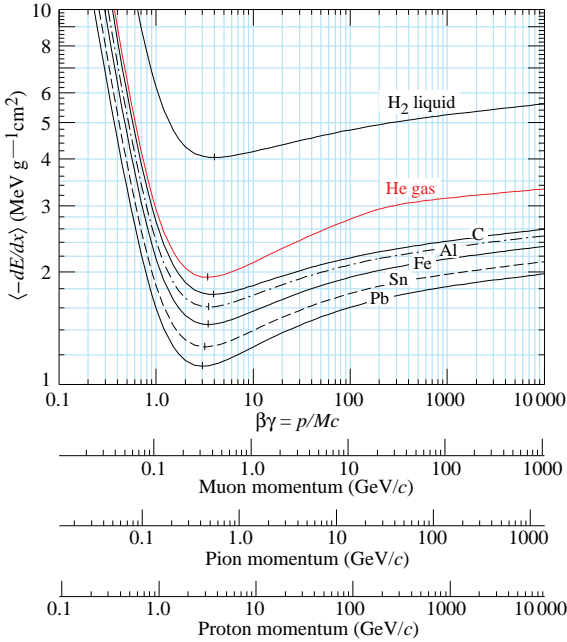


Figure 33.2: Mean energy loss rate in liquid (bubble chamber) hydrogen, gaseous helium, carbon, aluminum, iron, tin, and lead. Radiative effects, relevant for muons and pions, are not included. These become significant for muons in iron for $\beta\gamma \gtrsim 1000$, and at lower momenta in higher- Z absorbers. See Fig. 33.21.

for muons and pions.

Estimates of the mean excitation energy I based on experimental stopping-power measurements for protons, deuterons, and alpha particles are given in Ref. 11; see also pdg.lbl.gov/AtomicNuclearProperties.

33.2.5. Density effect: As the particle energy increases, its electric field flattens and extends, so that the distant-collision contribution to Eq. (33.5) increases as $\ln\beta\gamma$. However, real media become polarized, limiting the field extension and effectively truncating this part of the logarithmic rise [2–8,15–16]. At very high energies,

$$\delta/2 \rightarrow \ln(\hbar\omega_p/I) + \ln\beta\gamma - 1/2, \tag{33.6}$$

where $\delta(\beta\gamma)/2$ is the density effect correction introduced in Eq. (33.5) and $\hbar\omega_p$ is the plasma energy defined in Table 33.1. A comparison with Eq. (33.5) shows that $|dE/dx|$ then grows as $\ln\beta\gamma$ rather than $\ln\beta^2\gamma^2$, and that the mean excitation energy I is replaced by the plasma energy $\hbar\omega_p$. Since the plasma frequency scales as the square root of the electron density, the correction is much larger for a liquid or solid than for a gas, as is illustrated by the examples in Fig. 33.2.

The remaining relativistic rise comes from the $\beta^2\gamma^2$ growth of W_{\max} , which in turn is due to (rare) large energy transfers to a few electrons. When these events are excluded, the energy deposit in an absorbing layer approaches a constant value, the Fermi plateau (see Sec. 33.2.8 below). At extreme energies (*e.g.*, > 332 GeV for muons in iron, and

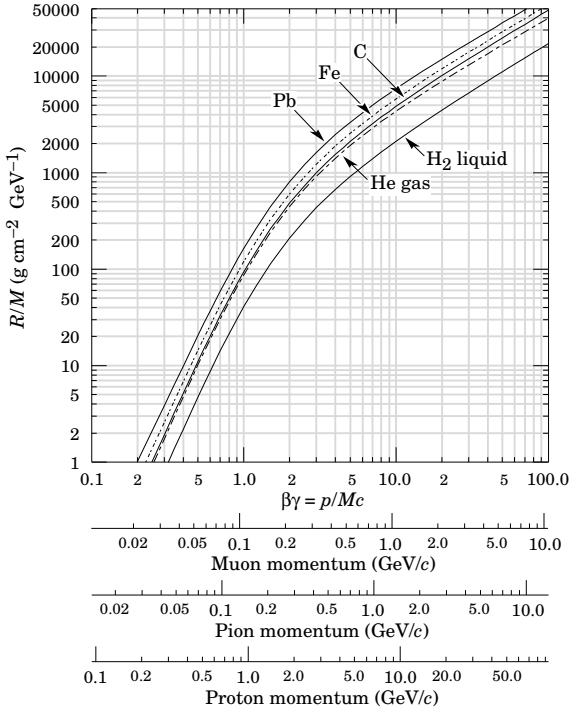


Figure 33.4: Range of heavy charged particles in liquid (bubble chamber) hydrogen, helium gas, carbon, iron, and lead. For example: For a K^+ whose momentum is 700 MeV/c, $\beta\gamma = 1.42$. For lead we read $R/M \approx 396$, and so the range is 195 g cm^{-2} (17 cm).

at a considerably higher energy for protons in iron), radiative effects are more important than ionization losses. These are especially relevant for high-energy muons, as discussed in Sec. 33.6.

33.2.7. Energetic knock-on electrons (δ rays): The distribution of secondary electrons with kinetic energies $T \gg I$ is [2]

$$\frac{d^2N}{dTdx} = \frac{1}{2} K z^2 \frac{Z}{A} \frac{1}{\beta^2} \frac{F(T)}{T^2} \quad (33.8)$$

for $I \ll T \leq W_{\max}$, where W_{\max} is given by Eq. (33.4). Here β is the velocity of the primary particle. The factor F is spin-dependent, but is about unity for $T \ll W_{\max}$. For spin-0 particles $F(T) = (1 - \beta^2 T/W_{\max})$; forms for spins 1/2 and 1 are also given by Rossi [2]. Additional formulae are given in Ref. 22. Equation (33.8) is inaccurate for T close to I .

δ rays of even modest energy are rare. For $\beta \approx 1$ particle, for example, on average only one collision with $T_e > 1$ keV will occur along a path length of 90 cm of Ar gas [1].

33.2.8. Restricted energy loss rates for relativistic ionizing particles: Further insight can be obtained by examining the mean energy deposit by an ionizing particle when energy transfers are restricted to $T \leq W_{\text{cut}} \leq W_{\max}$. The restricted energy loss rate is

$$-\frac{dE}{dx} \Big|_{T < W_{\text{cut}}} = Kz^2 \frac{Z}{A} \frac{1}{\beta^2} \left[\frac{1}{2} \ln \frac{2m_e c^2 \beta^2 \gamma^2 W_{\text{cut}}}{I^2} - \frac{\beta^2}{2} \left(1 + \frac{W_{\text{cut}}}{W_{\text{max}}} \right) - \frac{\delta}{2} \right]. \quad (33.10)$$

This form approaches the normal Bethe function (Eq. (33.5)) as $W_{\text{cut}} \rightarrow W_{\text{max}}$. It can be verified that the difference between Eq. (33.5) and Eq. (33.10) is equal to $\int_{W_{\text{cut}}}^{W_{\text{max}}} T(d^2N/dTdx)dT$, where $d^2N/dTdx$ is given by Eq. (33.8).

Since W_{cut} replaces W_{max} in the argument of the logarithmic term of Eq. (33.5), the $\beta\gamma$ term producing the relativistic rise in the close-collision part of dE/dx is replaced by a constant, and $|dE/dx|_{T < W_{\text{cut}}}$ approaches the constant ‘‘Fermi plateau.’’ (The density effect correction δ eliminates the explicit $\beta\gamma$ dependence produced by the distant-collision contribution.) This behavior is illustrated in Fig. 33.6, where restricted loss rates for two examples of W_{cut} are shown in comparison with the full Bethe dE/dx and the Landau-Vavilov most probable energy loss (to be discussed in Sec. 33.2.9 below).

33.2.9. Fluctuations in energy loss : For detectors of moderate thickness x (e.g. scintillators or LAr cells),* the energy loss probability distribution $f(\Delta; \beta\gamma, x)$ is adequately described by the highly-skewed Landau (or Landau-Vavilov) distribution [24,25]. The most probable energy loss is [26]

$$\Delta_p = \xi \left[\ln \frac{2mc^2 \beta^2 \gamma^2}{I} + \ln \frac{\xi}{I} + j - \beta^2 - \delta(\beta\gamma) \right], \quad (33.11)$$

where $\xi = (K/2) \langle Z/A \rangle (x/\beta^2)$ MeV for a detector with a thickness x in g cm^{-2} , and $j = 0.200$ [26].[†] While dE/dx is independent of thickness, Δ_p/x scales as $a \ln x + b$. The density correction $\delta(\beta\gamma)$ was not included in Landau’s or Vavilov’s work, but it was later included by Bichsel [26]. The high-energy behavior of $\delta(\beta\gamma)$ (Eq. (33.6)), is such that

$$\Delta_p \xrightarrow{\beta\gamma \gtrsim 100} \xi \left[\ln \frac{2mc^2 \xi}{(\hbar\omega_p)^2} + j \right]. \quad (33.12)$$

Thus the Landau-Vavilov most probable energy loss, like the restricted energy loss, reaches a Fermi plateau. The Bethe dE/dx and Landau-Vavilov-Bichsel Δ_p/x in silicon are shown as a function of muon energy in Fig. 33.6. The case $x/\rho = 1600 \mu\text{m}$ was chosen since it has about the same stopping power as does 3 mm of plastic scintillator. Folding in experimental resolution displaces the peak of the distribution, usually toward a higher value.

The mean of the energy-loss given by the Bethe equation, Eq. (33.5), is ill-defined experimentally and is not useful for describing energy loss by single particles. (It finds its application in dosimetry, where only bulk deposit is of relevance.) It rises as $\ln \beta\gamma$ because W_{max} increases as $\beta^2 \gamma^2$. The large single-collision energy transfers that increasingly extend the long tail are rare, making the mean of an experimental distribution consisting of a few hundred events subject to large fluctuations and sensitive to cuts as well as to background. The most probable energy loss should be used.

* $G \lesssim 0.05\text{--}0.1$, where G is given by Rossi [Ref. 2, Eq. 2.7(10)]. It is Vavilov’s κ [25].

[†] Rossi [2], Talman [27], and others give somewhat different values for j . The most probable loss is not sensitive to its value.

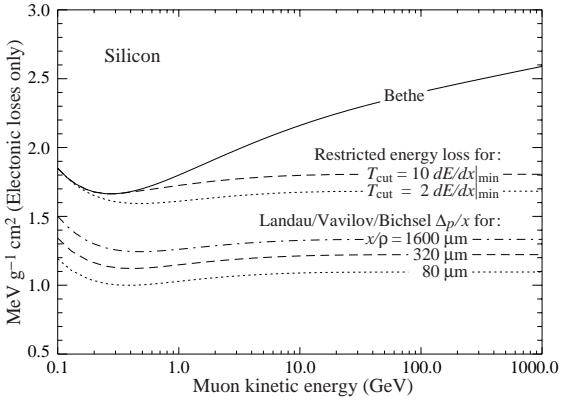


Figure 33.6: Bethe dE/dx , two examples of restricted energy loss, and the Landau most probable energy per unit thickness in silicon. The change of Δ_p/x with thickness x illustrates its $a \ln x + b$ dependence. Minimum ionization ($dE/dx|_{\min}$) is $1.664 \text{ MeV g}^{-1} \text{ cm}^2$. Radiative losses are excluded. The incident particles are muons.

For very thick absorbers the distribution is less skewed but never approaches a Gaussian. In the case of Si illustrated in Fig. 33.6, the most probable energy loss per unit thickness for $x \approx 35 \text{ g cm}^{-2}$ is very close to the restricted energy loss with $W_{\text{cut}} = 2 dE/dx|_{\min}$.

The Landau distribution fails to describe energy loss in thin absorbers such as gas TPC cells [1] and Si detectors [26], as shown clearly in Fig. 1 of Ref. 1 for an argon-filled TPC cell. Also see Talman [27]. While Δ_p/x may be calculated adequately with Eq. (33.11), the distributions are significantly wider than the Landau width $w = 4\xi$ [Ref. 26, Fig. 15]. Examples for thin silicon detectors are shown in Fig. 33.9.

33.2.10. Energy loss in mixtures and compounds : A mixture or compound can be thought of as made up of thin layers of pure elements in the right proportion (Bragg additivity). In this case,

$$\left\langle \frac{dE}{dx} \right\rangle = \sum w_j \left\langle \frac{dE}{dx} \right\rangle_j, \quad (33.13)$$

where $\langle dE/dx \rangle_j$ is the mean rate of energy loss (in MeV g cm^{-2}) in the j th element. Eq. (33.5) can be inserted into Eq. (33.13) to find expressions for $\langle Z/A \rangle$, $\langle I \rangle$, and $\langle \delta \rangle$; for example, $\langle Z/A \rangle = \sum w_j Z_j/A_j = \sum n_j Z_j / \sum n_j A_j$. However, $\langle I \rangle$ as defined this way is an underestimate, because in a compound electrons are more tightly bound than in the free elements, and $\langle \delta \rangle$ as calculated this way has little relevance, because it is the electron density that matters. If possible, one uses the tables given in Refs. 16 and 29, or the recipes given in 17 (repeated in Ref. 5), which include effective excitation energies and interpolation coefficients for calculating the density effect correction.

33.3. Multiple scattering through small angles

A charged particle traversing a medium is deflected by many small-angle scatters. Most of this deflection is due to Coulomb scattering from nuclei, and hence the effect is called multiple Coulomb scattering. (However, for hadronic projectiles, the strong interactions also contribute to multiple scattering.) The Coulomb scattering distribution is well represented by the

theory of Molière [34]. It is roughly Gaussian for small deflection angles, but at larger angles (greater than a few θ_0 , defined below) it behaves like Rutherford scattering, with larger tails than does a Gaussian distribution.

If we define

$$\theta_0 = \theta_{\text{plane}}^{\text{rms}} = \frac{1}{\sqrt{2}} \theta_{\text{space}}^{\text{rms}} . \quad (33.14)$$

then it is usually sufficient to use a Gaussian approximation for the central 98% of the projected angular distribution, with a width given by [39,40]

$$\theta_0 = \frac{13.6 \text{ MeV}}{\beta c p} z \sqrt{x/X_0} \left[1 + 0.038 \ln(x/X_0) \right] . \quad (33.15)$$

Here p , βc , and z are the momentum, velocity, and charge number of the incident particle, and x/X_0 is the thickness of the scattering medium in radiation lengths (defined below). This value of θ_0 is from a fit to Molière distribution for singly charged particles with $\beta = 1$ for all Z , and is accurate to 11% or better for $10^{-3} < x/X_0 < 100$.

33.4. Photon and electron interactions in matter

33.4.2. Radiation length : High-energy electrons predominantly lose energy in matter by bremsstrahlung, and high-energy photons by e^+e^- pair production. The characteristic amount of matter traversed for these related interactions is called the radiation length X_0 , usually measured in g cm^{-2} . It is both (a) the mean distance over which a high-energy electron loses all but $1/e$ of its energy by bremsstrahlung, and (b) $\frac{7}{9}$ of the mean free path for pair production by a high-energy photon [42]. It is also the appropriate scale length for describing high-energy electromagnetic cascades. X_0 has been calculated and tabulated by Y.S. Tsai [43]:

$$\frac{1}{X_0} = 4\alpha r_e^2 \frac{N_A}{A} \left\{ Z^2 [L_{\text{rad}} - f(Z)] + Z L'_{\text{rad}} \right\} . \quad (33.26)$$

For $A = 1 \text{ g mol}^{-1}$, $4\alpha r_e^2 N_A/A = (716.408 \text{ g cm}^{-2})^{-1}$. L_{rad} and L'_{rad} are given in Table 33.2. The function $f(Z)$ is an infinite sum, but for elements up to uranium can be represented to 4-place accuracy by

$$f(Z) = a^2 [(1+a^2)^{-1} + 0.20206 - 0.0369 a^2 + 0.0083 a^4 - 0.002 a^6] , \quad (33.27)$$

where $a = \alpha Z$ [44].

Table 33.2: Tsai's L_{rad} and L'_{rad} , for use in calculating the radiation length in an element using Eq. (33.26).

Element	Z	L_{rad}	L'_{rad}
H	1	5.31	6.144
He	2	4.79	5.621
Li	3	4.74	5.805
Be	4	4.71	5.924
Others	> 4	$\ln(184.15 Z^{-1/3})$	$\ln(1194 Z^{-2/3})$

33.4.3. Bremsstrahlung energy loss by e^\pm : At low energies electrons and positrons primarily lose energy by ionization, although other processes (Møller scattering, Bhabha scattering, e^+ annihilation) contribute, as shown in Fig. 33.10. While ionization loss rates rise logarithmically with energy, bremsstrahlung losses rise nearly linearly (fractional loss is nearly independent of energy), and dominates above a few tens of MeV in most materials.

Ionization loss by electrons and positrons differs from loss by heavy particles because of the kinematics, spin, and the identity of the incident electron with the electrons which it ionizes.

At very high energies and except at the high-energy tip of the bremsstrahlung spectrum, the cross section can be approximated in the “complete screening case” as [43]

$$d\sigma/dk = (1/k)4\alpha r_e^2 \left\{ \left(\frac{4}{3} - \frac{4}{3}y + y^2 \right) [Z^2(L_{\text{rad}} - f(Z)) + Z L'_{\text{rad}}] + \frac{1}{3}(1-y)(Z^2 + Z) \right\}, \quad (33.29)$$

where $y = k/E$ is the fraction of the electron’s energy transferred to the radiated photon. At small y (the “infrared limit”) the term on the second line ranges from 1.7% (low Z) to 2.5% (high Z) of the total. If it is ignored and the first line simplified with the definition of X_0 given in Eq. (33.26), we have

$$\frac{d\sigma}{dk} = \frac{A}{X_0 N_A k} \left(\frac{4}{3} - \frac{4}{3}y + y^2 \right). \quad (33.30)$$

This formula is accurate except in near $y = 1$, where screening may become incomplete, and near $y = 0$, where the infrared divergence is removed by the interference of bremsstrahlung amplitudes from nearby scattering centers (the LPM effect) [45,46] and dielectric suppression [47,48]. These and other suppression effects in bulk media are discussed in Sec. 33.4.6.

Except at these extremes, and still in the complete-screening approximation, the number of photons with energies between k_{min} and k_{max} emitted by an electron travelling a distance $d \ll X_0$ is

$$N_\gamma = \frac{d}{X_0} \left[\frac{4}{3} \ln \left(\frac{k_{\text{max}}}{k_{\text{min}}} \right) - \frac{4(k_{\text{max}} - k_{\text{min}})}{3E} + \frac{k_{\text{max}}^2 - k_{\text{min}}^2}{2E^2} \right]. \quad (33.31)$$

33.4.4. Critical energy: An electron loses energy by bremsstrahlung at a rate nearly proportional to its energy, while the ionization loss rate varies only logarithmically with the electron energy. The *critical energy* E_c is sometimes defined as the energy at which the two loss rates are equal [50]. Among alternate definitions is that of Rossi [2], who defines the critical energy as the energy at which the ionization loss per radiation length is equal to the electron energy. Equivalently, it is the same as the first definition with the approximation $|dE/dx|_{\text{brems}} \approx E/X_0$. This form has been found to describe transverse electromagnetic shower development more accurately (see below).

The accuracy of approximate forms for E_c has been limited by the failure to distinguish between gases and solid or liquids, where there is a substantial difference in ionization at the relevant energy because of the density effect. Separate fits to $E_c(Z)$, using the Rossi definition, have been made with functions of the form $a/(Z+b)^\alpha$, but α was found to be essentially unity. For $Z > 6$ we obtain

$$E_c \approx \frac{610 \text{ MeV}}{Z + 1.24} \quad (\text{solids and liquids}), \quad \approx \frac{710 \text{ MeV}}{Z + 0.92} \quad (\text{gases}).$$

Since E_c also depends on A , I , and other factors, such forms are at best approximate.

33.4.5. Energy loss by photons: Contributions to the photon cross section in a light element (carbon) and a heavy element (lead) are shown in Fig. 33.15. At low energies it is seen that the photoelectric effect dominates, although Compton scattering, Rayleigh scattering, and photonuclear absorption also contribute. The photoelectric cross section

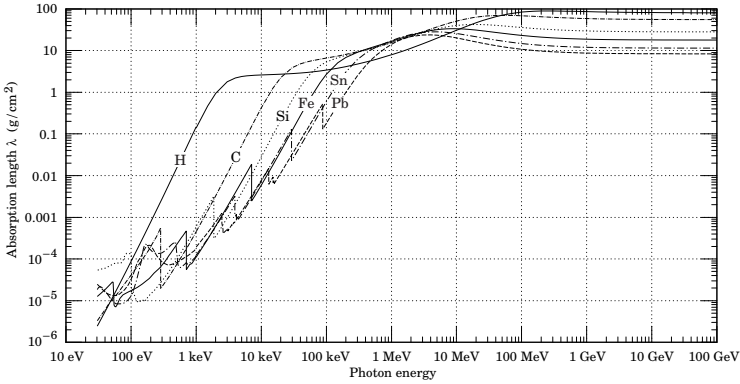


Fig. 33.16: The photon mass attenuation length (or mean free path) $\lambda = 1/(\mu/\rho)$ for various elemental absorbers as a function of photon energy. The mass attenuation coefficient is μ/ρ , where ρ is the density. The intensity I remaining after traversal of thickness t (in mass/unit area) is given by $I = I_0 \exp(-t/\lambda)$. The accuracy is a few percent. For a chemical compound or mixture, $1/\lambda_{\text{eff}} \approx \sum_{\text{elements}} w_Z/\lambda_Z$, where w_Z is the proportion by weight of the element with atomic number Z . The processes responsible for attenuation are given in Fig. 33.11. Since coherent processes are included, not all these processes result in energy deposition.

is characterized by discontinuities (absorption edges) as thresholds for photoionization of various atomic levels are reached. Photon attenuation lengths for a variety of elements are shown in Fig 33.16, and data for $30 \text{ eV} < k < 100 \text{ GeV}$ for all elements is available from the web pages given in the caption. Here k is the photon energy.

The increasing domination of pair production as the energy increases is shown in Fig. 33.17 of the full *Review*. Using approximations similar to those used to obtain Eq. (33.30), Tsai's formula for the differential cross section [43] reduces to

$$\frac{d\sigma}{dx} = \frac{A}{X_0 N_A} \left[1 - \frac{4}{3}x(1-x) \right] \quad (33.32)$$

in the complete-screening limit valid at high energies. Here $x = E/k$ is the fractional energy transfer to the pair-produced electron (or positron), and k is the incident photon energy. The cross section is very closely related to that for bremsstrahlung, since the Feynman diagrams are variants of one another. The cross section is of necessity symmetric between x and $1-x$, as can be seen by the solid curve in See the review by Motz, Olsen, & Koch for a more detailed treatment [53].

Eq. (33.32) may be integrated to find the high-energy limit for the total e^+e^- pair-production cross section:

$$\sigma = \frac{7}{9}(A/X_0 N_A) . \quad (33.33)$$

Equation Eq. (33.33) is accurate to within a few percent down to energies as low as 1 GeV, particularly for high- Z materials.

33.4.6. Bremsstrahlung and pair production at very high energies: At ultrahigh energies, Eqns. 33.29–33.33 will fail because of quantum mechanical interference between amplitudes from different scattering centers. Since the longitudinal momentum transfer to a given center is small ($\propto k/E(E-k)$, in the case of bremsstrahlung), the interaction is spread over a comparatively long distance called the formation length ($\propto E(E-k)/k$) via the uncertainty principle. In alternate language, the formation length is the distance over which the highly relativistic electron and the photon “split apart.” The interference is usually destructive. Calculations of the “Landau-Pomeranchuk-Migdal” (LPM) effect may be made semi-classically based on the average multiple scattering, or more rigorously using a quantum transport approach [45,46].

In amorphous media, bremsstrahlung is suppressed if the photon energy k is less than $E^2/(E + E_{LPM})$ [46], where*

$$E_{LPM} = \frac{(m_e c^2)^2 \alpha X_0}{4\pi \hbar c \rho} = (7.7 \text{ TeV/cm}) \times \frac{X_0}{\rho}. \quad (33.34)$$

Since physical distances are involved, X_0/ρ , in cm, appears. The energy-weighted bremsstrahlung spectrum for lead, $k d\sigma_{LPM}/dk$, is shown in Fig. 27.11 of the full *Review*. With appropriate scaling by X_0/ρ , other materials behave similarly.

For photons, pair production is reduced for $E(k-E) > k E_{LPM}$. The pair-production cross sections for different photon energies are shown in Fig. 33.18 of the full *Review*.

If $k \ll E$, several additional mechanisms can also produce suppression. When the formation length is long, even weak factors can perturb the interaction. For example, the emitted photon can coherently forward scatter off of the electrons in the media. Because of this, for $k < \omega_p E/m_e \sim 10^{-4}$, bremsstrahlung is suppressed by a factor $(k m_e / \omega_p E)^2$ [48]. Magnetic fields can also suppress bremsstrahlung. In crystalline media, the situation is more complicated, with coherent enhancement or suppression possible [55].

33.5. Electromagnetic cascades

When a high-energy electron or photon is incident on a thick absorber, it initiates an electromagnetic cascade as pair production and bremsstrahlung generate more electrons and photons with lower energy. The longitudinal development is governed by the high-energy part of the cascade, and therefore scales as the radiation length in the material. Electron energies eventually fall below the critical energy, and then dissipate their energy by ionization and excitation rather than by the generation of more shower particles. In describing shower behavior, it is therefore convenient to introduce the scale variables $t = x/X_0$ and $y = E/E_c$, so that distance is measured in units of radiation length and energy in units of critical energy.

The mean longitudinal profile of the energy deposition in an electromagnetic cascade is reasonably well described by a gamma distribution [60]:

$$\frac{dE}{dt} = E_0 b \frac{(bt)^{a-1} e^{-bt}}{\Gamma(a)} \quad (33.36)$$

The maximum t_{\max} occurs at $(a-1)/b$. We have made fits to shower profiles in elements ranging from carbon to uranium, at energies from 1

* This definition differs from that of Ref. 54 by a factor of two. E_{LPM} scales as the 4th power of the mass of the incident particle, so that $E_{LPM} = (1.4 \times 10^{10} \text{ TeV/cm}) \times X_0/\rho$ for a muon.

GeV to 100 GeV. The energy deposition profiles are well described by Eq. (33.36) with

$$t_{\max} = (a - 1)/b = 1.0 \times (\ln y + C_j), \quad j = e, \gamma, \quad (33.37)$$

where $C_e = -0.5$ for electron-induced cascades and $C_\gamma = +0.5$ for photon-induced cascades. To use Eq. (33.36), one finds $(a - 1)/b$ from Eq. (33.37), then finds a either by assuming $b \approx 0.5$ or by finding a more accurate value from Fig. 33.21. The results are very similar for the electron number profiles, but there is some dependence on the atomic number of the medium. A similar form for the electron number maximum was obtained by Rossi in the context of his “Approximation B,” [2] but with $C_e = -1.0$ and $C_\gamma = -0.5$; we regard this as superseded by the EGS4 result.

The “shower length” $X_s = X_0/b$ is less conveniently parameterized, since b depends upon both Z and incident energy, as shown in Fig. 33.21. As a corollary of this Z dependence, the number of electrons crossing a plane near shower maximum is underestimated using Rossi’s approximation for carbon and seriously overestimated for uranium. Essentially the same b values are obtained for incident electrons and photons. For many purposes it is sufficient to take $b \approx 0.5$.

The gamma function distribution is very flat near the origin, while the EGS4 cascade (or a real cascade) increases more rapidly. As a result Eq. (33.36) fails badly for about the first two radiation lengths, which are excluded from fits. Because fluctuations are important, Eq. (33.36) should be used only in applications where average behavior is adequate.

The transverse development of electromagnetic showers in different materials scales fairly accurately with the *Molière radius* R_M , given by [62,63]

$$R_M = X_0 E_s/E_c, \quad (33.38)$$

where $E_s \approx 21$ MeV (Table 33.1), and the Rossi definition of E_c is used.

Measurements of the lateral distribution in electromagnetic cascades are shown in Ref. 62 and 63. On the average, only 10% of the energy lies outside the cylinder with radius R_M . About 99% is contained inside of $3.5R_M$, but at this radius and beyond composition effects become important and the scaling with R_M fails. The distributions are characterized by a narrow core, and broaden as the shower develops. They are often represented as the sum of two Gaussians, and Grindhammer [61] describes them with the function

$$f(r) = \frac{2r R^2}{(r^2 + R^2)^2}, \quad (33.40)$$

where R is a phenomenological function of x/X_0 and $\ln E$.

At high enough energies, the LPM effect (Sec. 33.4.6) reduces the cross sections for bremsstrahlung and pair production, and hence can cause significant elongation of electromagnetic cascades [56].

33.6. Muon energy loss at high energy

At sufficiently high energies, radiative processes become more important than ionization for all charged particles. For muons and pions in materials such as iron, this “critical energy” occurs at several hundred GeV. (There is no simple scaling with particle mass, but for protons the “critical energy” is much, much higher.) Radiative effects dominate the energy loss of energetic muons found in cosmic rays or produced at the newest accelerators. These processes are characterized by small cross sections, hard spectra, large energy fluctuations, and the associated generation of electromagnetic and (in the case of photonuclear interactions) hadronic

showers [64–72]. At these energies the treatment of energy loss as a uniform and continuous process is for many purposes inadequate.

It is convenient to write the average rate of muon energy loss as [73]

$$-dE/dx = a(E) + b(E) E. \quad (33.41)$$

Here $a(E)$ is the ionization energy loss given by Eq. (33.5), and $b(E)$ is the sum of e^+e^- pair production, bremsstrahlung, and photonuclear contributions. To the approximation that these slowly-varying functions are constant, the mean range x_0 of a muon with initial energy E_0 is given by

$$x_0 \approx (1/b) \ln(1 + E_0/E_{\mu c}), \quad (33.42)$$

where $E_{\mu c} = a/b$.

The “muon critical energy” $E_{\mu c}$ can be defined more exactly as the energy at which radiative and ionization losses are equal, and can be found by solving $E_{\mu c} = a(E_{\mu c})/b(E_{\mu c})$. This definition corresponds to the solid-line intersection in 33.13 of the full *Review*, and is different from the Rossi definition we used for electrons. It serves the same function: below $E_{\mu c}$ ionization losses dominate, and above $E_{\mu c}$ radiative effects dominate. The dependence of $E_{\mu c}$ on atomic number Z is shown in Fig. 33.24 in the full *Review*.

The radiative cross sections are expressed as functions of the fractional energy loss ν . The bremsstrahlung cross section goes roughly as $1/\nu$ over most of the range, while for the pair production case the distribution goes as ν^{-3} to ν^{-2} [74]. “Hard” losses are therefore more probable in bremsstrahlung, and in fact energy losses due to pair production may very nearly be treated as continuous. The simulated [72] momentum distribution of an incident 1 TeV/ c muon beam after it crosses 3 m of iron is shown in Fig. 33.25 of the full *Review*. The hard bremsstrahlung photons and hadronic debris from photonuclear interactions induce cascades which can obscure muon tracks in detector planes and reduce tracking [76].

33.7. Cherenkov and transitional radiation[33,77,78]

A charged particle radiates if its velocity is greater than the local phase velocity of light (Cherenkov radiation) or if it crosses suddenly from one medium to another with different optical properties (transition radiation). Neither process is important for energy loss, but both are used in high-energy physics detectors.

33.7.1. Optical Cherenkov radiation : The cosine of the angle θ_c of Cherenkov radiation, relative to the particle’s direction, for a particle with velocity βc in a medium with index of refraction n , is $1/n\beta$, or

$$\tan \theta_c = \sqrt{\beta^2 n^2 - 1} \approx \sqrt{2(1 - 1/n\beta)} \quad (33.43)$$

for small θ_c , e.g., in gases. The threshold velocity β_t is $1/n$, and $\gamma_t = 1/(1 - \beta_t^2)^{1/2}$. Therefore, $\beta_t \gamma_t = 1/(2\delta + \delta^2)^{1/2}$, where $\delta = n - 1$.

Practical Cherenkov radiator materials are dispersive. Let ω be the photon’s frequency, and let $k = 2\pi/\lambda$ be its wavenumber. The photons propagate at the group velocity $v_g = d\omega/dk = c/[n(\omega) + \omega(dn/d\omega)]$. In a non-dispersive medium, this simplifies to $v_g = c/n$.

The number of photons produced per unit path length of a particle with charge ze and per unit energy interval of the photons is

$$\begin{aligned} \frac{d^2 N}{dE dx} &= \frac{\alpha z^2}{hc} \sin^2 \theta_c = \frac{\alpha^2 z^2}{r_e m_e c^2} \left(1 - \frac{1}{\beta^2 n^2(E)} \right) \\ &\approx 370 \sin^2 \theta_c(E) \text{ eV}^{-1} \text{ cm}^{-1} \quad (z = 1), \end{aligned} \quad (33.45)$$

or, equivalently,

$$\frac{d^2N}{dx d\lambda} = \frac{2\pi\alpha z^2}{\lambda^2} \left(1 - \frac{1}{\beta^2 n^2(\lambda)} \right). \quad (33.46)$$

The index of refraction n is a function of photon energy $E = \hbar\omega$. For practical use, Eq. (33.45) must be multiplied by the photodetector response function and integrated over the region for which $\beta n(\omega) > 1$.

When two particles are within $\lesssim 1$ wavelength, the electromagnetic fields from the particles may add coherently, affecting the Cherenkov radiation. The radiation from an e^+e^- pair at close separation is suppressed compared to two independent leptons [84].

33.7.2. Coherent radio Cherenkov radiation :

Coherent Cherenkov radiation is produced by many charged particles with a non-zero net charge moving through matter on an approximately common “wavefront”—for example, the electrons and positrons in a high-energy electromagnetic cascade. The signals can be visible above backgrounds for shower energies as low as 10^{17} eV; see Sec. 34.3.3 for more details. The phenomenon is called the Askaryan effect [85]. The photons can Compton-scatter atomic electrons, and positrons can annihilate with atomic electrons to contribute even more photons which can in turn Compton scatter. These processes result in a roughly 20% excess of electrons over positrons in a shower. The net negative charge leads to coherent radio Cherenkov emission. Because the emission is coherent, the electric field strength is proportional to the shower energy, and the signal power increases as its square. The electric field strength also increases linearly with frequency, up to a maximum frequency determined by the lateral spread of the shower. This cutoff occurs at about 1 GHz in ice, and scales inversely with the Moliere radius. At low frequencies, the radiation is roughly isotropic, but, as the frequency rises toward the cutoff frequency, the radiation becomes increasingly peaked around the Cherenkov angle.

33.7.3. Transition radiation : The energy I radiated when a particle with charge ze crosses the boundary between vacuum and a medium with plasma frequency ω_p is $\alpha z^2 \gamma \hbar\omega_p/3$, where

$$\hbar\omega_p = \sqrt{4\pi N_e r_e^3} m_e c^2 / \alpha = \sqrt{\rho \text{ (in g/cm}^3\text{)} \langle Z/A \rangle} \times 28.81 \text{ eV}. \quad (33.48)$$

For styrene and similar materials, $\hbar\omega_p \approx 20$ eV; for air it is 0.7 eV.

The number spectrum $dN_\gamma/d(\hbar\omega)$ diverges logarithmically at low energies and decreases rapidly for $\hbar\omega/\gamma\hbar\omega_p > 1$. About half the energy is emitted in the range $0.1 \leq \hbar\omega/\gamma\hbar\omega_p \leq 1$. Inevitable absorption in a practical detector removes the divergence. For a particle with $\gamma = 10^3$, the radiated photons are in the soft x-ray range 2 to 40 keV. The γ dependence of the emitted energy thus comes from the hardening of the spectrum rather than from an increased quantum yield.

The number of photons with energy $\hbar\omega > \hbar\omega_0$ is given by the answer to problem 13.15 in Ref. 33,

$$N_\gamma(\hbar\omega > \hbar\omega_0) = \frac{\alpha z^2}{\pi} \left[\left(\ln \frac{\gamma \hbar\omega_p}{\hbar\omega_0} - 1 \right)^2 + \frac{\pi^2}{12} \right], \quad (33.49)$$

within corrections of order $(\hbar\omega_0/\gamma\hbar\omega_p)^2$. The number of photons above a fixed energy $\hbar\omega_0 \ll \gamma\hbar\omega_p$ thus grows as $(\ln \gamma)^2$, but the number above a fixed fraction of $\gamma\hbar\omega_p$ (as in the example above) is constant. For example, for $\hbar\omega > \gamma\hbar\omega_p/10$, $N_\gamma = 2.519 \alpha z^2/\pi = 0.59\% \times z^2$.

The particle stays “in phase” with the x ray over a distance called the formation length, $d(\omega)$. Most of the radiation is produced in a distance

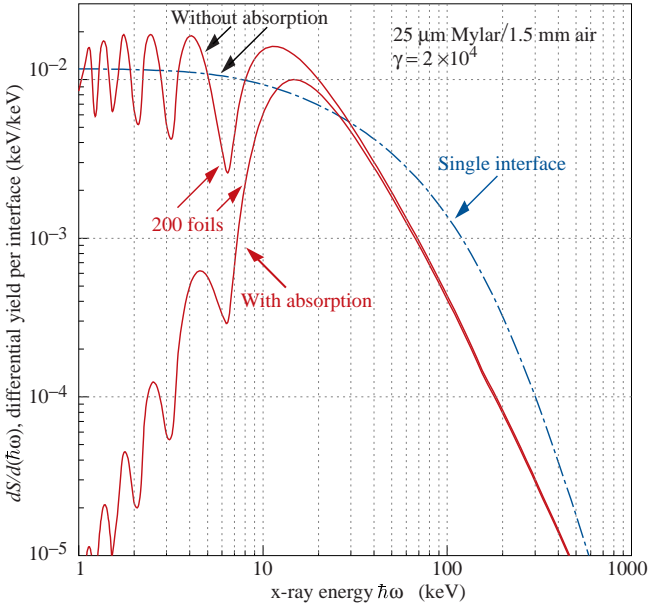


Figure 33.27: X-ray photon energy spectra for a radiator consisting of 200 $25\ \mu\text{m}$ thick foils of Mylar with $1.5\ \text{mm}$ spacing in air (solid lines) and for a single surface (dashed line). Curves are shown with and without absorption. Adapted from Ref. 88.

$d(\omega) = (2c/\omega)(1/\gamma^2 + \theta^2 + \omega_p^2/\omega^2)^{-1}$. Here θ is the x-ray emission angle, characteristically $1/\gamma$. For $\theta = 1/\gamma$ the formation length has a maximum at $d(\gamma\omega_p/\sqrt{2}) = \gamma c/\sqrt{2}\omega_p$. In practical situations it is tens of μm .

Since the useful x-ray yield from a single interface is low, in practical detectors it is enhanced by using a stack of N foil radiators—foils L thick, where L is typically several formation lengths—separated by gas-filled gaps. The amplitudes at successive interfaces interfere to cause oscillations about the single-interface spectrum. At increasing frequencies above the position of the last interference maximum ($L/d(\omega) = \pi/2$), the formation zones, which have opposite phase, overlap more and more and the spectrum saturates, $dI/d\omega$ approaching zero as $L/d(\omega) \rightarrow 0$. This is illustrated in Fig. 33.27 for a realistic detector configuration.

For regular spacing of the layers fairly complicated analytic solutions for the intensity have been obtained [88,89]. (See also Ref. 89 and references therein.) Although one might expect the intensity of coherent radiation from the stack of foils to be proportional to N^2 , the angular dependence of the formation length conspires to make the intensity $\propto N$.

Further discussion and all references may be found in the full *Review of Particle Physics*. The equation and reference numbering corresponds to that version.

34. PARTICLE DETECTORS AT ACCELERATORS

This is an abridgment of the discussion given in the full *Review of Particle Physics* (the “full *Review*”); the equation and reference numbering corresponds to that version. The quoted numbers are usually based on typical devices, and should be regarded only as rough approximations for new designs. A more detailed discussion of detectors can be found in Refs. 1 and 64.

34.1. Introduction

This review summarizes the detector technologies employed at accelerator particle physics experiments. Several of these detectors are also used in a non-accelerator context and examples of such applications will be provided. The detector techniques which are specific to non-accelerator particle physics experiments are the subject of Chap. 35. More detailed discussions of detectors and their underlying physics can be found in books by Ferbel [1], Kleinknecht [2], Knoll [3], Green [4], Leroy & Rancoita [5], and Grupen [6].

In Table 34.1 are given typical resolutions and deadtimes of common charged particle detectors. The quoted numbers are usually based on typical devices, and should be regarded only as rough approximations for new designs. The spatial resolution refers to the intrinsic detector resolution, i.e. without multiple scattering. We note that analog detector readout can provide better spatial resolution than digital readout by measuring the deposited charge in neighboring channels. Quoted ranges attempt to be representative of both possibilities. The time resolution is defined by how accurately the time at which a particle crossed the detector can be determined. The deadtime is the minimum separation in time between two resolved hits on the same channel. Typical performance of calorimetry and particle identification are provided in the relevant sections below.

Table 34.1: Typical resolutions and deadtimes of common charged particle detectors. Revised November 2011.

Detector Type	Intrinsic Spatial Resolution (rms)	Time Resolution	Dead Time
Resistive plate chamber	$\lesssim 10$ mm	1 ns (50 ps ^a)	—
Streamer chamber	300 μm^a	2 μs	100 ms
Liquid argon drift [7]	$\sim 175\text{--}450$ μm	~ 200 ns	~ 2 μs
Scintillation tracker	~ 100 μm	100 ps/ n^a	10 ns
Bubble chamber	10–150 μm	1 ms	50 ms ^a
Proportional chamber	50–100 μm^a	2 ns	20–200 ns
Drift chamber	50–100 μm	2 ns ^a	20–100 ns
Micro-pattern gas detectors	30–40 μm	< 10 ns	10–100 ns
Silicon strip	pitch/(3 to 7) ^a	few ns ^a	$\lesssim 50$ ns ^a
Silicon pixel	$\lesssim 10$ μm	few ns ^a	$\lesssim 50$ ns ^a
Emulsion	1 μm	—	—

^a See full *Review* for qualifications and assumptions.

34.2. Photon detectors

Updated August 2011 by D. Chakraborty (Northern Illinois U) and T. Sumiyoshi (Tokyo Metro U).

Most detectors in high-energy, nuclear, and astrophysics rely on the detection of photons in or near the visible range, $100 \text{ nm} \lesssim \lambda \lesssim 1000 \text{ nm}$, or $E \approx$ a few eV. This range covers scintillation and Cherenkov radiation as well as the light detected in many astronomical observations.

Generally, photodetection involves generating a detectable electrical signal proportional to the (usually very small) number of incident photons.

34.2.1. Vacuum photodetectors : Vacuum photodetectors can be broadly subdivided into three types: photomultiplier tubes, microchannel plates, and hybrid photodetectors.

34.2.1.1. Photomultiplier tubes: A versatile class of photon detectors, vacuum photomultiplier tubes (PMT) has been employed by a vast majority of all particle physics experiments to date [9]. Both “transmission-” and “reflection-type” PMT’s are widely used. In the former, the photocathode material is deposited on the inside of a transparent window through which the photons enter, while in the latter, the photocathode material rests on a separate surface that the incident photons strike. The cathode material has a low work function, chosen for the wavelength band of interest. When a photon hits the cathode and liberates an electron (the photoelectric effect), the latter is accelerated and guided by electric fields to impinge on a secondary-emission electrode, or dynode, which then emits a few (~ 5) secondary electrons. The multiplication process is repeated typically 10 times in series to generate a sufficient number of electrons, which are collected at the anode for delivery to the external circuit. The total gain of a PMT depends on the applied high voltage V as $G = AV^{kn}$, where $k \approx 0.7-0.8$ (depending on the dynode material), n is the number of dynodes in the chain, and A a constant (which also depends on n). Typically, G is in the range of 10^5-10^6 .

34.2.2. Gaseous photon detectors : In gaseous photomultipliers (GPM) a photoelectron in a suitable gas mixture initiates an avalanche in a high-field region, producing a large number of secondary impact-ionization electrons. In principle the charge multiplication and collection processes are identical to those employed in gaseous tracking detectors such as multiwire proportional chambers, micromesh gaseous detectors (Micromegas), or gas electron multipliers (GEM). These are discussed in Sec. 34.6.3.

34.2.3. Solid-state photon detectors : In a phase of rapid development, solid-state photodetectors are competing with vacuum- or gas-based devices for many existing applications and making way for a multitude of new ones. Compared to traditional vacuum- and gaseous photodetectors, solid-state devices are more compact, lightweight, rugged, tolerant to magnetic fields, and often cheaper. They also allow fine pixelization, are easy to integrate into large systems, and can operate at low electric potentials, while matching or exceeding most performance criteria. They are particularly well suited for detection of γ - and X-rays. Except for applications where coverage of very large areas or dynamic range is required, solid-state detectors are proving to be the better choice. Some hybrid devices attempt to combine the best features of different technologies while applications of nanotechnology are opening up exciting new possibilities.

Silicon photodiodes (PD) are widely used in high-energy physics as particle detectors and in a great number of applications (including solar

cells!) as light detectors. The structure is discussed in some detail in Sec. 34.7.

Very large arrays containing $O(10^7)$ of $O(10 \mu\text{m}^2)$ -sized photodiodes pixelizing a plane are widely used to photograph all sorts of things from everyday subjects at visible wavelengths to crystal structures with X-rays and astronomical objects from infrared to UV. To limit the number of readout channels, these are made into charge-coupled devices (CCD), where pixel-to-pixel signal transfer takes place over thousands of synchronous cycles with sequential output through shift registers [14]. Thus, high spatial resolution is achieved at the expense of speed and timing precision. Custom-made CCD's have virtually replaced photographic plates and other imagers for astronomy and in spacecraft.

In APD's, an exponential cascade of impact ionizations initiated by the original photogenerated $e-h$ pair under a large reverse-bias voltage leads to an avalanche breakdown [15]. As a result, detectable electrical response can be obtained from low-intensity optical signals down to single photons.

34.3. Organic scintillators

Revised August 2011 by Kurtis F. Johnson (FSU).

Organic scintillators are broadly classed into three types, crystalline, liquid, and plastic, all of which utilize the ionization produced by charged particles to generate optical photons, usually in the blue to green wavelength regions [19]. Plastic scintillators are by far the most widely used, liquid organic scintillator is finding increased use, and crystal organic scintillators are practically unused in high-energy physics. Plastic scintillator densities range from 1.03 to 1.20 g cm⁻³. Typical photon yields are about 1 photon per 100 eV of energy deposit [20]. A one-cm-thick scintillator traversed by a minimum-ionizing particle will therefore yield $\approx 2 \times 10^4$ photons. The resulting photoelectron signal will depend on the collection and transport efficiency of the optical package and the quantum efficiency of the photodetector.

Decay times are in the ns range; rise times are much faster. Ease of fabrication into desired shapes and low cost has made plastic scintillator a common detector element. In the form of scintillating fiber it has found widespread use in tracking and calorimetry [23].

34.3.2. Scintillating and wavelength-shifting fibers :

The clad optical fiber comprising scintillator and wavelength shifter (WLS) is particularly useful [31]. Since the initial demonstration of the scintillating fiber (SCIFI) calorimeter [32], SCIFI techniques have become mainstream [33]. SCIFI calorimeters are fast, dense, radiation hard, and can have leadglass-like resolution. SCIFI trackers can handle high rates and are radiation tolerant, but the low photon yield at the end of a long fiber (see below) forces the use of sensitive photodetectors. WLS scintillator readout of a calorimeter allows a very high level of hermeticity since the solid angle blocked by the fiber on its way to the photodetector is very small.

34.4. Inorganic scintillators

Revised November 2015 by R.-Y. Zhu (California Institute of Technology) and C.L. Woody (BNL).

Inorganic crystals form a class of scintillating materials with much higher densities than organic plastic scintillators (typically $\sim 4\text{--}8\text{ g/cm}^3$) with a variety of different properties for use as scintillation detectors. Due to their high density and high effective atomic number, they can be used in applications where high stopping power or a high conversion efficiency for electrons or photons is required. These include total absorption electromagnetic calorimeters (see Sec. 34.8.1), which consist of a totally active absorber (as opposed to a sampling calorimeter), as well as serving as gamma ray detectors over a wide range of energies. Many of these crystals also have very high light output, and can therefore provide excellent energy resolution down to very low energies (\sim few hundred keV).

34.5. Cherenkov detectors

Revised August 2015 by B.N. Ratcliff (SLAC).

Although devices using Cherenkov radiation are often thought of as only particle identification (PID) detectors, in practice they are used over a much broader range of applications including; (1) fast particle counters; (2) hadronic PID; and (3) tracking detectors performing complete event reconstruction. Examples of applications from each category include; (1) the Quartic fast timing counter designed to measure small angle scatters at the LHC [56]; (2) the hadronic PID detectors at the B factory detectors—DIRC in BaBar [57] and the aerogel threshold Cherenkov in Belle [58]; and (3) large water Cherenkov counters such as Super-Kamiokande [59]. Cherenkov counters contain two main elements; (1) a radiator through which the charged particle passes, and (2) a photodetector. As Cherenkov radiation is a weak source of photons, light collection and detection must be as efficient as possible. The refractive index n and the particle's path length through the radiator L appear in the Cherenkov relations allowing the tuning of these quantities for particular applications.

Cherenkov detectors utilize one or more of the properties of Cherenkov radiation discussed in the Passages of Particles through Matter section (Sec. 33 of this *Review*): the prompt emission of a light pulse; the existence of a velocity threshold for radiation; and the dependence of the Cherenkov cone half-angle θ_c and the number of emitted photons on the velocity of the particle and the refractive index of the medium.

34.6. Gaseous detectors

34.6.1. *Energy loss and charge transport in gases* : Revised March 2010 by F. Sauli (CERN) and M. Titov (CEA Saclay).

Gas-filled detectors localize the ionization produced by charged particles, generally after charge multiplication. The statistics of ionization processes having asymmetries in the ionization trails, affect the coordinate determination deduced from the measurement of drift time, or of the center of gravity of the collected charge. For thin gas layers, the width of the energy loss distribution can be larger than its average, requiring multiple sample or truncated mean analysis to achieve good particle identification. In the truncated mean method for calculating $\langle dE/dx \rangle$, the ionization measurements along the track length are broken into many samples and then a fixed fraction of high-side (and sometimes also low-side) values are rejected [64].

The energy loss of charged particles and photons in matter is discussed in Sec. 33. Table 34.2 provides values of relevant parameters in some commonly used gases at NTP (normal temperature, 20° C, and pressure, 1 atm) for unit-charge minimum-ionizing particles (MIPs) [65–71].

Table 34.2: Properties of noble and molecular gases at normal temperature and pressure (NTP: 20° C, one atm). E_X , E_I : first excitation, ionization energy; W_I : average energy per ion pair; $dE/dx|_{\min}$, N_P , N_T : differential energy loss, primary and total number of electron-ion pairs per cm, for unit charge minimum ionizing particles.

Gas	Density, mg cm ⁻³	E_x eV	E_I eV	W_I eV	$dE/dx _{\min}$ keV cm ⁻¹	N_P cm ⁻¹	N_T cm ⁻¹
He	0.179	19.8	24.6	41.3	0.32	3.5	8
Ne	0.839	16.7	21.6	37	1.45	13	40
Ar	1.66	11.6	15.7	26	2.53	25	97
Xe	5.495	8.4	12.1	22	6.87	41	312
CH ₄	0.667	8.8	12.6	30	1.61	28	54
C ₂ H ₆	1.26	8.2	11.5	26	2.91	48	112
iC ₄ H ₁₀	2.49	6.5	10.6	26	5.67	90	220
CO ₂	1.84	7.0	13.8	34	3.35	35	100
CF ₄	3.78	10.0	16.0	54	6.38	63	120

When an ionizing particle passes through the gas it creates electron-ion pairs, but often the ejected electrons have sufficient energy to further ionize the medium. As shown in Table 34.2, the total number of electron-ion pairs (N_T) is usually a few times larger than the number of primaries (N_P).

The probability for a released electron to have an energy E or larger follows an approximate $1/E^2$ dependence (Rutherford law), taking into account the electronic structure of the medium

The number of electron-ion pairs per primary ionization, or cluster size, has an exponentially decreasing probability; for argon, there is about 1% probability for primary clusters to contain ten or more electron-ion pairs [67].

Once released in the gas, and under the influence of an applied electric field, electrons and ions drift in opposite directions and diffuse towards the electrodes. The drift velocity and diffusion of electrons depend very strongly on the nature of the gas. Large drift velocities are achieved by adding polyatomic gases (usually CH₄, CO₂, or CF₄) having large inelastic cross sections at moderate energies, which results in “cooling” electrons into the energy range of the Ramsauer-Townsend minimum (at ~ 0.5 eV) of the elastic cross-section of argon. In a simple approximation, gas kinetic theory provides the drift velocity v as a function of the mean collision time τ and the electric field E : $v = eE\tau/m_e$ (Townsend’s expression). In the presence of an external magnetic field, the Lorentz force acting on electrons between collisions deflects the drifting electrons and modifies the drift properties.

If the electric field is increased sufficiently, electrons gain enough energy between collisions to ionize molecules. Above a gas-dependent threshold, the mean free path for ionization, λ_i , decreases exponentially with the field; its inverse, $\alpha = 1/\lambda_i$, is the first Townsend coefficient. In wire chambers,

most of the increase of avalanche particle density occurs very close to the anode wires, and a simple electrostatic consideration shows that the largest fraction of the detected signal is due to the motion of positive ions receding from the wires. The electron component, although very fast, contributes very little to the signal. This determines the characteristic shape of the detected signals in the proportional mode: a fast rise followed by a gradual increase.

34.6.2. Multi-Wire Proportional and Drift Chambers : Revised March 2010 by Fabio Sauli (CERN) and Maxim Titov (CEA Saclay).

Multiwire proportional chambers (MWPCs) [73,74], introduced in the late '60's, detect, localize and measure energy deposit by charged particles over large areas. A mesh of parallel anode wires at a suitable potential, inserted between two cathodes, acts almost as a set of independent proportional counters. Electrons released in the gas volume drift towards the anodes and produce avalanches in the increasing field.

Detection of charge on the wires over a predefined threshold provides the transverse coordinate to the wire with an accuracy comparable to that of the wire spacing. The coordinate along each wire can be obtained by measuring the ratio of collected charge at the two ends of resistive wires. Making use of the charge profile induced on segmented cathodes, the so-called center-of gravity (COG) method, permits localization of tracks to sub-mm accuracy.

Drift chambers, developed in the early '70's, can be used to estimate the longitudinal position of a track by exploiting the arrival time of electrons at the anodes if the time of interaction is known [77]. The distance between anode wires is usually several cm, allowing coverage of large areas at reduced cost.

34.6.3. Micro-Pattern Gas Detectors : Revised March 2010 by Fabio Sauli (CERN) and Maxim Titov (CEA Saclay)

By using pitch size of a few hundred μm , an order of magnitude improvement in granularity over wire chambers, these detectors offer intrinsic high rate capability ($> 10^6$ Hz/mm²), excellent spatial resolution ($\sim 30 \mu\text{m}$), multi-particle resolution ($\sim 500 \mu\text{m}$), and single photo-electron time resolution in the ns range.

The Gas Electron Multiplier (GEM) detector consists of a thin-foil copper-insulator-copper sandwich chemically perforated to obtain a high density of holes in which avalanches occur [94]. The hole diameter is typically between $25 \mu\text{m}$ and $150 \mu\text{m}$, while the corresponding distance between holes varies between $50 \mu\text{m}$ and $200 \mu\text{m}$. The central insulator is usually (in the original design) the polymer Kapton, with a thickness of $50 \mu\text{m}$. Application of a potential difference between the two sides of the GEM generates the electric fields. Each hole acts as an independent proportional counter. Electrons released by the primary ionization particle in the upper conversion region (above the GEM foil) drift into the holes, where charge multiplication occurs in the high electric field ($50\text{--}70$ kV/cm). Most of avalanche electrons are transferred into the gap below the GEM. Several GEM foils can be cascaded, allowing the multi-layer GEM detectors to operate at overall gas gain above 10^4 in the presence of highly ionizing particles, while strongly reducing the risk of discharges.

The micro-mesh gaseous structure (Micromegas) is a thin parallel-plate avalanche counter. It consists of a drift region and a narrow multiplication gap ($25\text{--}150 \mu\text{m}$) between a thin metal grid (micromesh) and the readout electrode (strips or pads of conductor printed on an insulator board). Electrons from the primary ionization drift through the holes of the mesh into the narrow multiplication gap, where they are amplified. The electric

field is homogeneous both in the drift (electric field ~ 1 kV/cm) and amplification (50–70 kV/cm) gaps. The small amplification gap produces a narrow avalanche, giving rise to excellent spatial resolution: 12 μm accuracy, limited by the micro-mesh pitch, has been achieved for MIPs, as well as very good time resolution and energy resolution ($\sim 12\%$ FWHM with 6 keV x rays) [97].

The performance and robustness of GEM and Micromegas have encouraged their use in high-energy and nuclear physics, UV and visible photon detection, astroparticle and neutrino physics, neutron detection and medical physics.

34.6.4. Time-projection chambers : Written August 2015 by C. Lippmann (GSI Helmholtzzentrum für Schwerionenforschung, Darmstadt, Germany)

The Time Projection Chamber (TPC) concept was invented by David Nygren in the late 1970's [82]. It consists of a cylindrical or square field cage filled with a detection medium that is usually a gas or a liquid. Charged particles produce tracks of ionization electrons that drift in a uniform electric field towards a position-sensitive amplification stage which provides a 2D projection of the particle trajectories. The third coordinate can be calculated from the arrival times of the drifted electrons. The start for this drift time measurement is usually derived from an external detector, e.g. a fast interaction trigger detector.

Identification of the charged particles crossing the TPC is possible by simultaneously measuring their momentum and specific energy deposit through ionisation (dE/dx). The momentum, as well as the charge sign, are calculated from a helix fit to the particle trajectory in the presence of a magnetic field (typically parallel to the drift field).

The greatest challenges for a large TPC are due to the length of the drift of up to several meters. In particular, it can make the device sensitive to small distortions in the electric field. Such distortions can arise from a number of sources, e.g. imperfections in the field cage construction or the presence of ions in the drift volume.

The drift and diffusion of electrons depend strongly on the nature of the gas that is used. The optimal gas mixture varies according to the environment in which the TPC will operate. In all cases, the oxygen concentration must be kept very low (few ten parts per million in a large TPC) in order to avoid electron loss through attachment.

Historically, the amplification stages used in gaseous TPCs have been planes of anode wires operated in proportional mode. The performance is limited by effects related to the feature size of a few mm (wire spacing). The smaller feature sizes of Micro-Pattern Gas Detectors (MPGDs) like GEMs and Micromegas lead to many advantages as compared to wire planes (see Sec. 34.6.3).

34.6.5. Transition radiation detectors (TRD's) : Revised August 2013 by P. Nevski (BNL) and A. Romaniouk (Moscow Eng. & Phys. Inst.)

Transition radiation (TR) x-rays are produced when a highly relativistic particle ($\gamma \gtrsim 10^3$) crosses a refractive index interface, as discussed in Sec. 33.7. The x-rays, ranging from a few keV to a few dozen keV or more, are emitted at a characteristic angle $1/\gamma$ from the particle trajectory. Since the TR yield is about 1% per boundary crossing, radiation from multiple surface crossings is used in practical detectors. In the simplest concept, a detector module might consist of low- Z foils followed by a high- Z active layer made of proportional counters filled with a Xe-rich gas mixture. The atomic number considerations follow from the dominant photoelectric absorption cross section per atom going roughly as Z^n/E_x^3 , where n varies

between 4 and 5 over the region of interest, and the x-ray energy is E_x . To minimize self-absorption, materials such as polypropylene, Mylar, carbon, and (rarely) lithium are used as radiators. The TR signal in the active regions is in most cases superimposed upon the particle ionization losses, which are proportional to Z .

The TR intensity for a single boundary crossing always increases with γ , but, for multiple boundary crossings, interference leads to saturation above a Lorentz factor $\gamma_{\text{sat}} = 0.6 \omega_1 \sqrt{\ell_1 \ell_2} / c$ [111], where ω_1 is the radiator material plasma frequency, ℓ_1 is its thickness, and ℓ_2 the spacing. In most of the detectors used in particle physics the radiator parameters are chosen to provide $\gamma_{\text{sat}} \approx 2000$. Those detectors normally work as threshold devices, ensuring the best electron/pion separation in the momentum range $1 \text{ GeV}/c \lesssim p \lesssim 150 \text{ GeV}/c$.

The discrimination between electrons and pions can be based on the charge deposition measured in each detection module, on the number of clusters – energy depositions observed above an optimal threshold (usually it is 5–7 keV), or on more sophisticated methods such as analyzing the pulse shape as a function of time. The total energy measurement technique is more suitable for thick gas volumes, which absorb most of the TR radiation and where the ionization loss fluctuations are small. The cluster-counting method works better for detectors with thin gas layers, where the fluctuations of the ionization losses are big. Recent TRDs for particle astrophysics are designed to directly measure the Lorentz factor of high-energy nuclei by using the quadratic dependence of the TR yield on nuclear charge; see Cherry and Müller papers in [113].

34.7. Semiconductor detectors

Updated November 2013 by H. Spieler.

Semiconductor detectors provide a unique combination of energy and position resolution. In collider detectors they are most widely used as position sensing devices and photodetectors (Sec. 34.2).

34.7.1. Materials Requirements :

Semiconductor detectors are essentially solid state ionization chambers. Absorbed energy forms electron-hole pairs, *i.e.*, negative and positive charge carriers, which under an applied electric field move towards their respective collection electrodes, where they induce a signal current. The energy required to form an electron-hole pair is proportional to the bandgap. In tracking detectors the energy loss in the detector should be minimal, whereas for energy spectroscopy the stopping power should be maximized, so for gamma rays high- Z materials are desirable.

Measurements on silicon photodiodes [141] show that for photon energies below 4 eV one electron-hole ($e-h$) pair is formed per incident photon. The mean energy E_i required to produce an $e-h$ pair peaks at 4.4 eV for a photon energy around 6 eV. Above ~ 1.5 keV it assumes a constant value, 3.67 eV at room temperature. It is larger than the bandgap energy because momentum conservation requires excitation of lattice vibrations (phonons). For minimum-ionizing particles, the most probable charge deposition in a 300 μm thick silicon detector is about 3.5 fC (22000 electrons). Other typical ionization energies are 2.96 eV in Ge, 4.2 eV in GaAs, and 4.43 eV in CdTe.

Since both electronic and lattice excitations are involved, the variance in the number of charge carriers $N = E/E_i$ produced by an absorbed energy E is reduced by the Fano factor F (about 0.1 in Si and Ge). Thus, $\sigma_N = \sqrt{FN}$ and the energy resolution $\sigma_E/E = \sqrt{FE_i/E}$. However, the measured signal fluctuations are usually dominated by electronic noise or energy loss fluctuations in the detector.

A major effort is to find high- Z materials with a bandgap that is sufficiently high to allow room-temperature operation while still providing good energy resolution. Compound semiconductors, *e.g.*, CdZnTe, can allow this, but typically suffer from charge collection problems, characterized by the product $\mu\tau$ of mobility and carrier lifetime. In Si and Ge $\mu\tau > 1 \text{ cm}^2 \text{ V}^{-1}$ for both electrons and holes, whereas in compound semiconductors it is in the range 10^{-3} – 10^{-8} . Since for holes $\mu\tau$ is typically an order of magnitude smaller than for electrons, detector configurations where the electron contribution to the charge signal dominates—*e.g.*, strip or pixel structures—can provide better performance.

34.7.2. Detector Configurations :

A p - n junction operated at reverse bias forms a sensitive region depleted of mobile charge and sets up an electric field that sweeps charge liberated by radiation to the electrodes. Detectors typically use an asymmetric structure, *e.g.*, a highly doped p electrode and a lightly doped n region, so that the depletion region extends predominantly into the lightly doped volume.

In a planar device the thickness of the depleted region is

$$W = \sqrt{2\epsilon(V + V_{bi})/Ne} = \sqrt{2\rho\mu\epsilon(V + V_{bi})}, \quad (34.19)$$

where V = external bias voltage

V_{bi} = “built-in” voltage (≈ 0.5 V for resistivities typically used in Si detectors)

N = doping concentration

e = electronic charge

ϵ = dielectric constant = $11.9 \epsilon_0 \approx 1$ pF/cm in Si

ρ = resistivity (typically 1–10 k Ω cm in Si)

μ = charge carrier mobility

= $1350 \text{ cm}^2 \text{ V}^{-1} \text{ s}^{-1}$ for electrons in Si

= $450 \text{ cm}^2 \text{ V}^{-1} \text{ s}^{-1}$ for holes in Si

In Si

$W = 0.5 [\mu\text{m}/\sqrt{\Omega\text{-cm}\cdot\text{V}}] \times \sqrt{\rho(V + V_{bi})}$ for n -type Si, and

$W = 0.3 [\mu\text{m}/\sqrt{\Omega\text{-cm}\cdot\text{V}}] \times \sqrt{\rho(V + V_{bi})}$ for p -type Si.

Large volume ($\sim 10^2$ – 10^3 cm^3) Ge detectors are commonly configured as coaxial detectors, *e.g.*, a cylindrical n -type crystal with 5–10 cm diameter and 10 cm length with an inner 5–10 mm diameter n^+ electrode and an outer p^+ layer forming the diode junction. Ge can be grown with very low impurity levels, 10^9 – 10^{10} cm^{-3} (HPGe), so these large volumes can be depleted with several kV.

34.7.3. Signal Formation :

The signal pulse shape depends on the instantaneous carrier velocity $v(x) = \mu E(x)$ and the electrode geometry, which determines the distribution of induced charge (*e.g.*, see Ref. 140, pp. 71–83). Charge collection time decreases with increasing bias voltage, and can be reduced further by operating the detector with “overbias,” *i.e.*, a bias voltage exceeding the value required to fully deplete the device. Note that in partial depletion the electric field goes to zero, whereas going beyond full depletion adds a constantly distributed field. The collection time is limited by velocity saturation at high fields (in Si approaching 10^7 cm/s at $E > 10^4 \text{ V/cm}$); at an average field of 10^4 V/cm the collection time is about 15 ps/ μm for electrons and 30 ps/ μm for holes. In typical fully-depleted detectors 300 μm thick, electrons are collected within about 10 ns, and holes within about 25 ns.

Position resolution is limited by transverse diffusion during charge collection (typically $5\ \mu\text{m}$ for $300\ \mu\text{m}$ thickness) and by knock-on electrons. Resolutions of $2\text{--}4\ \mu\text{m}$ (rms) have been obtained in beam tests. In magnetic fields, the Lorentz drift deflects the electron and hole trajectories and the detector must be tilted to reduce spatial spreading (see “Hall effect” in semiconductor textbooks).

Electrodes can be in the form of cm-scale pads, strips, or μm -scale pixels. Various readout structures have been developed for pixels, *e.g.*, CCDs, DEPFETs, monolithic pixel devices that integrate sensor and electronics (MAPS), and hybrid pixel devices that utilize separate sensors and readout ICs connected by two-dimensional arrays of solder bumps. For an overview and further discussion see Ref. 140.

Strip and pixel detectors have remained functional at fluences beyond $10^{15}\ \text{cm}^{-2}$ for minimum ionizing protons. At this damage level, charge loss due to recombination and trapping becomes significant and the high signal-to-noise ratio obtainable with low-capacitance pixel structures extends detector lifetime. The higher mobility of electrons makes them less sensitive to carrier lifetime than holes, so detector configurations that emphasize the electron contribution to the charge signal are advantageous, *e.g.*, n^+ strips or pixels on a p- or n-substrate. The occupancy of the defect charge states is strongly temperature dependent; competing processes can increase or decrease the required operating voltage. It is critical to choose the operating temperature judiciously (-10 to 0°C in typical collider detectors) and limit warm-up periods during maintenance. For a more detailed summary see Ref. 146 and the web-sites of the ROSE and RD50 collaborations at <http://RD48.web.cern.ch/rd48> and <http://RD50.web.cern.ch/rd50>. Materials engineering, *e.g.*, introducing oxygen interstitials, can improve certain aspects and is under investigation. At high fluences diamond is an alternative, but operates as an insulator rather than a reverse-biased diode.

34.8. Calorimeters

A calorimeter is designed to measure a particle’s (or jet’s) energy and direction for an (ideally) contained electromagnetic (EM) or hadronic shower. The characteristic interaction distance for an electromagnetic interaction is the radiation length X_0 , which ranges from $13.8\ \text{g cm}^{-2}$ in iron to $6.0\ \text{g cm}^{-2}$ in uranium.* Similarly, the characteristic nuclear interaction length λ_I varies from $132.1\ \text{g cm}^{-2}$ (Fe) to $209\ \text{g cm}^{-2}$ (U).† In either case, a calorimeter must be many interaction lengths deep, where “many” is determined by physical size, cost, and other factors. EM calorimeters tend to be $15\text{--}30\ X_0$ deep, while hadronic calorimeters are usually compromised at $5\text{--}8\ \lambda_I$. In real experiments there is likely to be an EM calorimeter in front of the hadronic section, which in turn has less sampling density in the back, so the hadronic cascade occurs in a succession of different structures.

In all cases there is a premium on small λ_I/ρ and X_0/ρ (both with units of length).

These considerations are for *sampling calorimeters* consisting of metallic absorber sandwiched or (threaded) with an active material which generates signal. The active medium may be a scintillator, an ionizing noble liquid, a gas chamber, a semiconductor, or a Cherenkov radiator.

There are also *homogeneous calorimeters*, in which the entire volume is sensitive, *i.e.*, contributes signal. Homogeneous calorimeters (so far

* $X_0 = 120\ \text{g cm}^{-2} Z^{-2/3}$ to better than 5% for $Z > 23$.

† $\lambda_I = 37.8\ \text{g cm}^{-2} A^{0.312}$ to within 0.8% for $Z > 15$.

See pdg.lbl.gov/AtomicNuclearProperties for actual values.

usually electromagnetic) may be built with inorganic heavy (high density, high $\langle Z \rangle$) scintillating crystals, or non-scintillating Cherenkov radiators such as lead glass and lead fluoride. Scintillation light and/or ionization in noble liquids can be detected. Nuclear interaction lengths in inorganic crystals range from 17.8 cm (LuAlO₃) to 42.2 cm (NaI).

34.8.1. Electromagnetic calorimeters :

Revised September 2015 by R.-Y. Zhu (California Institute of Technology).

The development of electromagnetic showers is discussed in the section on “Passage of Particles Through Matter” (Sec. 33 of this *Review*).

The energy resolution σ_E/E of a calorimeter can be parameterized as $a/\sqrt{E} \oplus b \oplus c/E$, where \oplus represents addition in quadrature and E is in GeV. The stochastic term a represents statistics-related fluctuations such as intrinsic shower fluctuations, photoelectron statistics, dead material at the front of the calorimeter, and sampling fluctuations. For a fixed number of radiation lengths, the stochastic term a for a sampling calorimeter is expected to be proportional to $\sqrt{t/f}$, where t is plate thickness and f is sampling fraction [152,153]. While a is at a few percent level for a homogeneous calorimeter, it is typically 10% for sampling calorimeters.

The main contributions to the systematic, or constant, term b are detector non-uniformity and calibration uncertainty. In the case of the hadronic cascades discussed below, non-compensation also contributes to the constant term. One additional contribution to the constant term for calorimeters built for modern high-energy physics experiments, operated in a high-beam intensity environment, is radiation damage of the active medium. This can be mitigated by developing radiation-hard active media [51], by reducing the signal path length [52] and by frequent *in situ* calibration and monitoring [50,153].

34.8.2. Hadronic calorimeters : [1–5,153]

Revised September 2013 by D. E. Groom (LBNL).

Most large hadron calorimeters are parts of large 4π detectors at colliding beam facilities. At present these are sampling calorimeters: plates of absorber (Fe, Pb, Cu, or occasionally U or W) alternating with plastic scintillators (plates, tiles, bars), liquid argon (LAr), or gaseous detectors. The ionization is measured directly, as in LAr calorimeters, or via scintillation light observed by photodetectors (usually PMT’s or silicon photodiodes). Wavelength-shifting fibers are often used to solve difficult problems of geometry and light collection uniformity. Silicon sensors are being studied for ILC detectors; in this case e - h pairs are collected.

In an inelastic hadronic collision a significant fraction f_{em} of the energy is removed from further hadronic interaction by the production of secondary π^0 ’s and η ’s, whose decay photons generate high-energy electromagnetic (EM) showers. Charged secondaries (π^\pm , p , ...) deposit energy via ionization and excitation, but also interact with nuclei, producing spallation protons and neutrons, evaporation neutrons, and spallation products. The charged collision products produce detectable ionization, as do the showering γ -rays from the prompt de-excitation of highly excited nuclei. The recoiling nuclei generate little or no detectable signal. The neutrons lose kinetic energy in elastic collisions, thermalize on a time scale of several μ s, and are captured, with the production of more γ -rays—usually outside the acceptance gate of the electronics. Between endothermic spallation losses, nuclear recoils, and late neutron capture, a significant fraction of the hadronic energy (20%–40%, depending on the absorber and energy of the incident particle) is used to overcome nuclear binding energies and is therefore lost or “invisible.”

For $\langle h/e \rangle \neq 1$ (*noncompensation*), fluctuations in f_{em} significantly contribute to or even dominate the resolution. Since the f_{em} distribution has a high-energy tail, the calorimeter response is non-Gaussian with a high-energy tail if $\langle h/e \rangle < 1$. Noncompensation thus seriously degrades resolution and produces a nonlinear response.

It is clearly desirable to *compensate* the response, *i.e.*, to design the calorimeter such that $\langle h/e \rangle = 1$. This is possible only with a sampling calorimeter, where several variables can be chosen or tuned:

1. Decrease the EM sensitivity. EM cross sections increase with Z ,[†] and most of the energy in an EM shower is deposited by low-energy electrons. A disproportionate fraction of the EM energy is thus deposited in the higher- Z absorber. The degree of EM signal suppression can be somewhat controlled by tuning the sensor/absorber thickness ratio.
2. Increase the hadronic sensitivity. The abundant neutrons produced in the cascade have large $n-p$ elastic scattering cross sections, so that low-energy scattered protons are produced in hydrogenous sampling materials such as butane-filled proportional counters or plastic scintillator.
3. Fabjan and Willis proposed that the additional signal generated in the aftermath of fission in ^{238}U absorber plates should compensate nuclear fluctuations [166].

Motivated very much by the work of Brau, Gabriel, Brückmann, and Wigmans [168], several groups built calorimeters which were very nearly compensating. The degree of compensation was sensitive to the acceptance gate width, and so could be somewhat further tuned.

After the first interaction of the incident hadron, the average longitudinal distribution rises to a smooth peak. The peak position increases slowly with energy. The distribution becomes nearly exponential after several interaction lengths. A gamma distribution fairly well describes the longitudinal development of an EM shower, as discussed in Sec. 33.5.

The transverse energy deposit is characterized by a central core dominated by EM cascades, together with a wide “skirt” produced by wide-angle hadronic interactions [174].

Further discussion and all references may be found in the full *Review of Particle Physics*. The numbering of references and equations used here corresponds to that version.

[†] The asymptotic pair-production cross section scales roughly as $Z^{0.75}$, and $|dE/dx|$ slowly decreases with increasing Z .

35. PARTICLE DETECTORS FOR NON-ACCELERATOR PHYSICS

This is an abridgment of the discussion given in the full *Review of Particle Physics* (the “full *Review*”); the equation and reference numbering corresponds to that version. The quoted numbers are usually based on typical devices, and should be regarded only as rough approximations for new designs.

35.1. Introduction

Non-accelerator experiments have become increasingly important in particle physics. These include classical cosmic ray experiments, neutrino oscillation measurements, and searches for double-beta decay, dark matter candidates, and magnetic monopoles. The experimental methods are sometimes those familiar at accelerators (plastic scintillators, drift chambers, TRD’s, *etc.*) but there is also instrumentation either not found at accelerators or applied in a radically different way. Examples are atmospheric scintillation detectors (Fly’s Eye), massive Cherenkov detectors (Super-Kamiokande, IceCube), ultracold solid state detectors (CDMS). And, except for the cosmic ray detectors, radiologically ultra-pure materials are required.

In this section, some more important detectors special to terrestrial non-accelerator experiments are discussed. Techniques used in both accelerator and non-accelerator experiments are described in Sec. 28, Particle Detectors at Accelerators, some of which have been modified to accommodate the non-accelerator nuances.

35.2. High-energy cosmic-ray hadron and gamma-ray detectors

35.2.1. Atmospheric fluorescence detectors :

Revised August 2015 by L.R. Wiencke (Colorado School of Mines).

Cosmic-ray fluorescence detectors (FDs) use the atmosphere as a giant calorimeter to measure isotropic scintillation light that traces the development profiles of extensive air showers. An extensive air shower (EAS) is produced by the interactions of ultra high-energy ($E > 10^{17}$ eV) subatomic particles in the stratosphere and upper troposphere. The amount of scintillation light generated is proportional to energy deposited in the atmosphere and nearly independent of the primary species.

The fluorescence light is emitted primarily between 290 and 430 nm, when relativistic charged particles, primarily electrons and positrons, excite nitrogen molecules in air, resulting in transitions of the 1P and 2P systems.

An FD element (telescope) consists of a non-tracking spherical mirror (3.5–13 m² and less than astronomical quality), a close-packed “camera” of photomultiplier tubes (PMTs) (for example, Hamamatsu R9508 or Photonis XP3062) near the focal plane, and a flash ADC readout system with a pulse and track-finding trigger scheme [10]. Simple reflector optics (12° × 16° degree field of view (FOV) on 256 PMTs) and Schmidt optics (30° × 30° FOV on 440 PMTs), including a correcting element, have been used.

The EAS generates a track consistent with a light source moving at $v = c$ across the FOV. The number of photons (N_γ) as a function of atmospheric depth (X) can be expressed as [8]

$$\frac{dN_\gamma}{dX} = \frac{dE_{\text{dep}}^{\text{tot}}}{dX} \int Y(\lambda, P, T, u) \cdot \tau_{\text{atm}}(\lambda, X) \cdot \varepsilon_{\text{FD}}(\lambda) d\lambda \quad , \quad (35.1)$$

where $\tau_{atm}(\lambda, X)$ is the atmospheric transmission, including wavelength (λ) dependence, and $\varepsilon_{FD}(\lambda)$ is the FD efficiency. $\varepsilon_{FD}(\lambda)$ includes geometric factors and collection efficiency of the optics, quantum efficiency of the PMTs, and other throughput factors. The typical systematic uncertainties, τ_{atm} (10%) and ε_{FD} (photometric calibration 10%), currently dominate the total reconstructed EAS energy uncertainty. $\Delta E/E$ of 20% is possible, provided the geometric fit of the EAS axis is constrained typically by multi-eye stereo projection, or by timing from a colocated sparse array of surface detectors.

35.2.2. Atmospheric Cherenkov telescopes for high-energy γ -ray astronomy :

Revised November 2015 by J. Holder (Dept. of Physics and Astronomy & Bartol Research Inst., Univ. of Delaware).

Atmospheric Cherenkov detectors achieve effective collection areas of $>10^5 \text{ m}^2$ by employing the Earth's atmosphere as an intrinsic part of the detection technique. A hadronic cosmic ray or high energy γ -ray incident on the Earth's atmosphere triggers a particle cascade, or air shower. Relativistic charged particles in the cascade generate Cherenkov radiation, which is emitted along the shower direction, resulting in a light pool on the ground with a radius of $\sim 130 \text{ m}$. Cherenkov light is produced throughout the cascade development, with the maximum emission occurring when the number of particles in the cascade is largest, at an altitude of $\sim 10 \text{ km}$ for primary energies of 100 GeV–1 TeV. Following absorption and scattering in the atmosphere, the Cherenkov light at ground level peaks at a wavelength, $\lambda \approx 300\text{--}350 \text{ nm}$. The photon density is typically $\sim 100 \text{ photons/m}^2$ for a 1 TeV primary, arriving in a brief flash of a few nanoseconds duration.

Modern atmospheric Cherenkov telescopes consist of large ($> 100 \text{ m}^2$) segmented mirrors on steerable altitude-azimuth mounts. A camera made from an array of photosensors is placed at the focus of each mirror and used to record a Cherenkov image of each air shower. Images are recorded at kHz rates, the vast majority of which are due to showers with hadronic cosmic-ray primaries. The shape and orientation of the Cherenkov images are used to discriminate γ -ray photon events from this cosmic-ray background, and to reconstruct the photon energy and arrival direction.

The total Cherenkov yield from the air shower is proportional to the energy of the primary particle. The energy resolution of this technique, also energy-dependent, is typically 15–20% at energies above a few hundred GeV. Energy spectra of γ -ray sources can be measured over a wide range, depending upon the instrument characteristics, source properties (flux, spectral slope, elevation angle, *etc.*), and exposure time.

35.3. Large neutrino detectors

35.3.1. Deep liquid detectors for rare processes :

Revised August 2015 by K. Scholberg & C.W. Walter (Duke University)

Deep, large detectors for rare processes tend to be multi-purpose with physics reach that includes not only solar, reactor, supernova and atmospheric neutrinos, but also searches for baryon number violation, searches for exotic particles such as magnetic monopoles, and neutrino and cosmic-ray astrophysics in different energy regimes. The detectors may also serve as targets for long-baseline neutrino beams for neutrino oscillation physics studies. In general, detector design considerations can be divided into high- and low-energy regimes, for which background and event reconstruction issues differ. The high-energy regime, from about 100 MeV to a few hundred GeV, is relevant for proton decay searches,

atmospheric neutrinos and high-energy astrophysical neutrinos. The low-energy regime (a few tens of MeV or less) is relevant for supernova, solar, reactor and geological neutrinos.

Large water Cherenkov and scintillator detectors usually consist of a volume of transparent liquid viewed by photomultiplier tubes (PMTs). Because photosensors lining an inner surface represent a driving cost that scales as surface area, very large volumes can be used for comparatively reasonable cost. A common configuration is to have at least one concentric outer layer of liquid material separated from the inner part of the detector to serve as shielding against ambient background. If optically separated and instrumented with PMTs, an outer layer may also serve as an active veto against entering cosmic rays and other background events.

Because in most cases one is searching for rare events, large detectors are usually sited underground to reduce cosmic-ray-related background (see Chapter 29). The minimum depth required varies according to the physics goals [29].

35.3.1.1. *Liquid scintillator detectors:*

Past and current large underground detectors based on hydrocarbon scintillators include LVD, MACRO, Baksan, Borexino, KamLAND and SNO+. Experiments at nuclear reactors include CHOOZ, Double CHOOZ, Daya Bay, and RENO. Organic liquid scintillators for large detectors are chosen for high light yield and attenuation length, good stability, compatibility with other detector materials, high flash point, low toxicity, appropriate density for mechanical stability, and low cost.

Scintillation detectors have an advantage over water Cherenkov detectors in the lack of Cherenkov threshold and the high light yield. However, scintillation light emission is nearly isotropic, and therefore directional capabilities are relatively weak.

35.3.1.2. *Water Cherenkov detectors:*

Very large imaging water detectors reconstruct ten-meter-scale Cherenkov rings produced by charged particles (see Sec. 34.5.0). The first such large detectors were IMB and Kamiokande. The only currently existing instance of this class of detector is Super-Kamiokande (Super-K).

Cherenkov detectors are excellent electromagnetic calorimeters, and the number of Cherenkov photons produced by an e/γ is nearly proportional to its kinetic energy. The number of collected photoelectrons depends on the scattering and attenuation in the water along with the photocathode coverage, quantum efficiency and the optical parameters of any external light collection systems or protective material surrounding them. Event-by-event corrections are made for geometry and attenuation.

High-energy (~ 100 MeV or more) neutrinos from the atmosphere or beams interact with nucleons; for the nucleons bound inside the ^{16}O nucleus, nuclear effects must be considered both at the interaction and as the particles leave the nucleus. Various event topologies can be distinguished by their timing and fit patterns, and by presence or absence of light in a veto.

Low-energy neutrino interactions of solar neutrinos in water are predominantly elastic scattering off atomic electrons; single electron events are then reconstructed. At solar neutrino energies, the visible energy resolution ($\sim 30\%/\sqrt{\xi E_{\text{vis}}(\text{MeV})}$) is about 20% worse than photoelectron counting statistics would imply. At these energies, radioactive backgrounds become a dominant issue.

The Sudbury Neutrino Observatory (SNO) detector [35] is the only instance of a large heavy water detector and deserves mention here. In addition to an outer 1.7 kton of light water, SNO contained 1 kton of D_2O ,

giving it unique sensitivity to neutrino neutral current ($\nu_x + d \rightarrow \nu_x + p + n$), and charged current ($\nu_e + d \rightarrow p + p + e^-$) deuteron breakup reactions.

35.3.2. Coherent radio Cherenkov radiation detectors :

Revised August 2015 by S.R. Klein (LBNL/UC Berkeley)

Radio-frequency detectors are an attractive way to search for coherent Cherenkov radiation from showers produced from interactions of ultra-high energy cosmic neutrinos.

Electromagnetic and hadronic showers produce radio pulses via the Askaryan effect [51], as discussed in Sec. 33. The shower contains more electrons than positrons, leading to coherent emission.

High-frequency radiation is concentrated around the Cherenkov angle. The electric field strength increases linearly with frequency, up to a cut-off f_c , which is set by the transverse size of the shower [53]. Near f_c , radiation is narrowly concentrated around the Cherenkov angle. At very low frequencies, the distribution is nearly isotropic. The signal is linearly polarized in the plane perpendicular to the neutrino direction.

35.3.3. The Moon as a target :

Because of its large size and non-conducting regolith, and the availability of large radio-telescopes, the Moon is an attractive target [60]. Conventional radio-telescopes are reasonably well suited to lunar neutrino searches, with natural beam widths not too dissimilar from the size of the Moon. The big limitation of lunar experiments is that the 240,000 km target-antenna separation leads to neutrino energy thresholds above 10^{20} eV.

Experiments so far include Parkes, Glue, NuMoon, Lunaska, and Resun. No signals have been detected. In the near future, several large radio detector arrays should reach significantly lower limits. The LOFAR array is beginning to take data with 36 detector clusters spread over Northwest Europe. In the longer term, the Square Kilometer Array (SKA) with 1 km² effective area will push thresholds down to near 10^{20} eV.

35.3.4. Ice-based detectors :

Lower energy thresholds require a smaller antenna-target separation. Natural ice is an attractive medium for this, with attenuation lengths over 300 m.

Although the ice is mostly uniform, the top ≈ 100 m of Antarctic ice, the 'firn,' contains a gradual transition from packed snow at the surface (typical surface density 0.35 g/cm³) to solid ice (density 0.92 g/cm³) below [62]. The index of refraction depends linearly on the density, so radio waves curve downward in the firn. This bending reduces the effectiveness of surface or aerial antennas.

There are two types of Antarctic neutrino experiments. In one class, antennas mounted on scientific balloons observe the ice from above. The ANITA experiment is one example. It made two flights around Antarctica, floating at an altitude around 35 km [63]. Because of the significant source-detector separation, ANITA is most sensitive at energies above 10^{19} eV, above the peak of the GZK neutrino spectrum. By using the several-meter separation between antennas, they achieved a pointing accuracy of 0.2-0.4^o in elevation, and 0.5-1.1^o in azimuth. ANITA has set the most stringent limits on GZK neutrinos to date.

The proposed EVA experiment will use a portion of a fixed-shape balloon as a large parabolic radio antenna. Because of the large antenna surface, they hope to achieve threshold around 10^{17} eV.

Other ice based experiments use antennas located within the active volume, allowing them to reach thresholds around 10^{17} eV. This approach

was pioneered by the RICE experiment, which buried 18 half-wave dipole antennas in holes drilled for AMANDA [64] at the South Pole.

Three groups are prototyping detectors, with the goal of a detector with a $\sim 100 \text{ km}^3$ active volume. The Askaryan Radio Array (ARA) is located at the South Pole [65], while the Antarctic Ross Iceshelf Antenna Neutrino Array (ARIANNA) is on the Ross Ice Shelf [66]. The Greenland Neutrino Observatory (GNO) collaboration is proposing a detector near the U.S. Summit Station in Greenland [67].

35.4. Large time-projection chambers for rare event detection

Written Nov. 2015 by T. Shutt (SLAC).

Rare event searches require detectors that combine large target masses and low levels of radioactivity, and that are located deep underground to eliminate cosmic-ray related backgrounds. Past and present efforts include searches for the scattering of particle dark matter, neutrinoless double beta decay, and the measurement of solar neutrinos, while next generation experiments will also probe coherent scattering of solar, atmospheric and diffuse supernova background neutrinos. Large time project chambers (TPCs), adapted from particle collider experiments, have emerged as a leading technology for these efforts. Events are measured in a central region confined by a field cage and usually filled with a liquid noble element target. Ionized electrons are drifted (in the z direction) to an anode region by use of electrode grids and field shaping rings, where their magnitude and $x - y$ location is measured. In low background TPCs, scintillation generated at the initial event site is also measured, and the time difference between this prompt signal and the later-arriving charge signal gives the event location in z for a known electron drift speed. Thus, 3D imaging is achieved in a monolithic central volume. Noble elements have relatively high light yields (comparable to or exceeding the best inorganic scintillators), and the charge signal can be amplified by multiplication or electroluminescence. Radioactive backgrounds are distinguished by event imaging, the separate measurements of charge and light, and scintillation pulse shape. For recent reviews of noble element detectors, see [70,71].

Methods for achieving very low radioactive backgrounds are discussed in general in section 34.6. The basic architecture of large TPCs is very favorable for this application because gas or liquid targets can be relatively easily purified, while the generally more radioactive readout and support materials are confined to the periphery. The use of higher density targets (i.e., liquid instead of gas and/or higher mass elements) maximizes the ratio of target to surrounding material mass.

An important technical challenge in liquid detectors is achieving the high voltages needed for electron drift and measurement. At low energies (e.g., in a dark matter search) it is also important to suppress low-level emission of electrons and associated photons. Drift of electrons over meter scales with minimal loss from attachment on trace levels of dissolved impurities (e.g., O_2) has so far required continuous circulating purification. The relatively slow readout due to $\sim \text{msec/m}$ drift speeds is not a major pile-up concern in low background experiments.

35.4.1. Dark matter and other low energy signals :

A major goal of low background experiments is detection of WIMP (Weakly Interacting Massive Particle) dark matter through scattering on nuclei in a terrestrial detector. Energy transfers are generally small, a few tens of keV at most. Liquid noble TPCs distinguish nuclear recoils (NR) from dark matter from the usually dominant background of electron recoils

(ER) from gamma rays and beta decays by requiring single scatters and based on their charge to light ratio or scintillation pulse shape. Neutrons are a NR background, but can be recognized in a large imaging TPC if they multiply scatter. To detect small charge signals, a dual phase technique is used wherein electrons from interactions in the liquid target are drifted to the liquid surface and extracted with high field (~ 5 kV/cm) into the gas phase leading to an amplified electroluminescence signal measured by an array of PMTs.

LXe experiments have had the best WIMP sensitivity for most WIMP masses for the last decade. Two experiments to date have produced dark matter limits using dual phase Ar TPCs. A variety of TPC configurations are being pursued to accomplish directional dark matter detection, most with a CF_4 target.

35.4.2. $0\nu\beta\beta$ Decay :

Another major class of rare event search is neutrinoless double beta decay ($0\nu\beta\beta$). The first detector to observe the standard model process 2 neutrino double beta decay was a gaseous TPC which imaged the two electrons tracks from ^{82}Se embedded in a foil. EXO-200, which currently has one of the best search limits for $0\nu\beta\beta$ [79], is a large single-phase LXe TPC with roughly 110 active kg of Xe enriched to 80.7% ^{136}Xe , and a multi-ton successor nEXO has been proposed. These detectors are similar to dark matter TPCs, but, not needing charge gain, use single phase with charge measured directly on crossed wire grids. Light readout is done with LAAPDs (EXO-200) and SiPMs (nEXO).

The NEXT collaboration uses a high pressure gas phase Xe TPC with electroluminescent readout of the charge to achieve mm spatial resolution so that the two-electron topology of $0\nu\beta\beta$ events can be distinguished from single electrons from photoabsorption of background gammas. In addition, the low recombination fraction in the gas phase suppresses recombination fluctuations, in principle allowing σ below 0.2% via the charge channel alone.

35.5. Sub-Kelvin detectors

Written September 2015 by K. Irwin (Stanford and SLAC).

Many particle physics experiments utilize detectors operated at temperatures below 1 K. These include WIMP searches, beta-decay experiments to measure the absolute mass of the electron neutrino, and searches for neutrinoless-double-beta decay ($0\nu\beta\beta$) to probe the properties of Majorana neutrinos. Sub-Kelvin detectors also provide important cosmological constraints on particle physics through sensitive measurement of the cosmic microwave background (CMB). CMB measurements probe the physics of inflation at $\sim 10^{16}$ GeV, and the absolute mass, hierarchy, and number of neutrino species.

Detectors that operate below 1 K benefit from reduced thermal noise and lower material specific heat and thermal conductivity. At these temperatures, superconducting materials, sensors with high responsivity, and cryogenic preamplifiers and multiplexers are available.

Sub-Kelvin detectors can be categorized as equilibrium thermal detectors or non-equilibrium detectors. Equilibrium detectors measure a temperature rise in a material when energy is deposited. Non-equilibrium detectors are based on the measurement of prompt, non-equilibrated signals and on the excitation of materials with an energy gap.

35.5.1. *Equilibrium thermal detectors* :

An equilibrium thermal detector consists of a thermometer and absorber with combined heat capacity C coupled to a heat bath through a weak

thermal conductance G . The rise time of a thermal detector is limited by the internal equilibration time of the thermometer-absorber system and the electrical time constant of the thermometer. The thermal relaxation time over which heat escapes to the heat bath is $\tau = C/G$. Thermal detectors are often designed so that an energy input to the absorber is thermalized and equilibrated through the absorber and thermometer on timescales shorter than τ , making the operation particularly simple. An equilibrium thermal detector can be operated as either a calorimeter, which measures an incident energy deposition E , or as a bolometer, which measures an incident power P .

The most commonly used sub-Kelvin thermometer is the superconducting transition-edge sensor (TES). The current flowing through a TES is read out by a superconducting quantum interference device (SQUID) amplifier. Neutron-transmutation-doped (NTD) germanium and implanted silicon semiconductors read out by cryogenic FET amplifiers are also used as thermometers. Finally, the temperature dependence of the permeability of a paramagnetic material is used as a thermometer, referred to as metallic magnetic calorimeters (MMC).

35.5.2. Nonequilibrium Detectors :

Nonequilibrium detectors use many of the same principles and techniques as equilibrium detectors, but are also sensitive to details of the energy down-conversion before thermalization. Sub-Kelvin nonequilibrium detectors measure athermal phonon signals in a dielectric crystal, electron-hole pairs in a semiconductor crystal, athermal quasiparticle excitations in a superconductor, photon emission from a scintillator, or a combination of two of the above to better discriminate recoils from nuclei or electrons. Because the phonons are athermal, sub-Kelvin nonequilibrium detectors can use absorbers with larger heat capacity, and they use information about the details of energy down-conversion pathways in order to better discriminate signal from background.

35.6. Low-radioactivity background techniques

Revised August 2015 by A. Piepke (University of Alabama).

The physics reach of low-energy rare-event searches *e.g.* for dark matter, neutrino oscillations, or double beta decay is often limited by background caused by radioactivity. Depending on the chosen detector design, the separation of the physics signal from this unwanted interference can be achieved on an event-by-event basis by active event tagging, utilizing some unique event features, or by reducing the flux of the background radiation by appropriate shielding and material selection. In both cases, the background rate is proportional to the flux of the interfering radiation. Its reduction is thus essential for realizing the full physics potential of the experiment. In this context, “low energy” may be defined as the regime of natural, anthropogenic, or cosmogenic radioactivity, all at energies up to about 10 MeV. Following the classification of [86], sources of background may be categorized into the following classes:

1. environmental radioactivity,
2. radio-impurities in detector or shielding components,
3. radon and its progeny,
4. cosmic rays,
5. neutrons from natural fission, (α, n) reactions and from cosmic-ray muon spallation and capture.

Further discussion and all references may be found in the full *Review*.

36. RADIOACTIVITY AND RADIATION PROTECTION

Revised August 2013 by S. Roesler and M. Silari (CERN).

36.1. Definitions

The International Commission on Radiation Units and Measurements (ICRU) recommends the use of SI units. Therefore we list SI units first, followed by cgs (or other common) units in parentheses, where they differ.

- **Activity** (unit: Becquerel):

1 Bq = 1 disintegration per second (= 27 pCi).

- **Absorbed dose** (unit: gray): The absorbed dose is the energy imparted by ionizing radiation in a volume element of a specified material divided by the mass of this volume element.

1 Gy = 1 J/kg (= 10^4 erg/g = 100 rad)

= 6.24×10^{12} MeV/kg deposited energy.

- **Kerma** (unit: gray): Kerma is the sum of the initial kinetic energies of all charged particles liberated by indirectly ionizing particles in a volume element of the specified material divided by the mass of this volume element.

- **Exposure** (unit: C/kg of air [= 3880 Roentgen[†]]): The exposure is a measure of photon fluence at a certain point in space integrated over time, in terms of ion charge of either sign produced by secondary electrons in a small volume of air about the point. Implicit in the definition is the assumption that the small test volume is embedded in a sufficiently large uniformly irradiated volume that the number of secondary electrons entering the volume equals the number leaving (so-called charged particle equilibrium).

Table 36.1: Radiation weighting factors, w_R .

Radiation type	w_R
Photons	1
Electrons and muons	1
Neutrons, $E_n < 1$ MeV	$2.5 + 18.2 \times \exp[-(\ln E_n)^2/6]$
1 MeV $\leq E_n \leq 50$ MeV	$5.0 + 17.0 \times \exp[-(\ln(2E_n))^2/6]$
$E_n > 50$ MeV	$2.5 + 3.25 \times \exp[-(\ln(0.04E_n))^2/6]$
Protons and charged pions	2
Alpha particles, fission fragments, heavy ions	20

- **Equivalent dose** (unit: Sievert [= 100 rem (roentgen equivalent in man)]): The equivalent dose H_T in an organ or tissue T is equal to the sum of the absorbed doses $D_{T,R}$ in the organ or tissue caused by different radiation types R weighted with so-called radiation weighting factors w_R :

$$H_T = \sum_R w_R \times D_{T,R} . \quad (36.1)$$

[†] This unit is somewhat historical, but appears on some measuring instruments. One R is the amount of radiation required to liberate positive and negative charges of one electrostatic unit of charge in 1 cm³ of air at standard temperature and pressure (STP)

It expresses long-term risks (primarily cancer and leukemia) from low-level chronic exposure. The values for w_R recommended recently by ICRP [2] are given in Table 36.1.

• **Effective dose** (unit: Sievert): The sum of the equivalent doses, weighted by the tissue weighting factors w_T ($\sum_T w_T = 1$) of several organs and tissues T of the body that are considered to be most sensitive [2], is called “effective dose” E :

$$E = \sum_T w_T \times H_T . \quad (36.2)$$

36.2. Radiation levels [4]

• **Natural annual background**, all sources: Most world areas, whole-body equivalent dose rate $\approx (1.0\text{--}13)$ mSv (0.1–1.3 rem). Can range up to 50 mSv (5 rem) in certain areas. U.S. average ≈ 3.6 mSv, including ≈ 2 mSv (≈ 200 mrem) from inhaled natural radioactivity, mostly radon and radon daughters. (Average is for a typical house and varies by more than an order of magnitude. It can be more than two orders of magnitude higher in poorly ventilated mines. 0.1–0.2 mSv in open areas.)

• **Cosmic ray background** (sea level, mostly muons): $\sim 1 \text{ min}^{-1} \text{ cm}^{-2} \text{ sr}^{-1}$. For more accurate estimates and details, see the Cosmic Rays section (Sec. 29 of this *Review*).

• **Fluence** (per cm^2) to deposit one Gy, assuming uniform irradiation: \approx (**charged particles**) $6.24 \times 10^9 / (dE/dx)$, where dE/dx (MeV $\text{g}^{-1} \text{ cm}^2$), the energy loss per unit length, may be obtained from Figs. 33.2 and 33.4 in Sec. 33 of the *Review*, and pdg.lbl.gov/AtomicNuclearProperties.

$\approx 3.5 \times 10^9 \text{ cm}^{-2}$ minimum-ionizing singly-charged particles in carbon.

\approx (**photons**) $6.24 \times 10^9 / [Ef/\ell]$, for photons of energy E (MeV), attenuation length ℓ (g cm^{-2}), and fraction $f \lesssim 1$ expressing the fraction of the photon’s energy deposited in a small volume of thickness $\ll \ell$ but large enough to contain the secondary electrons.

$\approx 2 \times 10^{11}$ photons cm^{-2} for 1 MeV photons on carbon ($f \approx 1/2$).

36.3. Health effects of ionizing radiation

• **Recommended limits of effective dose to radiation workers (whole-body dose):***

EU/Switzerland: 20 mSv yr^{-1}

U.S.: 50 mSv yr^{-1} (5 rem yr^{-1})[†]

• **Lethal dose:** The whole-body dose from penetrating ionizing radiation resulting in 50% mortality in 30 days (assuming no medical treatment) is 2.5–4.5 Gy (250–450 rad), as measured internally on body longitudinal center line. Surface dose varies due to variable body attenuation and may be a strong function of energy.

• **Cancer induction by low LET radiation:** The cancer induction probability is about 5% per Sv on average for the entire population [2].

Footnotes:

* The ICRP recommendation [2] is 20 mSv yr^{-1} averaged over 5 years, with the dose in any one year ≤ 50 mSv.

† Many laboratories in the U.S. and elsewhere set lower limits.

37. COMMONLY USED RADIOACTIVE SOURCES

Table 37.1. Revised November 1993 by E. Browne (LBNL).

Nuclide	Half-life	Type of decay	Particle		Photon	
			Energy (MeV)	Emission prob.	Energy (MeV)	Emission prob.
$^{22}_{11}\text{Na}$	2.603 y	β^+ , EC	0.545	90%	0.511	Annih.
					1.275	100%
$^{54}_{25}\text{Mn}$	0.855 y	EC			0.835	100%
						Cr K x rays 26%
$^{55}_{26}\text{Fe}$	2.73 y	EC			Mn K x rays:	
					0.00590	24.4%
					0.00649	2.86%
$^{57}_{27}\text{Co}$	0.744 y	EC			0.014	9%
					0.122	86%
					0.136	11%
						Fe K x rays 58%
$^{60}_{27}\text{Co}$	5.271 y	β^-	0.316	100%	1.173	100%
					1.333	100%
$^{68}_{32}\text{Ge}$	0.742 y	EC			Ga K x rays 44%	
$\rightarrow ^{68}_{31}\text{Ga}$		β^+ , EC	1.899	90%	0.511	Annih.
					1.077	3%
$^{90}_{38}\text{Sr}$	28.5 y	β^-	0.546	100%		
$\rightarrow ^{90}_{39}\text{Y}$		β^-	2.283	100%		
$^{106}_{44}\text{Ru}$	1.020 y	β^-	0.039	100%		
$\rightarrow ^{106}_{45}\text{Rh}$		β^-	3.541	79%	0.512	21%
					0.622	10%
$^{109}_{48}\text{Cd}$	1.267 y	EC	0.063 e^-	41%	0.088	3.6%
			0.084 e^-	45%		Ag K x rays 100%
			0.087 e^-	9%		
$^{113}_{50}\text{Sn}$	0.315 y	EC	0.364 e^-	29%	0.392	65%
			0.388 e^-	6%		In K x rays 97%
$^{137}_{55}\text{Cs}$	30.2 y	β^-	0.514	94%	0.662	85%
			1.176	6%		

300 37. Commonly used radioactive sources

$^{133}_{56}\text{Ba}$	10.54 y	EC	0.045 e^-	50%	0.081	34%
			0.075 e^-	6%	0.356	62%
			Cs K x rays 121%			
$^{207}_{83}\text{Bi}$	31.8 y	EC	0.481 e^-	2%	0.569	98%
			0.975 e^-	7%	1.063	75%
			1.047 e^-	2%	1.770	7%
			Pb K x rays 78%			
$^{228}_{90}\text{Th}$	1.912 y	6 α :	5.341 to 8.785		0.239	44%
		3 β^- :	0.334 to 2.246		0.583	31%
($\rightarrow^{224}_{88}\text{Ra} \rightarrow ^{220}_{86}\text{Rn} \rightarrow ^{216}_{84}\text{Po} \rightarrow ^{212}_{82}\text{Pb} \rightarrow ^{212}_{83}\text{Bi} \rightarrow ^{212}_{84}\text{Po}$)						
$^{241}_{95}\text{Am}$	432.7 y	α	5.443	13%	0.060	36%
			5.486	85%	Np L x rays 38%	
$^{241}_{95}\text{Am/Be}$	432.2 y	6×10^{-5} neutrons (4–8 MeV) and 4×10^{-5} γ 's (4.43 MeV) per Am decay				
$^{244}_{96}\text{Cm}$	18.11 y	α	5.763	24%	Pu L x rays \sim 9%	
			5.805	76%		
$^{252}_{98}\text{Cf}$	2.645 y	α (97%)	6.076	15%		
			6.118	82%		
			Fission (3.1%)			
			≈ 20 γ 's/fission; 80% < 1 MeV			
			≈ 4 neutrons/fission; $\langle E_n \rangle = 2.14$ MeV			

“Emission probability” is the probability per decay of a given emission; because of cascades these may total more than 100%. Only principal emissions are listed. EC means electron capture, and e^- means monoenergetic internal conversion (Auger) electron. The intensity of 0.511 MeV e^+e^- annihilation photons depends upon the number of stopped positrons. Endpoint β^\pm energies are listed. In some cases when energies are closely spaced, the γ -ray values are approximate weighted averages. Radiation from short-lived daughter isotopes is included where relevant.

Half-lives, energies, and intensities are from E. Browne and R.B. Firestone, *Table of Radioactive Isotopes* (John Wiley & Sons, New York, 1986), recent *Nuclear Data Sheets*, and *X-ray and Gamma-ray Standards for Detector Calibration*, IAEA-TECDOC-619 (1991).

Neutron data are from *Neutron Sources for Basic Physics and Applications* (Pergamon Press, 1983).

38. PROBABILITY

Revised September 2015 by G. Cowan (RHUL).

The following is a much-shortened version of Sec. 38 of the full *Review*. Equation, section, and figure numbers follow the *Review*.

38.2. Random variables

- *Probability density function* (p.d.f.): x is a *random variable*.

Continuous: $f(x; \theta) dx$ = probability x is between x to $x + dx$, given parameter(s) θ ;

Discrete: $f(x; \theta)$ = probability of x given θ .

- *Cumulative distribution function*:

$$F(a) = \int_{-\infty}^a f(x) dx . \quad (38.6)$$

Here and below, if x is discrete-valued, the integral is replaced by a sum. The endpoint a is included in the integral or sum.

- *Expectation values*: Given a function u :

$$E[u(x)] = \int_{-\infty}^{\infty} u(x) f(x) dx . \quad (38.7)$$

- *Moments*:

$$n\text{th moment of a random variable: } \alpha_n = E[x^n] , \quad (38.8a)$$

$$n\text{th central moment: } m_n = E[(x - \alpha_1)^n] . \quad (38.8b)$$

$$\text{Mean: } \mu \equiv \alpha_1 . \quad (38.9a)$$

$$\text{Variance: } \sigma^2 \equiv V[x] \equiv m_2 = \alpha_2 - \mu^2 . \quad (38.9b)$$

$$\text{Coefficient of skewness: } \gamma_1 \equiv m_3/\sigma^3 .$$

$$\text{Kurtosis: } \gamma_2 = m_4/\sigma^4 - 3 .$$

$$\text{Median: } F(x_{\text{med}}) = 1/2 .$$

- *Marginal* p.d.f.: Let x, y be two random variables with joint p.d.f. $f(x, y)$.

$$f_1(x) = \int_{-\infty}^{\infty} f(x, y) dy ; \quad f_2(y) = \int_{-\infty}^{\infty} f(x, y) dx . \quad (38.10)$$

- *Conditional* p.d.f.:

$$f_4(x|y) = f(x, y)/f_2(y) ; \quad f_3(y|x) = f(x, y)/f_1(x) .$$

- *Bayes' theorem*:

$$f_4(x|y) = \frac{f_3(y|x)f_1(x)}{f_2(y)} = \frac{f_3(y|x)f_1(x)}{\int f_3(y|x')f_1(x') dx'} . \quad (38.11)$$

- *Correlation coefficient and covariance*:

$$\mu_x = \int_{-\infty}^{\infty} \int_{-\infty}^{\infty} x f(x, y) dx dy , \quad (38.12)$$

$$\rho_{xy} = E [(x - \mu_x)(y - \mu_y)] / \sigma_x \sigma_y \equiv \text{cov}[x, y] / \sigma_x \sigma_y ,$$

$$\sigma_x = \int_{-\infty}^{\infty} \int_{-\infty}^{\infty} (x - \mu_x)^2 f(x, y) dx dy . \text{ Note } \rho_{xy}^2 \leq 1.$$

• *Independence:* x, y are independent if and only if $f(x, y) = f_1(x) \cdot f_2(y)$; then $\rho_{xy} = 0$, $E[u(x) v(y)] = E[u(x)] E[v(y)]$ and $V[x + y] = V[x] + V[y]$.

• *Change of variables:* From $\mathbf{x} = (x_1, \dots, x_n)$ to $\mathbf{y} = (y_1, \dots, y_n)$: $g(\mathbf{y}) = f(\mathbf{x}(\mathbf{y})) \cdot |J|$ where $|J|$ is the absolute value of the determinant of the Jacobian $J_{ij} = \partial x_i / \partial y_j$. For discrete variables, use $|J| = 1$.

38.3. Characteristic functions

Given a pdf $f(x)$ for a continuous random variable x , the characteristic function $\phi(u)$ is given by (31.6). Its derivatives are related to the algebraic moments of x by (31.7).

$$\phi(u) = E \left[e^{iux} \right] = \int_{-\infty}^{\infty} e^{iux} f(x) dx . \tag{38.17}$$

$$i^{-n} \left. \frac{d^n \phi}{du^n} \right|_{u=0} = \int_{-\infty}^{\infty} x^n f(x) dx = \alpha_n . \tag{38.18}$$

If the p.d.f.s $f_1(x)$ and $f_2(y)$ for independent random variables x and y have characteristic functions $\phi_1(u)$ and $\phi_2(u)$, then the characteristic function of the weighted sum $ax + by$ is $\phi_1(au)\phi_2(bu)$. The additional rules for several important distributions (*e.g.*, that the sum of two Gaussian distributed variables also follows a Gaussian distribution) easily follow from this observation.

38.4. Some probability distributions

See Table 38.1.

38.4.2. Poisson distribution :

The Poisson distribution $f(n; \nu)$ gives the probability of finding exactly n events in a given interval of x (*e.g.*, space or time) when the events occur independently of one another and of x at an average rate of ν per the given interval. The variance σ^2 equals ν . It is the limiting case $p \rightarrow 0$, $N \rightarrow \infty$, $Np = \nu$ of the binomial distribution. The Poisson distribution approaches the Gaussian distribution for large ν .

38.4.3. Normal or Gaussian distribution :

Its cumulative distribution, for mean 0 and variance 1, is often tabulated as the *error function*

$$F(x; 0, 1) = \frac{1}{2} \left[1 + \operatorname{erf}(x/\sqrt{2}) \right] . \tag{38.24}$$

For mean μ and variance σ^2 , replace x by $(x - \mu)/\sigma$.

$$P(x \text{ in range } \mu \pm \sigma) = 0.6827,$$

$$P(x \text{ in range } \mu \pm 0.6745\sigma) = 0.5,$$

$$E[|x - \mu|] = \sqrt{2/\pi}\sigma = 0.7979\sigma,$$

$$\text{half-width at half maximum} = \sqrt{2 \ln 2} \cdot \sigma = 1.177\sigma.$$

Table 38.1. Some common probability density functions, with corresponding characteristic functions and means and variances. In the Table, $\Gamma(k)$ is the gamma function, equal to $(k - 1)!$ when k is an integer.

Distribution	Probability density function f (variable; parameters)	Characteristic function $\phi(u)$	Mean	Variance σ^2
Uniform	$f(x; a, b) = \begin{cases} 1/(b - a) & a \leq x \leq b \\ 0 & \text{otherwise} \end{cases}$	$\frac{e^{ibu} - e^{iau}}{(b - a)iu}$	$\frac{a + b}{2}$	$\frac{(b - a)^2}{12}$
Binomial	$f(r; N, p) = \frac{N!}{r!(N - r)!} p^r q^{N-r}$ $r = 0, 1, 2, \dots, N; \quad 0 \leq p \leq 1; \quad q = 1 - p$	$(q + pe^{iu})^N$	Np	Npq
Poisson	$f(n; \nu) = \frac{\nu^n e^{-\nu}}{n!}; \quad n = 0, 1, 2, \dots; \quad \nu > 0$	$\exp[\nu(e^{iu} - 1)]$	ν	ν
Normal (Gaussian)	$f(x; \mu, \sigma^2) = \frac{1}{\sigma\sqrt{2\pi}} \exp(-(x - \mu)^2/2\sigma^2)$ $-\infty < x < \infty; \quad -\infty < \mu < \infty; \quad \sigma > 0$	$\exp(i\mu u - \frac{1}{2}\sigma^2 u^2)$	μ	σ^2
Multivariate Gaussian	$f(\mathbf{x}; \boldsymbol{\mu}, V) = \frac{1}{(2\pi)^{n/2} \sqrt{ V }}$ $\times \exp[-\frac{1}{2}(\mathbf{x} - \boldsymbol{\mu})^T V^{-1}(\mathbf{x} - \boldsymbol{\mu})]$ $-\infty < x_j < \infty; \quad -\infty < \mu_j < \infty; \quad V > 0$	$\exp[i\boldsymbol{\mu} \cdot \mathbf{u} - \frac{1}{2}\mathbf{u}^T V \mathbf{u}]$	$\boldsymbol{\mu}$	V_{jk}
χ^2	$f(z; n) = \frac{z^{n/2-1} e^{-z/2}}{2^{n/2} \Gamma(n/2)}; \quad z \geq 0$	$(1 - 2iu)^{-n/2}$	n	$2n$
Student's t	$f(t; n) = \frac{1}{\sqrt{n\pi}} \frac{\Gamma[(n+1)/2]}{\Gamma(n/2)} \left(1 + \frac{t^2}{n}\right)^{-(n+1)/2}$ $-\infty < t < \infty; \quad n \text{ not required to be integer}$	—	0 for $n > 1$	$n/(n - 2)$ for $n > 2$
Gamma	$f(x; \lambda, k) = \frac{x^{k-1} \lambda^k e^{-\lambda x}}{\Gamma(k)}; \quad 0 \leq x < \infty; \quad k \text{ not required to be integer}$	$(1 - iu/\lambda)^{-k}$	k/λ	k/λ^2

For n Gaussian random variables \mathbf{x}_i , the joint p.d.f. is the multivariate Gaussian:

$$f(\mathbf{x}; \boldsymbol{\mu}, V) = \frac{1}{(2\pi)^{n/2} \sqrt{|V|}} \exp \left[-\frac{1}{2}(\mathbf{x} - \boldsymbol{\mu})^T V^{-1}(\mathbf{x} - \boldsymbol{\mu}) \right], \quad |V| > 0. \quad (38.25)$$

V is the $n \times n$ covariance matrix; $V_{ij} \equiv E[(x_i - \mu_i)(x_j - \mu_j)] \equiv \rho_{ij} \sigma_i \sigma_j$, and $V_{ii} = V[x_i]$; $|V|$ is the determinant of V . For $n = 2$, $f(\mathbf{x}; \boldsymbol{\mu}, V)$ is

$$f(x_1, x_2; \mu_1, \mu_2, \sigma_1, \sigma_2, \rho) = \frac{1}{2\pi\sigma_1\sigma_2\sqrt{1-\rho^2}} \times \exp \left\{ \frac{-1}{2(1-\rho^2)} \left[\frac{(x_1 - \mu_1)^2}{\sigma_1^2} - \frac{2\rho(x_1 - \mu_1)(x_2 - \mu_2)}{\sigma_1\sigma_2} + \frac{(x_2 - \mu_2)^2}{\sigma_2^2} \right] \right\}. \quad (38.26)$$

The marginal distribution of any x_i is a Gaussian with mean μ_i and variance V_{ii} . V is $n \times n$, symmetric, and positive definite. Therefore for any vector \mathbf{X} , the quadratic form $\mathbf{X}^T V^{-1} \mathbf{X} = C$, where C is any positive number, traces an n -dimensional ellipsoid as \mathbf{X} varies. If $X_i = x_i - \mu_i$, then C is a random variable obeying the χ^2 distribution with n degrees of freedom, discussed in the following section. The probability that \mathbf{X} corresponding to a set of Gaussian random variables x_i lies outside the ellipsoid characterized by a given value of C ($= \chi^2$) is given by $1 - F_{\chi^2}(C; n)$, where F_{χ^2} is the cumulative χ^2 distribution. This may be read from Fig. 39.1. For example, the “ s -standard-deviation ellipsoid” occurs at $C = s^2$. For the two-variable case ($n = 2$), the point \mathbf{X} lies outside the one-standard-deviation ellipsoid with 61% probability. The use of these ellipsoids as indicators of probable error is described in Sec. 39.4.2.2; the validity of those indicators assumes that $\boldsymbol{\mu}$ and V are correct.

38.4.5. χ^2 distribution :

If x_1, \dots, x_n are independent Gaussian random variables, the sum $z = \sum_{i=1}^n (x_i - \mu_i)^2 / \sigma_i^2$ follows the χ^2 p.d.f. with n degrees of freedom, which we denote by $\chi^2(n)$. More generally, for n correlated Gaussian variables as components of a vector \mathbf{X} with covariance matrix V , $z = \mathbf{X}^T V^{-1} \mathbf{X}$ follows $\chi^2(n)$ as in the previous section. For a set of z_i , each of which follows $\chi^2(n_i)$, $\sum z_i$ follows $\chi^2(\sum n_i)$. For large n , the χ^2 p.d.f. approaches a Gaussian with mean $\mu = n$ and variance $\sigma^2 = 2n$.

The χ^2 p.d.f. is often used in evaluating the level of compatibility between observed data and a hypothesis for the p.d.f. that the data might follow. This is discussed further in Sec. 39.3.2 on tests of goodness-of-fit.

38.4.7. Gamma distribution :

For a process that generates events as a function of x (e.g., space or time) according to a Poisson distribution, the distance in x from an arbitrary starting point (which may be some particular event) to the k^{th} event follows a gamma distribution, $f(x; \lambda, k)$. The Poisson parameter μ is λ per unit x . The special case $k = 1$ (i.e., $f(x; \lambda, 1) = \lambda e^{-\lambda x}$) is called the exponential distribution. A sum of k' exponential random variables x_i is distributed as $f(\sum x_i; \lambda, k')$.

The parameter k is not required to be an integer. For $\lambda = 1/2$ and $k = n/2$, the gamma distribution reduces to the $\chi^2(n)$ distribution.

See the full *Review* for further discussion and all references.

39. STATISTICS

Revised September 2015 by G. Cowan (RHUL).

There are two main approaches to statistical inference, which we may call frequentist and Bayesian. In frequentist statistics, probability is interpreted as the frequency of the outcome of a repeatable experiment. The most important tools in this framework are parameter estimation, covered in Section 39.2, statistical tests, discussed in Section 39.3, and confidence intervals, which are constructed so as to cover the true value of a parameter with a specified probability, as described in Section 39.4.2. Note that in frequentist statistics one does not define a probability for a hypothesis or for the value of a parameter.

In Bayesian statistics, the interpretation of probability is more general and includes *degree of belief* (called subjective probability). One can then speak of a probability density function (p.d.f.) for a parameter, which expresses one's state of knowledge about where its true value lies. Using Bayes' theorem (Eq. (38.4)), the prior degree of belief is updated by the data from the experiment. Bayesian methods for interval estimation are discussed in Sections 39.4.1 and 39.4.2.4.

Following common usage in physics, the word "error" is often used in this chapter to mean "uncertainty." More specifically it can indicate the size of an interval as in "the standard error" or "error propagation," where the term refers to the standard deviation of an estimator.

39.2. Parameter estimation

Here we review *point estimation* of parameters. An *estimator* $\hat{\theta}$ (written with a hat) is a function of the data used to estimate the value of the parameter θ .

39.2.1. Estimators for mean, variance, and median :

Suppose we have a set of n independent measurements, x_1, \dots, x_n , each assumed to follow a p.d.f. with unknown mean μ and unknown variance σ^2 (the measurements do not necessarily have to follow a Gaussian distribution). Then

$$\hat{\mu} = \frac{1}{n} \sum_{i=1}^n x_i \quad (39.5)$$

$$\hat{\sigma}^2 = \frac{1}{n-1} \sum_{i=1}^n (x_i - \hat{\mu})^2 \quad (39.6)$$

are unbiased estimators of μ and σ^2 . The variance of $\hat{\mu}$ is σ^2/n and the variance of $\hat{\sigma}^2$ is

$$V[\hat{\sigma}^2] = \frac{1}{n} \left(m_4 - \frac{n-3}{n-1} \sigma^4 \right), \quad (39.7)$$

where m_4 is the 4th central moment of x (see Eq. (38.8b)). For Gaussian distributed x_i , this becomes $2\sigma^4/(n-1)$ for any $n \geq 2$, and for large n the standard deviation of $\hat{\sigma}$ (the "error of the error") is $\sigma/\sqrt{2n}$. For any n and Gaussian x_i , $\hat{\mu}$ is an efficient estimator for μ , and the estimators $\hat{\mu}$ and $\hat{\sigma}^2$ are uncorrelated. Otherwise the arithmetic mean (39.5) is not necessarily the most efficient estimator.

If the x_i have different, known variances σ_i^2 , then the weighted average

$$\hat{\mu} = \frac{1}{w} \sum_{i=1}^n w_i x_i, \quad (39.8)$$

where $w_i = 1/\sigma_i^2$ and $w = \sum_i w_i$, is an unbiased estimator for μ with a smaller variance than an unweighted average. The standard deviation of $\hat{\mu}$ is $1/\sqrt{w}$.

39.2.2. The method of maximum likelihood :

Suppose we have a set of measured quantities \mathbf{x} and the likelihood $L(\boldsymbol{\theta}) = P(\mathbf{x}|\boldsymbol{\theta})$ for a set of parameters $\boldsymbol{\theta} = (\theta_1, \dots, \theta_N)$. The *maximum likelihood* (ML) estimators for $\boldsymbol{\theta}$ are defined as the values that give the maximum of L . Because of the properties of the logarithm, it is usually easier to work with $\ln L$, and since both are maximized for the same parameter values $\boldsymbol{\theta}$, the ML estimators can be found by solving the *likelihood equations*,

$$\frac{\partial \ln L}{\partial \theta_i} = 0, \quad i = 1, \dots, N. \tag{39.9}$$

In evaluating the likelihood function, it is important that any normalization factors in the p.d.f. that involve $\boldsymbol{\theta}$ be included.

The inverse V^{-1} of the covariance matrix $V_{ij} = \text{cov}[\hat{\theta}_i, \hat{\theta}_j]$ for a set of ML estimators can be estimated by using

$$(\hat{V}^{-1})_{ij} = - \left. \frac{\partial^2 \ln L}{\partial \theta_i \partial \theta_j} \right|_{\hat{\boldsymbol{\theta}}}; \tag{39.12}$$

for finite samples, however, Eq. (39.12) can result in a misestimate of the variances. In the large sample limit (or in a linear model with Gaussian errors), L has a Gaussian form and $\ln L$ is (hyper)parabolic. In this case, it can be seen that a numerically equivalent way of determining s -standard-deviation errors is from the hypersurface defined by the $\boldsymbol{\theta}$ such that

$$\ln L(\boldsymbol{\theta}) = \ln L_{\max} - s^2/2, \tag{39.13}$$

where $\ln L_{\max}$ is the value of $\ln L$ at the solution point (compare with Eq. (39.68)). The minimum and maximum values of θ_i on the hypersurface then give an approximate s -standard deviation confidence interval for θ_i (see Section 39.4.2.2).

39.2.3. The method of least squares :

The *method of least squares* (LS) coincides with the method of maximum likelihood in the following special case. Consider a set of N independent measurements y_i at known points x_i . The measurement y_i is assumed to be Gaussian distributed with mean $\mu(x_i; \boldsymbol{\theta})$ and known variance σ_i^2 . The goal is to construct estimators for the unknown parameters $\boldsymbol{\theta}$. The log-likelihood function contains the sum of squares

$$\chi^2(\boldsymbol{\theta}) = -2 \ln L(\boldsymbol{\theta}) + \text{constant} = \sum_{i=1}^N \frac{(y_i - \mu(x_i; \boldsymbol{\theta}))^2}{\sigma_i^2}. \tag{39.19}$$

The parameter values that maximize L are the same as those which minimize χ^2 .

The minimum of the chi-square function in Equation (39.19) defines the least-squares estimators $\hat{\boldsymbol{\theta}}$ for the more general case where the y_i are not Gaussian distributed as long as they are independent. If they are not independent but rather have a covariance matrix $V_{ij} = \text{cov}[y_i, y_j]$, then the LS estimators are determined by the minimum of

$$\chi^2(\boldsymbol{\theta}) = (\mathbf{y} - \boldsymbol{\mu}(\boldsymbol{\theta}))^T V^{-1} (\mathbf{y} - \boldsymbol{\mu}(\boldsymbol{\theta})), \tag{39.20}$$

where $\mathbf{y} = (y_1, \dots, y_N)$ is the (column) vector of measurements, $\boldsymbol{\mu}(\boldsymbol{\theta})$ is the corresponding vector of predicted values, and the superscript T denotes the transpose. If the y_i are not Gaussian distributed, then the LS and ML estimators will not in general coincide.

Often one further restricts the problem to the case where $\mu(x_i; \boldsymbol{\theta})$ is a linear function of the parameters, *i.e.*,

$$\mu(x_i; \boldsymbol{\theta}) = \sum_{j=1}^m \theta_j h_j(x_i). \quad (39.21)$$

Here the $h_j(x)$ are m linearly independent functions, *e.g.*, $1, x, x^2, \dots, x^{m-1}$ or Legendre polynomials. We require $m < N$ and at least m of the x_i must be distinct.

Minimizing χ^2 in this case with m parameters reduces to solving a system of m linear equations. Defining $H_{ij} = h_j(x_i)$ and minimizing χ^2 by setting its derivatives with respect to the θ_i equal to zero gives the LS estimators,

$$\hat{\boldsymbol{\theta}} = (H^T V^{-1} H)^{-1} H^T V^{-1} \mathbf{y} \equiv D \mathbf{y}. \quad (39.22)$$

The covariance matrix for the estimators $U_{ij} = \text{cov}[\hat{\theta}_i, \hat{\theta}_j]$ is given by

$$U = D V D^T = (H^T V^{-1} H)^{-1}. \quad (39.23)$$

Expanding $\chi^2(\boldsymbol{\theta})$ about $\hat{\boldsymbol{\theta}}$, one finds that the contour in parameter space defined by

$$\chi^2(\boldsymbol{\theta}) = \chi^2(\hat{\boldsymbol{\theta}}) + 1 = \chi_{\min}^2 + 1 \quad (39.29)$$

has tangent planes located at approximately plus-or-minus-one standard deviation $\sigma_{\hat{\boldsymbol{\theta}}}$ from the LS estimates $\hat{\boldsymbol{\theta}}$.

As the minimum value of the χ^2 represents the level of agreement between the measurements and the fitted function, it can be used for assessing the goodness-of-fit; this is discussed further in Section 39.3.2.

39.2.5. Propagation of errors :

Consider a set of n quantities $\boldsymbol{\theta} = (\theta_1, \dots, \theta_n)$ and a set of m functions $\boldsymbol{\eta}(\boldsymbol{\theta}) = (\eta_1(\boldsymbol{\theta}), \dots, \eta_m(\boldsymbol{\theta}))$. Suppose we have estimated $\hat{\boldsymbol{\theta}} = (\hat{\theta}_1, \dots, \hat{\theta}_n)$, using, say, maximum-likelihood or least-squares, and we also know or have estimated the covariance matrix $V_{ij} = \text{cov}[\theta_i, \theta_j]$. The goal of *error propagation* is to determine the covariance matrix for the functions, $U_{ij} = \text{cov}[\hat{\eta}_i, \hat{\eta}_j]$, where $\hat{\boldsymbol{\eta}} = \boldsymbol{\eta}(\hat{\boldsymbol{\theta}})$. In particular, the diagonal elements $U_{ii} = V[\hat{\eta}_i]$ give the variances. The new covariance matrix can be found by expanding the functions $\boldsymbol{\eta}(\boldsymbol{\theta})$ about the estimates $\hat{\boldsymbol{\theta}}$ to first order in a Taylor series. Using this one finds

$$U_{ij} \approx \sum_{k,l} \frac{\partial \eta_i}{\partial \theta_k} \frac{\partial \eta_j}{\partial \theta_l} \Big|_{\hat{\boldsymbol{\theta}}} V_{kl}. \quad (39.37)$$

This can be written in matrix notation as $U \approx A V A^T$ where the matrix of derivatives A is

$$A_{ij} = \frac{\partial \eta_i}{\partial \theta_j} \Big|_{\hat{\boldsymbol{\theta}}}, \quad (39.38)$$

and A^T is its transpose. The approximation is exact if $\boldsymbol{\eta}(\boldsymbol{\theta})$ is linear.

39.3. Statistical tests

39.3.1. Hypothesis tests :

A frequentist *test* of a hypothesis (often called the null hypothesis, H_0) is a rule that states for which data values \mathbf{x} the hypothesis is rejected. A region of \mathbf{x} -space called the critical region, w , is specified such that there is no more than a given probability under H_0 , α , called the *size* or *significance level* of the test, to find $\mathbf{x} \in w$. If the data are discrete, it may not be possible to find a critical region with exact probability content α ,

and thus we require $P(\mathbf{x} \in w|H_0) \leq \alpha$. If the data are observed in the critical region, H_0 is rejected.

The critical region is not unique. Its choice should take into account the probabilities for the data predicted by some alternative hypothesis (or set of alternatives) H_1 . Rejecting H_0 if it is true is called a *type-I error*, and occurs by construction with probability no greater than α . Not rejecting H_0 if an alternative H_1 is true is called a *type-II error*, and for a given test this will have a certain probability $\beta = P(\mathbf{x} \notin w|H_1)$. The quantity $1 - \beta$ is called the *power* of the test of H_0 with respect to the alternative H_1 . A strategy for defining the critical region can therefore be to maximize the power with respect to some alternative (or alternatives) given a fixed size α .

To maximize the power of a test of H_0 with respect to the alternative H_1 , the *Neyman–Pearson lemma* states that the critical region w should be chosen such that for all data values \mathbf{x} inside w , the ratio

$$\lambda(\mathbf{x}) = \frac{f(\mathbf{x}|H_1)}{f(\mathbf{x}|H_0)}, \quad (39.39)$$

is greater than a given constant, the value of which is determined by the size of the test α . Here H_0 and H_1 must be simple hypotheses, i.e., they should not contain undetermined parameters.

The lemma is equivalent to the statement that (39.39) represents the optimal test statistic where the critical region is defined by a single cut on λ . This test will lead to the maximum power for a given probability α to reject H_0 if H_0 is in fact true. It can be difficult in practice, however, to determine $\lambda(\mathbf{x})$, since this requires knowledge of the joint p.d.f.s $f(\mathbf{x}|H_0)$ and $f(\mathbf{x}|H_1)$. Often one does not have explicit formulae for these, but rather Monte Carlo models that allow one to generate instances of \mathbf{x} (events) that follow the p.d.f.s.

39.3.2. Tests of significance (goodness-of-fit) :

Often one wants to quantify the level of agreement between the data and a hypothesis without explicit reference to alternative hypotheses. This can be done by defining a statistic t that is a function of the data whose value reflects in some way the level of agreement between the data and the hypothesis.

The hypothesis in question, H_0 , will determine the p.d.f. $f(t|H_0)$ for the statistic. The significance of a discrepancy between the data and what one expects under the assumption of H_0 is quantified by giving the p -value, defined as the probability to find t in the region of equal or lesser compatibility with H_0 than the level of compatibility observed with the actual data. For example, if t is defined such that large values correspond to poor agreement with the hypothesis, then the p -value would be

$$p = \int_{t_{\text{obs}}}^{\infty} f(t|H_0) dt, \quad (39.40)$$

where t_{obs} is the value of the statistic obtained in the actual experiment.

The p -value should not be confused with the size (significance level) of a test, or the confidence level of a confidence interval (Section 39.4), both of which are pre-specified constants. We may formulate a hypothesis test, however, by defining the critical region to correspond to the data outcomes that give the lowest p -values, so that finding $p \leq \alpha$ implies that the data outcome was in the critical region. When constructing a p -value, one generally chooses the region of data space deemed to have lower compatibility with the model being tested as one having higher compatibility with a given alternative, such that the corresponding test

will have a high power with respect to this alternative.

The p -value is a function of the data, and is therefore itself a random variable. If the hypothesis used to compute the p -value is true, then for continuous data p will be uniformly distributed between zero and one. Note that the p -value is not the probability for the hypothesis; in frequentist statistics, this is not defined.

39.3.2.3. Goodness-of-fit with the method of Least Squares:

When estimating parameters using the method of least squares, one obtains the minimum value of the quantity χ^2 (39.19). This statistic can be used to test the *goodness-of-fit*, *i.e.*, the test provides a measure of the significance of a discrepancy between the data and the hypothesized functional form used in the fit. It may also happen that no parameters are estimated from the data, but that one simply wants to compare a histogram, *e.g.*, a vector of Poisson distributed numbers $\mathbf{n} = (n_1, \dots, n_N)$, with a hypothesis for their expectation values $\mu_i = E[n_i]$. As the distribution is Poisson with variances $\sigma_i^2 = \mu_i$, the χ^2 (39.19) becomes *Pearson's χ^2 statistic*,

$$\chi^2 = \sum_{i=1}^N \frac{(n_i - \mu_i)^2}{\mu_i}. \quad (39.48)$$

If the hypothesis $\boldsymbol{\mu} = (\mu_1, \dots, \mu_N)$ is correct, and if the expected values μ_i in (39.48) are sufficiently large (or equivalently, if the measurements n_i can be treated as following a Gaussian distribution), then the χ^2 statistic will follow the χ^2 p.d.f. with the number of degrees of freedom equal to the number of measurements N minus the number of fitted parameters.

Assuming the goodness-of-fit statistic follows a χ^2 p.d.f., the p -value for the hypothesis is then

$$p = \int_{\chi^2}^{\infty} f(z; n_d) dz, \quad (39.49)$$

where $f(z; n_d)$ is the χ^2 p.d.f. and n_d is the appropriate number of degrees of freedom. Values are shown in Fig. 39.1 or obtained from the ROOT function `TMath::Prob`.

Since the mean of the χ^2 distribution is equal to n_d , one expects in a "reasonable" experiment to obtain $\chi^2 \approx n_d$. Hence the quantity χ^2/n_d is sometimes reported. Since the p.d.f. of χ^2/n_d depends on n_d , however, one must report n_d as well if one wishes to determine the p -value. The p -values obtained for different values of χ^2/n_d are shown in Fig. 39.2.

39.3.3. Bayes factors :

In Bayesian statistics, all of one's knowledge about a model is contained in its posterior probability, which one obtains using Bayes' theorem. Thus one could reject a hypothesis H if its posterior probability $P(H|\mathbf{x})$ is sufficiently small. The difficulty here is that $P(H|\mathbf{x})$ is proportional to the prior probability $P(H)$, and there will not be a consensus about the prior probabilities for the existence of new phenomena. Nevertheless one can construct a quantity called the Bayes factor (described below), which can be used to quantify the degree to which the data prefer one hypothesis over another, and is independent of their prior probabilities.

Consider two models (hypotheses), H_i and H_j , described by vectors of parameters $\boldsymbol{\theta}_i$ and $\boldsymbol{\theta}_j$, respectively. Some of the components will be common to both models and others may be distinct. The full prior probability for each model can be written in the form

$$\pi(H_i, \boldsymbol{\theta}_i) = P(H_i)\pi(\boldsymbol{\theta}_i|H_i). \quad (39.50)$$

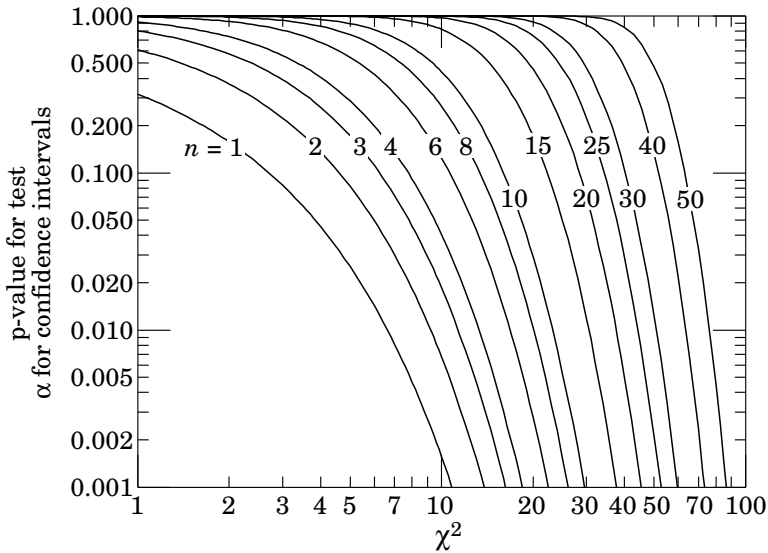


Figure 39.1: One minus the χ^2 cumulative distribution, $1 - F(\chi^2; n)$, for n degrees of freedom. This gives the p -value for the χ^2 goodness-of-fit test as well as one minus the coverage probability for confidence regions (see Sec. 39.4.2.2).

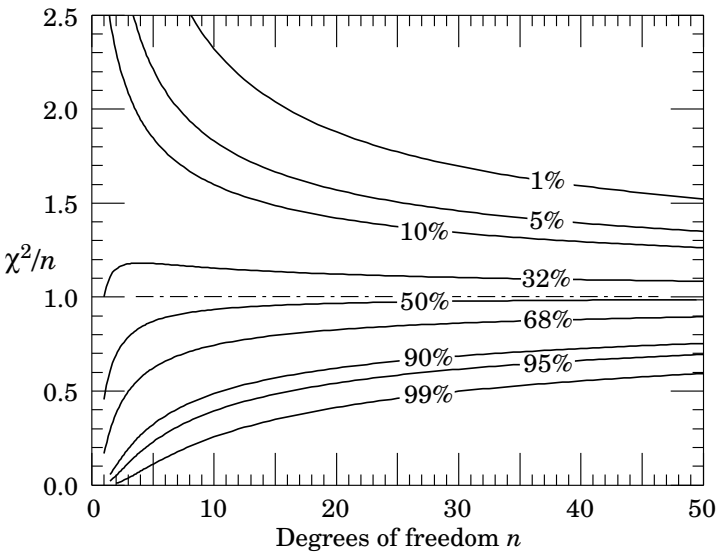


Figure 39.2: The ‘reduced’ χ^2 , equal to χ^2/n , for n degrees of freedom. The curves show as a function of n the χ^2/n that corresponds to a given p -value.

Here $P(H_i)$ is the overall prior probability for H_i , and $\pi(\boldsymbol{\theta}_i|H_i)$ is the normalized p.d.f. of its parameters. For each model, the posterior probability is found using Bayes' theorem,

$$P(H_i|\mathbf{x}) = \frac{\int P(\mathbf{x}|\boldsymbol{\theta}_i, H_i)P(H_i)\pi(\boldsymbol{\theta}_i|H_i) d\boldsymbol{\theta}_i}{P(\mathbf{x})}, \quad (39.51)$$

where the integration is carried out over the internal parameters $\boldsymbol{\theta}_i$ of the model. The ratio of posterior probabilities for the models is therefore

$$\frac{P(H_i|\mathbf{x})}{P(H_j|\mathbf{x})} = \frac{\int P(\mathbf{x}|\boldsymbol{\theta}_i, H_i)\pi(\boldsymbol{\theta}_i|H_i) d\boldsymbol{\theta}_i}{\int P(\mathbf{x}|\boldsymbol{\theta}_j, H_j)\pi(\boldsymbol{\theta}_j|H_j) d\boldsymbol{\theta}_j} \frac{P(H_i)}{P(H_j)}. \quad (39.52)$$

The *Bayes factor* is defined as

$$B_{ij} = \frac{\int P(\mathbf{x}|\boldsymbol{\theta}_i, H_i)\pi(\boldsymbol{\theta}_i|H_i) d\boldsymbol{\theta}_i}{\int P(\mathbf{x}|\boldsymbol{\theta}_j, H_j)\pi(\boldsymbol{\theta}_j|H_j) d\boldsymbol{\theta}_j}. \quad (39.53)$$

This gives what the ratio of posterior probabilities for models i and j would be if the overall prior probabilities for the two models were equal. If the models have no nuisance parameters, *i.e.*, no internal parameters described by priors, then the Bayes factor is simply the likelihood ratio. The Bayes factor therefore shows by how much the probability ratio of model i to model j changes in the light of the data, and thus can be viewed as a numerical measure of evidence supplied by the data in favour of one hypothesis over the other.

Although the Bayes factor is by construction independent of the overall prior probabilities $P(H_i)$ and $P(H_j)$, it does require priors for all internal parameters of a model, *i.e.*, one needs the functions $\pi(\boldsymbol{\theta}_i|H_i)$ and $\pi(\boldsymbol{\theta}_j|H_j)$. In a Bayesian analysis where one is only interested in the posterior p.d.f. of a parameter, it may be acceptable to take an unnormalizable function for the prior (an improper prior) as long as the product of likelihood and prior can be normalized. But improper priors are only defined up to an arbitrary multiplicative constant, and so the Bayes factor would depend on this constant. Furthermore, although the range of a constant normalized prior is unimportant for parameter determination (provided it is wider than the likelihood), this is not so for the Bayes factor when such a prior is used for only one of the hypotheses. So to compute a Bayes factor, all internal parameters must be described by normalized priors that represent meaningful probabilities over the entire range where they are defined.

39.4. Intervals and limits

When the goal of an experiment is to determine a parameter θ , the result is usually expressed by quoting, in addition to the point estimate, some sort of interval which reflects the statistical precision of the measurement. In the simplest case, this can be given by the parameter's estimated value $\hat{\theta}$ plus or minus an estimate of the standard deviation of $\hat{\theta}$, $\hat{\sigma}_{\hat{\theta}}$. If, however, the p.d.f. of the estimator is not Gaussian or if there are physical boundaries on the possible values of the parameter, then one usually quotes instead an interval according to one of the procedures described below.

39.4.1. Bayesian intervals :

A Bayesian posterior probability may be used to determine regions that will have a given probability of containing the true value of a parameter. In the single parameter case, for example, an interval (called a Bayesian or credible interval) $[\theta_{\text{lo}}, \theta_{\text{up}}]$ can be determined which contains a given fraction $1 - \alpha$ of the posterior probability, *i.e.*,

$$1 - \alpha = \int_{\theta_{\text{lo}}}^{\theta_{\text{up}}} p(\theta|\mathbf{x}) d\theta. \quad (39.55)$$

Sometimes an upper or lower limit is desired, *i.e.*, θ_{lo} or θ_{up} can be set to a physical boundary or to plus or minus infinity. In other cases, one might be interested in the set of θ values for which $p(\theta|\mathbf{x})$ is higher than for any θ not belonging to the set, which may constitute a single interval or a set of disjoint regions; these are called highest posterior density (HPD) intervals. Note that HPD intervals are not invariant under a nonlinear transformation of the parameter.

If a parameter is constrained to be non-negative, then the prior p.d.f. can simply be set to zero for negative values. An important example is the case of a Poisson variable n , which counts signal events with unknown mean s , as well as background with mean b , assumed known. For the signal mean s , one often uses the prior

$$\pi(s) = \begin{cases} 0 & s < 0 \\ 1 & s \geq 0 \end{cases} . \tag{39.56}$$

For example, to obtain an upper limit on s , one may proceed as follows. The likelihood for s is given by the Poisson distribution for n with mean $s + b$,

$$P(n|s) = \frac{(s + b)^n}{n!} e^{-(s+b)} , \tag{39.57}$$

along with the prior (Eq. 39.56) in Bayes' theorem gives the posterior density for s . An upper limit s_{up} at confidence level (or here, rather, credibility level) $1 - \alpha$ can be obtained by requiring

$$1 - \alpha = \int_{-\infty}^{s_{up}} p(s|n) ds = \frac{\int_{-\infty}^{s_{up}} P(n|s) \pi(s) ds}{\int_{-\infty}^{\infty} P(n|s) \pi(s) ds} , \tag{39.58}$$

where the lower limit of integration is effectively zero because of the cut-off in $\pi(s)$. By relating the integrals in Eq. (39.58) to incomplete gamma functions, the solution for the upper limit is found to be

$$s_{up} = \frac{1}{2} F_{\chi^2}^{-1} [p, 2(n + 1)] - b , \tag{39.59}$$

where $F_{\chi^2}^{-1}$ is the quantile of the χ^2 distribution (inverse of the cumulative distribution). Here the quantity p is

$$p = 1 - \alpha \left(1 - F_{\chi^2} [2b, 2(n + 1)] \right) , \tag{39.60}$$

where F_{χ^2} is the cumulative χ^2 distribution. For both F_{χ^2} and $F_{\chi^2}^{-1}$ above, the argument $2(n + 1)$ gives the number of degrees of freedom. For the special case of $b = 0$, the limit reduces to

$$s_{up} = \frac{1}{2} F_{\chi^2}^{-1} (1 - \alpha; 2(n + 1)) . \tag{39.61}$$

It happens that for the case of $b = 0$, the upper limit from Eq. (39.61) coincides numerically with the frequentist upper limit discussed in Section 39.4.2.3. Values for $1 - \alpha = 0.9$ and 0.95 are given by the values μ_{up} in Table 39.3.

39.4.2. Frequentist confidence intervals :

39.4.2.1. The Neyman construction for confidence intervals:

Consider a p.d.f. $f(x; \theta)$ where x represents the outcome of the experiment and θ is the unknown parameter for which we want to construct a confidence interval. The variable x could (and often does) represent an estimator for θ . Using $f(x; \theta)$, we can find for a pre-specified probability $1 - \alpha$, and for every value of θ , a set of values $x_1(\theta, \alpha)$ and $x_2(\theta, \alpha)$ such that

$$P(x_1 < x < x_2; \theta) = \int_{x_1}^{x_2} f(x; \theta) dx \geq 1 - \alpha . \tag{39.62}$$

If x is discrete, the integral is replaced by the corresponding sum. In that case there may not exist a range of x values whose summed probability is exactly equal to a given value of $1 - \alpha$, and one requires by convention $P(x_1 < x < x_2; \theta) \geq 1 - \alpha$.

This is illustrated for continuous x in Fig. 39.3: a horizontal line segment $[x_1(\theta, \alpha), x_2(\theta, \alpha)]$ is drawn for representative values of θ . The union of such intervals for all values of θ , designated in the figure as $D(\alpha)$, is known as the *confidence belt*. Typically the curves $x_1(\theta, \alpha)$ and $x_2(\theta, \alpha)$ are monotonic functions of θ , which we assume for this discussion.

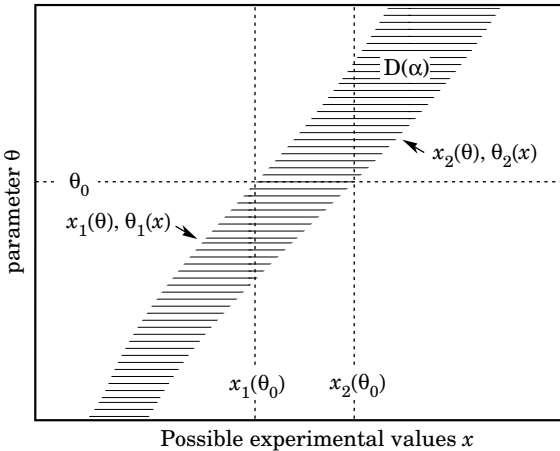


Figure 39.3: Construction of the confidence belt (see text).

Upon performing an experiment to measure x and obtaining a value x_0 , one draws a vertical line through x_0 . The confidence interval for θ is the set of all values of θ for which the corresponding line segment $[x_1(\theta, \alpha), x_2(\theta, \alpha)]$ is intercepted by this vertical line. Such confidence intervals are said to have a *confidence level* (CL) equal to $1 - \alpha$.

Now suppose that the true value of θ is θ_0 , indicated in the figure. We see from the figure that θ_0 lies between $\theta_1(x)$ and $\theta_2(x)$ if and only if x lies between $x_1(\theta_0)$ and $x_2(\theta_0)$. The two events thus have the same probability, and since this is true for any value θ_0 , we can drop the subscript 0 and obtain

$$1 - \alpha = P(x_1(\theta) < x < x_2(\theta)) = P(\theta_2(x) < \theta < \theta_1(x)). \quad (39.63)$$

In this probability statement, $\theta_1(x)$ and $\theta_2(x)$, *i.e.*, the endpoints of the interval, are the random variables and θ is an unknown constant. If the experiment were to be repeated a large number of times, the interval $[\theta_1, \theta_2]$ would vary, covering the fixed value θ in a fraction $1 - \alpha$ of the experiments.

The condition of coverage in Eq. (39.62) does not determine x_1 and x_2 uniquely, and additional criteria are needed. One possibility is to choose *central intervals* such that the probabilities to find x below x_1 and above x_2 are each $\alpha/2$. In other cases, one may want to report only an upper or lower limit, in which case one of $P(x \leq x_1)$ or $P(x \geq x_2)$ can be set to α and the other to zero.

When the observed random variable x is continuous, the coverage probability obtained with the Neyman construction is $1 - \alpha$, regardless of the true value of the parameter. Because of the requirement $P(x_1 < x < x_2) \geq 1 - \alpha$ when x is discrete, one obtains in that case confidence intervals that include the true parameter with a probability greater than or equal to $1 - \alpha$.

39.4.2.2. Gaussian distributed measurements:

An important example of constructing a confidence interval is when the data consists of a single random variable x that follows a Gaussian distribution; this is often the case when x represents an estimator for a parameter and one has a sufficiently large data sample. If there is more than one parameter being estimated, the multivariate Gaussian is used. For the univariate case with known σ , the probability that the measured value x will fall within $\pm\delta$ of the true value μ is

$$1 - \alpha = \frac{1}{\sqrt{2\pi}\sigma} \int_{\mu-\delta}^{\mu+\delta} e^{-(x-\mu)^2/2\sigma^2} dx = \text{erf}\left(\frac{\delta}{\sqrt{2}\sigma}\right) = 2\Phi\left(\frac{\delta}{\sigma}\right) - 1, \tag{39.65}$$

where erf is the Gaussian error function, which is rewritten in the final equality using Φ , the Gaussian cumulative distribution. Fig. 39.4 shows a $\delta = 1.64\sigma$ confidence interval unshaded. The choice $\delta = \sigma$ gives an interval called the *standard error* which has $1 - \alpha = 68.27\%$ if σ is known. Values of α for other frequently used choices of δ are given in Table 39.1.

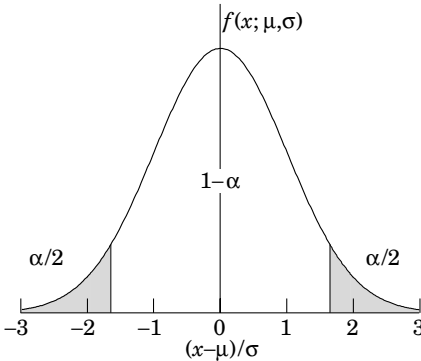


Figure 39.4: Illustration of a symmetric 90% confidence interval (unshaded) for a measurement of a single quantity with Gaussian errors. Integrated probabilities, defined by $\alpha = 0.1$, are as shown.

We can set a one-sided (upper or lower) limit by excluding above $x + \delta$ (or below $x - \delta$). The values of α for such limits are half the values in Table 39.1.

The relation (39.65) can be re-expressed using the cumulative distribution function for the χ^2 distribution as

$$\alpha = 1 - F(\chi^2; n), \tag{39.66}$$

for $\chi^2 = (\delta/\sigma)^2$ and $n = 1$ degree of freedom. This can be seen as the $n = 1$ curve in Fig. 39.1 or obtained by using the ROOT function `TMath::Prob`.

For multivariate measurements of, say, n parameter estimates $\hat{\theta} = (\hat{\theta}_1, \dots, \hat{\theta}_n)$, one requires the full covariance matrix $V_{ij} = \text{cov}[\hat{\theta}_i, \hat{\theta}_j]$,

Table 39.1: Area of the tails α outside $\pm\delta$ from the mean of a Gaussian distribution.

α	δ	α	δ
0.3173	1σ	0.2	1.28σ
4.55×10^{-2}	2σ	0.1	1.64σ
2.7×10^{-3}	3σ	0.05	1.96σ
6.3×10^{-5}	4σ	0.01	2.58σ
5.7×10^{-7}	5σ	0.001	3.29σ
2.0×10^{-9}	6σ	10^{-4}	3.89σ

which can be estimated as described in Sections 39.2.2 and 39.2.3. Under fairly general conditions with the methods of maximum-likelihood or least-squares in the large sample limit, the estimators will be distributed according to a multivariate Gaussian centered about the true (unknown) values θ , and furthermore, the likelihood function itself takes on a Gaussian shape.

The standard error ellipse for the pair $(\hat{\theta}_i, \hat{\theta}_j)$ is shown in Fig. 39.5, corresponding to a contour $\chi^2 = \chi^2_{\min} + 1$ or $\ln L = \ln L_{\max} - 1/2$. The ellipse is centered about the estimated values $\hat{\theta}$, and the tangents to the ellipse give the standard deviations of the estimators, σ_i and σ_j . The angle of the major axis of the ellipse is given by

$$\tan 2\phi = \frac{2\rho_{ij}\sigma_i\sigma_j}{\sigma_j^2 - \sigma_i^2}, \tag{39.67}$$

where $\rho_{ij} = \text{cov}[\hat{\theta}_i, \hat{\theta}_j]/\sigma_i\sigma_j$ is the correlation coefficient.

The correlation coefficient can be visualized as the fraction of the distance σ_i from the ellipse's horizontal center-line at which the ellipse becomes tangent to vertical, *i.e.*, at the distance $\rho_{ij}\sigma_i$ below the center-line as shown. As ρ_{ij} goes to $+1$ or -1 , the ellipse thins to a diagonal line.

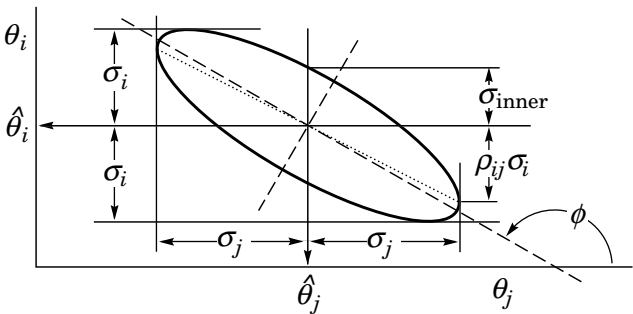


Figure 39.5: Standard error ellipse for the estimators $\hat{\theta}_i$ and $\hat{\theta}_j$. In the case shown the correlation is negative.

As in the single-variable case, because of the symmetry of the Gaussian function between θ and $\hat{\theta}$, one finds that contours of constant $\ln L$ or χ^2 cover the true values with a certain, fixed probability. That is, the

Table 39.2: Values of $\Delta\chi^2$ or $2\Delta \ln L$ corresponding to a coverage probability $1 - \alpha$ in the large data sample limit, for joint estimation of m parameters.

$(1 - \alpha)$ (%)	$m = 1$	$m = 2$	$m = 3$
68.27	1.00	2.30	3.53
90.	2.71	4.61	6.25
95.	3.84	5.99	7.82
95.45	4.00	6.18	8.03
99.	6.63	9.21	11.34
99.73	9.00	11.83	14.16

confidence region is determined by

$$\ln L(\boldsymbol{\theta}) \geq \ln L_{\max} - \Delta \ln L, \quad (39.68)$$

or where a χ^2 has been defined for use with the method of least-squares,

$$\chi^2(\boldsymbol{\theta}) \leq \chi_{\min}^2 + \Delta\chi^2. \quad (39.69)$$

Values of $\Delta\chi^2$ or $2\Delta \ln L$ are given in Table 39.2 for several values of the coverage probability $1 - \alpha$ and number of fitted parameters m . For Gaussian distributed data, these are related by $\Delta\chi^2 = 2\Delta \ln L = F_{\chi_m^2}^{-1}(1 - \alpha)$, where $F_{\chi_m^2}^{-1}$ is the chi-square quantile (inverse of the cumulative distribution) for m degrees of freedom.

For finite non-Gaussian data samples, these are not exact confidence regions according to our previous definition.

39.4.2.3. Poisson or binomial data:

Another important class of measurements consists of counting a certain number of events, n . In this section, we will assume these are all events of the desired type, *i.e.*, there is no background. If n represents the number of events produced in a reaction with cross section σ , say, in a fixed integrated luminosity \mathcal{L} , then it follows a Poisson distribution with mean $\mu = \sigma\mathcal{L}$. If, on the other hand, one has selected a larger sample of N events and found n of them to have a particular property, then n follows a binomial distribution where the parameter p gives the probability for the event to possess the property in question. This is appropriate, *e.g.*, for estimates of branching ratios or selection efficiencies based on a given total number of events.

For the case of Poisson distributed n , limits on the mean value μ can be found from the Neyman procedure as discussed in Section 39.4.2.1 with n used directly as the statistic x . The upper and lower limits are found to be

$$\mu_{\text{lo}} = \frac{1}{2}F_{\chi^2}^{-1}(\alpha_{\text{lo}}; 2n), \quad (39.71a)$$

$$\mu_{\text{up}} = \frac{1}{2}F_{\chi^2}^{-1}(1 - \alpha_{\text{up}}; 2(n + 1)), \quad (39.71b)$$

where confidence levels of $1 - \alpha_{\text{lo}}$ and $1 - \alpha_{\text{up}}$, refer separately to the corresponding intervals $\mu \geq \mu_{\text{lo}}$ and $\mu \leq \mu_{\text{up}}$, and $F_{\chi^2}^{-1}$ is the quantile of the χ^2 distribution (inverse of the cumulative distribution). The quantiles $F_{\chi^2}^{-1}$ can be obtained from standard tables or from the ROOT routine `TMath::ChisquareQuantile`. For central confidence intervals at confidence level $1 - \alpha$, set $\alpha_{\text{lo}} = \alpha_{\text{up}} = \alpha/2$.

Table 39.3: Lower and upper (one-sided) limits for the mean μ of a Poisson variable given n observed events in the absence of background, for confidence levels of 90% and 95%.

n	$1 - \alpha = 90\%$		$1 - \alpha = 95\%$	
	μ_{lo}	μ_{up}	μ_{lo}	μ_{up}
0	–	2.30	–	3.00
1	0.105	3.89	0.051	4.74
2	0.532	5.32	0.355	6.30
3	1.10	6.68	0.818	7.75
4	1.74	7.99	1.37	9.15
5	2.43	9.27	1.97	10.51
6	3.15	10.53	2.61	11.84
7	3.89	11.77	3.29	13.15
8	4.66	12.99	3.98	14.43
9	5.43	14.21	4.70	15.71
10	6.22	15.41	5.43	16.96

It happens that the upper limit from Eq. (39.71b) coincides numerically with the Bayesian upper limit for a Poisson parameter, using a uniform prior p.d.f. for μ . Values for confidence levels of 90% and 95% are shown in Table 39.3. For the case of binomially distributed n successes out of N trials with probability of success p , the upper and lower limits on p are found to be

$$p_{\text{lo}} = \frac{nF_F^{-1}[\alpha_{\text{lo}}; 2n, 2(N - n + 1)]}{N - n + 1 + nF_F^{-1}[\alpha_{\text{lo}}; 2n, 2(N - n + 1)]}, \quad (39.72a)$$

$$p_{\text{up}} = \frac{(n + 1)F_F^{-1}[1 - \alpha_{\text{up}}; 2(n + 1), 2(N - n)]}{(N - n) + (n + 1)F_F^{-1}[1 - \alpha_{\text{up}}; 2(n + 1), 2(N - n)]}. \quad (39.72b)$$

Here F_F^{-1} is the quantile of the F distribution (also called the Fisher–Snedecor distribution; see Ref. 4).

A number of issues arise in the construction and interpretation of confidence intervals when the parameter can only take on values in a restricted range. Important examples are where the mean of a Gaussian variable is constrained on physical grounds to be non-negative and where the experiment finds a Poisson-distributed number of events, n , which includes both signal and background. Application of some standard recipes can lead to intervals that are partially or entirely in the unphysical region. Furthermore, if the decision whether to report a one- or two-sided interval is based on the data, then the resulting intervals will not in general cover the parameter with the stated probability $1 - \alpha$.

Several problems with such intervals are overcome by using the unified approach of Feldman and Cousins [35]. Properties of these intervals are described further in the *Review*. Table 39.4 gives the unified confidence intervals $[\mu_1, \mu_2]$ for the mean of a Poisson variable given n observed events in the absence of background, for confidence levels of 90% and 95%. The values of $1 - \alpha$ given here refer to the coverage of the true parameter

by the whole interval $[\mu_1, \mu_2]$. In Table 39.3 for the one-sided upper and lower limits, however, $1 - \alpha$ referred to the probability to have individually $\mu_{\text{up}} \geq \mu$ or $\mu_{\text{lo}} \leq \mu$.

Table 39.4: Unified confidence intervals $[\mu_1, \mu_2]$ for a the mean of a Poisson variable given n observed events in the absence of background, for confidence levels of 90% and 95%.

n	$1 - \alpha = 90\%$		$1 - \alpha = 95\%$	
	μ_1	μ_2	μ_1	μ_2
0	0.00	2.44	0.00	3.09
1	0.11	4.36	0.05	5.14
2	0.53	5.91	0.36	6.72
3	1.10	7.42	0.82	8.25
4	1.47	8.60	1.37	9.76
5	1.84	9.99	1.84	11.26
6	2.21	11.47	2.21	12.75
7	3.56	12.53	2.58	13.81
8	3.96	13.99	2.94	15.29
9	4.36	15.30	4.36	16.77
10	5.50	16.50	4.75	17.82

Another possibility is to construct a Bayesian interval as described in Section 39.4.1. The presence of the boundary can be incorporated simply by setting the prior density to zero in the unphysical region. Advantages and pitfalls of this approach are discussed further in the *Review*.

Another alternative is presented by the intervals found from the likelihood function or χ^2 using the prescription of Equations (39.68) or (39.69). As in the case of the Bayesian intervals, the coverage probability is not, in general, independent of the true parameter. Furthermore, these intervals can for some parameter values undercover.

In any case it is important to report sufficient information so that the result can be combined with other measurements. Often this means giving an unbiased estimator and its standard deviation, even if the estimated value is in the unphysical region. It is also useful to report the likelihood function or an appropriate summary of it. Although this by itself is not sufficient to construct a frequentist confidence interval, it can be used to find the Bayesian posterior probability density for any desired prior p.d.f.

Further discussion and all references may be found in the full *Review of Particle Physics*; the equation and reference numbering corresponds to that version.

$$d_{m',m}^j = (-1)^{m-m'} d_{-m,-m'}^j = d_{-m,-m'}^j \quad d_{m,0}^\ell = \sqrt{\frac{4\pi}{2\ell+1}} Y_\ell^m e^{-im\phi} \quad 3/2 \times 3/2 \quad \begin{matrix} 3 \\ +3 \\ 2 \\ +2 \end{matrix} \quad d_{0,0}^1 = \cos \theta \quad d_{1/2,1/2}^{1/2} = \cos \frac{\theta}{2} \quad d_{1,1}^1 = \frac{1 + \cos \theta}{2}$$

$$2 \times 3/2 \quad \begin{matrix} 7/2 & 5/2 \\ +7/2 \\ 1 \end{matrix} \quad \begin{matrix} 7/2 & 5/2 \\ +5/2 + 5/2 \end{matrix} \quad \begin{matrix} 3 & 2 \\ +3/2 + 1/2 & 1/2 & 1/2 \\ +1/2 + 3/2 & 1/2 & -1/2 \end{matrix} \quad \begin{matrix} 3 & 2 & 1 \\ +1 & +1 & +1 \end{matrix} \quad d_{1/2,-1/2}^{1/2} = -\sin \frac{\theta}{2} \quad d_{1,0}^1 = -\frac{\sin \theta}{\sqrt{2}} \quad d_{1,-1}^1 = \frac{1 - \cos \theta}{2}$$

$$\begin{matrix} +2+1/2 & 3/7 & 4/7 & 7/2 & 5/2 & 3/2 \\ +1+3/2 & 4/7-3/7 & +3/2 & +3/2 & +3/2 \end{matrix} \quad \begin{matrix} +3/2-1/2 & 1/5 & 1/2 & 3/10 \\ +1/2+1/2 & 3/5 & 0 & -2/5 \\ -1/2+3/2 & 1/5 & -1/2 & 3/10 \end{matrix} \quad \begin{matrix} 3 & 2 & 1 & 0 \\ 0 & 0 & 0 & 0 \end{matrix}$$

$$2 \times 2 \quad \begin{matrix} 4 \\ +2+2 \\ 1 \end{matrix} \quad \begin{matrix} 4 & 3 \\ +3 & +3 \end{matrix} \quad \begin{matrix} 7/2 & 5/2 & 3/2 & 1/2 \\ +1/2 & +1/2 & +1/2 & +1/2 \end{matrix} \quad \begin{matrix} +3/2 & -3/2 & 1/20 & 1/4 & 9/20 & 1/4 \\ +1/2 & -1/2 & 9/20 & 1/4 & -1/20 & -1/4 \\ -1/2 & +1/2 & 9/20 & -1/4 & -1/20 & 1/4 \\ -3/2 & +3/2 & 1/20 & -1/4 & 9/20 & -1/4 \end{matrix} \quad \begin{matrix} 3 & 2 & 1 \\ -1 & -1 & -1 \end{matrix}$$

$$\begin{matrix} +2+1 & 1/2 & 1/2 & 4 & 3 & 2 \\ +1+2 & 1/2-1/2 & +2 & +2 & +2 \end{matrix} \quad \begin{matrix} +2-3/2 & 1/35 & 6/35 & 2/5 & 2/5 \\ +1-1/2 & 12/35 & 5/14 & 0 & -3/10 \\ 0+1/2 & 18/35 & -3/35 & -1/5 & 1/5 \\ -1+3/2 & 4/35 & -2/70 & 2/5 & -1/10 \end{matrix} \quad \begin{matrix} 7/2 & 5/2 & 3/2 & 1/2 \\ -1/2 & -1/2 & -1/2 & -1/2 \end{matrix} \quad \begin{matrix} +1/2-3/2 & 1/5 & 1/2 & 3/10 \\ -1/2-1/2 & 3/5 & 0 & -2/5 \\ -3/2+1/2 & 1/5 & -1/2 & 3/10 \end{matrix} \quad \begin{matrix} 3 & 2 \\ -2 & -2 \end{matrix}$$

$$\begin{matrix} +2 & 0 & 3/14 & 1/2 & 2/7 \\ +1 & +1 & 4/7 & 0 & -3/7 \\ 0 & +2 & 3/14-1/2 & 2/7 \end{matrix} \quad \begin{matrix} 4 & 3 & 2 & 1 \\ +1 & +1 & +1 & +1 \end{matrix} \quad \begin{matrix} +1-3/2 & 4/35 & 27/70 & 2/5 & 1/10 \\ 0 & -1/2 & 18/35 & 3/35 & -1/5 \\ -1 & +1/2 & 12/35 & -5/14 & 0 \\ -2 & +3/2 & 1/35 & -6/35 & 2/5 & -2/5 \end{matrix} \quad \begin{matrix} 7/2 & 5/2 & 3/2 & 1/2 \\ -3/2 & -3/2 & -3/2 \end{matrix} \quad \begin{matrix} -1/2 & -3/2 & 1/2 & 1/2 & 3 \\ -3/2 & -1/2 & 1/2 & -1/2 & -3 \\ -3/2 & -3/2 & 1 \end{matrix}$$

$$\begin{matrix} +2 & -1 & 1/14 & 3/10 & 3/7 & 1/5 \\ +1 & 0 & 3/7 & 1/5 & -1/14 & -3/10 \\ 0 & +1 & 3/7 & -1/5 & -1/14 & 3/10 \\ -1 & +2 & 1/14-3/10 & 3/7 & -1/5 \end{matrix} \quad \begin{matrix} 4 & 3 & 2 & 1 & 0 \\ 0 & 0 & 0 & 0 & 0 \end{matrix} \quad \begin{matrix} 0 & -3/2 & 2/7 & 18/35 & 1/5 \\ -1 & -1/2 & 4/7 & -1/35 & -2/5 \\ -2 & +1/2 & 1/7-16/35 & 2/5 \end{matrix} \quad \begin{matrix} 7/2 & 5/2 \\ -5/2 & -5/2 \end{matrix}$$

$$d_{3/2,3/2}^{3/2} = \frac{1 + \cos \theta}{2} \cos \frac{\theta}{2} \quad d_{3/2,1/2}^{3/2} = -\sqrt{3} \frac{1 + \cos \theta}{2} \sin \frac{\theta}{2} \quad d_{3/2,-1/2}^{3/2} = \sqrt{3} \frac{1 - \cos \theta}{2} \cos \frac{\theta}{2} \quad d_{3/2,-3/2}^{3/2} = -\frac{1 - \cos \theta}{2} \sin \frac{\theta}{2}$$

$$d_{1/2,1/2}^{3/2} = \frac{3 \cos \theta - 1}{2} \cos \frac{\theta}{2} \quad d_{1/2,-1/2}^{3/2} = -\frac{3 \cos \theta + 1}{2} \sin \frac{\theta}{2} \quad d_{2,2}^2 = \left(\frac{1 + \cos \theta}{2}\right)^2 \quad d_{2,1}^2 = -\frac{1 + \cos \theta}{2} \sin \theta$$

$$d_{2,0}^2 = \frac{\sqrt{6}}{4} \sin^2 \theta \quad d_{2,-1}^2 = -\frac{1 - \cos \theta}{2} \sin \theta \quad d_{2,-2}^2 = \left(\frac{1 - \cos \theta}{2}\right)^2 \quad d_{1,1}^2 = \frac{1 + \cos \theta}{2} (2 \cos \theta - 1)$$

$$d_{1,0}^2 = -\sqrt{\frac{3}{2}} \sin \theta \cos \theta \quad d_{1,-1}^2 = \frac{1 - \cos \theta}{2} (2 \cos \theta + 1) \quad d_{0,0}^2 = \left(\frac{3}{2} \cos^2 \theta - \frac{1}{2}\right)$$

47. KINEMATICS

Revised January 2000 by J.D. Jackson (LBNL) and September 2016 by D.R. Tovey (Sheffield).

Throughout this section units are used in which $\hbar = c = 1$. The following conversions are useful: $\hbar c = 197.3$ MeV fm, $(\hbar c)^2 = 0.3894$ (GeV)² mb.

47.1. Lorentz transformations

The energy E and 3-momentum \mathbf{p} of a particle of mass m form a 4-vector $p = (E, \mathbf{p})$ whose square $p^2 \equiv E^2 - |\mathbf{p}|^2 = m^2$. The velocity of the particle is $\boldsymbol{\beta} = \mathbf{p}/E$. The energy and momentum (E^*, \mathbf{p}^*) viewed from a frame moving with velocity $\boldsymbol{\beta}_f$ are given by

$$\begin{pmatrix} E^* \\ p_{\parallel}^* \end{pmatrix} = \begin{pmatrix} \gamma_f & -\gamma_f \beta_f \\ -\gamma_f \beta_f & \gamma_f \end{pmatrix} \begin{pmatrix} E \\ p_{\parallel} \end{pmatrix}, \quad p_T^* = p_T, \quad (47.1)$$

where $\gamma_f = (1 - \beta_f^2)^{-1/2}$ and p_T (p_{\parallel}) are the components of \mathbf{p} perpendicular (parallel) to $\boldsymbol{\beta}_f$. Other 4-vectors, such as the space-time coordinates of events, of course transform in the same way. The scalar product of two 4-momenta $p_1 \cdot p_2 = E_1 E_2 - \mathbf{p}_1 \cdot \mathbf{p}_2$ is invariant (frame independent).

47.2. Center-of-mass energy and momentum

In the collision of two particles of masses m_1 and m_2 the total center-of-mass energy can be expressed in the Lorentz-invariant form

$$\begin{aligned} E_{\text{cm}} &= \left[(E_1 + E_2)^2 - (\mathbf{p}_1 + \mathbf{p}_2)^2 \right]^{1/2}, \\ &= \left[m_1^2 + m_2^2 + 2E_1 E_2 (1 - \beta_1 \beta_2 \cos \theta) \right]^{1/2}, \end{aligned} \quad (47.2)$$

where θ is the angle between the particles. In the frame where one particle (of mass m_2) is at rest (lab frame),

$$E_{\text{cm}} = (m_1^2 + m_2^2 + 2E_{1\text{lab}} m_2)^{1/2}. \quad (47.3)$$

The velocity of the center-of-mass in the lab frame is

$$\boldsymbol{\beta}_{\text{cm}} = \mathbf{p}_{\text{lab}} / (E_{1\text{lab}} + m_2), \quad (47.4)$$

where $\mathbf{p}_{\text{lab}} \equiv \mathbf{p}_{1\text{lab}}$ and

$$\gamma_{\text{cm}} = (E_{1\text{lab}} + m_2) / E_{\text{cm}}. \quad (47.5)$$

The c.m. momenta of particles 1 and 2 are of magnitude

$$p_{\text{cm}} = p_{\text{lab}} \frac{m_2}{E_{\text{cm}}}. \quad (47.6)$$

For example, if a 0.80 GeV/ c kaon beam is incident on a proton target, the center of mass energy is 1.699 GeV and the center of mass momentum of either particle is 0.442 GeV/ c . It is also useful to note that

$$E_{\text{cm}} dE_{\text{cm}} = m_2 dE_{1\text{lab}} = m_2 \beta_{1\text{lab}} dp_{\text{lab}}. \quad (47.7)$$

47.3. Lorentz-invariant amplitudes

The matrix elements for a scattering or decay process are written in terms of an invariant amplitude $-i\mathcal{M}$. As an example, the S -matrix for $2 \rightarrow 2$ scattering is related to \mathcal{M} by

$$\begin{aligned} \langle p'_1 p'_2 | S | p_1 p_2 \rangle &= I - i(2\pi)^4 \delta^4(p_1 + p_2 - p'_1 - p'_2) \\ &\times \frac{\mathcal{M}(p_1, p_2; p'_1, p'_2)}{(2E_1)^{1/2} (2E_2)^{1/2} (2E'_1)^{1/2} (2E'_2)^{1/2}}. \end{aligned} \quad (47.8)$$

The state normalization is such that

$$\langle p' | p \rangle = (2\pi)^3 \delta^3(\mathbf{p} - \mathbf{p}') . \quad (47.9)$$

47.4. Particle decays

The partial decay rate of a particle of mass M into n bodies in its rest frame is given in terms of the Lorentz-invariant matrix element \mathcal{M} by

$$d\Gamma = \frac{(2\pi)^4}{2M} |\mathcal{M}|^2 d\Phi_n(P; p_1, \dots, p_n), \quad (47.10)$$

where $d\Phi_n$ is an element of n -body phase space given by

$$d\Phi_n(P; p_1, \dots, p_n) = \delta^4(P - \sum_{i=1}^n p_i) \prod_{i=1}^n \frac{d^3 p_i}{(2\pi)^3 2E_i} . \quad (47.11)$$

This phase space can be generated recursively, viz.

$$\begin{aligned} d\Phi_n(P; p_1, \dots, p_n) &= d\Phi_j(q; p_1, \dots, p_j) \\ &\times d\Phi_{n-j+1}(P; q, p_{j+1}, \dots, p_n) (2\pi)^3 dq^2 , \end{aligned} \quad (47.12)$$

where $q^2 = (\sum_{i=1}^j E_i)^2 - |\sum_{i=1}^j \mathbf{p}_i|^2$. This form is particularly useful in the case where a particle decays into another particle that subsequently decays.

47.4.1. Survival probability: If a particle of mass M has mean proper lifetime τ ($= 1/\Gamma$) and has momentum (E, \mathbf{p}) , then the probability that it lives for a time t_0 or greater before decaying is given by

$$P(t_0) = e^{-t_0 \Gamma/\gamma} = e^{-Mt_0 \Gamma/E} , \quad (47.13)$$

and the probability that it travels a distance x_0 or greater is

$$P(x_0) = e^{-Mx_0 \Gamma/|\mathbf{p}|} . \quad (47.14)$$

47.4.2. Two-body decays :

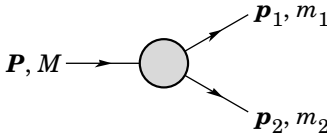


Figure 47.1: Definitions of variables for two-body decays.

In the rest frame of a particle of mass M , decaying into 2 particles labeled 1 and 2,

$$E_1 = \frac{M^2 - m_2^2 + m_1^2}{2M} , \quad (47.15)$$

$$|\mathbf{p}_1| = |\mathbf{p}_2|$$

$$= \frac{[(M^2 - (m_1 + m_2)^2)(M^2 - (m_1 - m_2)^2)]^{1/2}}{2M} , \quad (47.16)$$

and

$$d\Gamma = \frac{1}{32\pi^2} |\mathcal{M}|^2 \frac{|\mathbf{p}_1|}{M^2} d\Omega , \quad (47.17)$$

where $d\Omega = d\phi_1 d(\cos\theta_1)$ is the solid angle of particle 1. The invariant mass M can be determined from the energies and momenta using Eq. (47.2) with $M = E_{\text{cm}}$.

47.4.3. Three-body decays :

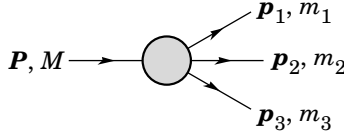


Figure 47.2: Definitions of variables for three-body decays.

Defining $p_{ij} = p_i + p_j$ and $m_{ij}^2 = p_{ij}^2$, then $m_{12}^2 + m_{23}^2 + m_{13}^2 = M^2 + m_1^2 + m_2^2 + m_3^2$ and $m_{12}^2 = (P - p_3)^2 = M^2 + m_3^2 - 2ME_3$, where E_3 is the energy of particle 3 in the rest frame of M . In that frame, the momenta of the three decay particles lie in a plane. The relative orientation of these three momenta is fixed if their energies are known. The momenta can therefore be specified in space by giving three Euler angles (α, β, γ) that specify the orientation of the final system relative to the initial particle [1]. Then

$$d\Gamma = \frac{1}{(2\pi)^5} \frac{1}{16M} |\mathcal{M}|^2 dE_1 dE_3 d\alpha d(\cos\beta) d\gamma. \quad (47.18)$$

Alternatively

$$d\Gamma = \frac{1}{(2\pi)^5} \frac{1}{16M^2} |\mathcal{M}|^2 |\mathbf{p}_1^*| |\mathbf{p}_3| dm_{12} d\Omega_1^* d\Omega_3, \quad (47.19)$$

where $(|\mathbf{p}_1^*|, \Omega_1^*)$ is the momentum of particle 1 in the rest frame of 1 and 2, and Ω_3 is the angle of particle 3 in the rest frame of the decaying particle. $|\mathbf{p}_1^*|$ and $|\mathbf{p}_3|$ are given by

$$|\mathbf{p}_1^*| = \frac{[(m_{12}^2 - (m_1 + m_2)^2)(m_{12}^2 - (m_1 - m_2)^2)]^{1/2}}{2m_{12}}, \quad (47.20a)$$

and

$$|\mathbf{p}_3| = \frac{[(M^2 - (m_{12} + m_3)^2)(M^2 - (m_{12} - m_3)^2)]^{1/2}}{2M}. \quad (47.20b)$$

[Compare with Eq. (47.16).]

If the decaying particle is a scalar or we average over its spin states, then integration over the angles in Eq. (47.18) gives

$$\begin{aligned} d\Gamma &= \frac{1}{(2\pi)^3} \frac{1}{8M} \overline{|\mathcal{M}|^2} dE_1 dE_3 \\ &= \frac{1}{(2\pi)^3} \frac{1}{32M^3} \overline{|\mathcal{M}|^2} dm_{12}^2 dm_{23}^2. \end{aligned} \quad (47.21)$$

This is the standard form for the Dalitz plot.

47.4.3.1. Dalitz plot: For a given value of m_{12}^2 , the range of m_{23}^2 is determined by its values when \mathbf{p}_2 is parallel or antiparallel to \mathbf{p}_3 :

$$(m_{23}^2)_{\max} = (E_2^* + E_3^*)^2 - \left(\sqrt{E_2^{*2} - m_2^2} - \sqrt{E_3^{*2} - m_3^2} \right)^2, \quad (47.22a)$$

$$(m_{23}^2)_{\min} = (E_2^* + E_3^*)^2 - \left(\sqrt{E_2^{*2} - m_2^2} + \sqrt{E_3^{*2} - m_3^2} \right)^2. \quad (47.22b)$$

Here $E_2^* = (m_{12}^2 - m_1^2 + m_2^2)/2m_{12}$ and $E_3^* = (M^2 - m_{12}^2 - m_3^2)/2m_{12}$ are the energies of particles 2 and 3 in the m_{12} rest frame. The scatter plot in m_{12}^2 and m_{23}^2 is called a Dalitz plot. If $|\mathcal{M}|^2$ is constant, the allowed region of the plot will be uniformly populated with events [see Eq. (47.21)]. A nonuniformity in the plot gives immediate information on $|\mathcal{M}|^2$. For example, in the case of $D \rightarrow K\pi\pi$, bands appear when $m_{(K\pi)} = m_{K^*(892)}$, reflecting the appearance of the decay chain $D \rightarrow K^*(892)\pi \rightarrow K\pi\pi$.

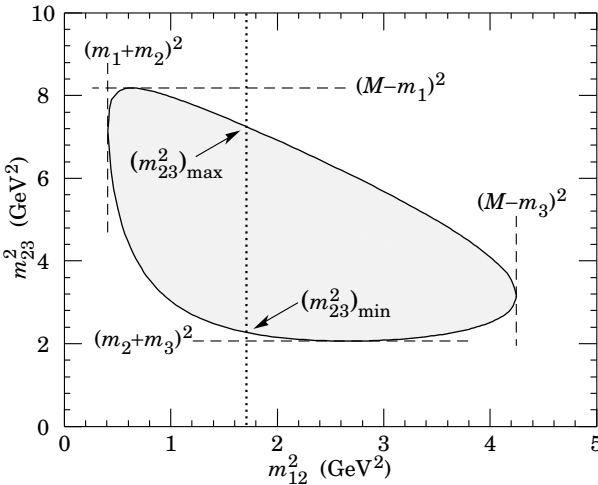


Figure 47.3: Dalitz plot for a three-body final state. In this example, the state is π^+K^0p at 3 GeV. Four-momentum conservation restricts events to the shaded region.

47.4.4. Kinematic limits :

47.4.4.1. Three-body decays: In a three-body decay (Fig. 47.2) the maximum of $|\mathbf{p}_3|$, [given by Eq. (47.20)], is achieved when $m_{12} = m_1 + m_2$, *i.e.*, particles 1 and 2 have the same vector velocity in the rest frame of the decaying particle. If, in addition, $m_3 > m_1, m_2$, then $|\mathbf{p}_3|_{\max} > |\mathbf{p}_1|_{\max}, |\mathbf{p}_2|_{\max}$. The distribution of m_{12} values possesses an end-point or maximum value at $m_{12} = M - m_3$. This can be used to constrain the mass difference of a parent particle and one invisible decay product.

47.4.5. Multibody decays : The above results may be generalized to final states containing any number of particles by combining some of the particles into “effective particles” and treating the final states as 2 or 3 “effective particle” states. Thus, if $p_{ijk\dots} = p_i + p_j + p_k + \dots$, then

$$m_{ijk\dots} = \sqrt{p_{ijk\dots}^2}, \quad (47.25)$$

and $m_{ijk\dots}$ may be used in place of *e.g.*, m_{12} in the relations in Sec. 47.4.3 or Sec. 47.4.4 above.

47.5. Cross sections

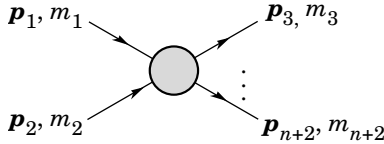


Figure 47.5: Definitions of variables for production of an n -body final state.

The differential cross section is given by

$$d\sigma = \frac{(2\pi)^4 |\mathcal{M}|^2}{4\sqrt{(p_1 \cdot p_2)^2 - m_1^2 m_2^2}} \times d\Phi_n(p_1 + p_2; p_3, \dots, p_{n+2}). \quad (47.26)$$

[See Eq. (47.11).] In the rest frame of m_2 (lab),

$$\sqrt{(p_1 \cdot p_2)^2 - m_1^2 m_2^2} = m_2 p_{1\text{lab}}; \quad (47.27a)$$

while in the center-of-mass frame

$$\sqrt{(p_1 \cdot p_2)^2 - m_1^2 m_2^2} = p_{1\text{cm}} \sqrt{s}. \quad (47.27b)$$

47.5.1. Two-body reactions :

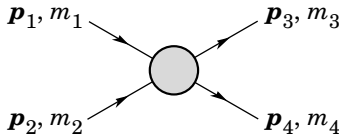


Figure 47.6: Definitions of variables for a two-body final state.

Two particles of momenta p_1 and p_2 and masses m_1 and m_2 scatter to particles of momenta p_3 and p_4 and masses m_3 and m_4 ; the Lorentz-invariant Mandelstam variables are defined by

$$s = (p_1 + p_2)^2 = (p_3 + p_4)^2 = m_1^2 + 2E_1 E_2 - 2\mathbf{p}_1 \cdot \mathbf{p}_2 + m_2^2, \quad (47.28)$$

$$t = (p_1 - p_3)^2 = (p_2 - p_4)^2 = m_1^2 - 2E_1 E_3 + 2\mathbf{p}_1 \cdot \mathbf{p}_3 + m_3^2, \quad (47.29)$$

$$\begin{aligned} u &= (p_1 - p_4)^2 = (p_2 - p_3)^2 \\ &= m_1^2 - 2E_1E_4 + 2\mathbf{p}_1 \cdot \mathbf{p}_4 + m_4^2, \end{aligned} \quad (47.30)$$

and they satisfy

$$s + t + u = m_1^2 + m_2^2 + m_3^2 + m_4^2. \quad (47.31)$$

The two-body cross section may be written as

$$\frac{d\sigma}{dt} = \frac{1}{64\pi s} \frac{1}{|\mathbf{p}_{1\text{cm}}|^2} |\mathcal{M}|^2. \quad (47.32)$$

In the center-of-mass frame

$$\begin{aligned} t &= (E_{1\text{cm}} - E_{3\text{cm}})^2 - (p_{1\text{cm}} - p_{3\text{cm}})^2 - 4p_{1\text{cm}} p_{3\text{cm}} \sin^2(\theta_{\text{cm}}/2) \\ &= t_0 - 4p_{1\text{cm}} p_{3\text{cm}} \sin^2(\theta_{\text{cm}}/2), \end{aligned} \quad (47.33)$$

where θ_{cm} is the angle between particle 1 and 3. The limiting values t_0 ($\theta_{\text{cm}} = 0$) and t_1 ($\theta_{\text{cm}} = \pi$) for $2 \rightarrow 2$ scattering are

$$t_0(t_1) = \left[\frac{m_1^2 - m_3^2 - m_2^2 + m_4^2}{2\sqrt{s}} \right]^2 - (p_{1\text{cm}} \mp p_{3\text{cm}})^2. \quad (47.34)$$

In the literature the notation t_{\min} (t_{\max}) for t_0 (t_1) is sometimes used, which should be discouraged since $t_0 > t_1$. The center-of-mass energies and momenta of the incoming particles are

$$E_{1\text{cm}} = \frac{s + m_1^2 - m_2^2}{2\sqrt{s}}, \quad E_{2\text{cm}} = \frac{s + m_2^2 - m_1^2}{2\sqrt{s}}, \quad (47.35)$$

For $E_{3\text{cm}}$ and $E_{4\text{cm}}$, change m_1 to m_3 and m_2 to m_4 . Then

$$p_{i\text{cm}} = \sqrt{E_{i\text{cm}}^2 - m_i^2} \text{ and } p_{1\text{cm}} = \frac{p_{1\text{lab}} m_2}{\sqrt{s}}. \quad (47.36)$$

Here the subscript lab refers to the frame where particle 2 is at rest. [For other relations see Eqs. (47.2)–(47.4).]

47.5.2. Inclusive reactions : Choose some direction (usually the beam direction) for the z -axis; then the energy and momentum of a particle can be written as

$$E = m_T \cosh y, \quad p_x, p_y, p_z = m_T \sinh y, \quad (47.37)$$

where m_T , conventionally called the ‘transverse mass’, is given by

$$m_T^2 = m^2 + p_x^2 + p_y^2. \quad (47.38)$$

and the rapidity y is defined by

$$\begin{aligned} y &= \frac{1}{2} \ln \left(\frac{E + p_z}{E - p_z} \right) \\ &= \ln \left(\frac{E + p_z}{m_T} \right) = \tanh^{-1} \left(\frac{p_z}{E} \right). \end{aligned} \quad (47.39)$$

Note that the definition of the transverse mass in Eq. (47.38) differs from that used by experimentalists at hadron colliders (see Sec. 47.6.1 below). Under a boost in the z -direction to a frame with velocity β , $y \rightarrow y - \tanh^{-1} \beta$. Hence the shape of the rapidity distribution dN/dy is invariant, as are differences in rapidity. The invariant cross section may

also be rewritten

$$E \frac{d^3 \sigma}{d^3 p} = \frac{d^3 \sigma}{d\phi dy p_T dp_T} \implies \frac{d^2 \sigma}{\pi dy d(p_T^2)}. \quad (47.40)$$

The second form is obtained using the identity $dy/dp_z = 1/E$, and the third form represents the average over ϕ .

Feynman's x variable is given by

$$x = \frac{p_z}{p_{z \max}} \approx \frac{E + p_z}{(E + p_z)_{\max}} \quad (p_T \ll |p_z|). \quad (47.41)$$

In the c.m. frame,

$$x \approx \frac{2p_{z \text{ cm}}}{\sqrt{s}} = \frac{2m_T \sinh y_{\text{cm}}}{\sqrt{s}} \quad (47.42)$$

and

$$= (y_{\text{cm}})_{\max} = \ln(\sqrt{s}/m). \quad (47.43)$$

The invariant mass M of the two-particle system described in Sec. 47.4.2 can be written in terms of these variables as

$$M^2 = m_1^2 + m_2^2 + 2[E_T(1)E_T(2) \cosh \Delta y - \mathbf{p}_T(1) \cdot \mathbf{p}_T(2)], \quad (47.44)$$

where

$$E_T(i) = \sqrt{|\mathbf{p}_T(i)|^2 + m_i^2}, \quad (47.45)$$

and $\mathbf{p}_T(i)$ denotes the transverse momentum vector of particle i .

For $p \gg m$, the rapidity [Eq. (47.39)] may be expanded to obtain

$$\begin{aligned} y &= \frac{1}{2} \ln \frac{\cos^2(\theta/2) + m^2/4p^2 + \dots}{\sin^2(\theta/2) + m^2/4p^2 + \dots} \\ &\approx -\ln \tan(\theta/2) \equiv \eta \end{aligned} \quad (47.46)$$

where $\cos \theta = p_z/p$. The pseudorapidity η defined by the second line is approximately equal to the rapidity y for $p \gg m$ and $\theta \gg 1/\gamma$, and in any case can be measured when the mass and momentum of the particle are unknown. From the definition one can obtain the identities

$$\sinh \eta = \cot \theta, \quad \cosh \eta = 1/\sin \theta, \quad \tanh \eta = \cos \theta. \quad (47.47)$$

47.5.3. Partial waves: The amplitude in the center of mass for elastic scattering of spinless particles may be expanded in Legendre polynomials

$$f(k, \theta) = \frac{1}{k} \sum_{\ell} (2\ell + 1) a_{\ell} P_{\ell}(\cos \theta), \quad (47.48)$$

where k is the c.m. momentum, θ is the c.m. scattering angle, $a_{\ell} = (\eta_{\ell} e^{2i\delta_{\ell}} - 1)/2i$, $0 \leq \eta_{\ell} \leq 1$, and δ_{ℓ} is the phase shift of the ℓ^{th} partial wave. For purely elastic scattering, $\eta_{\ell} = 1$. The differential cross section is

$$\frac{d\sigma}{d\Omega} = |f(k, \theta)|^2. \quad (47.49)$$

The optical theorem states that

$$\sigma_{\text{tot}} = \frac{4\pi}{k} \text{Im} f(k, 0), \quad (47.50)$$

and the cross section in the ℓ^{th} partial wave is therefore bounded:

$$\sigma_{\ell} = \frac{4\pi}{k^2} (2\ell + 1) |a_{\ell}|^2 \leq \frac{4\pi(2\ell + 1)}{k^2}. \quad (47.51)$$

47.5.3.1. Resonances: The Breit-Wigner (nonrelativistic) form for an elastic amplitude a_ℓ with a resonance at c.m. energy E_R , elastic width Γ_{el} , and total width Γ_{tot} is

$$a_\ell = \frac{\Gamma_{\text{el}}/2}{E_R - E - i\Gamma_{\text{tot}}/2}, \quad (47.54)$$

where E is the c.m. energy.

The spin-averaged Breit-Wigner cross section for a spin- J resonance produced in the collision of particles of spin S_1 and S_2 is

$$\sigma_{BW}(E) = \frac{(2J+1)}{(2S_1+1)(2S_2+1)} \frac{\pi}{k^2} \frac{B_{\text{in}}B_{\text{out}}\Gamma_{\text{tot}}^2}{(E-E_R)^2 + \Gamma_{\text{tot}}^2/4}, \quad (47.55)$$

where k is the c.m. momentum, E is the c.m. energy, and B_{in} and B_{out} are the branching fractions of the resonance into the entrance and exit channels. The $2S+1$ factors are the multiplicities of the incident spin states, and are replaced by 2 for photons. This expression is valid only for an isolated state. If the width is not small, Γ_{tot} cannot be treated as a constant independent of E . There are many other forms for σ_{BW} , all of which are equivalent to the one given here in the narrow-width case. Some of these forms may be more appropriate if the resonance is broad.

The relativistic Breit-Wigner form corresponding to Eq. (47.54) is:

$$a_\ell = \frac{-m\Gamma_{\text{el}}}{s - m^2 + im\Gamma_{\text{tot}}}. \quad (47.56)$$

A better form incorporates the known kinematic dependences, replacing $m\Gamma_{\text{tot}}$ by $\sqrt{s}\Gamma_{\text{tot}}(s)$, where $\Gamma_{\text{tot}}(s)$ is the width the resonance particle would have if its mass were \sqrt{s} , and correspondingly $m\Gamma_{\text{el}}$ by $\sqrt{s}\Gamma_{\text{el}}(s)$ where $\Gamma_{\text{el}}(s)$ is the partial width in the incident channel for a mass \sqrt{s} :

$$a_\ell = \frac{-\sqrt{s}\Gamma_{\text{el}}(s)}{s - m^2 + i\sqrt{s}\Gamma_{\text{tot}}(s)}. \quad (47.57)$$

For the Z boson, all the decays are to particles whose masses are small enough to be ignored, so on dimensional grounds $\Gamma_{\text{tot}}(s) = \sqrt{s}\Gamma_0/m_Z$, where Γ_0 defines the width of the Z , and $\Gamma_{\text{el}}(s)/\Gamma_{\text{tot}}(s)$ is constant. A full treatment of the line shape requires consideration of dynamics, not just kinematics. For the Z this is done by calculating the radiative corrections in the Standard Model.

47.6. Transverse variables

At hadron colliders, a significant and unknown proportion of the energy of the incoming hadrons in each event escapes down the beam-pipe. Consequently if invisible particles are created in the final state, their net momentum can only be constrained in the plane transverse to the beam direction. Defining the z -axis as the beam direction, this net momentum is equal to the missing energy vector

$$\mathbf{E}_T^{\text{miss}} = - \sum_i \mathbf{p}_T(i), \quad (47.58)$$

where the sum runs over the transverse momenta of all visible final state particles.

47.6.1. Single production with semi-invisible final state :

Consider a single heavy particle of mass M produced in association with visible particles which decays as in Fig. 47.1 to two particles, of which one (labeled particle 1) is invisible. The mass of the parent particle can be constrained with the quantity M_T defined by

$$\begin{aligned} M_T^2 &\equiv [E_T(1) + E_T(2)]^2 - [\mathbf{p}_T(1) + \mathbf{p}_T(2)]^2 \\ &= m_1^2 + m_2^2 + 2[E_T(1)E_T(2) - \mathbf{p}_T(1) \cdot \mathbf{p}_T(2)] , \end{aligned} \quad (47.59)$$

where

$$\mathbf{p}_T(1) = \mathbf{E}_T^{\text{miss}} . \quad (47.60)$$

This quantity is called the ‘transverse mass’ by hadron collider experimentalists but it should be noted that it is quite different from that used in the description of inclusive reactions [Eq. (47.38)]. The distribution of event M_T values possesses an end-point at $M_T^{\text{max}} = M$. If $m_1 = m_2 = 0$ then

$$M_T^2 = 2|\mathbf{p}_T(1)||\mathbf{p}_T(2)|(1 - \cos\phi_{12}) , \quad (47.61)$$

where ϕ_{ij} is defined as the angle between particles i and j in the transverse plane.

47.6.2. Pair production with semi-invisible final states :

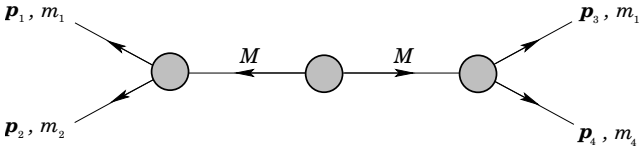


Figure 47.9: Definitions of variables for pair production of semi-invisible final states. Particles 1 and 3 are invisible while particles 2 and 4 are visible.

Consider two identical heavy particles of mass M produced such that their combined center-of-mass is at rest in the transverse plane (Fig. 47.9). Each particle decays to a final state consisting of an invisible particle of fixed mass m_1 together with an additional visible particle. M and m_1 can be constrained with the variables M_{T2} and M_{CT} which are defined in Refs. [4] and [5].

Further discussion and all references may be found in the full *Review of Particle Physics*. The numbering of references and equations used here corresponds to that version.

49. CROSS-SECTION FORMULAE FOR SPECIFIC PROCESSES

Revised October 2009 by H. Baer (University of Oklahoma) and R.N. Cahn (LBNL).

PART I: STANDARD MODEL PROCESSES

Setting aside leptoproduction (for which, see Sec. 16 of this *Review*), the cross sections of primary interest are those with light incident particles, e^+e^- , $\gamma\gamma$, $q\bar{q}$, gq , gg , etc., where g and q represent gluons and light quarks. The produced particles include both light particles and heavy ones - t , W , Z , and the Higgs boson H . We provide the production cross sections calculated within the Standard Model for several such processes.

49.1. Resonance Formation

Resonant cross sections are generally described by the Breit-Wigner formula (Sec. 19 of this *Review*).

$$\sigma(E) = \frac{2J+1}{(2S_1+1)(2S_2+1)} \frac{4\pi}{k^2} \left[\frac{\Gamma^2/4}{(E-E_0)^2 + \Gamma^2/4} \right] B_{in}B_{out}, \quad (49.1)$$

where E is the c.m. energy, J is the spin of the resonance, and the number of polarization states of the two incident particles are $2S_1+1$ and $2S_2+1$. The c.m. momentum in the initial state is k , E_0 is the c.m. energy at the resonance, and Γ is the full width at half maximum height of the resonance. The branching fraction for the resonance into the initial-state channel is B_{in} and into the final-state channel is B_{out} . For a narrow resonance, the factor in square brackets may be replaced by $\pi\Gamma\delta(E-E_0)/2$.

49.2. Production of light particles

The production of point-like, spin-1/2 fermions in e^+e^- annihilation through a virtual photon, $e^+e^- \rightarrow \gamma^* \rightarrow f\bar{f}$, at c.m. energy squared s is

$$\frac{d\sigma}{d\Omega} = N_c \frac{\alpha^2}{4s} \beta [1 + \cos^2\theta + (1-\beta^2)\sin^2\theta] Q_f^2, \quad (49.2)$$

where β is v/c for the produced fermions in the c.m., θ is the c.m. scattering angle, and Q_f is the charge of the fermion. The factor N_c is 1 for charged leptons and 3 for quarks. In the ultrarelativistic limit, $\beta \rightarrow 1$,

$$\sigma = N_c Q_f^2 \frac{4\pi\alpha^2}{3s} = N_c Q_f^2 \frac{86.8 \text{ nb}}{s(\text{GeV}^2)}. \quad (49.3)$$

The cross section for the annihilation of a $q\bar{q}$ pair into a distinct pair $q'\bar{q}'$ through a gluon is completely analogous up to color factors, with the replacement $\alpha \rightarrow \alpha_s$. Treating all quarks as massless, averaging over the colors of the initial quarks and defining $t = -s \sin^2(\theta/2)$, $u = -s \cos^2(\theta/2)$, one finds

$$\frac{d\sigma}{d\Omega}(q\bar{q} \rightarrow q'\bar{q}') = \frac{\alpha_s^2}{9s} \frac{t^2 + u^2}{s^2}. \quad (49.4)$$

Crossing symmetry gives

$$\frac{d\sigma}{d\Omega}(qq' \rightarrow qq') = \frac{\alpha_s^2}{9s} \frac{s^2 + u^2}{t^2}. \quad (49.5)$$

If the quarks q and q' are identical, we have

$$\frac{d\sigma}{d\Omega}(q\bar{q} \rightarrow q\bar{q}) = \frac{\alpha_s^2}{9s} \left[\frac{t^2 + u^2}{s^2} + \frac{s^2 + u^2}{t^2} - \frac{2u^2}{3st} \right], \quad (49.6)$$

and by crossing

$$\frac{d\sigma}{d\Omega}(qq \rightarrow qq) = \frac{\alpha_s^2}{9s} \left[\frac{t^2 + s^2}{u^2} + \frac{s^2 + u^2}{t^2} - \frac{2s^2}{3ut} \right]. \quad (49.7)$$

Annihilation of e^+e^- into $\gamma\gamma$ has the cross section

$$\frac{d\sigma}{d\Omega}(e^+e^- \rightarrow \gamma\gamma) = \frac{\alpha^2}{2s} \frac{u^2 + t^2}{tu}. \quad (49.8)$$

The related QCD process also has a triple-gluon coupling. The cross section is

$$\frac{d\sigma}{d\Omega}(q\bar{q} \rightarrow gg) = \frac{8\alpha_s^2}{27s}(t^2 + u^2)\left(\frac{1}{tu} - \frac{9}{4s^2}\right). \quad (49.9)$$

The crossed reactions are

$$\frac{d\sigma}{d\Omega}(qg \rightarrow qg) = \frac{\alpha_s^2}{9s}(s^2 + u^2)\left(-\frac{1}{su} + \frac{9}{4t^2}\right), \quad (49.10)$$

$$\frac{d\sigma}{d\Omega}(gg \rightarrow q\bar{q}) = \frac{\alpha_s^2}{24s}(t^2 + u^2)\left(\frac{1}{tu} - \frac{9}{4s^2}\right), \quad (49.11)$$

$$\frac{d\sigma}{d\Omega}(gg \rightarrow gg) = \frac{9\alpha_s^2}{8s}\left(3 - \frac{ut}{s^2} - \frac{su}{t^2} - \frac{st}{u^2}\right). \quad (49.12)$$

Lepton-quark scattering is analogous (neglecting Z exchange)

$$\frac{d\sigma}{d\Omega}(eq \rightarrow eq) = \frac{\alpha^2}{2s} e_q^2 \frac{s^2 + u^2}{t^2}, \quad (49.13)$$

e_q is the quark charge. For ν -scattering with the four-Fermi interaction

$$\frac{d\sigma}{d\Omega}(\nu d \rightarrow \ell^- u) = \frac{G_F^2 s}{4\pi^2}, \quad (49.14)$$

where the Cabibbo angle suppression is ignored. Similarly

$$\frac{d\sigma}{d\Omega}(\nu\bar{u} \rightarrow \ell^- \bar{d}) = \frac{G_F^2 s}{4\pi^2} \frac{(1 + \cos\theta)^2}{4}. \quad (49.15)$$

For deep inelastic scattering (presented in more detail in Section 19) we consider quarks of type i carrying a fraction $x = Q^2/(2M\nu)$ of the nucleon's energy, where $\nu = E - E'$ is the energy lost by the lepton in the nucleon rest frame. With $y = \nu/E$ we have the correspondences

$$1 + \cos\theta \rightarrow 2(1 - y), \quad d\Omega_{cm} \rightarrow 4\pi f_i(x) dx dy, \quad (49.16)$$

where the latter incorporates the quark distribution, $f_i(x)$. We find

$$\begin{aligned} \frac{d\sigma}{dx dy}(eN \rightarrow eX) &= \frac{4\pi\alpha^2 xs}{Q^4} \frac{1}{2} \left[1 + (1 - y)^2 \right] \\ &\times \left[\frac{4}{9}(u(x) + \bar{u}(x) + \dots) + \frac{1}{9}(d(x) + \bar{d}(x) + \dots) \right] \end{aligned} \quad (49.17)$$

where now $s = 2ME$ is the cm energy squared for the electron-nucleon collision and we have suppressed contributions from higher mass quarks.

Similarly,

$$\frac{d\sigma}{dx dy}(\nu N \rightarrow \ell^- X) = \frac{G_F^2 xs}{\pi} [(d(x) + \dots) + (1 - y)^2(\bar{u}(x) + \dots)], \quad (49.18)$$

$$\frac{d\sigma}{dx dy}(\bar{\nu} N \rightarrow \ell^+ X) = \frac{G_F^2 xs}{\pi} [(\bar{d}(x) + \dots) + (1 - y)^2(u(x) + \dots)]. \quad (49.19)$$

Quasi-elastic neutrino scattering ($\nu_\mu n \rightarrow \mu^- p$, $\bar{\nu}_\mu p \rightarrow \mu^+ n$) is directly related to the crossed reaction, neutron decay.

49.3. Hadroproduction of heavy quarks

For hadroproduction of heavy quarks $Q = c, b, t$, it is important to include mass effects in the formulae. For $q\bar{q} \rightarrow Q\bar{Q}$, one has

$$\frac{d\sigma}{d\Omega}(q\bar{q} \rightarrow Q\bar{Q}) = \frac{\alpha_s^2}{9s^3} \sqrt{1 - \frac{4m_Q^2}{s}} \left[(m_Q^2 - t)^2 + (m_Q^2 - u)^2 + 2m_Q^2 s \right], \quad (49.20)$$

while for $gg \rightarrow Q\bar{Q}$ one has

$$\begin{aligned} \frac{d\sigma}{d\Omega}(gg \rightarrow Q\bar{Q}) = & \frac{\alpha_s^2}{32s} \sqrt{1 - \frac{4m_Q^2}{s}} \left[\frac{6}{s^2} (m_Q^2 - t)(m_Q^2 - u) \right. \\ & - \frac{m_Q^2(s - 4m_Q^2)}{3(m_Q^2 - t)(m_Q^2 - u)} + \frac{4(m_Q^2 - t)(m_Q^2 - u) - 2m_Q^2(m_Q^2 + t)}{3(m_Q^2 - t)^2} \\ & + \frac{4(m_Q^2 - t)(m_Q^2 - u) - 2m_Q^2(m_Q^2 + u)}{3(m_Q^2 - u)^2} \\ & \left. - 3 \frac{(m_Q^2 - t)(m_Q^2 - u) + m_Q^2(u - t)}{s(m_Q^2 - t)} - 3 \frac{(m_Q^2 - t)(m_Q^2 - u) + m_Q^2(t - u)}{s(m_Q^2 - u)} \right]. \end{aligned} \quad (49.21)$$

49.4. Production of Weak Gauge Bosons

49.4.1. W and Z resonant production :

Resonant production of a single W or Z is governed by the partial widths

$$\Gamma(W \rightarrow \ell_i \bar{\nu}_i) = \frac{\sqrt{2} G_F m_W^3}{12\pi} \quad (49.22)$$

$$\Gamma(W \rightarrow q_i \bar{q}_j) = 3 \frac{\sqrt{2} G_F |V_{ij}|^2 m_W^3}{12\pi} \quad (49.23)$$

$$\begin{aligned} \Gamma(Z \rightarrow f\bar{f}) = & N_c \frac{\sqrt{2} G_F m_Z^3}{6\pi} \\ & \times \left[(T_3 - Q_f \sin^2 \theta_W)^2 + (Q_f \sin^2 \theta_W)^2 \right]. \end{aligned} \quad (49.24)$$

The weak mixing angle is θ_W . The CKM matrix elements are V_{ij} . N_c is 3 for $q\bar{q}$ and 1 for leptonic final states. These widths along with associated branching fractions may be applied to the resonance production formula of Sec. 49.1 to gain the total W or Z production cross section.

49.4.2. Production of pairs of weak gauge bosons :

The cross section for $f\bar{f} \rightarrow W^+W^-$ is given in term of the couplings of the left-handed and right-handed fermion f , $\ell = 2(T_3 - Qx_W)$, $r = -2Qx_W$, where T_3 is the third component of weak isospin for the left-handed f , Q is its electric charge (in units of the proton charge), and $x_W = \sin^2 \theta_W$:

$$\begin{aligned} \frac{d\sigma}{dt} = & \frac{2\pi\alpha^2}{N_c s^2} \left\{ \left[\left(Q + \frac{\ell + r}{4x_W} \frac{s}{s - m_Z^2} \right)^2 + \left(\frac{\ell - r}{4x_W} \frac{s}{s - m_Z^2} \right)^2 \right] A(s, t, u) \right. \\ & + \frac{1}{2x_W} \left(Q + \frac{\ell}{2x_W} \frac{s}{s - m_Z^2} \right) (\Theta(-Q)I(s, t, u) - \Theta(Q)I(s, u, t)) \\ & \left. + \frac{1}{8x_W^2} (\Theta(-Q)E(s, t, u) + \Theta(Q)E(s, u, t)) \right\}, \end{aligned} \quad (49.26)$$

where $\Theta(x)$ is 1 for $x > 0$ and 0 for $x < 0$, and where

$$\begin{aligned} A(s, t, u) &= \left(\frac{tu}{m_W^4} - 1 \right) \left(\frac{1}{4} - \frac{m_W^2}{s} + 3 \frac{m_W^4}{s^2} \right) + \frac{s}{m_W^2} - 4, \\ I(s, t, u) &= \left(\frac{tu}{m_W^4} - 1 \right) \left(\frac{1}{4} - \frac{m_W^2}{2s} - \frac{m_W^4}{st} \right) + \frac{s}{m_W^2} - 2 + 2 \frac{m_W^2}{t}, \\ E(s, t, u) &= \left(\frac{tu}{m_W^4} - 1 \right) \left(\frac{1}{4} + \frac{m_W^4}{t^2} \right) + \frac{s}{m_W^2}, \end{aligned} \quad (49.27)$$

and s, t, u are the usual Mandelstam variables with $s = (p_f + p_{\bar{f}})^2$, $t = (p_f - p_{W^-})^2$, $u = (p_f - p_{W^+})^2$. The factor N_c is 3 for quarks and 1 for leptons.

The analogous cross-section for $q_i \bar{q}_j \rightarrow W^\pm Z^0$ is

$$\begin{aligned} \frac{d\sigma}{dt} &= \frac{\pi \alpha^2 |V_{ij}|^2}{6s^2 x_W^2} \left\{ \left(\frac{1}{s - m_W^2} \right)^2 \left[\left(\frac{9 - 8x_W}{4} \right) (ut - m_W^2 m_Z^2) \right. \right. \\ &\quad \left. \left. + (8x_W - 6) s (m_W^2 + m_Z^2) \right] \right. \\ &\quad \left. + \left[\frac{ut - m_W^2 m_Z^2 - s(m_W^2 + m_Z^2)}{s - m_W^2} \right] \left[\frac{\ell_j}{t} - \frac{\ell_i}{u} \right] \right. \\ &\quad \left. + \frac{ut - m_W^2 m_Z^2}{4(1 - x_W)} \left[\frac{\ell_j^2}{t^2} + \frac{\ell_i^2}{u^2} \right] + \frac{s(m_W^2 + m_Z^2)}{2(1 - x_W)} \frac{\ell_i \ell_j}{tu} \right\}, \end{aligned} \quad (49.28)$$

where ℓ_i and ℓ_j are the couplings of the left-handed q_i and q_j as defined above. The CKM matrix element between q_i and q_j is V_{ij} .

The cross section for $q_i \bar{q}_i \rightarrow Z^0 Z^0$ is

$$\frac{d\sigma}{dt} = \frac{\pi \alpha^2}{96} \frac{\ell_i^4 + r_i^4}{x_W^2 (1 - x_W^2)^2 s^2} \left[\frac{t}{u} + \frac{u}{t} + \frac{4m_Z^2 s}{tu} - m_Z^4 \left(\frac{1}{t^2} + \frac{1}{u^2} \right) \right]. \quad (49.29)$$

49.5. Production of Higgs Bosons

49.5.1. Resonant Production :

The Higgs boson of the Standard Model can be produced resonantly in the collisions of quarks, leptons, W or Z bosons, gluons, or photons. The production cross section is thus controlled by the partial width of the Higgs boson into the entrance channel and its total width. The partial widths are given by the relations

$$\Gamma(H \rightarrow f \bar{f}) = \frac{G_F m_f^2 m_H N_c}{4\pi\sqrt{2}} \left(1 - 4m_f^2/m_H^2 \right)^{3/2}, \quad (49.30)$$

$$\Gamma(H \rightarrow W^+ W^-) = \frac{G_F m_H^3 \beta_W}{32\pi\sqrt{2}} \left(4 - 4a_W + 3a_W^2 \right), \quad (49.31)$$

$$\Gamma(H \rightarrow ZZ) = \frac{G_F m_H^3 \beta_Z}{64\pi\sqrt{2}} \left(4 - 4a_Z + 3a_Z^2 \right). \quad (49.32)$$

where N_c is 3 for quarks and 1 for leptons and where $a_W = 1 - \beta_W^2 = 4m_W^2/m_H^2$ and $a_Z = 1 - \beta_Z^2 = 4m_Z^2/m_H^2$. The decay to two gluons proceeds through quark loops, with the t quark dominating. Explicitly,

$$\Gamma(H \rightarrow gg) = \frac{\alpha_s^2 G_F m_H^3}{36\pi^3 \sqrt{2}} \left| \sum_q I(m_q^2/m_H^2) \right|^2, \quad (49.33)$$

where $I(z)$ is complex for $z < 1/4$. For $z < 2 \times 10^{-3}$, $|I(z)|$ is small so the light quarks contribute negligibly. For $m_H < 2m_t$, $z > 1/4$ and

$$I(z) = 3 \left[2z + 2z(1 - 4z) \left(\sin^{-1} \frac{1}{2\sqrt{z}} \right)^2 \right], \quad (49.34)$$

which has the limit $I(z) \rightarrow 1$ as $z \rightarrow \infty$.

49.5.2. Higgs Boson Production in W^* and Z^* decay :

The Standard Model Higgs boson can be produced in the decay of a virtual W or Z (“Higgstrahlung”): In particular, if k is the c.m. momentum of the Higgs boson,

$$\sigma(q_i \bar{q}_j \rightarrow WH) = \frac{\pi \alpha^2 |V_{ij}|^2}{36 \sin^4 \theta_W} \frac{2k}{\sqrt{s}} \frac{k^2 + 3m_W^2}{(s - m_W^2)^2} \quad (49.35)$$

$$\sigma(f \bar{f} \rightarrow ZH) = \frac{2\pi \alpha^2 (\ell_f^2 + r_f^2)}{48 N_c \sin^4 \theta_W \cos^4 \theta_W} \frac{2k}{\sqrt{s}} \frac{k^2 + 3m_Z^2}{(s - m_Z^2)^2}. \quad (49.36)$$

where ℓ and r are defined as above.

49.5.3. W and Z Fusion :

Just as high-energy electrons can be regarded as sources of virtual photon beams, at very high energies they are sources of virtual W and Z beams. For Higgs boson production, it is the longitudinal components of the W s and Z s that are important. The distribution of longitudinal W s carrying a fraction y of the electron’s energy is

$$f(y) = \frac{g^2}{16\pi^2} \frac{1-y}{y}, \quad (49.37)$$

where $g = e/\sin \theta_W$. In the limit $s \gg m_H \gg m_W$, the rate $\Gamma(H \rightarrow W_L W_L) = (g^2/64\pi)(m_H^3/m_W^2)$ and in the equivalent W approximation

$$\begin{aligned} \sigma(e^+ e^- \rightarrow \bar{\nu}_e \nu_e H) &= \frac{1}{16m_W^2} \left(\frac{\alpha}{\sin^2 \theta_W} \right)^3 \\ &\times \left[\left(1 + \frac{m_H^2}{s} \right) \log \frac{s}{m_H^2} - 2 + 2 \frac{m_H^2}{s} \right]. \end{aligned} \quad (49.38)$$

There are significant corrections to this relation when m_H is not large compared to m_W . For $m_H = 150$ GeV, the estimate is too high by 51% for $\sqrt{s} = 1000$ GeV, 32% too high at $\sqrt{s} = 2000$ GeV, and 22% too high at $\sqrt{s} = 4000$ GeV. Fusion of ZZ to make a Higgs boson can be treated similarly. Identical formulae apply for Higgs production in the collisions of quarks whose charges permit the emission of a W^+ and a W^- , except that QCD corrections and CKM matrix elements are required. Even in the absence of QCD corrections, the fine-structure constant ought to be evaluated at the scale of the collision, say m_W . All quarks contribute to the ZZ fusion process.

Further discussion and all references may be found in the full *Review*; the equation and reference numbering corresponds to that version.

50. Neutrino Cross Section Measurements*

Revised August 2015 by G.P. Zeller (Fermilab)

This section has been abridged from the full version of the *Review*.

Neutrino cross sections are an essential ingredient in all neutrino experiments. Interest in neutrino scattering has recently increased due to the need for such information in the interpretation of neutrino oscillation data. Both charged current (CC) and neutral current (NC) channels have been collected over many decades using a variety of targets, analysis techniques, and detector technologies. This work summarizes accelerator-based neutrino cross section measurements performed in the $\sim 0.1 - 300$ GeV range with an emphasis on inclusive, quasi-elastic, and pion production processes, areas where we have the most experimental input at present (Table 50.1 and Table 50.2).

Table 50.1: List of beam properties, nuclear targets, and durations for modern accelerator-based neutrino experiments.

Experiment	beam	$\langle E_\nu \rangle, \langle E_{\bar{\nu}} \rangle$ GeV	neutrino target(s)	run period
ArgoNeuT	$\nu, \bar{\nu}$	4.3, 3.6	Ar	2009 – 2010
ICARUS	ν	20.0	Ar	2010 – 2012
K2K	ν	1.3	CH, H ₂ O	2003 – 2004
MicroBooNE	ν	0.8	Ar	2015 –
MINERvA	$\nu, \bar{\nu}$	3.5 (LE), 5.5 (ME)	He, CH, H ₂ O, Fe, Pb	2009 –
MiniBooNE	$\nu, \bar{\nu}$	0.8, 0.7	CH ₂	2002 – 2012
MINOS	$\nu, \bar{\nu}$	3.5, 6.1	Fe	2004 –
NOMAD	$\nu, \bar{\nu}$	23.4, 19.7	C	1995 – 1998
NOvA	$\nu, \bar{\nu}$	2.0, 2.0	CH ₂	2010 –
SciBooNE	$\nu, \bar{\nu}$	0.8, 0.7	CH	2007 – 2008
T2K	$\nu, \bar{\nu}$	0.6, 0.6	CH, H ₂ O	2010 –

Table 50.2: Summary of published neutrino cross section measurements. All measurements are ν_μ or $\bar{\nu}_\mu$ scattering with the exception of the last column which is a ν_e measurement.

Experiment	inclusive	0π	π^\pm	π^0	ν_e
ArgoNeuT	CC	2p	CC	–	–
K2K	–	CC	CC	CC,NC	–
MINERvA	CC	CC,1p	CC	CC	–
MiniBooNE	–	CC, M_A ,NC	CC	CC,	–
MINOS	CC	M_A	–	–	–
NOMAD	CC	CC	–	NC	–
SciBooNE	CC	–	CC	NC	–
T2K	CC	CC,NC	–	–	CC

50.1. Inclusive Scattering

Experiments have measured the total inclusive cross section for neutrino ($\nu_\mu N \rightarrow \mu^- X$) and antineutrino ($\bar{\nu}_\mu N \rightarrow \mu^+ X$) scattering off nucleons covering a broad range of neutrino energies. As can be seen in Fig. 50.1, the inclusive cross section approaches a linear dependence on neutrino energy. Such behavior is expected for point-like scattering of neutrinos from quarks, an assumption which breaks down at lower energies.

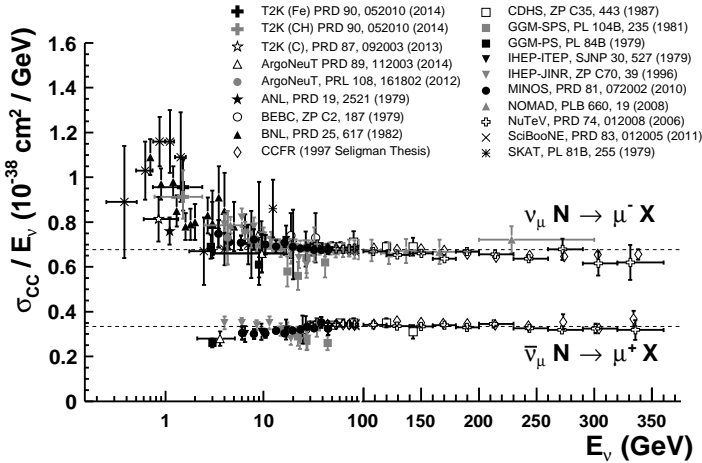


Figure 50.1: Measurements of ν_μ and $\bar{\nu}_\mu$ CC inclusive scattering cross sections (per nucleon) divided by neutrino energy as a function of neutrino energy.

50.2. Quasi-elastic scattering

Quasi-elastic (QE) scattering is the dominant neutrino interaction for neutrino energies less than ~ 1 GeV and represents a large fraction of the signal samples in many neutrino oscillation experiments. Historically, neutrino (antineutrino) quasi-elastic scattering refers to the process, $\nu_\mu n \rightarrow \mu^- p$ ($\bar{\nu}_\mu p \rightarrow \mu^+ n$), where a charged lepton and single nucleon are ejected in the elastic interaction of a neutrino (or antineutrino) with a nucleon in the target material.

50.3. Pion Production

In addition to such elastic processes, neutrinos can also inelastically scatter producing a nucleon excited state (Δ , N^*). Such baryonic resonances quickly decay, most often to a nucleon and single-pion final state. Furthermore, neutrinos can also coherently scatter off of the entire nucleus and produce a distinctly forward-scattered single pion final state. Both CC ($\nu_\mu A \rightarrow \mu^- A \pi^+$, $\bar{\nu}_\mu A \rightarrow \mu^+ A \pi^-$) and NC ($\nu_\mu A \rightarrow \nu_\mu A \pi^0$, $\bar{\nu}_\mu A \rightarrow \bar{\nu}_\mu A \pi^0$) processes are possible in this case. Even though the level of coherent pion production is small compared to resonant processes, observations exist across a broad energy range and on multiple nuclear targets [64].

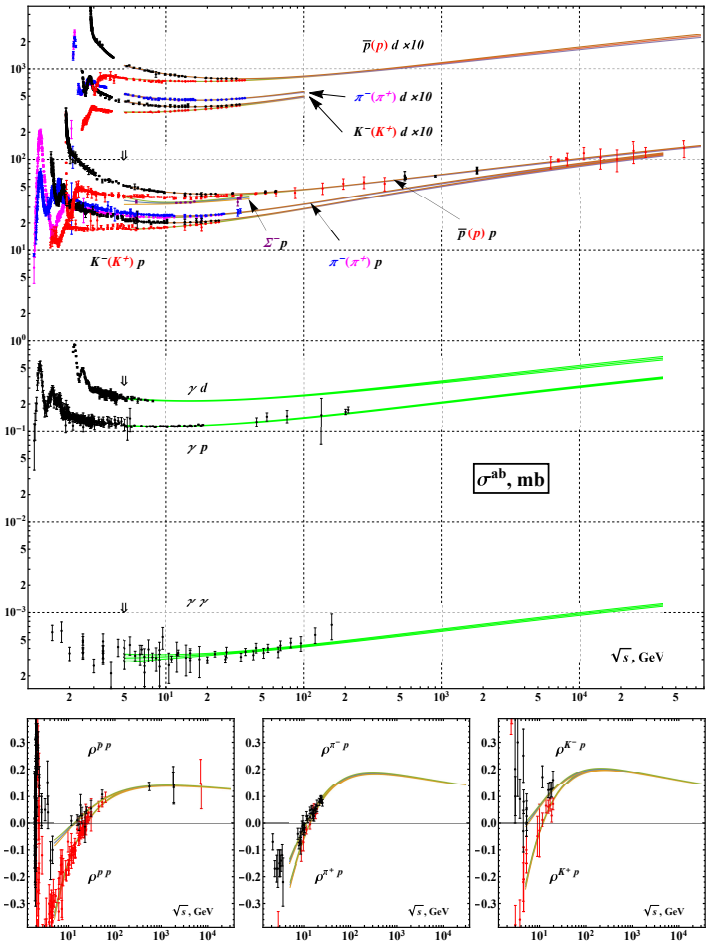


Figure 51.8: Summary of $h^\mp p \rightarrow \text{anything}$, $\gamma p \rightarrow \text{hadrons}$, $\gamma\gamma \rightarrow \text{hadrons}$ total cross sections σ^{ab} in mb and $\rho^{h^\mp p}$ the ratio of real to imaginary parts of the forward hadronic amplitudes. Also for qualitative comparison of the uniformity of data description by HPR₁R₂-mod el across the different collisions and observables. The uncertainties for the experimental data points include both the statistical and systematic errors. Curves, corresponding to fit above 5 GeV cut, are plotted with error bands calculated with parameter covariance matrix constructed on MC-propagated vectors from 95% quantile of the empirical distribution. Corresponding computer-readable data files may be found at <http://pdg.lbl.gov/current/xsect/>. (Courtesy of the COMPAS group, IHEP, Protvino, June 2016.)

6. ATOMIC AND NUCLEAR PROPERTIES OF MATERIALS

Table 6.1. Abridged from pdg.lbl.gov/AtomicNuclearProperties by D. E. Groom (2015). Quantities in parentheses are for gases at 20° C and 1 atm. Boiling points are at 1 atm. Refractive indices n are evaluated at the sodium D line blend (589.2 nm); values $\gg 1$ in brackets are for $(n - 1) \times 10^6$ (gases) at 0° C and 1 atm.

Material	Z	A	$\langle Z/A \rangle$	Nucl.coll. length λ_T {g cm ⁻² }	Nucl.inter. length λ_I {g cm ⁻² }	Rad.len. X_0 {g cm ⁻² }	$dE/dx _{\min}$ { MeV g ⁻¹ cm ² }	Density {g cm ⁻³ } {(gℓ ⁻¹)}	Melting point (K)	Boiling point (K)	Refract. index @ Na D
H ₂	1	1.008(7)	0.99212	42.8	52.0	63.04	(4.103)	0.071(0.084)	13.81	20.28	1.11[132.]
D ₂	1	2.01410177803(8)	0.49650	51.3	71.8	125.97	(2.053)	0.169(0.168)	18.7	23.65	1.11[138.]
He	2	4.002602(2)	0.49967	51.8	71.0	94.32	(1.937)	0.125(0.166)		4.220	1.02[35.0]
Li	3	6.94(2)	0.43221	52.2	71.3	82.78	1.639	0.534	453.6	1615.	
Be	4	9.0121831(5)	0.44384	55.3	77.8	65.19	1.595	1.848	1560.	2744.	
C diamond	6	12.0107(8)	0.49955	59.2	85.8	42.70	1.725	3.520			2.42
C graphite	6	12.0107(8)	0.49955	59.2	85.8	42.70	1.742	2.210			
N ₂	7	14.007(2)	0.49976	61.1	89.7	37.99	(1.825)	0.807(1.165)	63.15	77.29	1.20[298.]
O ₂	8	15.999(3)	0.50002	61.3	90.2	34.24	(1.801)	1.141(1.332)	54.36	90.20	1.22[271.]
F ₂	9	18.998403163(6)	0.47372	65.0	97.4	32.93	(1.676)	1.507(1.580)	53.53	85.03	[195.]
Ne	10	20.1797(6)	0.49555	65.7	99.0	28.93	(1.724)	1.204(0.839)	24.56	27.07	1.09[67.1]
Al	13	26.9815385(7)	0.48181	69.7	107.2	24.01	1.615	2.699	933.5	2792.	
Si	14	28.0855(3)	0.49848	70.2	108.4	21.82	1.664	2.329	1687.	3538.	3.95
Cl ₂	17	35.453(2)	0.47951	73.8	115.7	19.28	(1.630)	1.574(2.980)	171.6	239.1	[773.]
Ar	18	39.948(1)	0.45059	75.7	119.7	19.55	(1.519)	1.396(1.662)	83.81	87.26	1.23[281.]
Ti	22	47.867(1)	0.45961	78.8	126.2	16.16	1.477	4.540	1941.	3560.	
Fe	26	55.845(2)	0.46557	81.7	132.1	13.84	1.451	7.874	1811.	3134.	
Cu	29	63.546(3)	0.45636	84.2	137.3	12.86	1.403	8.960	1358.	2835.	
Ge	32	72.630(1)	0.44053	86.9	143.0	12.25	1.370	5.323	1211.	3106.	
Sn	50	118.710(7)	0.42119	98.2	166.7	8.82	1.263	7.310	505.1	2875.	
Xe	54	131.293(6)	0.41129	100.8	172.1	8.48	(1.255)	2.953(5.483)	161.4	165.1	1.39[701.]
W	74	183.84(1)	0.40252	110.4	191.9	6.76	1.145	19.300	3695.	5828.	
Pt	78	195.084(9)	0.39983	112.2	195.7	6.54	1.128	21.450	2042.	4098.	
Au	79	196.966569(5)	0.40108	112.5	196.3	6.46	1.134	19.320	1337.	3129.	
Pb	82	207.2(1)	0.39575	114.1	199.6	6.37	1.122	11.350	600.6	2022.	
U	92	[238.02891(3)]	0.38651	118.6	209.0	6.00	1.081	18.950	1408.	4404.	

Air (dry, 1 atm)	0.49919	61.3	90.1	36.62	(1.815)	(1.205)		78.80	
Shielding concrete	0.50274	65.1	97.5	26.57	1.711	2.300			
Borosilicate glass (Pyrex)	0.49707	64.6	96.5	28.17	1.696	2.230			
Lead glass	0.42101	95.9	158.0	7.87	1.255	6.220			
Standard rock	0.50000	66.8	101.3	26.54	1.688	2.650			
Methane (CH ₄)	0.62334	54.0	73.8	46.47	(2.417)	(0.667)	90.68	111.7	[444.]
Ethane (C ₂ H ₆)	0.59861	55.0	75.9	45.66	(2.304)	(1.263)	90.36	184.5	
Butane (C ₄ H ₁₀)	0.59497	55.5	77.1	45.23	(2.278)	(2.489)	134.9	272.6	
Octane (C ₈ H ₁₈)	0.57778	55.8	77.8	45.00	2.123	0.703	214.4	398.8	
Paraffin (CH ₃ (CH ₂) _n ≈23CH ₃)	0.57275	56.0	78.3	44.85	2.088	0.930			
Nylon (type 6, 6/6)	0.54790	57.5	81.6	41.92	1.973	1.18			
Polycarbonate (Lexan)	0.52697	58.3	83.6	41.50	1.886	1.20			
Polyethylene ((CH ₂ CH ₂) _n)	0.57034	56.1	78.5	44.77	2.079	0.89			
Polyethylene terephthalate (Mylar)	0.52037	58.9	84.9	39.95	1.848	1.40			
Polymethylmethacrylate (acrylic)	0.53937	58.1	82.8	40.55	1.929	1.19			1.49
Polypropylene	0.55998	56.1	78.5	44.77	2.041	0.90			
Polystyrene ((C ₆ H ₅ CHCH ₂) _n)	0.53768	57.5	81.7	43.79	1.936	1.06			1.59
Polytetrafluoroethylene (Teflon)	0.47992	63.5	94.4	34.84	1.671	2.20			
Polyvinyltoluene	0.54141	57.3	81.3	43.90	1.956	1.03			1.58
Aluminum oxide (sapphire)	0.49038	65.5	98.4	27.94	1.647	3.970	2327.	3273.	1.77
Barium fluoride (BaF ₂)	0.42207	90.8	149.0	9.91	1.303	4.893	1641.	2533.	1.47
Carbon dioxide gas (CO ₂)	0.49989	60.7	88.9	36.20	1.819	(1.842)			[449.]
Solid carbon dioxide (dry ice)	0.49989	60.7	88.9	36.20	1.787	1.563	Sublimes at 194.7 K		
Cesium iodide (CsI)	0.41569	100.6	171.5	8.39	1.243	4.510	894.2	1553.	1.79
Lithium fluoride (LiF)	0.46262	61.0	88.7	39.26	1.614	2.635	1121.	1946.	1.39
Lithium hydride (LiH)	0.50321	50.8	68.1	79.62	1.897	0.820	965.		
Lead tungstate (PbWO ₄)	0.41315	100.6	168.3	7.39	1.229	8.300	1403.		2.20
Silicon dioxide (SiO ₂ , fused quartz)	0.49930	65.2	97.8	27.05	1.699	2.200	1986.	3223.	1.46
Sodium chloride (NaCl)	0.47910	71.2	110.1	21.91	1.847	2.170	1075.	1738.	1.54
Sodium iodide (NaI)	0.42697	93.1	154.6	9.49	1.305	3.667	933.2	1577.	1.77
Water (H ₂ O)	0.55509	58.5	83.3	36.08	1.992	1.000(0.756)	273.1	373.1	1.33
Silica aerogel	0.50093	65.0	97.3	27.25	1.740	0.200	(0.03 H ₂ O, 0.97 SiO ₂)		

Table 4.1. Revised June 2016 by D.E. Groom (LBNL). The atomic number (top left) is the number of protons in the nucleus. The atomic masses (bottom) of stable elements are weighted by isotopic abundances in the Earth's surface. Atomic masses are relative to the mass of ^{12}C , defined to be exactly 12 unified atomic mass units (u) (approx. g/mole). The exceptions are Th, Pa, and U, which have no stable isotopes but do have characteristic terrestrial compositions. Relative isotopic abundances often vary considerably, both in natural and commercial samples; this is reflected in the number of significant figures given for the mass. Masses may be found at http://physics.nist.gov/cgi-bin/Compositions/stand_alone.pl. If there is no stable isotope the atomic mass of the most stable isotope is given in parentheses. IUPAC announced verification of the discoveries of elements 113, 115, 117, and 118 in December 2015. Provisional names were assigned in June 2016. The 7th period of the periodic table is now complete.

1 IA																		18 VIIIA									
1 H hydrogen 1.008	2 He helium 4.002602																										
3 Li lithium 6.94		4 Be beryllium 9.012182		PERIODIC TABLE OF THE ELEMENTS														5 B boron 10.81	6 C carbon 12.0107	7 N nitrogen 14.007	8 O oxygen 15.999	9 F fluorine 18.998403163	10 Ne neon 20.1797				
11 Na sodium 22.98976928		12 Mg magnesium 24.305		13 Al aluminum 26.9815385	14 Si silicon 28.085	15 P phosph. 30.973761998	16 S sulfur 32.06	17 Cl chlorine 35.45	18 Ar argon 39.948																		
19 K potassium 39.0983	20 Ca calcium 40.078	21 Sc scandium 44.955908	22 Ti titanium 47.867	23 V vanadium 50.9415	24 Cr chromium 51.9961	25 Mn manganese 54.938044	26 Fe iron 55.845	27 Co cobalt 58.933195	28 Ni nickel 58.6934	29 Cu copper 63.546	30 Zn zinc 65.38	31 Ga gallium 69.723	32 Ge german. 72.630	33 As arsenic 74.921595	34 Se selenium 78.971	35 Br bromine 79.904	36 Kr krypton 83.798										
37 Rb rubidium 85.4678	38 Sr strontium 87.62	39 Y yttrium 88.90584	40 Zr zirconium 91.224	41 Nb niobium 92.90637	42 Mo molybd. 95.95	43 Tc technet. 97.907212	44 Ru ruthen. 101.07	45 Rh rhodium 102.90550	46 Pd palladium 106.42	47 Ag silver 107.8682	48 Cd cadmium 112.414	49 In indium 114.818	50 Sn tin 118.710	51 Sb antimony 121.760	52 Te tellurium 127.60	53 I iodine 126.90447	54 Xe xenon 131.293										
55 Cs cesium 132.90545196	56 Ba barium 137.327	57-71 Lanthanides	72 Hf hafnium 178.49	73 Ta tantalum 180.94788	74 W tungsten 183.84	75 Re rhenium 186.207	76 Os osmium 190.23	77 Ir iridium 192.217	78 Pt platinum 195.084	79 Au gold 196.966569	80 Hg mercury 200.592	81 Tl thallium 204.38	82 Pb lead 207.2	83 Bi bismuth 208.98040	84 Po polonium (208.98243)	85 At astatine (209.98715)	86 Rn radon (222.01758)										
87 Fr francium (223.01974)	88 Ra radium (226.02541)	89-103 Actinides	104 Rf rutherford. (267.12169)	105 Db dubnium (268.12567)	106 Sg seaborg. (271.13393)	107 Bh bohrium (270.13429)	108 Hs hassium (269.13429)	109 Mt meitner. (276.15159)	110 Ds darmstadt. (281.16451)	111 Rg roentgen. (280.16514)	112 Cn copernicium (285.17712)	113 Nh nihonium (284.17873)	114 Fl flerovium (289.19042)	115 Mc (moscovium) (288.19274)	116 Lv livermorium (293.20449)	117 Ts (tennessine) (292.20746)	118 Og (oganesson) (294.21392)										
Lanthanide series		57 La lanthan. 138.90547	58 Ce cerium 140.116	59 Pr praseodym. 140.90765	60 Nd neodym. 144.242	61 Pm prometh. (144.91276)	62 Sm samarium 150.36	63 Eu europium 151.964	64 Gd gadolin. 157.25	65 Tb terbium 158.92535	66 Dy dyspros. 162.500	67 Ho holmium 164.93033	68 Er erbium 167.259	69 Tm thulium 168.93422	70 Yb ytterbium 173.054	71 Lu lutetium 174.9668											
Actinide series		89 Ac actinium (227.02775)	90 Th thorium 232.0377	91 Pa protactin. 231.03588	92 U uranium 238.02891	93 Np neptunium (237.04817)	94 Pu plutonium (244.06420)	95 Am americ. (243.06138)	96 Cm curium (247.07035)	97 Bk berkelium (247.07031)	98 Cf californ. (251.07959)	99 Es einstein. (252.08298)	100 Fm fermium (257.09511)	101 Md mendelev. (258.09844)	102 No nobelium (259.10103)	103 Lr lawrenc. (262.10961)											